

W E A T H E R F O R E C A S T S
AND
THE EFFECTS OF THE SUB-GRID SCALE PROCESSES

B Y

K. M I Y A K O D A

GEOPHYSICAL FLUID DYNAMICS LABORATORY
PRINCETON UNIVERSITY
PRINCETON, NEW JERSEY, U.S.A.

1. Outline

The atmospheric disturbances and meteorological phenomena extend over a wide range of spectra in the time and space scales. In discussing weather forecasts, therefore, it is necessary to define precisely what time and space scales of disturbance are to be treated.

Is there any simple way to classify atmospheric disturbances? An example of the time spectrum for wind intensity was obtained by Oort and Taylor (1969) (Fig. 1.1), using the wind observation at 30 ~ 80 feet above the ground at Caribou, Maine (46.9°N latitude, 150 miles away from the coast). In this spectrum, one finds that there are several peaks in the magnitude, i.e., 24 hour (diurnal) 3~ 6 days, approximately 12 hours (inertia), 1 year (annual), 2 minutes (thermals), 30 days, 0.5 year (semi-annual). It is known, however, that the intensity of diurnal variation decreases rapidly with increasing height.

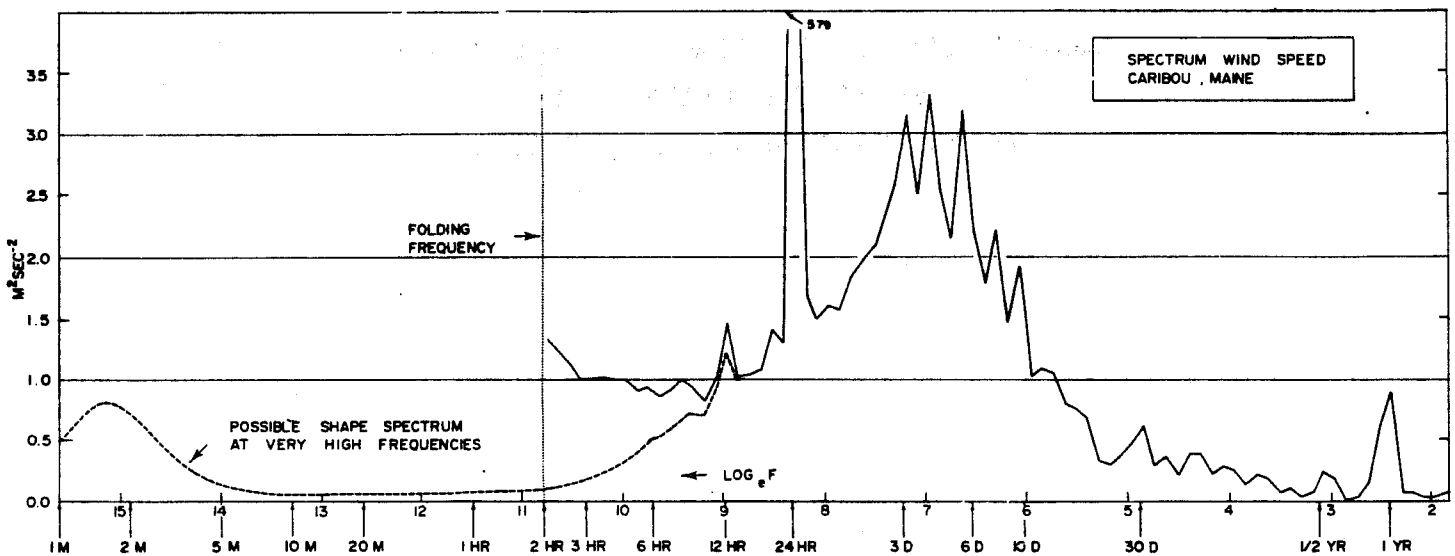


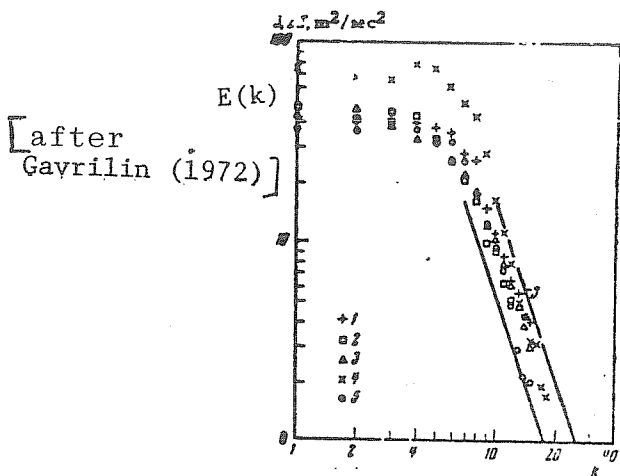
FIGURE 1.1 Results of an attempt to correct the spectrum at Caribou, Maine, for the effects of aliasing from periods between 1 min (the basic averaging period of the wind reports) and 2 hr (the Nyquist frequency). Frequency F in cycles/4096 days.

(after Oort and Taylor, 1969)

The largest peak is at 3~6 days corresponding to the passage of cyclones in the middle latitude. One interesting aspect is that there is apparently a spectral gap between 2 hour and 10 minutes, where little energy is contained. Another point is that there is no significant peaks beyond the period 3~6 days except probably the 30 day, 0.5 year and 1 year periods. The biennial oscillation is well known, but it does not show up in the spectrum at this latitude. This means that the idea of utilizing any particular frequency does not work for weather forecasts except for the annual variation, of course.

Let us next turn to the spatial spectrum. If one takes a zonal belt at the middle latitude and decomposes the wind velocity in the belt into the one-dimensional Fourier series, the spectrum of the kinetic energy appears as in figure 1.2. Let k be the wave number in the zonal direction, and $E(k)$ be the spectral intensity defined by

$$\int_0^{\infty} E(k) dk = \frac{1}{2} (u^2 + v^2)$$



- 1) Saltzman and Fleischer (1962)
 - 2) Horn and Bryson (1963)
(-8/3 law)
 - 3) Wiin-Nielsen (1967)
(-3 law)
 - 4) Kao and Wendell (1970)
 - 5) Julian et al. (1970)
- Morel and Necco (1973)

Fig. 1.2: One-dimensional kinetic energy spectra according to various authors.

One important characteristic is that, in contrast to the frequency spectrum, no peak is found in the wavenumber spectrum except the first mode. The largest energy is retained in the planetary scale and long waves (wavenumber 1 ~5), and secondly in the baroclinic waves (wavenumber 6 ~10), and then the spectral curve declines monotonously with increase of wavenumber. Thus the quantitative representation of the spectrum for the atmospheric kinetic energy does not provide a guide to the classification of atmospheric disturbances. However, we know in practice that there are many meteorological phenomena in which kinetic energy is intensely concentrated. For the purpose of defining our forecast problems, therefore, it is more appropriate to classify the atmospheric disturbances in a somewhat subjective way as shown in Figure 1.3.

This diagram was prepared by Orlanski (1975) for the SESAME planning conference (Severe Environmental Storms and Meso-Scale Experiment). In atmospheric dynamics there are some basic characteristic scales of length and time such as the radius of the earth (a), the scale height of the atmosphere (H), a period ($2\pi/\Omega$) of the sun's diurnal cycle, and the local effective period (f^{-1}) of the earth's rotation. Further, there are some combined auxiliary scales such as Rossby's radius of deformation

$$L_R = H/f \left[\frac{g}{\theta} \frac{\partial \theta}{\partial z} \right]^{1/2},$$

the variation of the earth's rotation with latitude (Rossby parameter), and the Brunt-Väisälä period, $N^{-1} = \left[\frac{g}{\theta} \frac{\partial \theta}{\partial z} \right]^{-1}$.

Utilizing figure 1.3 we may construct another diagram to delineate the prediction problem (figure 1.4). It is customary to classify weather

SCALE DEFINITION				10,000 KM	2,000 KM	200 KM	20 KM	2 KM	200 M	20 M	MONTH $(\frac{1}{24} \frac{dt}{dt})$	DAY $(\frac{1}{24})$	HOUR $(\frac{1}{24} \frac{dt}{dt})^{-1/2}$	MINUTE $(\frac{1}{24})^{-1/2} (\frac{1}{60})$	SEC
MACRO-SCALE	MACRO-SCALE		MACRO-SCALE	Standing waves	Ultra long waves	Tidal waves									MACRO- α SCALE
					Beroclinic waves										MACRO- β SCALE
INTERMEDIATE SCALE						Fronts and Hurricanes									MESO- α SCALE
							Nocturnal low level jet Squall lines Inertial waves Cloud clusters Mtn. & Lake Disturbances								MESO- β SCALE
MESO-SCALE	MESO-SCALE		MESO-SCALE					Thunderstorms I.G.W. C.A.T. Urban effects							MESO- γ SCALE
									Tornadoes Deep convection Short gravity waves						MICRO- α SCALE
										Dust devils Thermals Wakes					MICRO- β SCALE
MICRO-SCALE	MICRO-SCALE		MICRO-SCALE												MICRO- γ SCALE
JAPANESE NOMENCLATURE	EUROPEAN NOMENCLATURE	G.A.T.E.	U.S.A. NOMENCLATURE	C.A.S.	CLIMATOLOGICAL SCALE	SYNOPTIC AND PLANETARY SCALE	MESO-SCALE	MICRO-SCALE							PROPOSED DEFINITION

Fig. 1.3: Scale definitions and different processes with characteristic time and horizontal scales. (After Orlanski, 1975).

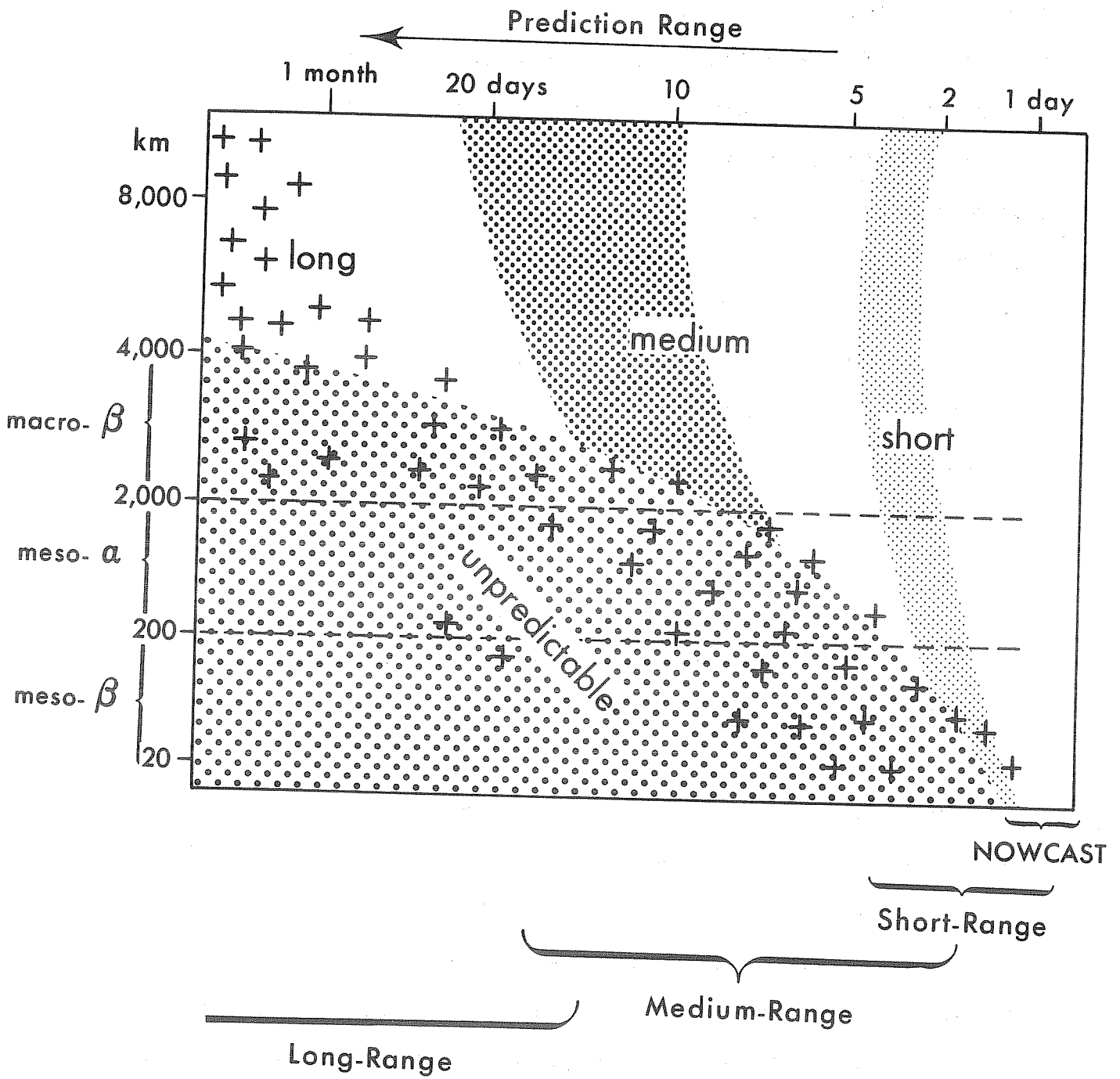
forecasts into two categories, i.e., the short range and the long range, where the former forecast is deterministic and the latter is probably non-deterministic, that is, of a statistical nature. The time limit for dividing these two ranges is considered to be two or 3 weeks. Recently people have been talking about the "nowcast" and "climate forecasts," but we did not include these two in the present discussion, since the nowcast is useful but not a prediction problem and the climate problem is interesting but has not developed into a really tractable problem.

It is a current practice to further divide the short-range forecast into the short range in a narrow sense and the medium range. The former treats the forecasts for time range of less than 2 days, which is being implemented successfully at a number of the operational centers all over the world. The medium range forecasts cover the rest of the deterministic range, i.e., from 2 days to 20 days. Thus the present short range forecast of 2 days does not include the 3~ 6 day peak in the frequency spectrum. However, in the foreseeable future the time range of the operational forecast may be extended, to say 5 days.

In 1971, a GARP study conference met at Oslo, Norway and specified four types of prediction experiments as described in Table 1.

<i>Type of Experiment</i>	<i>Time Span</i>	<i>Space scale</i>		
		<i>Large</i>	<i>Medium</i>	<i>Small</i>
I	12 to 48 hours		X	X
II	2 to 5 days	X	X	X
III	10 to 15 days	X	X	
IV	more than 15 days	X	X	

Note: It should be noted that the types of experiments are defined as a combination of the space and time scales. In view of the fact that each number corresponds to a particular time-span, one might be tempted to associated these intervals with ranges of predictability.



In this table, large scale includes wavelengths larger than 6,000 km; medium scale wavelengths between 2,000 km and 6,000 km, and small scale is wavelengths smaller than 2,000 km. Therefore this table does not entirely differ from the classifications discussed earlier.

Let us specify for this lecture that the short-range forecast corresponds to the predictions in Experiment I, in which the spatial scale of disturbances are meso- α (200 ~ 2,000 km), and macro- β (2,000 ~ 10,000 km). Macro- α (> 10,000 km) can be included but is not the main target. The medium range forecasts are the prediction Experiments II and III, in which the scale of disturbances are mostly macro β and macro α . In this range forecast, one geographic location experiences passage of more than two cyclones. Old cyclones decay or merge into other cyclones, and second generation cyclones will be created in about 5 days.

In this lecture, we discuss the problems of the short range and medium range forecasts, leaving out the long range forecasts. First, the present status will be explained, and secondly we will discuss possible improvements of these forecasts. The possibilities for revision are numerous, for example, the initial data, the model's resolution, the internal physics, the external effects and the numerical accuracy. In this respect, however, we shall discuss only the problem of subgrid scale parameterization. This lecture is by no means a review in this field, but is my personal view. It is the picture spot-lighted from the speaker's particular angle at GFDL/NOAA, Princeton, New Jersey. U.S.A.

2. Progress in the short-range forecasts

(i) Examples

We show examples here from two different numerical models at GFDL. The first example is the forecast by a global finite difference model made by Umscheid in 1974 (see Figure 2.1). The resolution is $N=48$ and 9 vertical levels in the latitude-longitude grid model where N is the number of gridpoints between the equator and pole; the grid size is $\Delta S = 220$ km in the meridional direction. The initial time is 00 GMT March 1, 1965. The 2 day prognostic charts of the geopotential height is shown.

The second example is the forecast of the same case done by Gordon and Stern in 1974 with a global spectral model (Figure 2.2). The model has a horizontal resolution of $M=15$ as well as $M=32$ and 9 vertical levels, where M is the zonal wave number of the spherical harmonic function. The latitudinal gridpoints are $N=40$ and $N=20$ for $M=32$ at $M=15$, respectively. $M=32$ seems to roughly correspond to $N=40$ finite difference model, and $M=15$ to $N=20$. The original barotropic version of the model was constructed by Bourke when he was in Montreal, Canada, and the model was given to Gordon in GFDL, who constructed the general circulation model from it. In this particular example, the spectral model did not include any physics besides the basic dynamics; the horizontal eddy viscosity was not incorporated.

(ii) Progress of operational forecasts

Figure 2.3 is a long record of the S1-score of operational 30 hour surface pressure forecast and 36 hour 500 mb height forecast at NMC, Washington, D. C. The "S1 score" developed by Teweles and Wobus (1954) is defined as

$$S_1 = 100 \frac{\sum |e_G|}{\sum |G_L|} \quad (2.1)$$

where e_G is an error in the forecast pressure difference (gradient) between selected stations or geographic locations, and G_L , is observed or forecast pressure difference(gradient), whichever is larger, and the data of specified stations over the U. S. are used. This record tells, therefore, how the skill has improved with the evolution of numerical models. Numerical weather prediction was started in 1958. It is seen that prior to 1958 the surface forecast had stayed at the same level of skill for a decade, and since April 1958,^{*} a significant improvement has been achieved. The NMC operational numerical prediction has gone through three eras in 17 years characterized by three different prognostic models, i.e., the barotropic, the 3-level geostrophic, and the 6-level primitive equation (PE) models.

When the 2-dimensional vorticity equation model was first introduced, the sudden improvement in the 500 mb height forecast was really remarkable. The surface forecast, however, remained almost the same level of

^{*} According to J. Smagorinsky, the numerical forecasts with machines were started at the Joint Numerical Weather Prediction Unit in 1955. It is, however, not certain whether the record in this figure includes these forecasts.

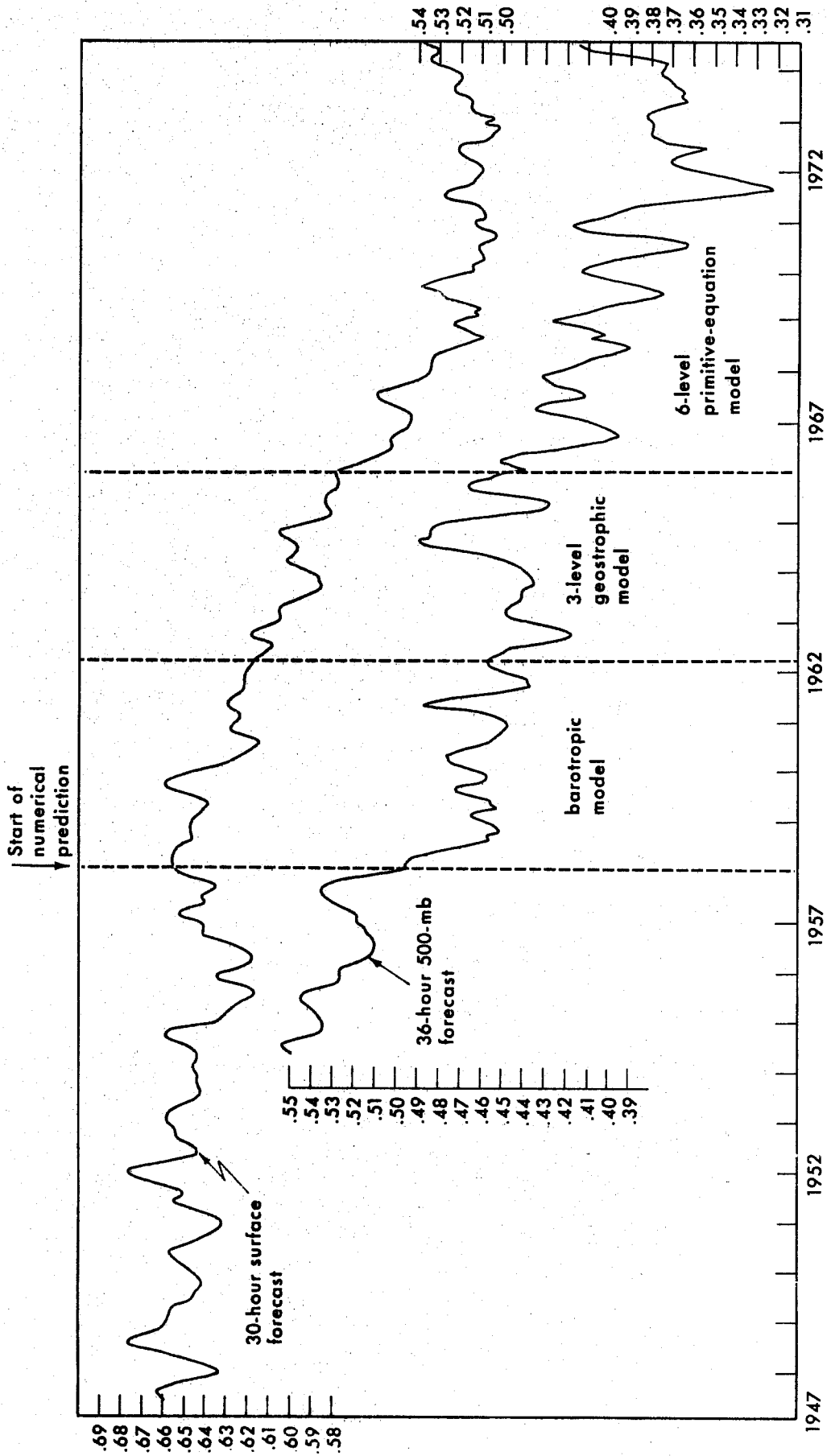


Fig. 2.3 NMC S1 - Scores

performance. In the 2nd era (July 1962 is the beginning) the 3-level quasi-geostrophic baroclinic model amended the surface pressure forecasts appreciably but not much for the 500 mb forecasts. In the 3rd era starting June, 1966, the 6-level non-filtered equation model replaced the geostrophic model, and the improvement was very pronounced. Even within the reign of one model the skill score was gradually improved; for example, from 1966 until 1972. Probably a number of minor improvements were made from time to time for example in detecting small code errors, adopting a better initialization, more accurate initial data, and probably more optimal physics. However, it is not known why the skill becomes worse after 1972. It may be that the natural trend is that way.

The skill score reflects the seasonal variations; it is better in the summer than in the winter. This tendency is clearer in the 500 mb score than in the surface pressure.

All these operational forecasts at NMC were based on the models in which grid size = 381 km. In 1971, the limited domain fine mesh model (LFM) was completed by Howcroft; the grid size is 190 km. Since then this model has been run experimentally and after February, 1975, it has been implemented operationally. Figure 2.4 is the S1-score for the 36 hour surface pressure and 36 hour 500 mb forecasts. It is demonstrated unquestionably that LFM gives a better score. Since 1972 some concern has been expressed that the numerical weather forecast may have reached an asymptotic level in performance. The LFM model has proven that the score could be further improved.



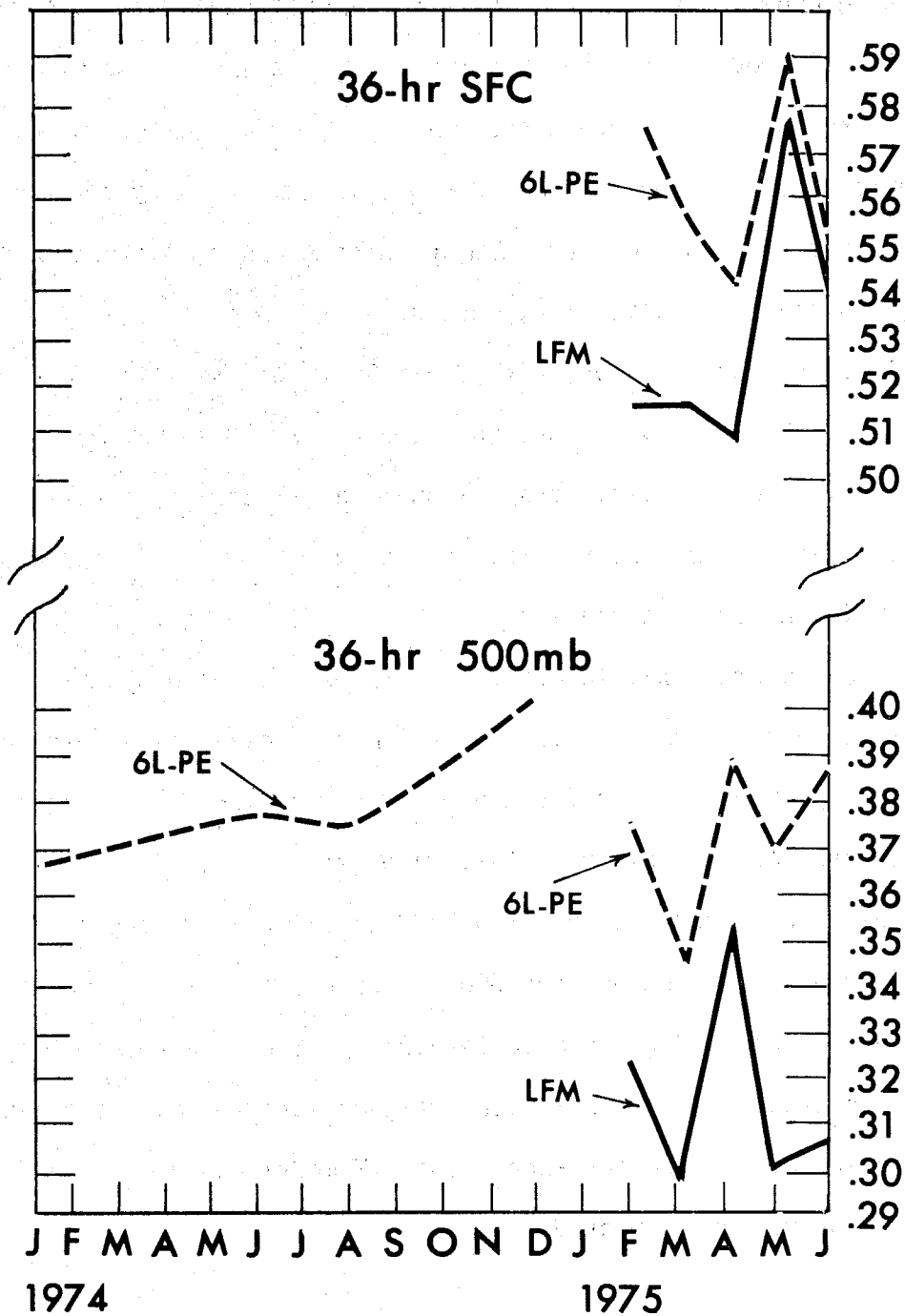


Figure 2.4

Let us next discuss the precipitation forecasts, which is one of the basic elements in weather prediction. The rain forecast has been particularly improved by LFM. The 12-24 hour forecast of measurable precipitation gave a threat score (explained below) of 0.37 for the LFM versus 0.33 for the PE. The threat score is the score of yes-or-no-rain (hit-and-miss) forecast, and calculated at one station, using a long series of rain forecast. The score is defined by

$$\frac{H}{O+F-H},$$

where O is the number of observed rain days, F is the number of forecasted rain days, and H is the number of correctly forecasted rain days.

Therefore, the perfect forecast is 1.00.

For a long time, the skill of the rain forecast at NMC was not raised until LFM was applied. NMC Newsletter reported that "in the first 6 months of 1975, the forecasters in the Basic Weather Branch reached new high levels of skill in forecasting the occurrence of precipitation in the 12 to 24-hour period." However, a number of LFM runs terminated before reaching 24 hours."

Figures 2.5 are the two monthly distributions of the threat score over the U.S. The rain forecasts were made by LFM in NMC and the threat scores have been calculated and accumulated for each month from December 1971 to June, 1975.

Looking at these figures, it may be found that (i) the maximum score is about .70; (ii) the score is better in winter than in summer; there is almost no skill in summer except in small areas in the northeast. (iii) the bad verification areas start to spread northward in June and rapidly in the western U.S. (iv) the mountain areas are generally worse, especially in summer.

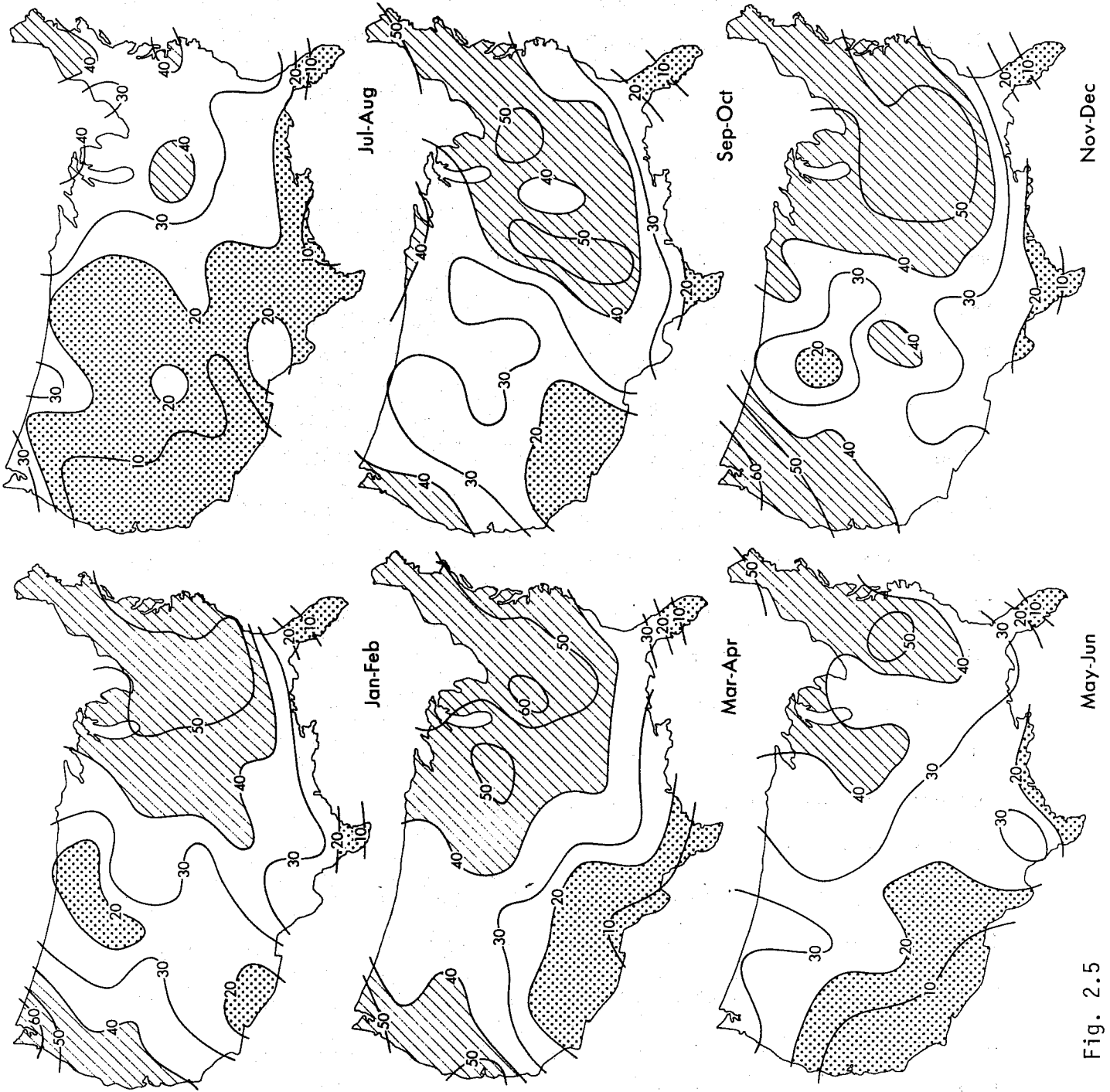


Fig. 2.5

(v) New England, Ohio Valley, State of Washington and the Eastern Seaboard are always in the regions of better skill scores, whereas Miami, Florida, and Brownsville, Texas are always in the regions of no skill.

3. Potential improvement of short-range forecasts

In order to make our discussion simple and clear, let us assume that our present operational level of technology is that of the NMC's LFM model (190 km grid size and 6 vertical levels) including the internal physics as well as the objective analysis and initialization. Then consider what possible changes in the system might improve the present short-range forecasts. Robert (1974) has discussed the error budget for the short-range prediction of the 500 mb geopotential over North America. He took a five-level model with a grid length of 381 km at 60°N, in which second order finite differences are used. His estimate of the error due to various factors is the following.

Horizontal truncation errors	38%
Vertical resolution	9
Time integration scheme	1
Data problems	18
Subgrid-scale physics	E 34%

He noted that the last item is only a crude estimate.

Our starting point is already better than Robert's as far as horizontal truncation errors is concerned, because LFM is available. Before proceeding to our discussion on the problem of improvement, let us first enumerate the factors to be considered. The numbers in brackets are index numbers.

Data: accurate initial condition	[1.1]
initialization (adjustment to model)	[1.2]
Model: spatial resolution	
horizontal (from 190 to 50 km grid size)	[2.1]

Vertical (from 6 to 30 levels)	[2.2]
Subgrid-scale processes	
Horizontal diffusion	[2.3]
Vertical diffusion	[2.4]
Planetary boundary layer	[2.5]
Cumulus convection	[2.6]
Cloud forecast	[2.7]

Computational stability and accuracy

More stable calculation of advective terms in connection with time derivative	[3.1]
Accurate calculation (from second order to fourth order finite difference)	[3.2]
Accurate calculation of water vapor advection	[3.3]
Accurate calculation of pressure gradient term	[3.4]
Lateral boundary condition (nested mesh)	[3.5]

External effects:

Diurnal variation	[4.1]
Soil moisture, snow, and heat conduction	[4.2]
Accurate sea surface temperature	[4.3]
Air-sea coupling	[4.4]
Steeper mountain	[4.5]

The degree of importance of these factors depends on the meteorological element to be forecasted. A forecast of the wind field at 500 mb requires different priorities from those needed for forecast of surface temperature or rain distribution. The situation is also different with respect to forecasts over North America or over the surrounding waters.

My tentative view on the order of importance for improving the 500 mb wind field forecast over North America, for example, is as follows, [2.1], [1.1], [2.2], [3.5], [2.6], [2.5], [1.2], [2.4], [4.1], [2.3], [3.3], [3.4], [2.7], [4.2], [4.3], [4.4].

This opinion is, however, not based on any firm ground.

The importance of the observed data in connection with accurate initial condition is clear; we will discuss this problem later in section 9. Likewise the subgrid-scale physics is also important, but it is convenient to discuss it separately later. In this section, we will take up the problems of spatial resolution, the nested grid model, and the isentropic analysis.

(1) Spatial resolution

How fine the resolution must be for weather forecasting is a practical question, but a clear-cut answer is not easy. Mathematical discussions have been attempted in numerous papers. But the practical problem requires us to consider complicated factors such as multiple wave components, the non-linearity of the governing equation, three dimensionality, and the inclusion of physical processes.

It has long been known that truncation error makes the predicted propagation speeds of waves too slow and more dispersive. This conclusion from the linear theory can be applied to practical numerical results with complicated models. Chouinard and Robert (1971, 1972), however, obtained the relationship between truncation error and spatial resolution from a model experiment. Figure 3.1 is the error as a function of the horizontal resolution in terms of N , the number of gridpoints between equator and pole. For example, $N=40$ corresponds to the grid size $S=270$ km. From this curve, Chouinard and Robert (1971) mentioned that the error is proportional to $(\Delta S)^2$, and $N=60$ km ($\Delta S \sim 203$ km) gives about 5% of the error in vorticity advection with the second order finite difference scheme. Merilees (1974) has recently studied this problem theoretically, using the wavenumber spectrum of the atmospheric disturbances, and mentioned that Chouinard and Robert's estimate is too optimistic, that the percentage of error estimates given were too small.

Merilees obtain the percentage of error formula as

$$E = \left\{ \begin{array}{ll} 147 \left(\frac{\Delta x_e}{\Delta x_o} \right)^2 & \text{2nd order finite difference} \\ 200 \left(\frac{\Delta x_e}{\Delta x_o} \right)^4 & \text{4th order finite difference} \end{array} \right.$$

where Δx_e is the computational grid size and Δx_o is the observational grid size.

Chouinard and Robert (1972) investigated the growth of vertical truncation error for 5 level and 14 level models. Figure 3.2 is the rms difference of geopotential height between the two models as a function of time. They concluded from this curve that 8 ~ 10 levels may be

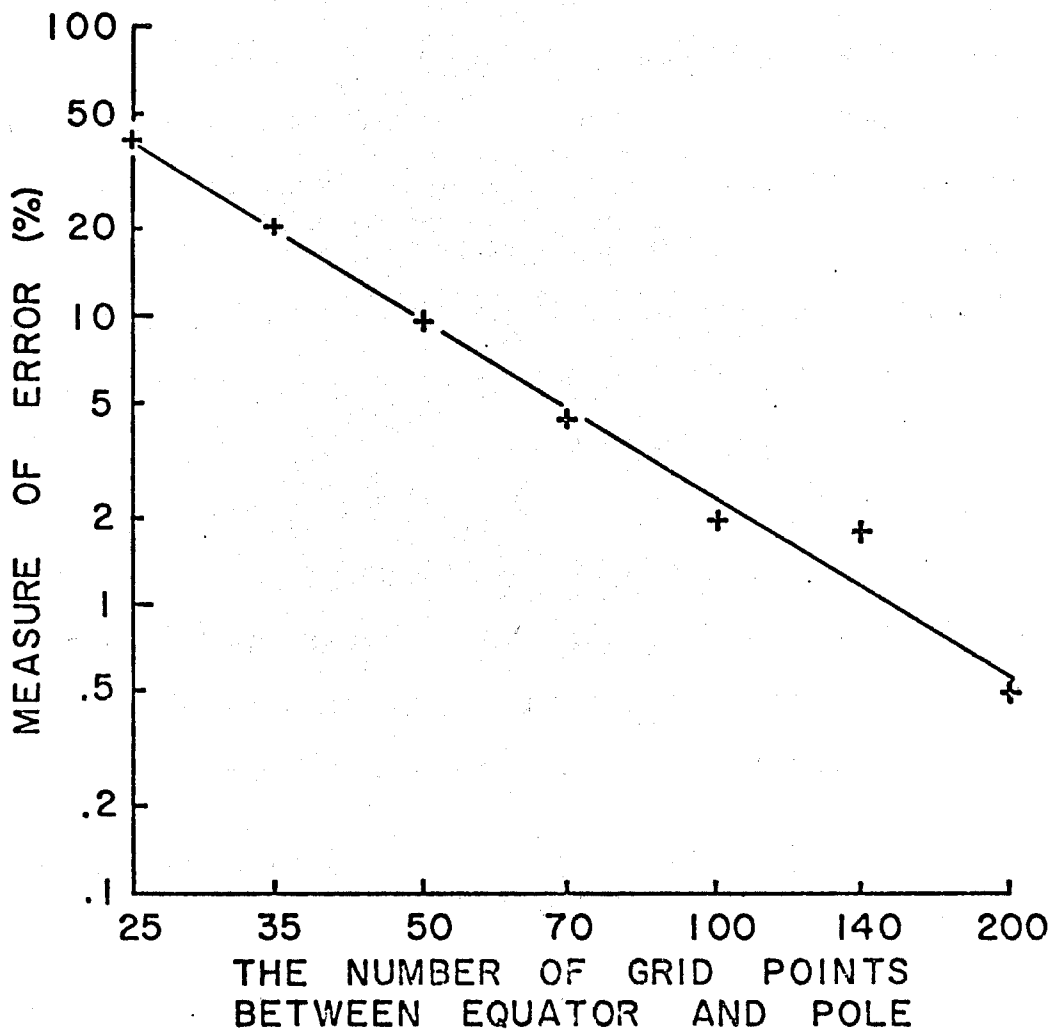


Fig. 3.1: Percentage error in the calculation of vorticity advection with second order finite difference approximations on a polar stereographic projection. Calculations were made from the 500 mb stream function over North America for 00 GMT 6 Nov. 1969. The full line is the curve with a -2 slope obtained from the autocorrelation statistics. (After Chouinard and Robert, 1971)

reasonable for the short-range forecasts. It is interesting to note that the rms difference is very large for 1000 mb maps, whereas it is small for 900 mb and increases with higher levels.

The advantage of the fourth order finite difference in the short-range forecasts has recently been discussed by Gerrity, McPherson and Polger (1972). However, a study on this problem with the full PE model including physics has not been made, so far as I know. The higher order difference should be applied to all terms in the model. Otherwise the advantages of the accurate scheme will be lost, and only the disadvantage might show up, because the higher order difference tends to lead to computational instability and makes it more difficult to maintain the conservation of the second order moment at the edge of the domain.

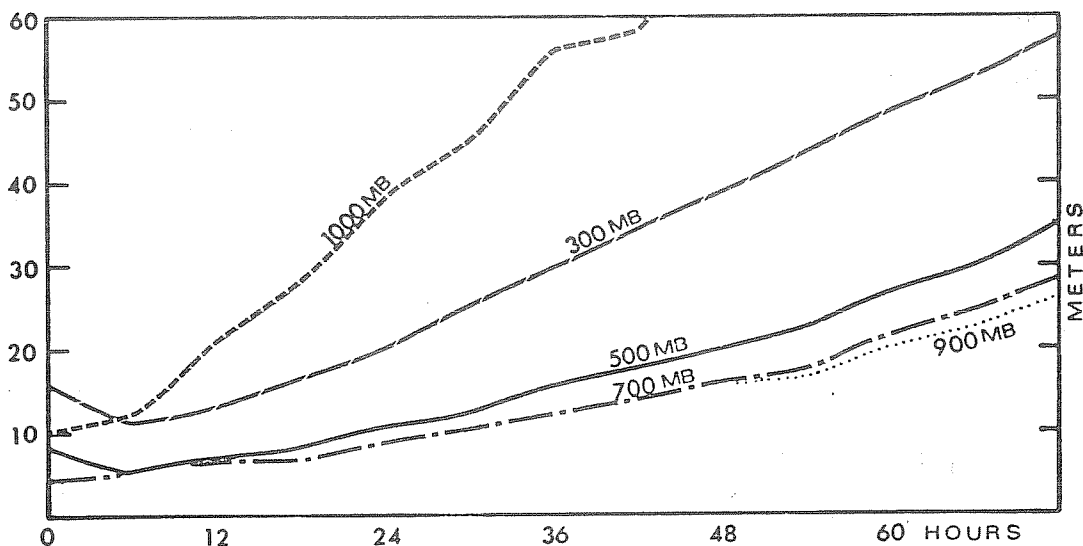


FIG. 3.2 Root-mean-square differences as a function of time between an integration with 5 levels and another one with 14 levels.

(after Chouinard and Robert, 1972)

The second point is that the aspect ratio of the horizontal and vertical resolution should be properly maintained, because otherwise, some imbalance will appear. This will be discussed later. Third, when more sophisticated physics are incorporated, the spatial mesh should be fine enough to resolve the physics. For example, the sophisticated parameterization of cumulus convection needs more vertical levels.

(ii) Nested grid model

The problem is old. In the 1960's, Birchfield (1960), Matsuno (1966), and Hill (1968) studied this problem. A model with a smaller domain of fine resolution is imbedded in the larger domain model of coarse resolution; the purpose is economy. There are two types of nesting procedures. One is the two way interaction between the smaller domain model and the surrounding model. The other is the one way action, i.e., the time series of lateral boundary condition is taken from the larger domain model and is imposed at the boundary of the small domain. For the hurricane problem, two-way interaction models have been used by several groups, but for the purpose of the short-range forecast, the one way action model tends to be more widely used.

Mathematically speaking, there is no perfect solution for the smaller domain in the nested grid system, in that the grids of the large and small domain are different. Yet in practice, the nested model is necessary, and it appears that an imperfect but reasonable solution does exist. In pursuing this solution, one encounters these questions concerning the nesting scheme. (i) What are the well posed boundary conditions for the set of equations in the prediction model, including the consideration of the finite difference approximation? (ii) Which variables, among many,

from the coarse mesh solution are appropriate to use for lateral boundary conditions for the fine mesh? It was demonstrated that methods utilizing their characteristics are too complicated to be used for this problem. (iii) which interpolation scheme is useful and efficient for getting the fine mesh boundary values from the coarse mesh solution? (iv) In order to minimize the computational sources of gravity waves, what methods are useful and desirable in preparing the boundary conditions? Is the balance arrangement required for the imposed variables? (v) Once the computational gravity waves are generated, which method is best for letting the waves go out smoothly from within the fine mesh domain to the outside? For example, is the radiation boundary condition satisfactory? For the purpose of alleviating the computational gravity waves, are Newtonian damping methods or the "sponge" method helpful in obtaining accurate solutions?

There are several groups that have recently been engaged in constructing and using nested, 3-dimensional PE models. One successful example is Williamson and Browning (1974), NCAR. They used one-way nesting and took the advected values from the coarse mesh as boundary conditions and applied the "sponge" treatment. A sample of their results is shown here (figure 3.3) for the two-day forecasts of surface pressure, in which the coarse grid is 5° , and the fine grids are of resolutions $2\text{-}1/2^\circ$, $1\text{-}1/4^\circ$ and $5/8^\circ$.

(iii) Isentropic analysis

In the last 3 years there has been a new surge of interest in the isentropic analysis (for example, Eliassen and Raustein, 1968, Shapiro and Hastings, 1974, Bleck, 1973, 1974, Danielsen, 1975, Shapiro, 1975). More than 20 years ago, the intense concentration of vorticity near the

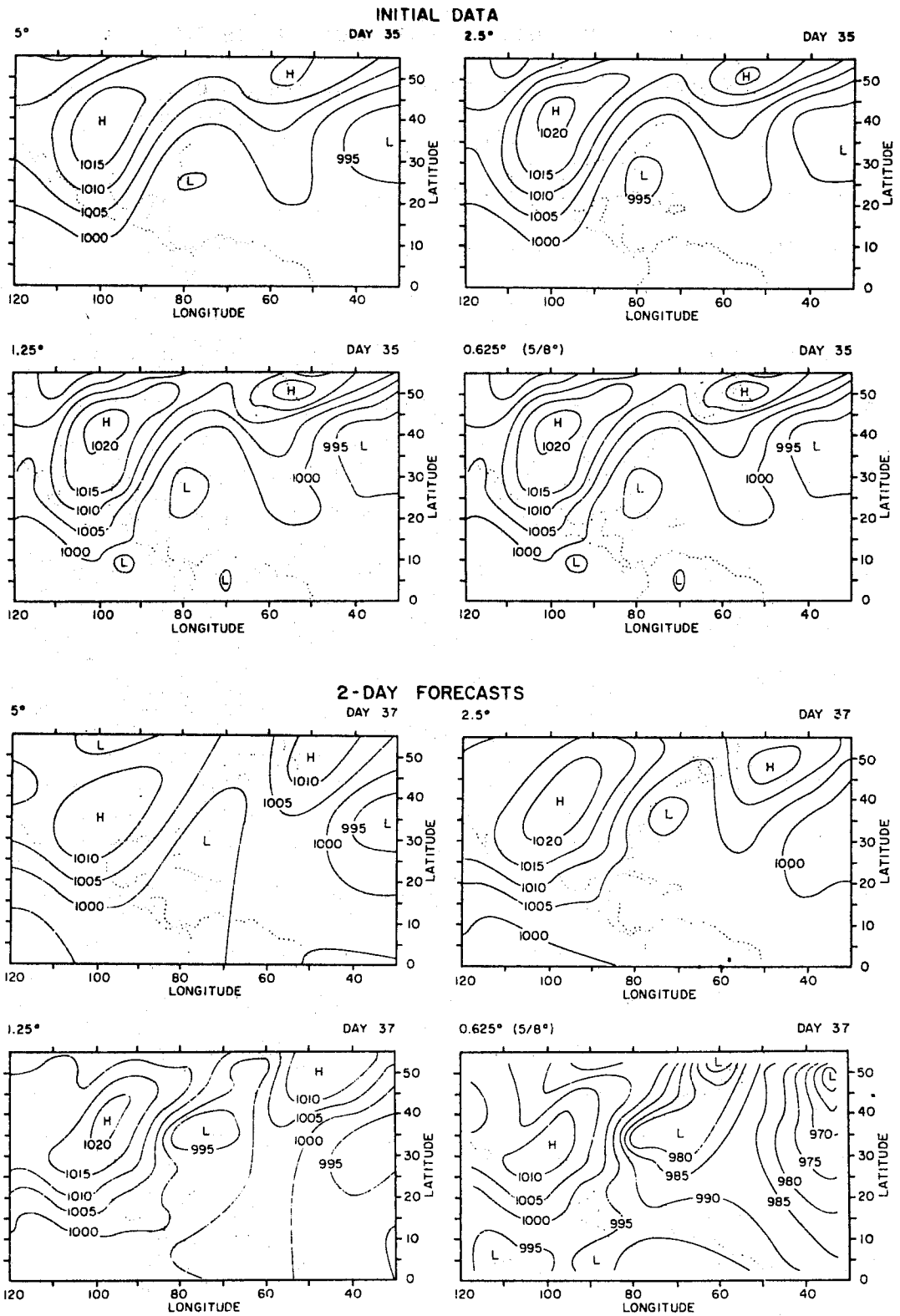


Fig. 3.3 Initial and two-day forecasts of surface pressure with a 5° global model and 2½°, 1½° and 5/8° Limited-Area Models. The contours were slightly smoothed in drafting.

(after Williamson and Browning, 1974)

frontal zone was pointed out by Reed and Sanders (1953) and Reed and Danielsen (1959). The importance of this vorticity concentration has recently been re-examined observationally, theoretically and numerically.

Figure 3.4 is the cross-section of the potential temperature θ and the normal component of geostrophic wind, which were objectively analysed. Figure 3.5 is the geostrophic potential vorticity associated with the front in figure 3.4. This demonstrates that the wind intensity in the frontal zone has a sharp spatial gradient. It is very likely that this vorticity distribution is crucial for an accurate prediction of the frontal waves. The horizontal scale of wavelength of frontal waves is 1000 ~ 2000 km, which belongs to the meso- α scale, and the frontal zone is of the order of 100 km. The intense vorticity in such a narrow zone must be represented accurately in the analysis. As seen in this figure, the vorticity appears to be confined to the area of concentrated isentropic surfaces. Therefore, the isentropic analysis, among other systems of coordinate analyses, seems to be the most appropriate way to represent this important atmospheric characteristics.

Figure 3.6 is two examples of 500 mb temperature maps, compared with NMC operational maps (Shapiro, 1974). The difference in the two maps is clear. The isentropic analysis gives a sharper gradient in the temperature field. In this isentropic analysis, the horizontal resolution was grid size = 381 km with 10 vertical θ - levels. Shapiro and Bleck think that a finer resolution, say 190 km and 25 vertical levels, is desirable. Figure 3.7 is the stream function map on an

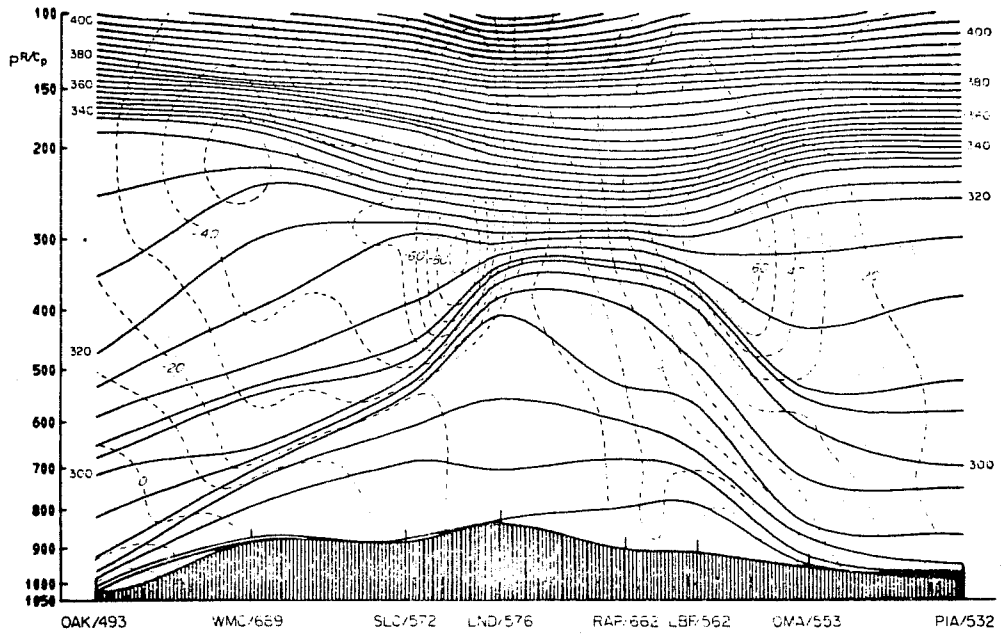


Fig. 3.4 Objective cross-section analysis of potential temperature and normal component of geostrophic velocity at 1200 GMT 7 December 1963: isentropes ($^{\circ}\text{K}$), solid lines; isotachs (m sec^{-1}), dashed lines.
(after Shapiro and Hastings, 1973)

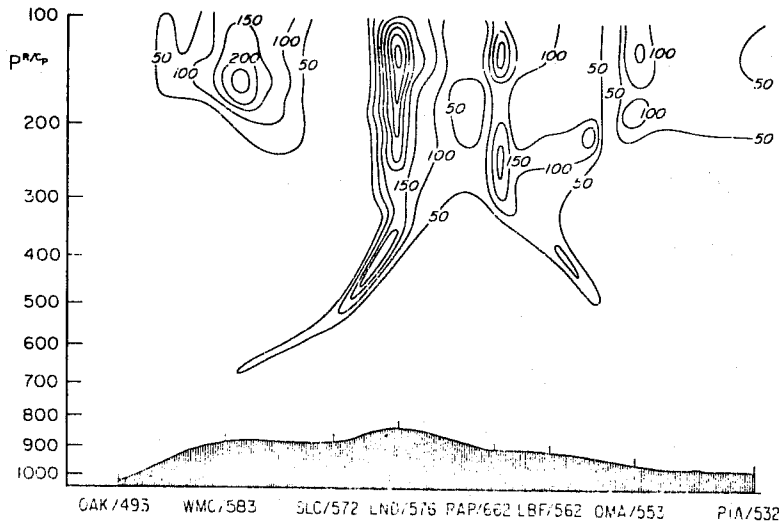
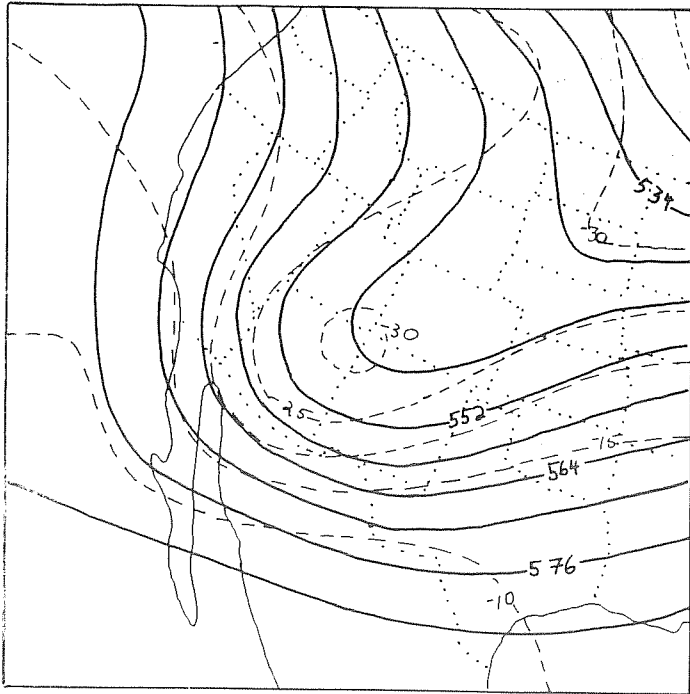
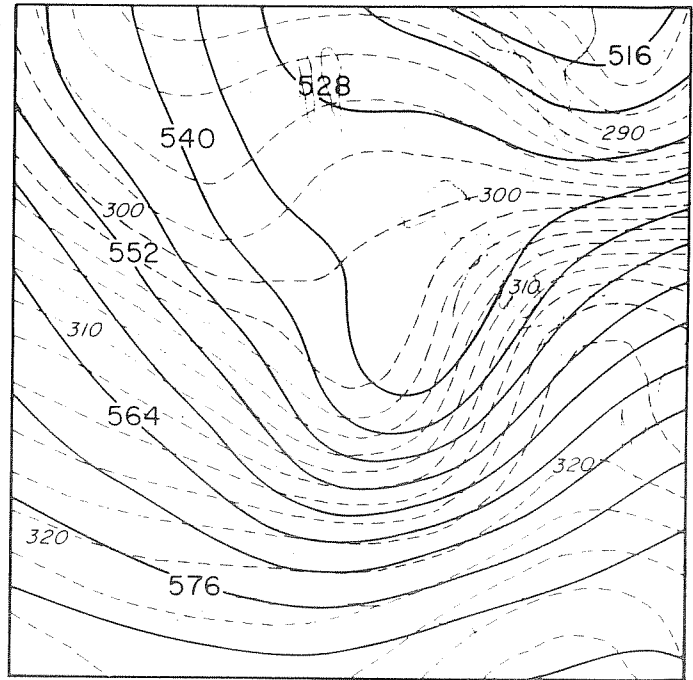


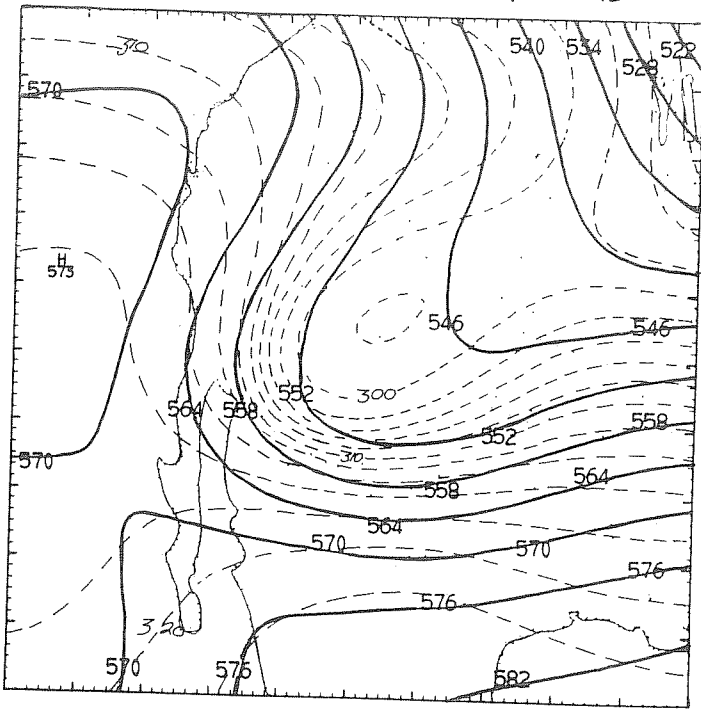
Fig. 3.5 Objectively derived analysis of geostrophic potential vorticity obtained from the analysis in Fig. 3, at intervals of $50 \times 10^{-6} \text{K sec}^{-1} \text{mb}^{-1}$.
(after Shapiro and Hastings, 1973)



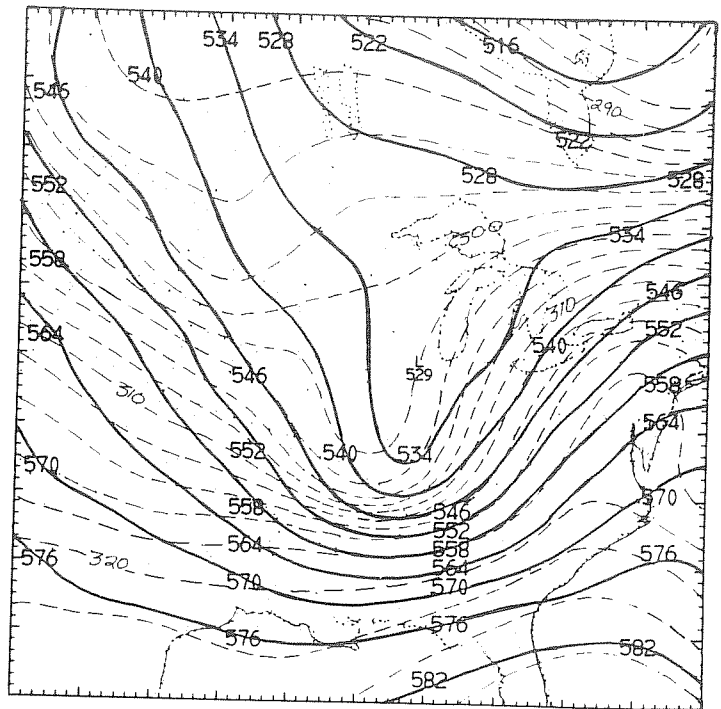
NMC 500mb HEIGHT
TEMPERATURE



NMC 500mb HEIGHT
POTENTIAL TEMPERATURE



70040112 HEIGHT
POTENTIAL TEMP 500 MB



70040212 HEIGHT
POTENTIAL TEMPERATURE 500 MB

Fig. 3.6: (After Shapiro, 1974)

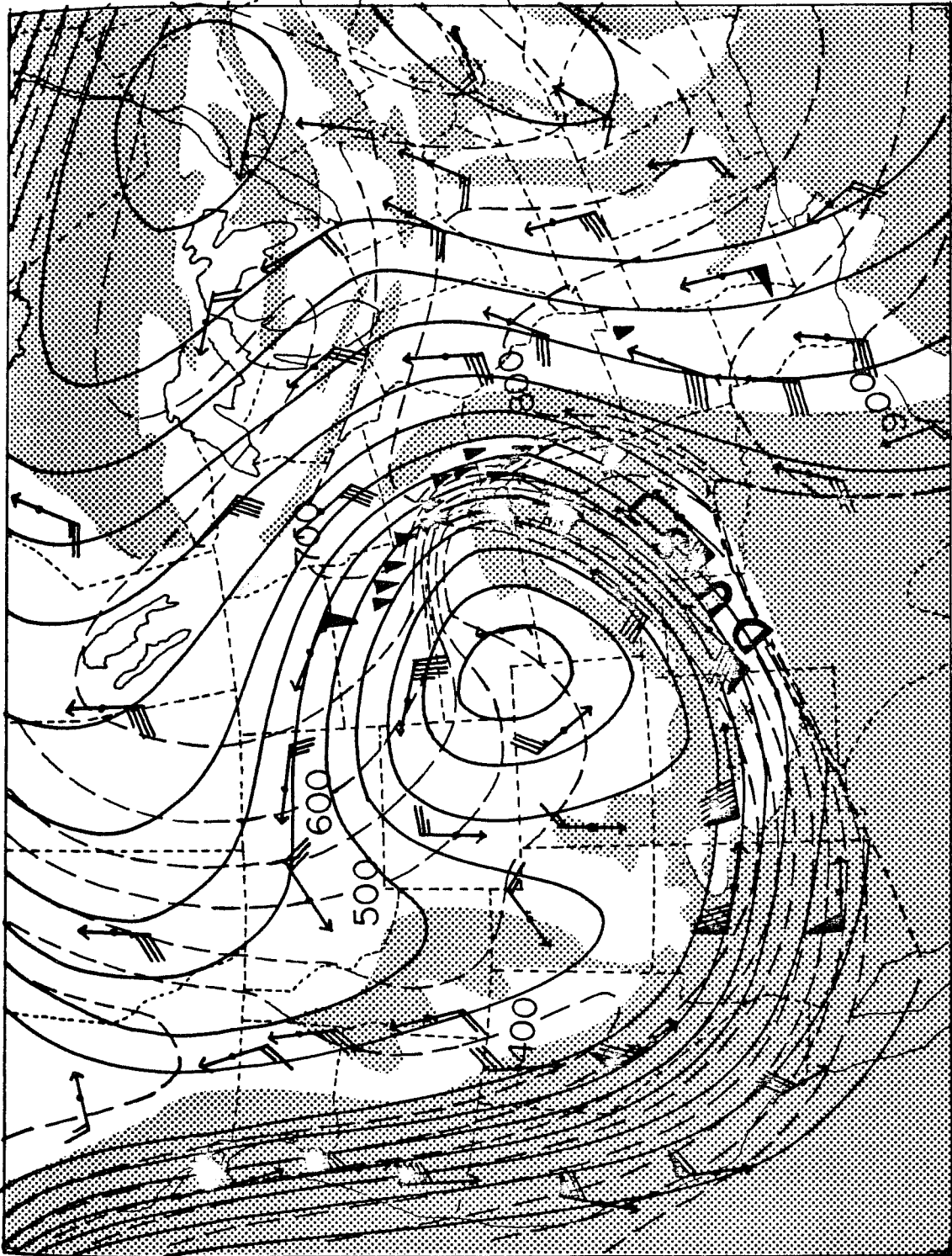


Fig. 3.6b

305°K isentropic surface, 0000 GMT, 20 April 1973. Continuous lines are Montgomery stream function, contoured at equivalent of 30 m. Dashed lines are isobars, contoured at 50 mb. White areas are clouds observed by satellite and ▽ are tornados reported within ± 1.5 hours.

(after Danielsen, 1975)



~~is the stream function map on an~~ isentropic surface, where the Montgomery stream function, i.e.,

$$M = C_p T + gz$$

is used. If the atmosphere is adiabatic, the geostrophic wind on θ -surface is parallel to the contour lines of this function, and otherwise, the case is either non-adiabatic or non-geostrophic.

(IV) SESAME

The main target of the project is the meso-scale forecast; namely, meso- β and meso- γ , and possibly meso- α . Such effort in this direction will definitely contribute to the improvement of the short range forecasts of less than 2 days. But SESAME (1975) operation has not been OPENED yet.

References for Sections 1, 2, and 3

- Bleck, R., 1974: Short-range prediction in isentropic coordinates with filtered and unfiltered numerical models. Mon. Wea. Rev. 102, No. 72, 813-829.
- Chouinard, C. and A. Robert. 1972: The vertical resolution in numerical models. Progress Report, JOC Working Group on NUMerical Experimentation.
- Chouinard, C., and A. Robert. 1972: Truncation errors in a filtered barotropic model. Proceedings of the Ninth Stanstead Seminar. Dept. of Meteor. McGill Univ. 13-28.
- Danielson, E. F. 1975: The generation and triggering of severe convective storms by large-scale motions. OPEN SESAME, 165-185.
- Deardorff, J. W. 1971: On the magnitude of the subgrid scale eddy coefficient. J. Comp. Phys. 7, 120-133.
- Eliassen, A., and E. Raustein, 1968: A numerical integration experiment with a model atmosphere based on isentropic coordinates. Meteorologische Annaler, 5, 45-63.
- Gavrilin, B. L., A. P. Mirabel', and A. S. Monin, 1972: The energy spectrum of synoptic processes. Izvestia, 8, No.5, 275-280.
- Gerrity, J. P., R. D. McPherson and P. D. Polger, 1972: On the efficient reduction of truncation error in numerical weather prediction models. Mon Wea. Rev. 100, 637-643.
- Hill, G. E. 1968: Grid telescoping in numerical weather prediction. J. Appl. Meteor. 7, 29-38.
- Leith, C. E., 1968: Diffusion approximation for two-dimensional turbulence Phys. Fluid, 11, No. 3, 671-674.
- Merilees, P. E. 1974: On estimation of truncation errors using the -3 law for kinetic energy. Tellus, 26, No.4, 456-463.
- Oort, A. H. and A. Taylor, 1969: On the kinetic energy spectrum near the ground. Mon. Wea. Rev. 97, No.9, 623-636.
- Orlanski, I. 1975: A rational subdivision of scales for atmospheric processes. Bull. Amer. Met. Soc. 56, No.5, 527-530.
- Reed, R. J. and F. Sanders, 1953: An investigation of the development of a midtroposphere frontal zone and its associated vorticity fields. J. Meteor. 10, 338-349.

- Saltzman, B. and A. Fleisher, 1962: Spectral statistics of the wind at 500 mb. J. Atmos. Sci. 19, No. 3.
- SESAME, 1975: Open SESAME, Severe Environmental Storms and Mesoscale Experiment. Proceedings of the opening meeting at Boulder, Colorado, September 4-6, 1974. Edited by D. K. Lilly, 499 p.
- Shapiro, M. A. and J. T. Hastings, 1973: Objective cross-section analyses by Hermite Polynomial interpolation on isentropic surfaces. J. Appl. Meteor. 12, No. 5, 753-762.
- Shapiro, M. A. 1974: Objective analysis in isentropic coordinates Subsynoptic extratropical Weather Systems. Summer Colloq. NCAR Vol. 2, 339-349.
- Shuman, F. G. and J. B. Hovermale, 1968: An operational six-layer primitive equation model. J. Appl. Meteor. 7, 525-547.
- Tewles, S. and H. Wobus, 1954: Verification of prognostic charts. Bull. Amer. Meteor. Soc. 35, 455-463.
- Williamson, D. L. and G. L. Browning, 1974: Formulation of the lateral boundary conditions for the NCAR limited-area model. J. Appl. Meteor. 13, No. 1, 8-16.
- Wiin-Nielsen, A. 1967: On the annual variation and spectral distribution of atmospheric energy. Tellus, 19, 540-559.

4. Medium range forecasts

4.1 Examples of forecasts

Here we show an example of the 4 and 6 day forecasts of geopotential height with GFDL hemispheric general circulation model (Miyakoda et al. 1969), and another example of the 10.5 day forecasts with the GFDL global finite difference model (Umscheid and Bannon, 1975).

The hemispheric model used is what we call the 1967 version model, in which the primitive equations on the $N=40$ (270 km) grid with 9 vertical levels are used, and the moisture and orography are incorporated.

The Cartesian coordinates on stereographic projection map, and the σ -coordinate are used. The domain is hemispheric and is bounded by an equatorial wall which is insulated and free-slip. The number of grid-points at one level is 5025. The term of $\nabla\phi$ is calculated on the constant pressure surface instead of the σ -surface. The non-linear viscosity ($k_0=0.4$) and surface friction with a spatially constant drag coefficient are used. The internal physics, as usual, from the general circulation models are incorporated.

Figures 4.1 are the geopotential height maps for the prediction and the observation for day 4 and 6. The blocking ridges over Iceland were well maintained in the predictions. The general positions of troughs are in agreement, but the sharpness of the troughs is lost. A part of the reason for the smoothness is the adoption of a large value for k_0 in the non-linear viscosity term.

The 1000 mb height maps are shown in figure 4.2. A new cyclone A' and a third generation cyclone B'' were formed over Japan and the East Coast of the U.S., respectively. They were predicted, though the amplitude of A' was slightly overpredicted.

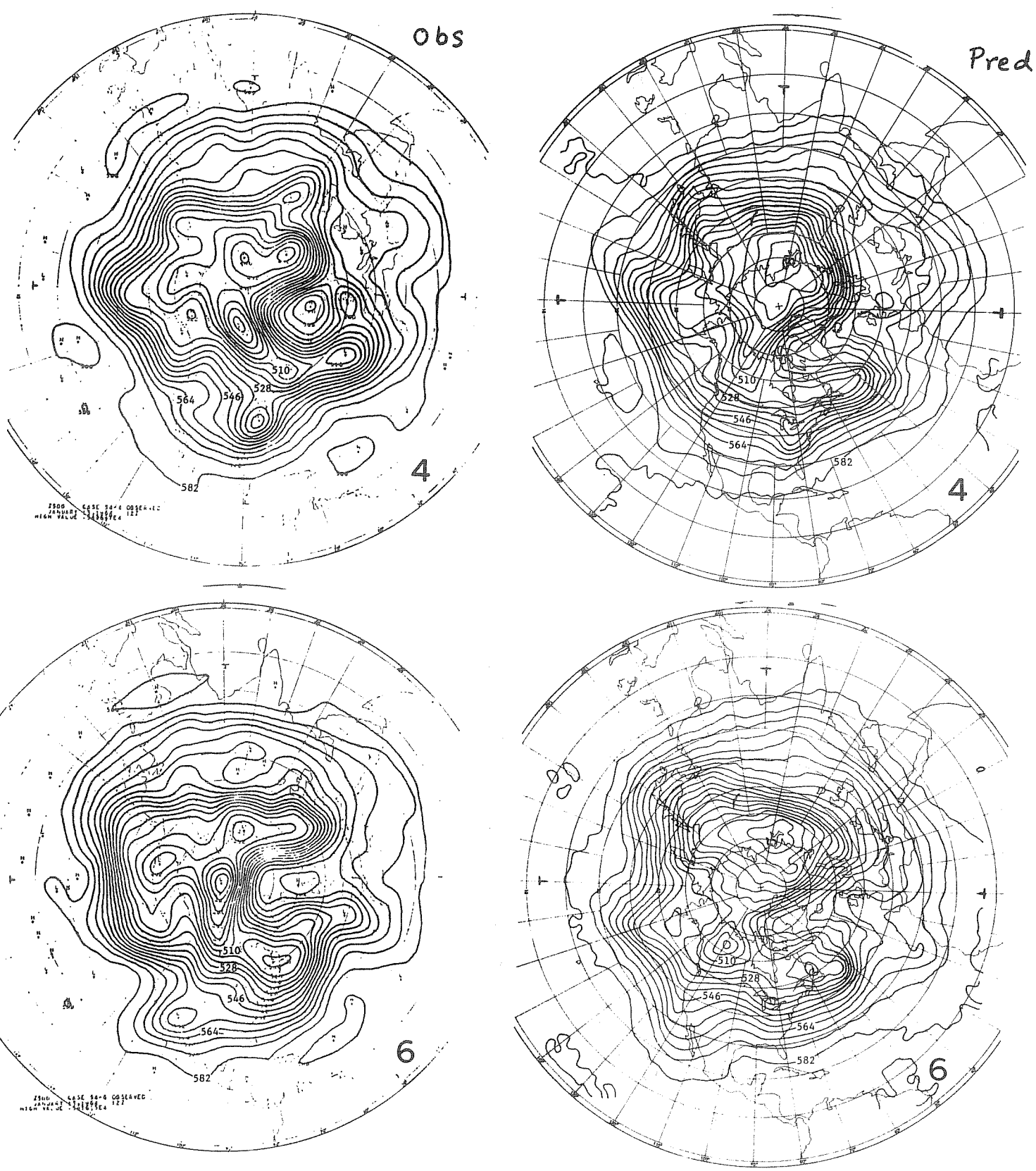


Fig. 4.1 (after Miyakoda, Smagorinski et al, 1969)

Obs

Pres

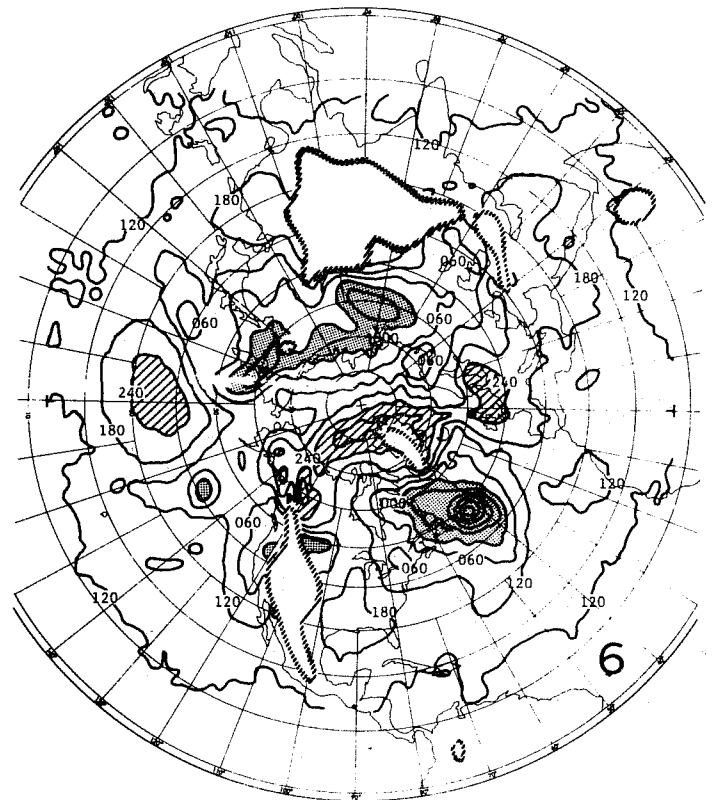
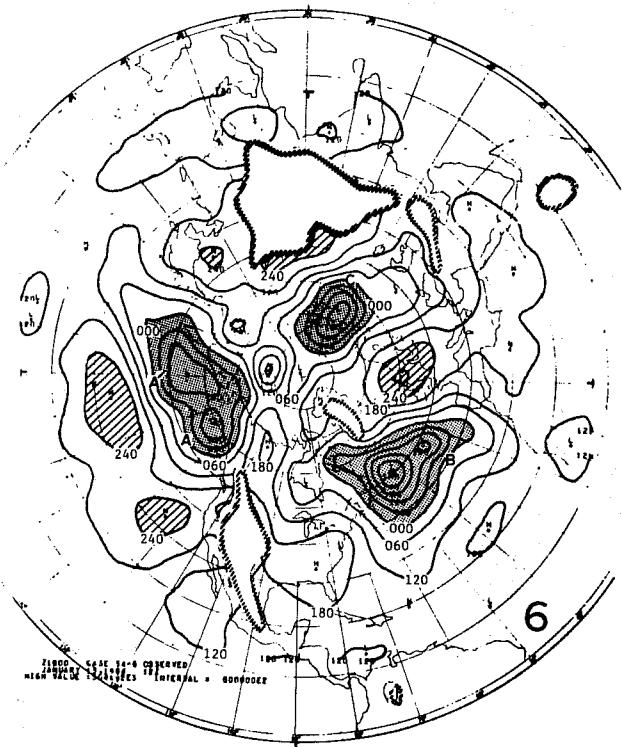
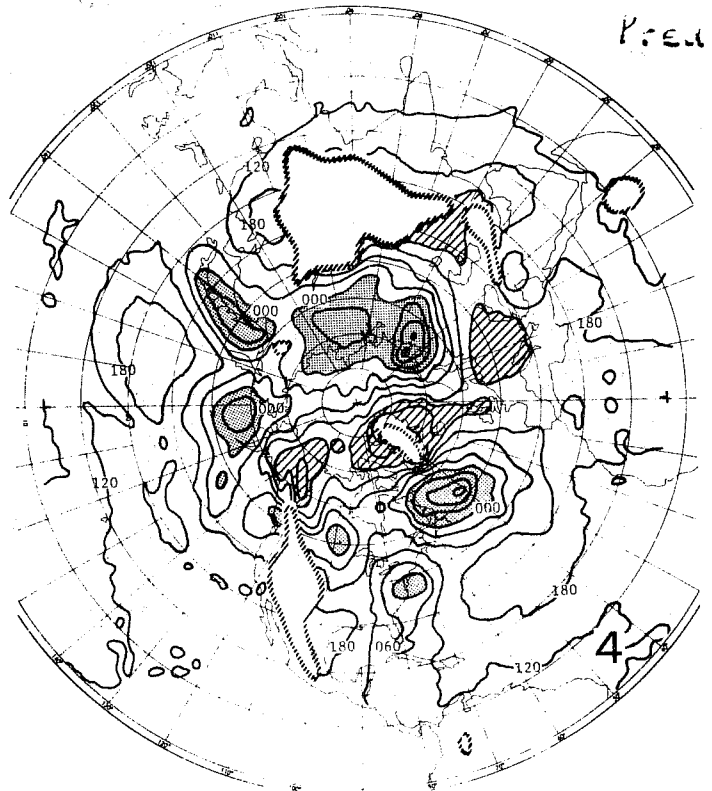
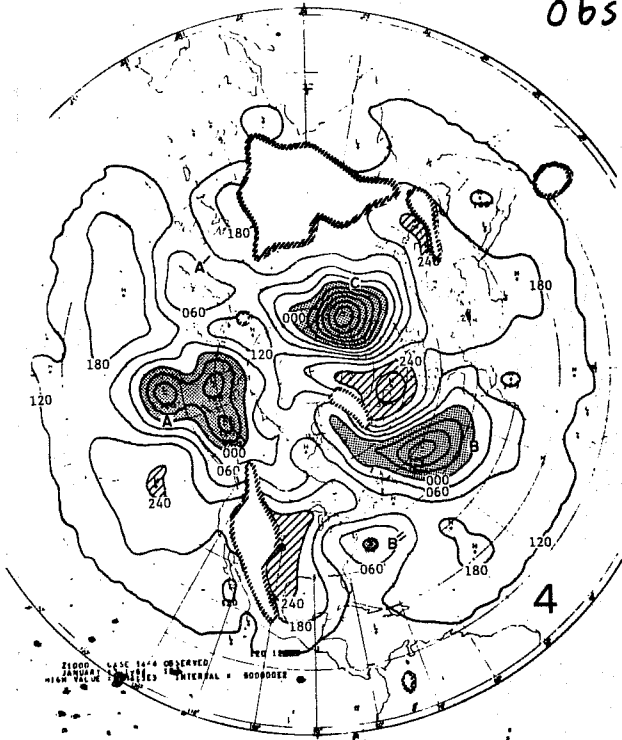


Fig. 4.2

For this case, Hovmöller's trough-ridge diagram (time-longitude chart) was constructed for the prediction and the observation for the height field in the zonal belt between 35° and 45° N (figure 4.3). In the two week period, a trough at 120° E at day 0, for example, crossed the Pacific Ocean and the North American Continent and reached 80° W. One may trace the forecast-observation correspondence of the trough's movement even for 2 weeks. An example of the wave spectral analysis is shown in figure 4.4. The wave components are grouped in the planetary waves (wavenumber 1 and 2), the long waves ($3 \sim 5$), the baroclinic waves ($6 \sim 10$) and others ($11 \sim 15$). These grouped waves are synthesized and shown in trough-ridge diagrams. The planetary and long waves seem to be more or less stationary, whereas the baroclinic waves propagate eastward.

Another example of the 10.5 day forecast is shown in figure 4.5. This was predicted with the global finite difference model on the latitude-longitude grid with $N=48$ (220 km) and 9 vertical levels. The initial condition is the global data set for 00 GMT March 1, 1965. The number of grid points is 18,200, which is far more for the same area than in the hemispheric counterpart. The internal physics is almost the same as in the hemispheric model except that here the ground hydrology is predicted thus affecting the evaporation on land, and the snow deposit affects the surface albedo.

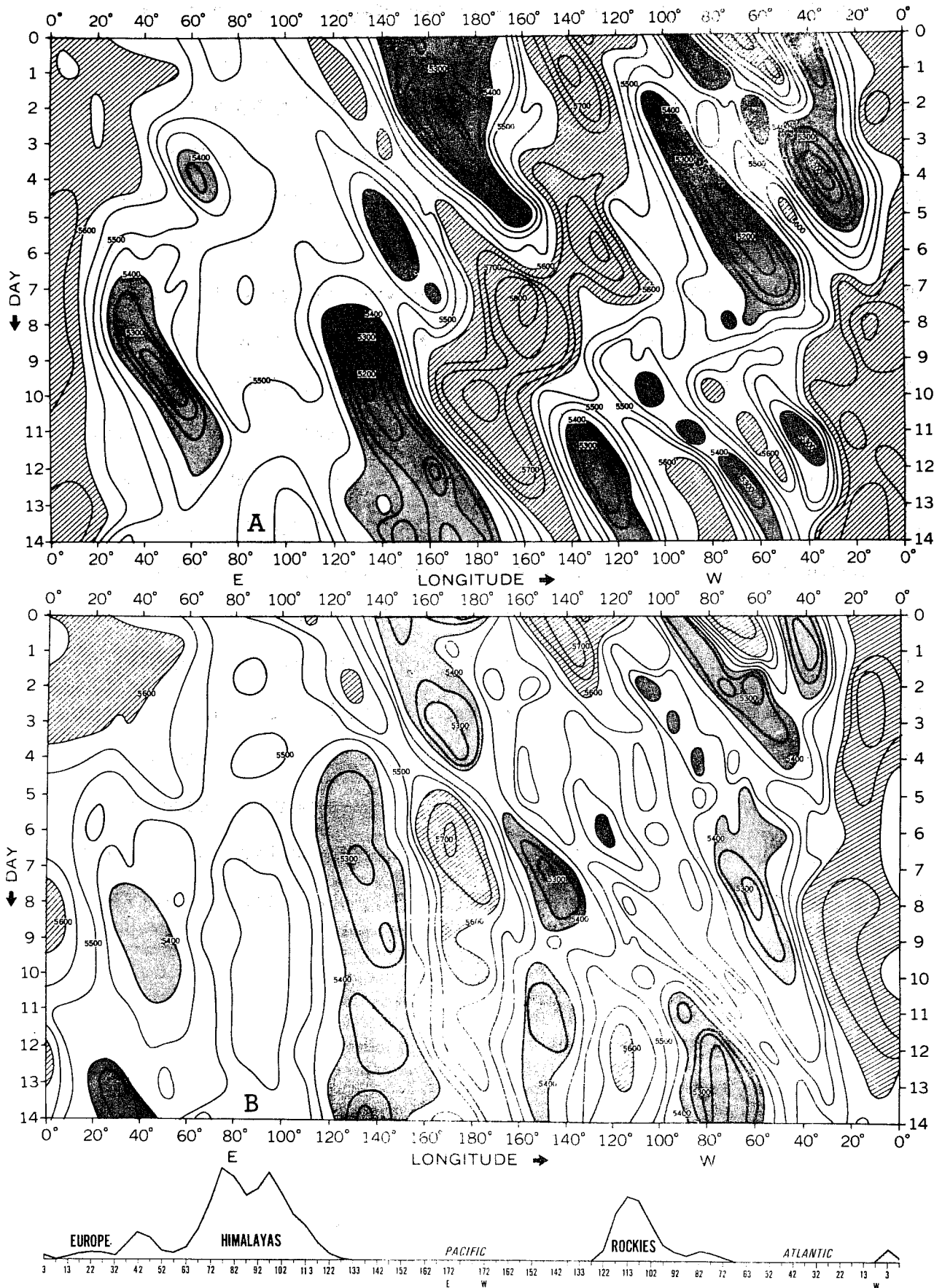


Fig. 4.3: Trough-and-ridge diagrams of the 500-mb level for the 1964 case. (A) the observed, and (B) the prediction of Experiment 3. The contours are for the 500-mb geopotential height in a zonal belt between 35° and 45°N. The units are decameters. The interval is 50 m. The ordinate is time in days, and the abscissa is longitude. The ridge areas with geopotential greater than 5600 m are hatched, and the trough areas with values lower than 5400 m are stippled.

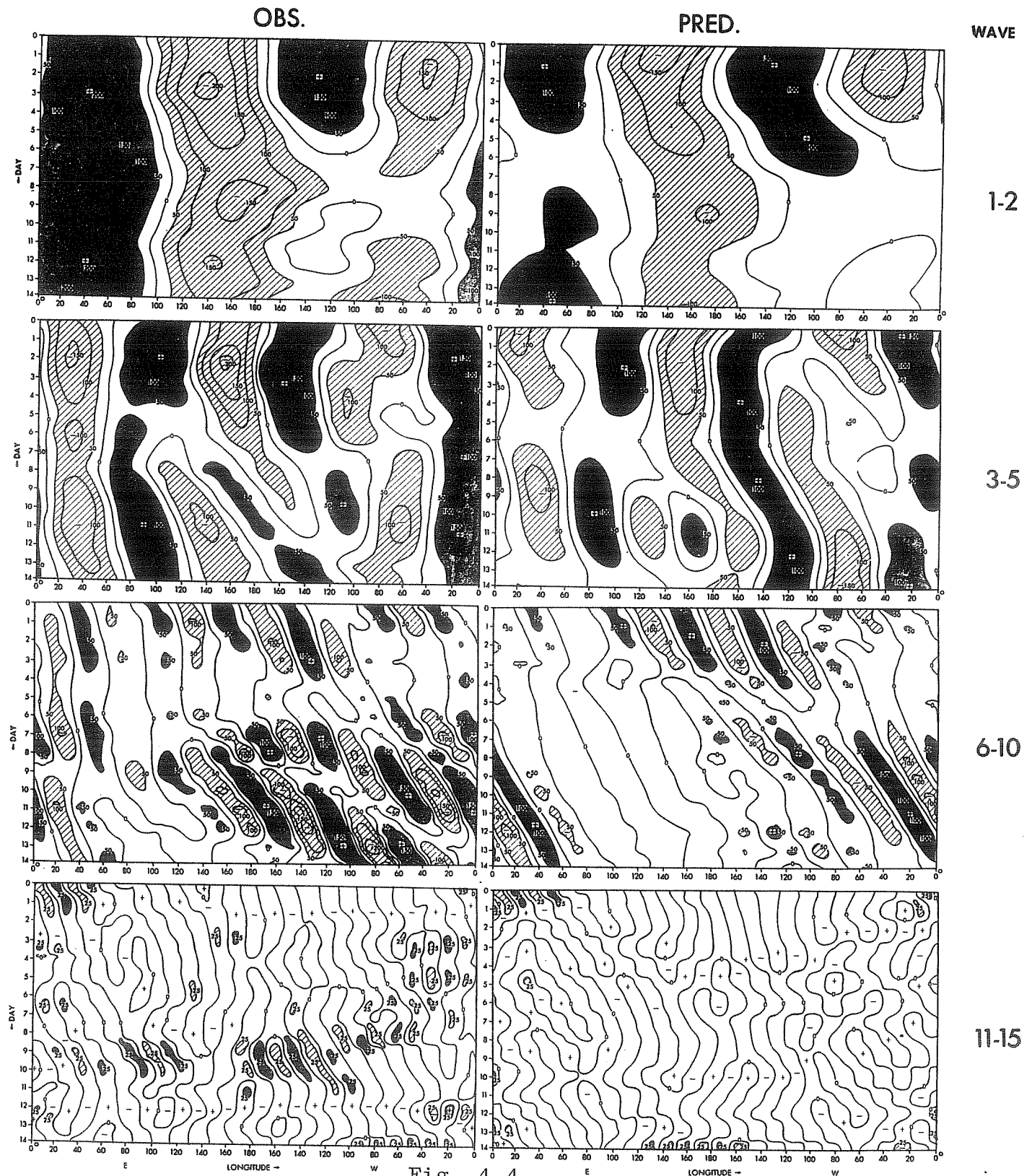
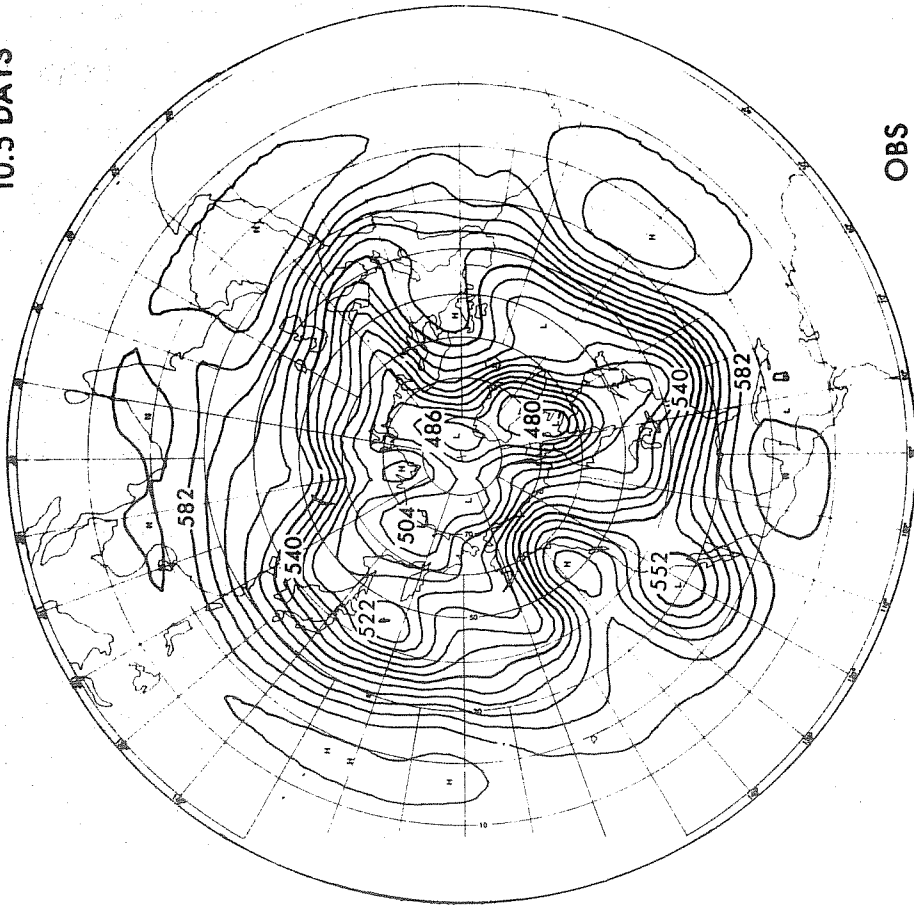


Fig. 4.4

An example of a 500-mb trough-ridge diagram for various wave numbers. The units of geopotential height contours are meters. Ridge areas with height values greater than 50 m (25 m) are stippled, and trough areas with values less than -50 m (-25 m) are hatched for wave numbers 1-2, 3-5, and 6-10 (11-15). (After Miyakoda, Hembree et al., 1972)

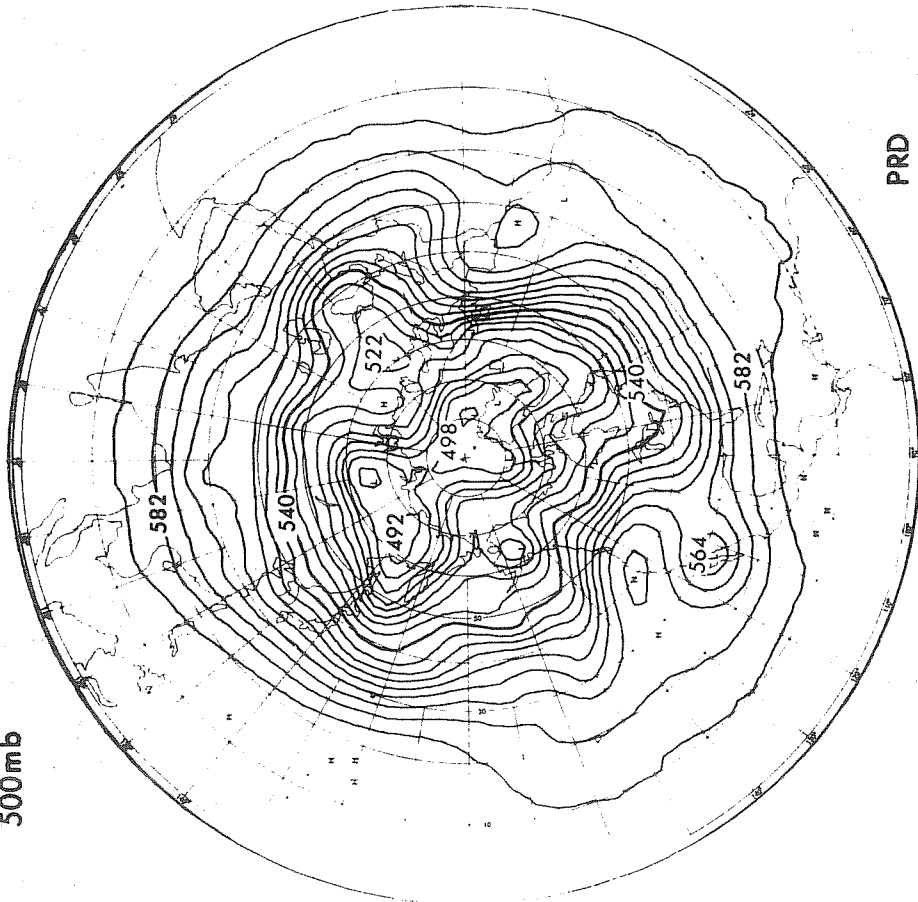
Figure 4.5 is the 500 mb height forecasts. The agreement between the forecast and the observation is good. Note that this case was not well predicted by the hemispheric model for $N=40$. The reason is very possibly the effect of the equatorial wall in the latter model. The same case was extended to one month by the global model. In the stratosphere, a polar vortex breakdown occurred at 20 days. This event was precisely predicted, implying that the planetary scale wave pattern in the troposphere was reasonably predicted as long as 20 days. However, the phenomena which followed the breakdown were completely mispredicted.

10.5 DAYS



OBS

500mb



PRD

Fig. 4.5

4.2 Statistics of forecast performance

Two experiments will be shown in this subsection; one is based on the GFDL "1967 version" model, which was explained earlier. (Miyakoda et al. 1972), and the other is on the GISS model (Goddard Institute of Space Studies), New York (Druryan, Somerville, and Quirk, 1975). The latter model uses the global latitude-longitude grid of $\Delta\varphi = 4^\circ$ and $\Delta\lambda = 5^\circ$ (φ is latitude, and λ is the longitude), 9 vertical levels which are equally spaced in σ . (Somerville et al. 1974). The space finite difference scheme in the former is the Arakawa-Lilly's kinetic energy conservation method, and that in the latter is the Arakawa's method of kinetic energy conservation and enstrophy conservation for the rotational component of wind vector. The time differencing in the former is the Leap-frog method with the occasional application of the Euler-backward (Matsuno) scheme, whereas in the latter, TASU (Time-alternative-space-uncentered) method is used. The subgrid scale physics are different in the two models. Non-linear diffusion with $k_0 = 0.25$ was used by GFDL, whereas no explicit horizontal diffusion was employed at GISS. On the other hand, no vertical diffusion in the free atmosphere was included at GFDL, whereas vertical diffusion was used for all levels in the GISS model. The parameterization of the ensemble of cumulus convection was based on the "moist convective adjustment" in GFDL, whereas the modified Arakawa 1969 version was used in GISS. Other aspects of the two models are very similar except in the treatment of soil moisture.

(i) Error growth

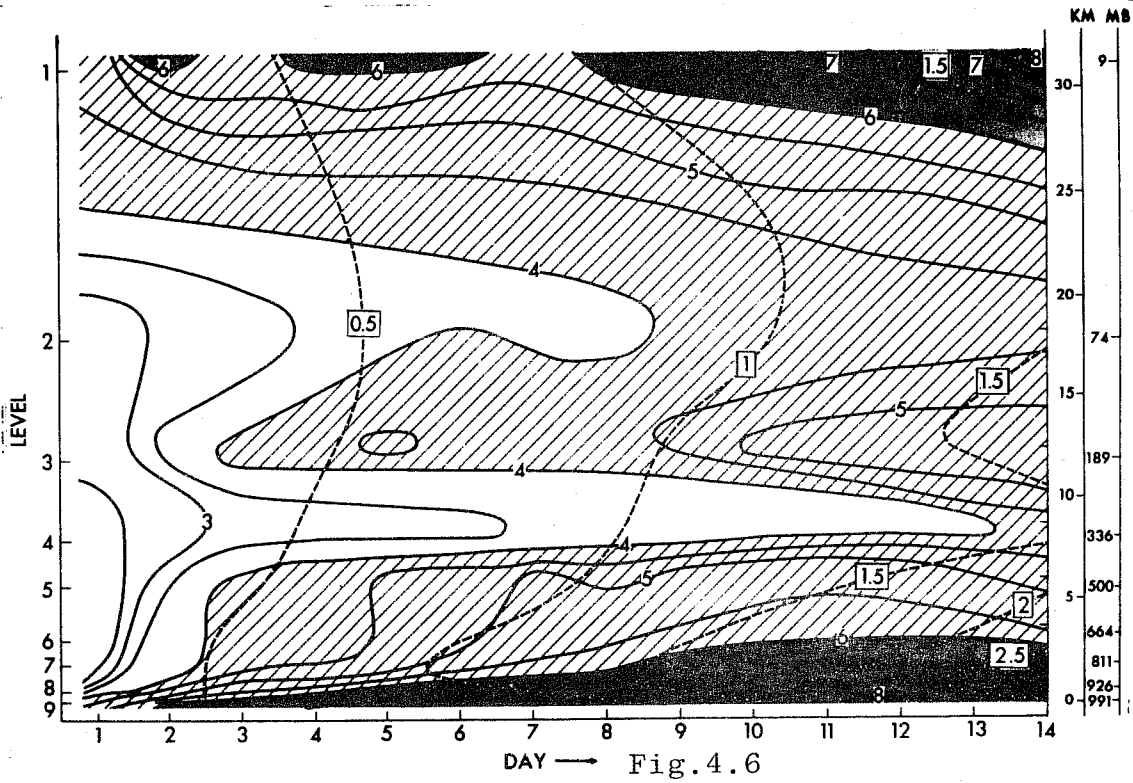
Figure 4.6 is the temporal evolution of the rms temperature error $\sqrt{E(\delta T)^2}$ for 6 winter cases in the GFDL experiment.

A similar figure was obtained in the GISS experiment for 6 winter cases, (figure 4.7). The common features in the two figures are: (a) the temperature error starts to grow at the surface and at the tropopause level, (b) the error minimum is near the 300 ~ 400 mb levels.

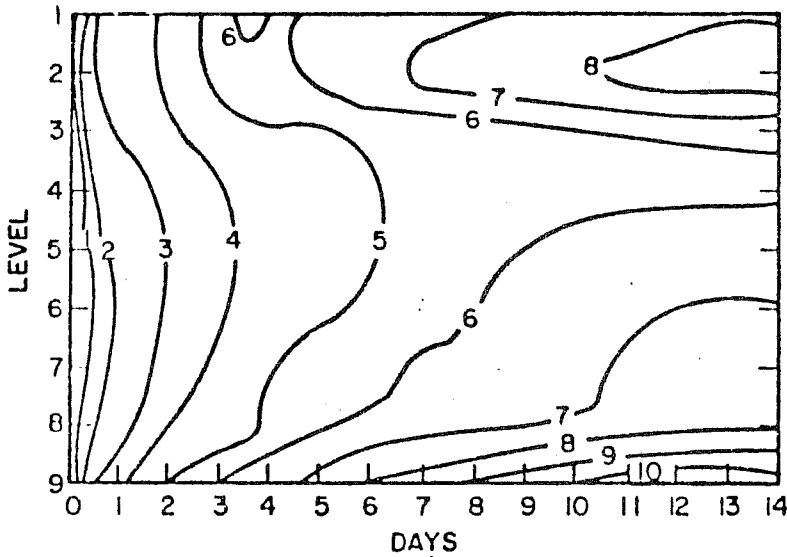
The GFDL figure indicates that the error also develops rapidly in the stratosphere. In this picture, we superposed the error development in temperature in the predictability study (Smagorinsky, 1969), which is the theoretical growth of error. The magnitudes are therefore much less than those developed in real data. However, the tendency of the error development is similar, in the sense that the surface and the tropopause levels are the regions of error maxima. Summarizing the above, one can conclude that the way to reduce the overall prediction error is to suppress these error sources.

Figure 4.8 shows the rms height error, $\sqrt{E(\delta z)^2}$, for the 1000 mb level in the GFDL experiment summarized for the 14 days of 12 winter cases. This may indicate that the surface errors are particularly large over the Aleution, Iceland and the North Siberian areas. The reasons why these areas have large errors are: (a) the activities of the disturbances are large in these areas in the winter, (b) the sea surface temperature was not adequately specified, and (c) the heat transfer processes in the model may be responsible for much of the error.

The wind error growth is quite different as seen in figure 4.9, which was obtained in the GISS experiment. It is understandable that the error maximum appears at the 300 mb level.



—Time evolution of the rms temperature error ($^{\circ}\text{K}$), $\sqrt{E(\delta T)^2}$. The dashed lines are rms error for the predictability experiment by Smagorinsky (1969).



(after Druyan, et al, 1975)

Fig. 4.7

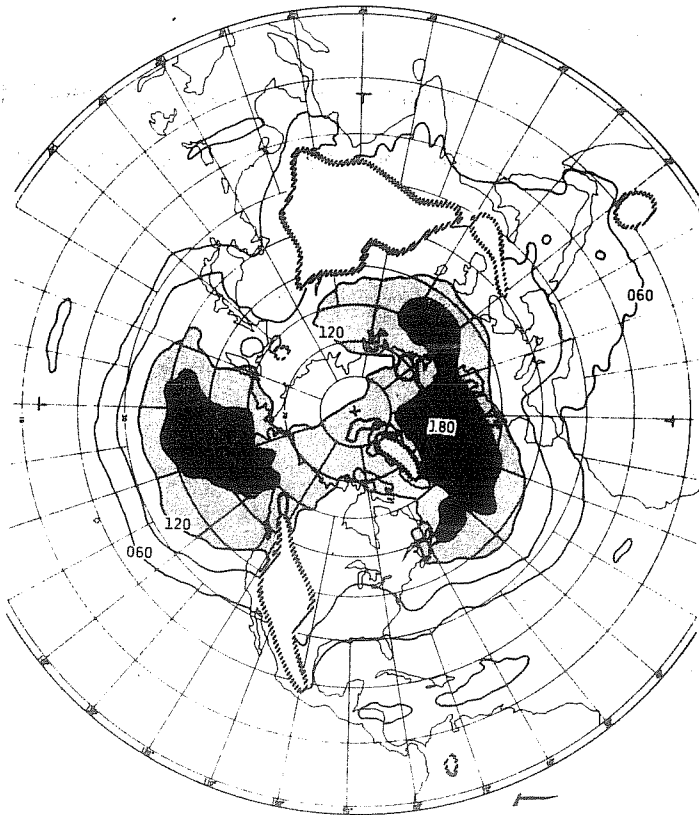


Fig. 4.8 The rms height error, $\sqrt{E(\delta z)^2}$, for the 1000-mb level. The contour interval is 30 m.

(after Miyakoda et al, 1972)

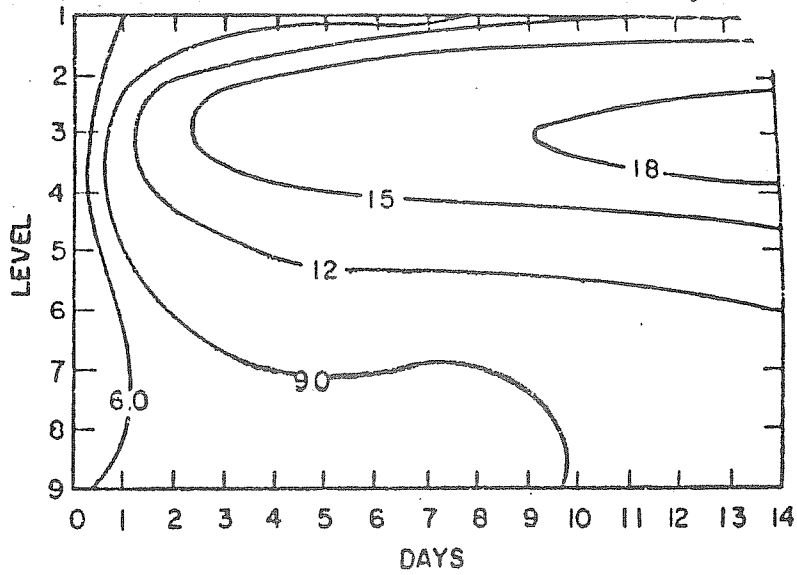


Fig. 4.9 (after Druyan et al, 1975)

(ii) Verification scores

The measures of skill which are used are the standard deviation of error, the correlation coefficient between the observed and the predicted height anomaly

The error of geopotential height, z , is given by

$$\delta z(t) = Z_p(t) - Z_t(t) \quad (4.1)$$

and the anomaly is defined by

$$\Delta z(t) = z(t) - z_n, \quad (4.2)$$

where z_n is the normal height.

The spatial average is defined by

$$\bar{X} = \frac{\sum_i \frac{1}{m^2} X_i}{\sum_i \frac{1}{m^2}}, \quad (4.3)$$

where X_i is an arbitrary variable at the gridpoint i , m is the map scale factor. Except for mountain areas in the lower troposphere, the summation is made over all gridpoints north of 20°N. The ensemble mean for a sample of 12 winter cases is

$$E(x) = \frac{\sum_l X_l}{12} \quad (4.4)$$

Thus the rms error is

$$\text{rms} = \sqrt{(\delta z^2)} \quad (4.5)$$

For comparison, two auxiliary measures are used. One concerns the persistence; that is,

$$\text{Persist} = E \sqrt{\{z_t(t) - z_t(0)\}^2}, \quad (4.6)$$

where $z_t(0)$ is the initial condition, and the other concerns the normal, (or climate) that is,

$$\text{norm} = E \sqrt{\Delta z_t(t)^2} \quad (4.7)$$

These two measures indicate the rms error or the standard deviation of error for two types of "no-skill forecasts,"; the first predicts that initial values will not change, while the other predicts the climatological (normal) value.

Another group of scores involves correlation coefficients. The correlation for the anomaly is given by

$$\text{correl. anom} = \frac{\overline{\Delta z_p(t) \cdot \Delta z_t(t)}}{\sqrt{(\overline{\Delta z_p})^2} \sqrt{(\overline{\Delta z_t})^2}} \quad (4.8)$$

As an auxiliary score, the correlation for persistence is taken and is defined by

$$\text{correl. persist.} = E \left[\frac{\overline{\Delta z_t(0) \Delta z_t(t)}}{\sqrt{\overline{\Delta z_t(0)^2}} \sqrt{\overline{\Delta z_t(t)^2}}} \right] \quad (4.9)$$



As known to those who are acquainted with verification statistics these scores are not independent of each other. Let us write

$$z_t(t) = z_n + \Delta z_t(t)$$

and

$$z_p(t) = z_n + D z_p + \Delta z_p(t) \quad (4.10)$$

Δz_t , is the anomaly, and $D z_p$ is the systematic bias of the z_p . For convenience of discussion, it is assumed that

$$\begin{aligned} \overline{D z_p \cdot \Delta z_p(t)} &\rightarrow 0, \\ \overline{D z_p \cdot \Delta z_t(t)} &\rightarrow 0, \end{aligned} \quad (4.11)$$

and

$$\overline{\Delta z_t(t)^2} \rightarrow w^2 \quad (4.12)$$

where w is the intensity of anomaly, which we assume is not a function of t .

With these assumptions, one can readily show that, for $t \rightarrow \infty$

$$\begin{aligned} \text{norm.} &\rightarrow w \\ \text{persist.} &\rightarrow \sqrt{2w} \\ \text{rms} &\rightarrow \sqrt{2(1+q)w} \end{aligned} \quad (4.13)$$

where

$$q = \frac{D z_p^2}{2w^2} \quad (4.14)$$

This means that the persistence error at its asymptotic level is $\sqrt{2}$ times larger than that of the normal (Thompson 1961, DØs 1970) because both the forecast and the observation deviate from the normal.

The 1000-mb standard deviation curve (figure 4.10) crosses the normal curve at the 3rd day but does not reach the level of persistence until the 7th day. On the other hand, the standard deviation curve at 500-mb is always lower than persistence for the 2-week period, and it crosses the normal curve at the 5th day. The 50-mb standard deviation is always higher than the persistence level. It is interesting to note that the score becomes slightly better at 4-6 days relative to persistence. This tendency is also noticed in the correlation coefficients, as will be seen later. Perhaps this is related to the "initial adjustment"; namely, a considerable discrepancy between the initial condition and the model solution is produced partly by the incomplete initialization and partly by the model bias in the stratosphere.

Figure 4.11 and 4.12 are the rms of 500 mb height error and sea level pressure error, obtained in the GISS experiment, where 6 winter cases were taken from one winter. It is difficult to compare the performances of the two models. Overall, it seems that the skill in both models is similar in spite of the fact that GISS has coarser resolution.

Figure 4.13 shows the correlations for anomalies of the 1000-, 500-, and 50-mb heights. As in figure 4.10, the area between the envelope for 10 cases is shaded, and persistence is also indicated for reference. The correlation at 1000 mb becomes zero at the 9th day, but the curve crosses persistence on the 6th day. For the 500-mb correlations, the mean of the 12 cases starts at 0.9, decreases monotonically, and drops to near zero at the 11th day. Although the ensemble mean of 50-mb

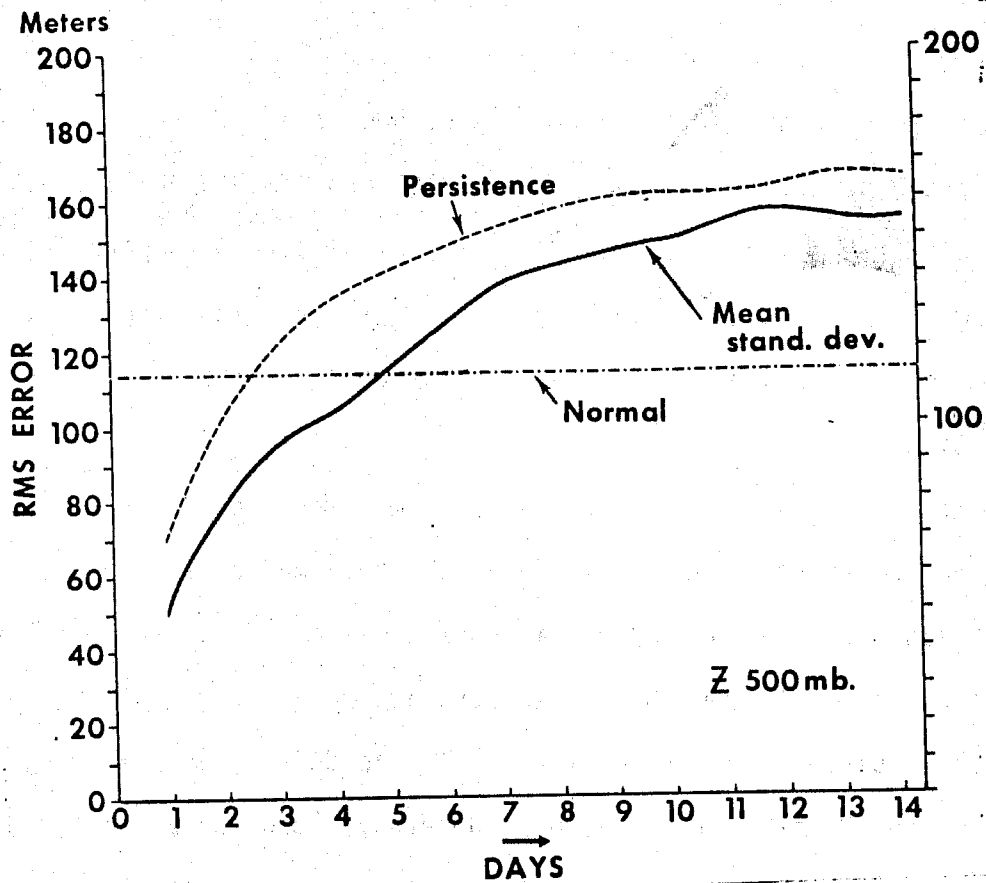
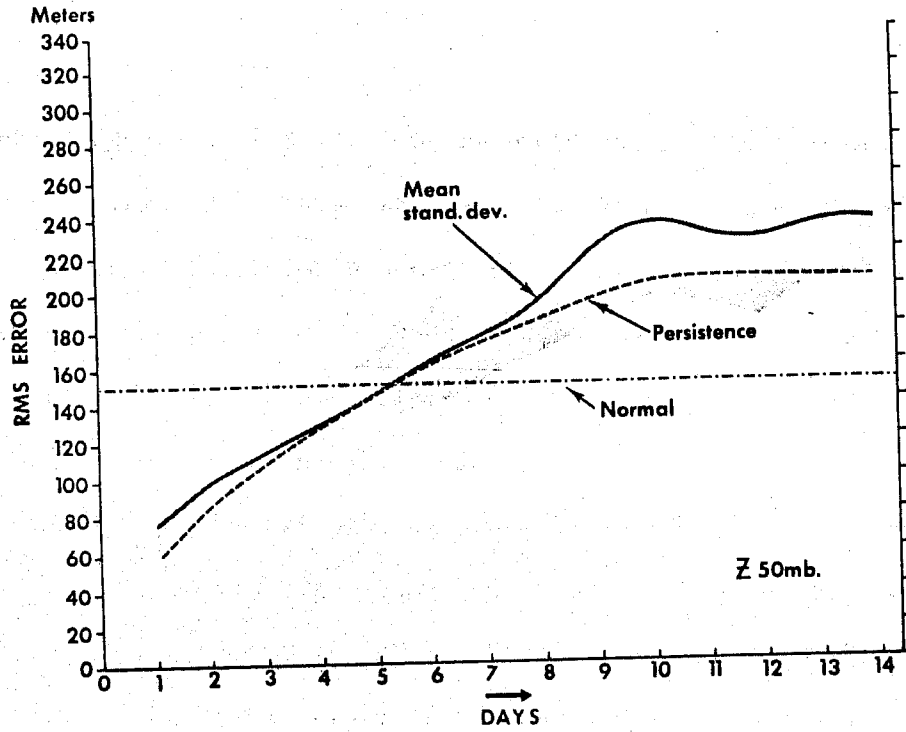


Fig. 4.10-1 Standard deviations

(after Miyakoda, Hembree et al, 1972)

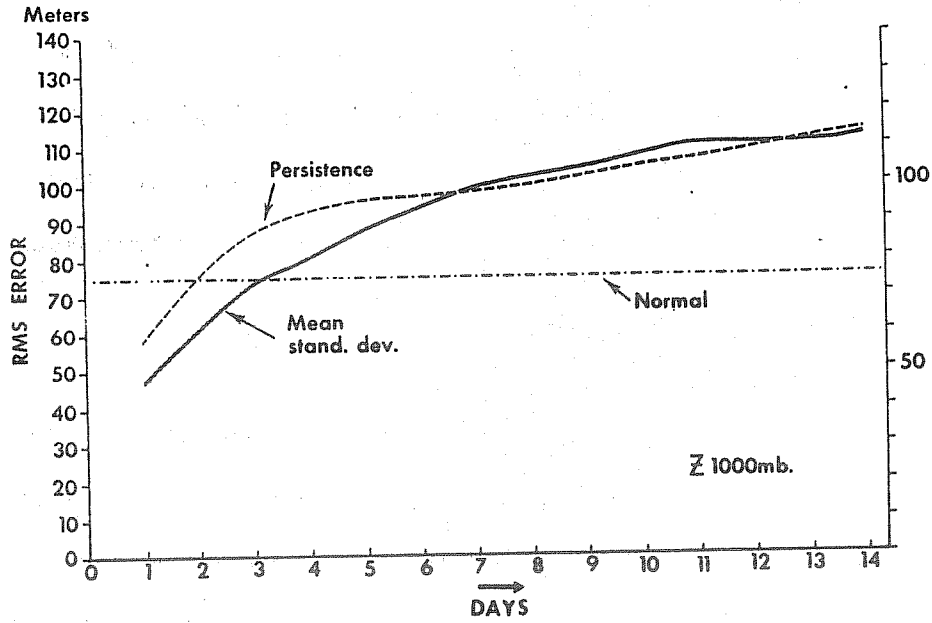


Fig. 4.10-2 The standard deviations of height error.

coefficients is positive for the entire 2-week period, it is always lower than persistence.

Summarizing the GFDL and GISS experiments, it is concluded that (a) 500 mb forecasts have better skill than 1000 mb forecasts, (b) the skill of summer forecasts in terms of the correlation coefficient is better than that in winter forecasts (not shown here) (c) the skill of 500 mb forecasts becomes 0 at 10 days in winter, whereas the skill of 1000 mb forecasts becomes 0 at 6 days, (d) the 500 mb forecasts are better than persistence for at least two weeks; whereas the 1000 mb or SLP forecasts are better than persistence for 6 days.

(iii) Spectral analysis of forecasts

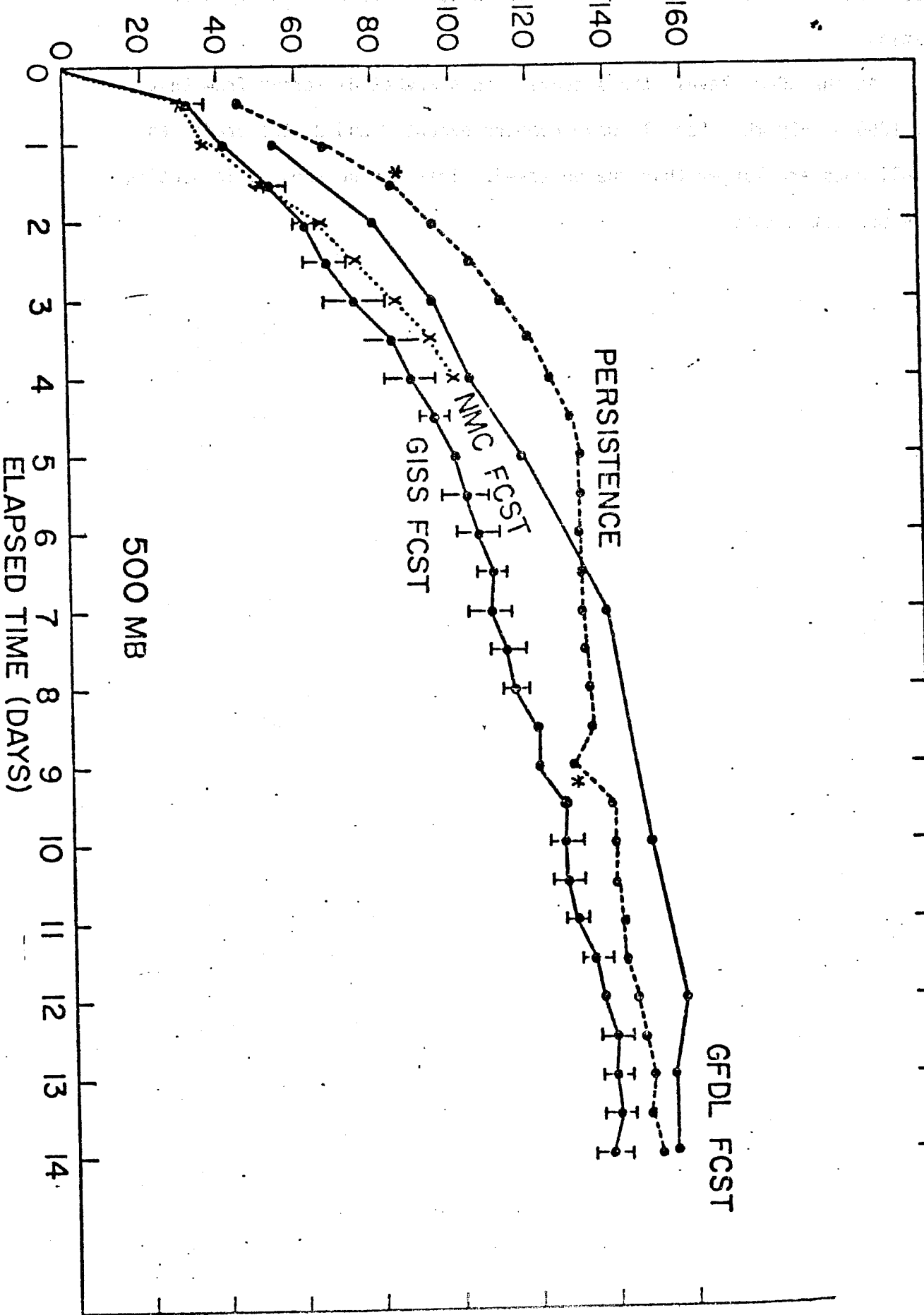
Figure 4.14 compares the observed and the predicted spectra of geopotential height for the belt between 35° and 45° N at the 1000-, 500- and 500-mb levels. Both the observed and the predicted curves are calculated by averaging the spectra over 4-14 days using 12 cases. The spectra for the January normals are also calculated and shown for comparison.

In the results for 1000 and 500 mb, large discrepancies of the predicted amplitudes from the observed are noticed at wave numbers 1-3. This is a serious problem that has already been discussed to a certain extent by Miyakoda et al. (1971). Surprisingly, higher horizontal grid resolution is apparently needed to improve the amplitude of the planetary waves. We speculate that these waves are the so-called "forced Rossby" waves and are influenced considerably by condensational heating. Note that the amplitudes of the predicted cyclone waves (wave nos. 6-10) are also smaller than the observed. This suggests that the predicted rate of energy release due to baroclinicity in the medium spectral range is

too weak, a result, in part, of the erroneously large viscosity dissipation.

At the 50-mb level, the situation is somewhat different from that at 1000 or 500 mb. For all wave numbers except 2 and 3, the predicted amplitudes are larger than the observed. This can be seen by inspecting the predicted maps.

AVERAGE STANDARD DEV. 500MB. HEIGHT ERROR (M)



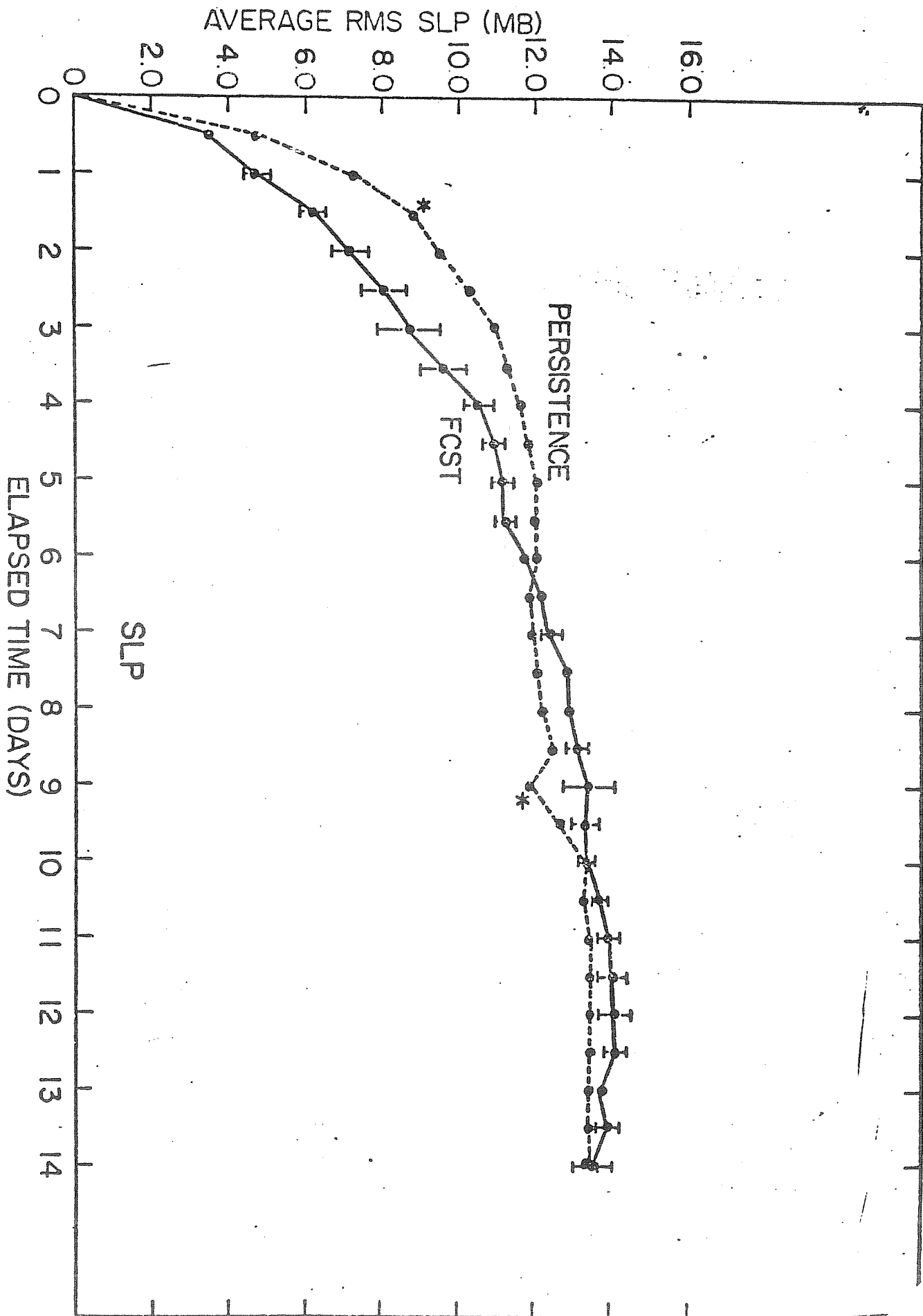


Fig. 4.12: (After Druyan et al, 1975)

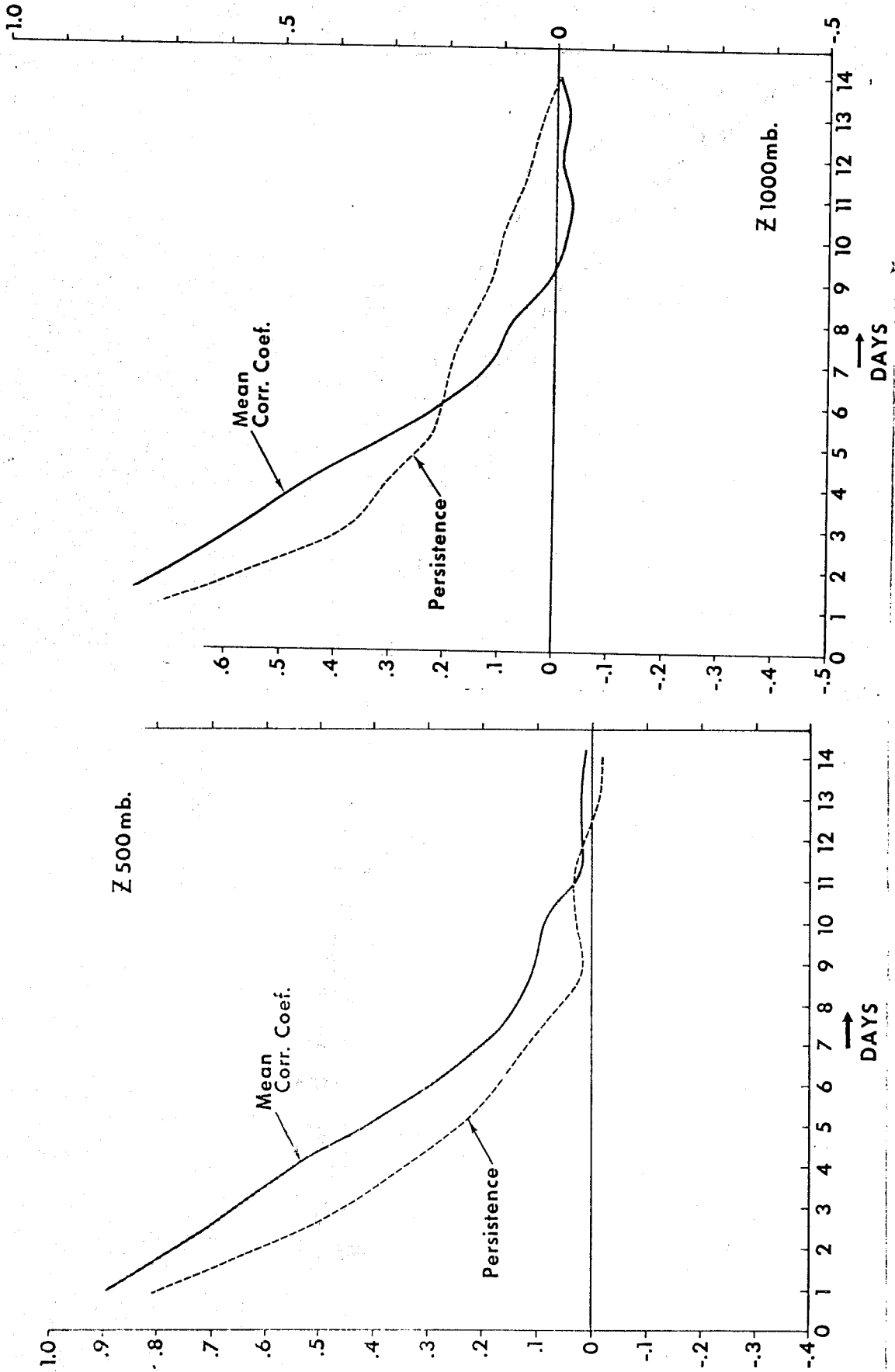


Fig. 4.13-1 : The correlation coefficients for height anomalies.

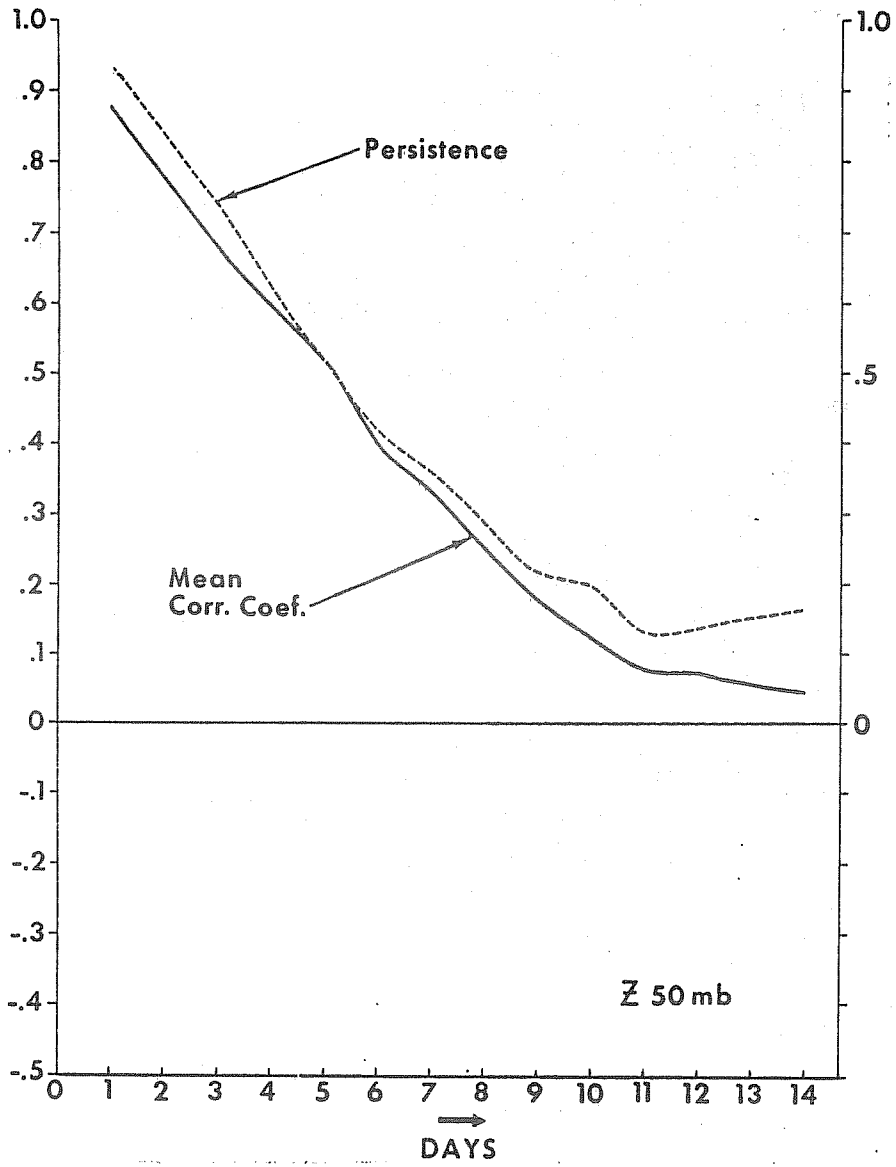


Fig. 4.13-2

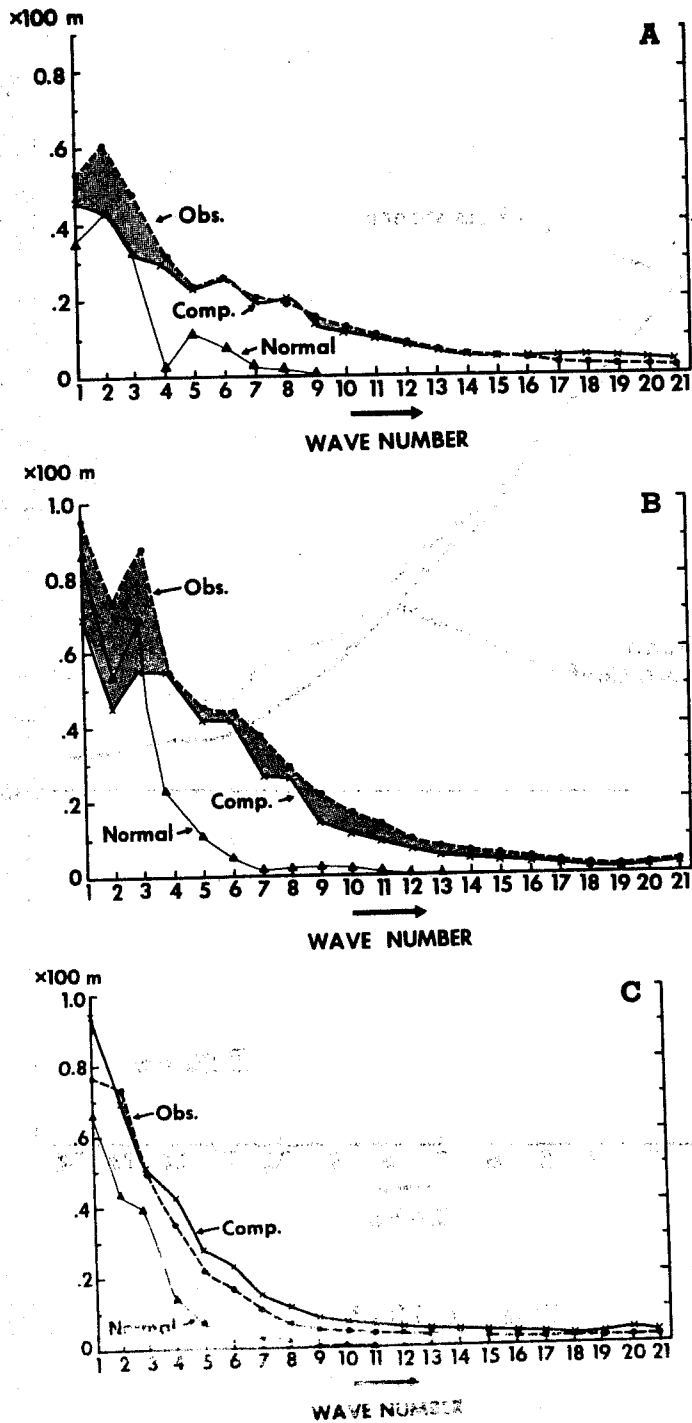


Fig. 4 14: Spectra of geopotential height for (A) 1000 mb, (B) 500 mb, and (C) 50 mb.

(After Miyakoda, Hembree et al, 1972)

Prediction performance of the solutions is assessed for each of the four spectral bands. The following verification measures are used: the correlation coefficient for anomalies of height (labeled "Anomaly"), the correlation coefficient for the total height; that is, normal plus anomaly (labeled "Total"), and the correlation for persistence of the initial anomaly (labeled "Persist.")

Figure 4.15 presents the scores averaged over the 12 January cases for the 500-mb height. Numbers are plotted along the abscissa in these figures; for example, 8 is the number indicated for waves 1-2 and 10 for waves 3-5. These numbers indicate the days at which the correlation for anomaly becomes zero. Therefore, the limits of predictability of the 500-mb height with this model are approximately 8 days for wave numbers 1-2, 10 days for waves 3-5, 8 days for waves 6-10, and just 3 days for waves 11-15.

4.3 Simulation of time averaged maps

Geopotential Fields

Hemispheric mean maps of 1000-, 500-, and 50-mb geopotential heights are computed both for the observed (Z_{obs}) and the predicted fields (Z_{pred}), averaged over 4-14 days in 12 cases (figures 4.16, 4.17, 4.18). The height differences; that is, the predicted minus the observed geopotential, are also shown ($\Delta z = z_{pred} - z_{obs}$). The observed mean 1000- and 500-mb maps are similar to the January normal maps by Crutcher and Jenne (1970) (not shown here), indicating that the sample numbers taken in this study are sufficiently large for calculating mean maps.

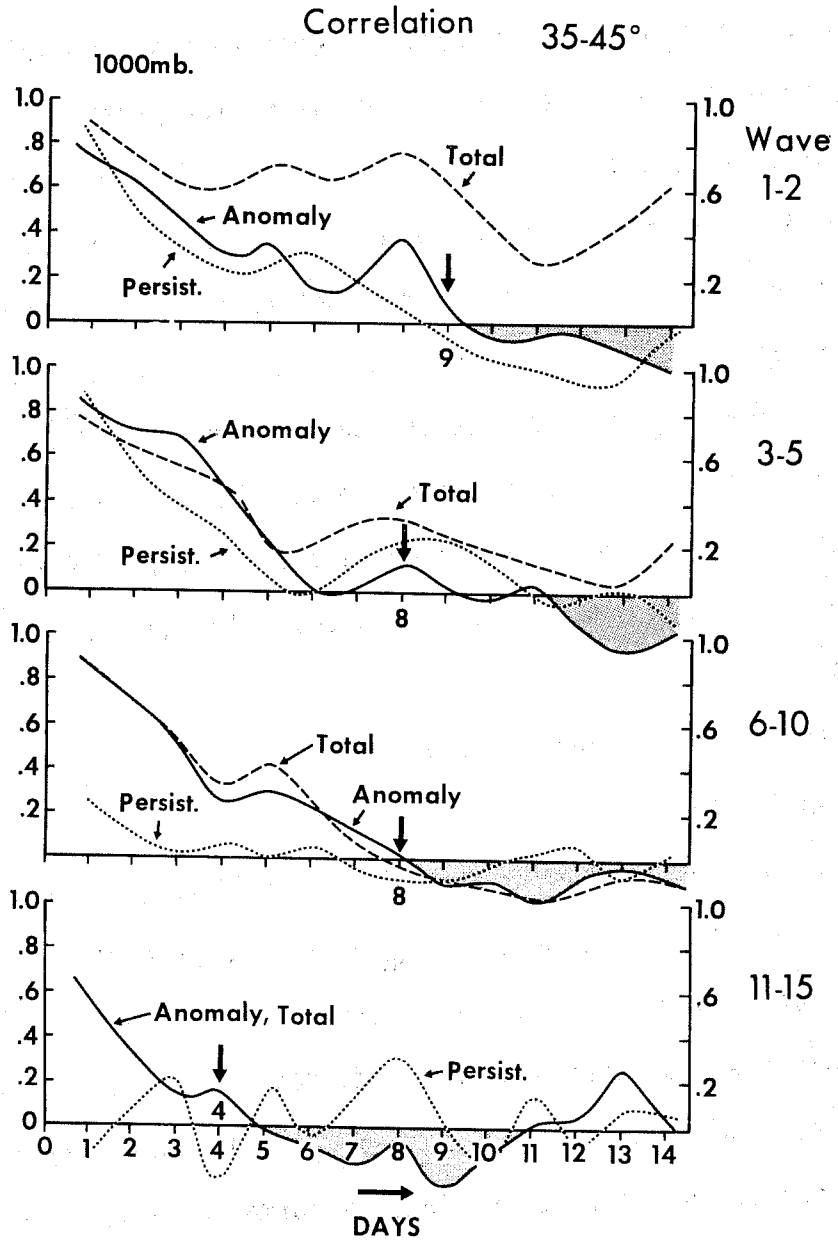


Fig. 4.15

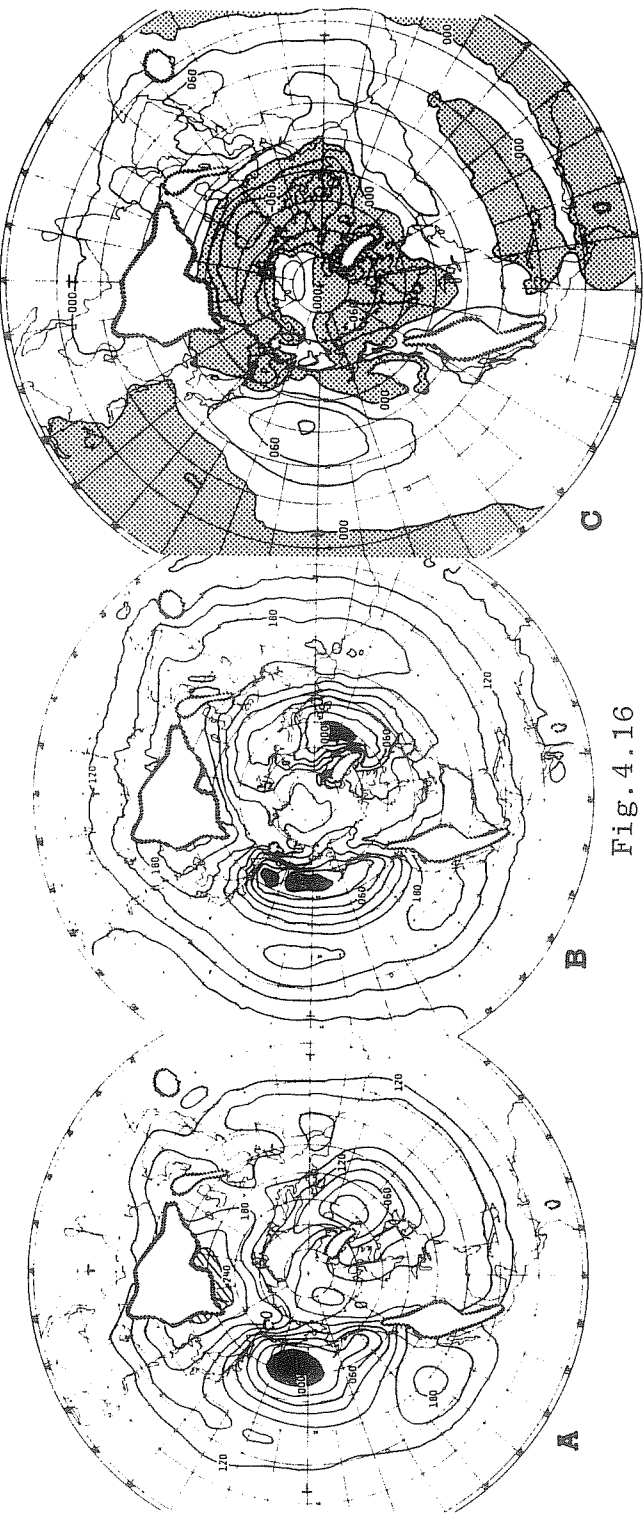


Fig. 4.16

(A) observed and (B) predicted mean maps of 1000-mb geopotential height and (C) the error map (i.e., the predicted minus the observed). Contours are at 30-m intervals. Negative areas of height error are shaded. The loci of small segmented lines mark the mountain areas.

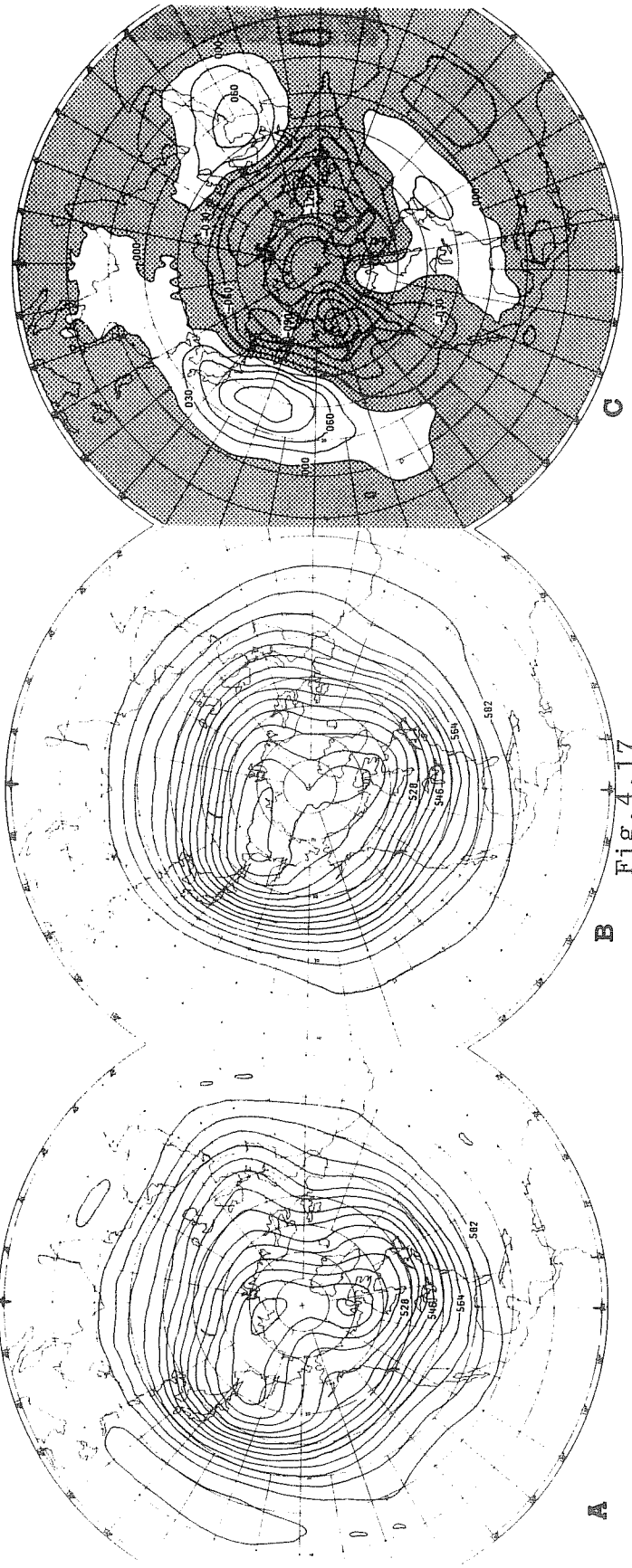


Fig. 4.17

Same as figure 4 for 500 mb except mean height contours are at 60-m intervals and height error contours are at 30-m intervals.

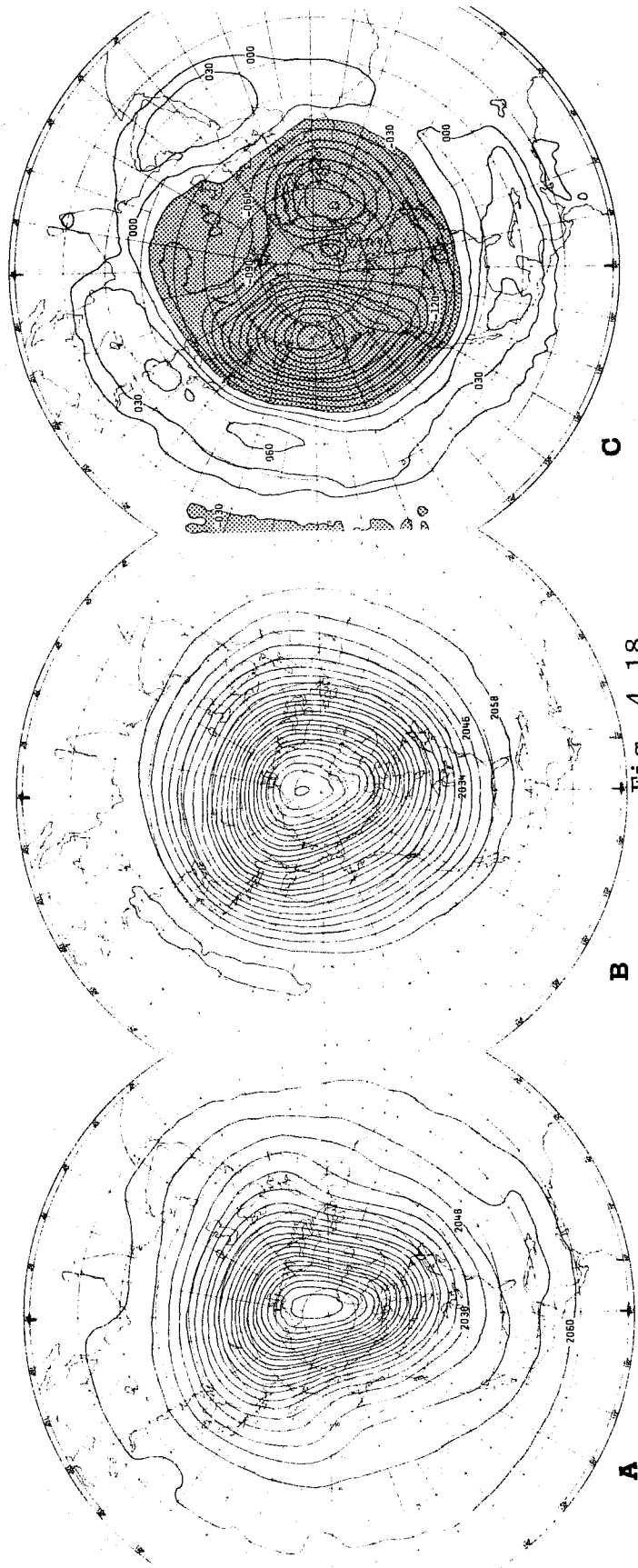


Fig. 4.18 Same as figure 4 for 50 mb except mean height contours are at 60-m intervals and height error contours are at 30-m intervals.

The height errors in this experiment are by no means small; the maxima are more than 100, 150, and 350 m for 1000-, 500-, and 50-mb fields, respectively. They are roughly composed of two modes: one is concentric around the pole, and the other is of zonal wave numbers 2 and 3 for high and middle latitudes, respectively. The latitudinal distribution of error is quite systematic; the modes of error are, from the Equator to the pole, lower, higher, lower, and higher. These features are consistent with the facts that the calculated subtropical jet stream is too intense and its latitudinal position is shifted poleward.

Zonal Wind

The meridional cross-section of the zonal wind is shown in figures 4.19 and 4.20. Overall, the observed and predicted zonal winds coincide well. It is important, however, to note several discrepancies. The predicted subtropical jet at the tropopause level in figure 4.19 is more intense than the observed jet. This feature may be related to the vertical transfer of momentum (Lilly 1972). Also, the observed winter westerlies in the troposphere at high latitude, say 65° - 75° N, has another intensity maximum, and this peak is associated with the polar frontal zone, as indicated by Palmen and Newton (1969). The predicted intensity of these tropospheric westerlies is too weak.

Figure 4.20 is the result of the GISS experiment for the 2nd week and is an average of the 6 cases. In this result the wind intensity in the forecast is weaker; this is logical because vertical diffusion was included.

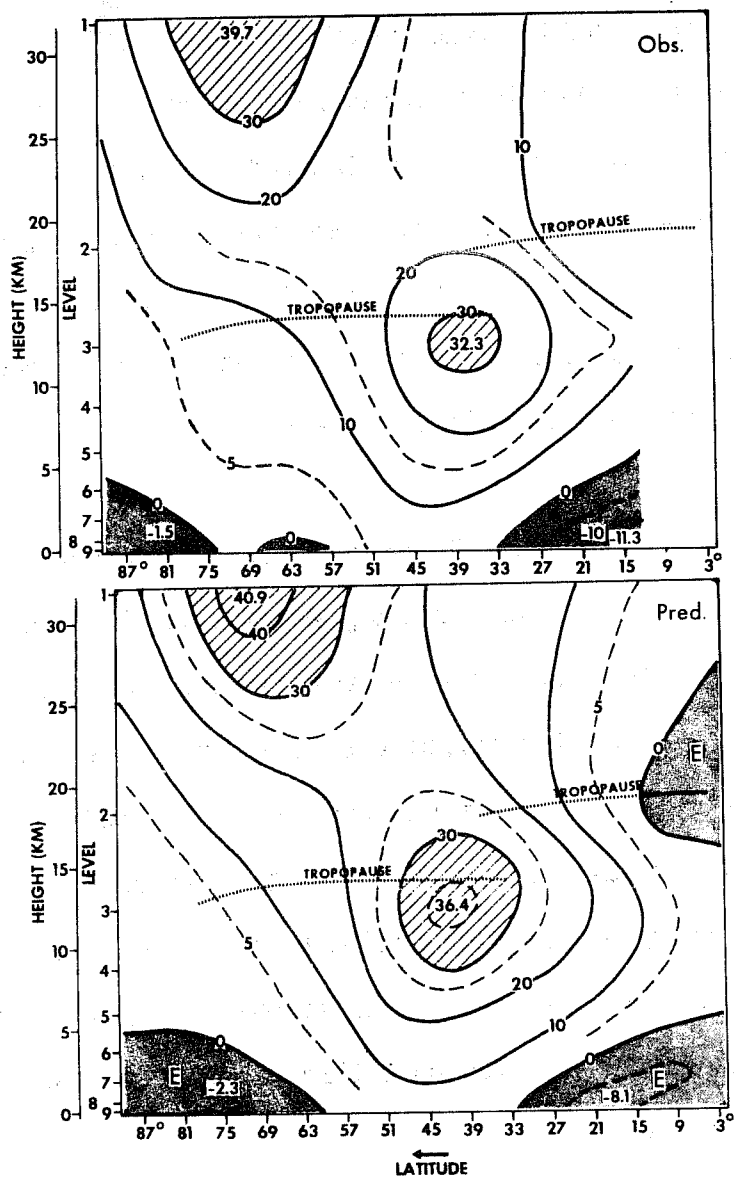
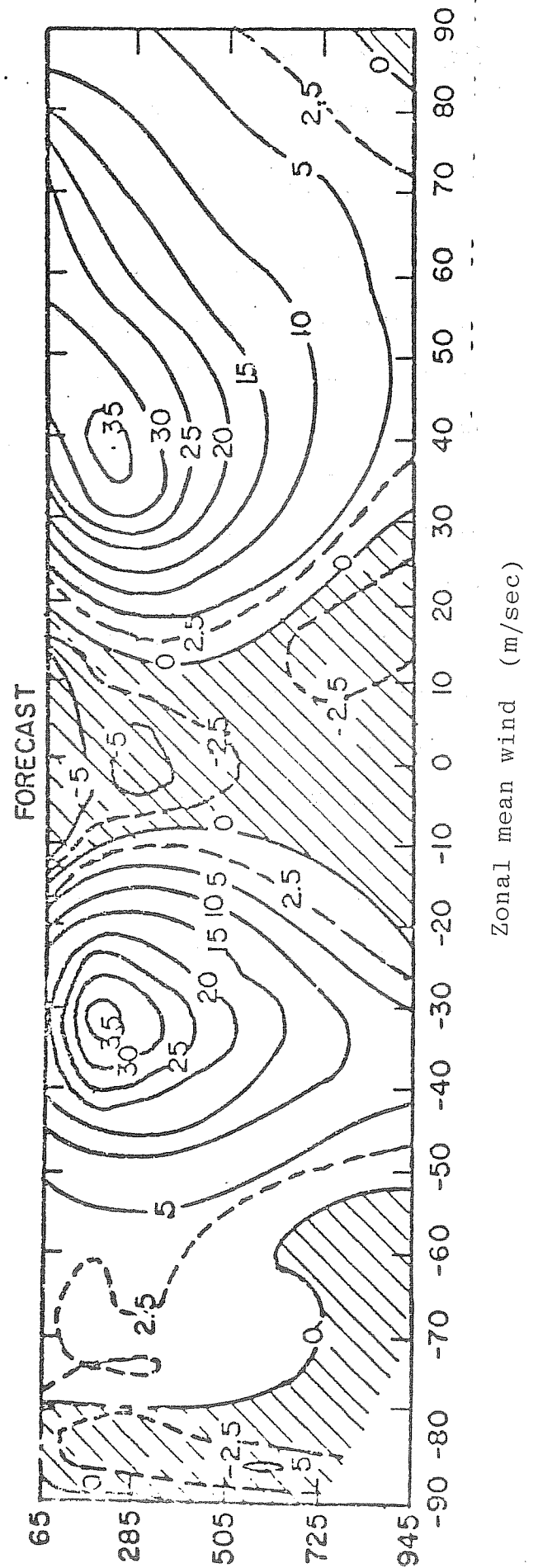
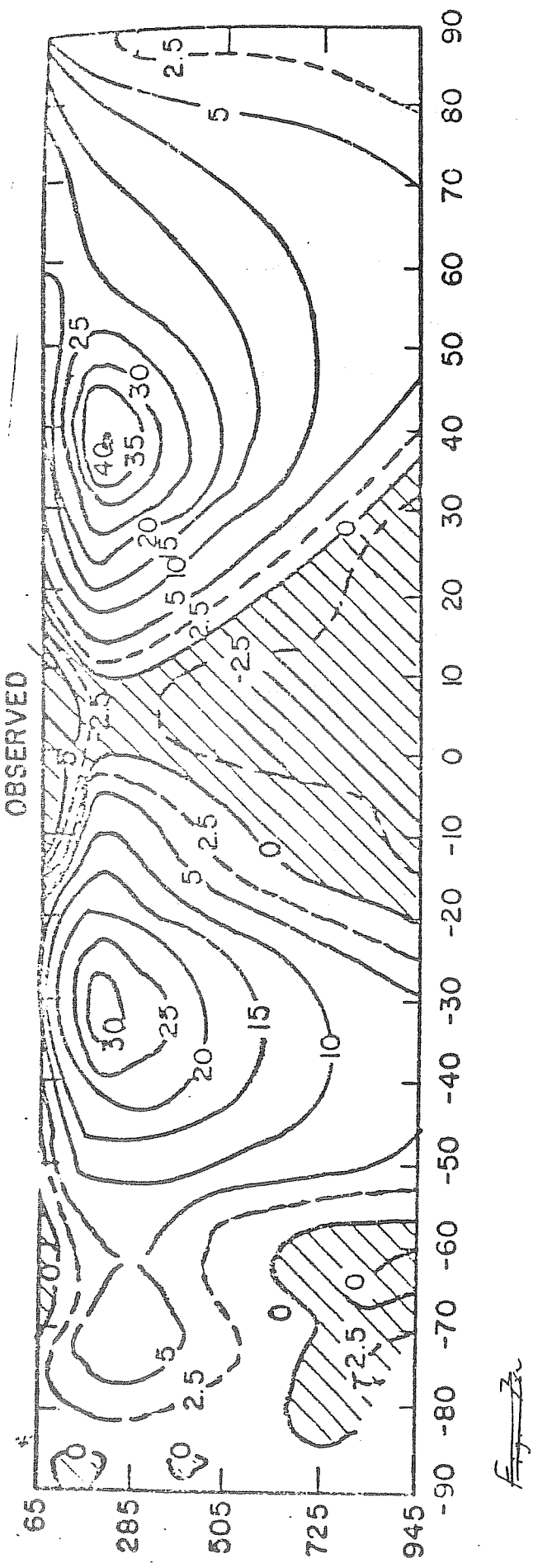


Fig. 4.19 Meridional cross-sections of observed and predicted zonal wind (m/s). The regions of westerlies with intensity greater than 30 m/s are hatched and easterlies are shaded. Extreme values are plotted.

(after Miyakoda, Hembree et al, 1972)





Zonal mean wind (m/sec)
(after Druyan, et al, 1975)

Eddy Kinetic Energy

The definition of eddy kinetic energy, K_E , is given by

$$K_E = \frac{1}{2} \rho (\overline{u'^2} + \overline{v'^2})$$

where $u' = u - \bar{u}$ and $v' = v - \bar{v}$, are the eastward and the northward eddy components of the wind vector, respectively, and ρ is the air density. The bar notation denotes the zonal average with respect to the longitude.

The meridional cross-section of K_E shown in figure 4.21 was obtained by the same averaging process as was used to obtain the temperature or zonal wind. The figure clearly indicates that the model eddy kinetic energy is weaker than the observed. The computed intensity is lower by 25 percent. Miyakoda et al. (1971) mentioned in the study of nonlinear viscosity that, if the viscosity coefficient is reduced to 0.10 (0.25 in the present study), the predicted ratio K_z/K_E is close to the observed value, K_z being the zonal mean kinetic energy. Reduction of the coefficient is difficult, however, because the solution becomes computationally unreasonable (a lot of wiggling).

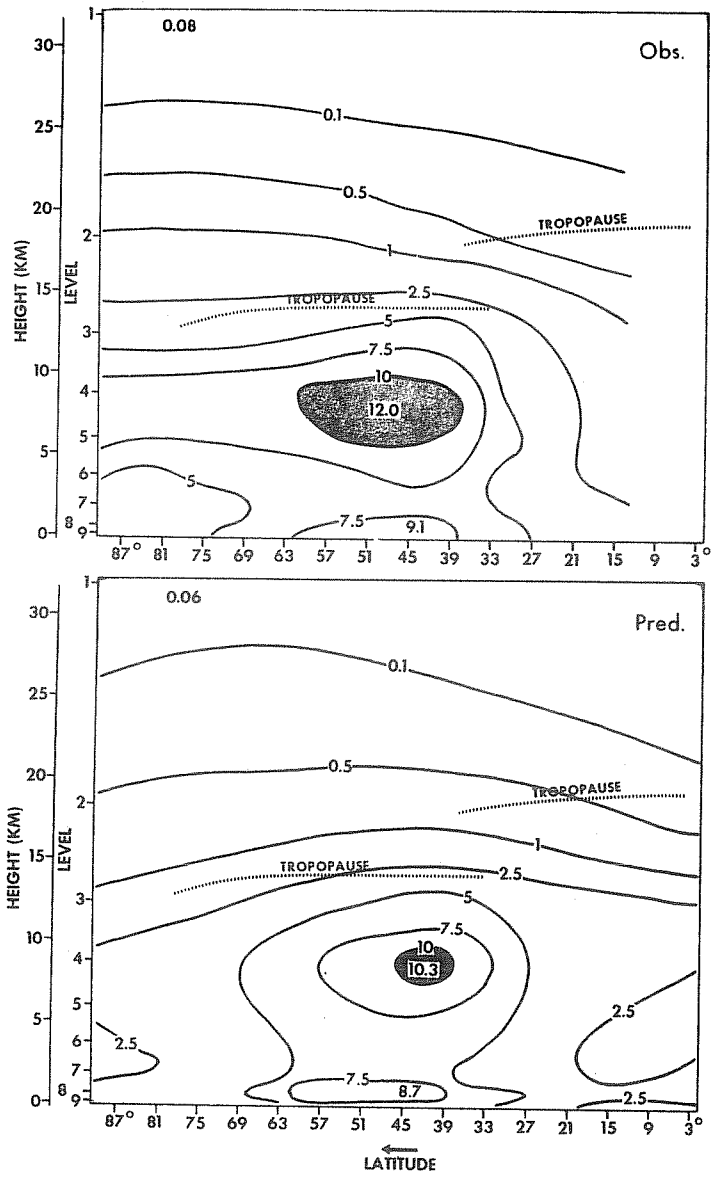


Fig. 4.21 Meridional sections of observed and predicted eddy kinetic energy ($10^{-5} \text{ J} \cdot \text{cm}^{-3}$). The maxima are plotted.

5. The energy sources and sinks in the atmosphere

The current consensus on the picture of the energy cycle in the atmosphere-earth system is shown in Figure 5.1 (Oort, 1971). Let us assume that the sun provided 100 units of energy to the atmosphere. Among them, 30 units are reflected back to space intact, 50 units reach the earth's surface, and 20 units heat up the atmosphere directly. Among the 50 units reaching the surface, 20 units are reflected back to space, and 30 units are absorbed by the soil and water. Then among 30 units of energy, 24 units are given to the atmosphere in the form of evaporation and 6 units are emitted to the atmosphere from the earth as sensible heat. In any event, 30 units of energy are added either in latent or sensible heat to the internal energy of the atmosphere. We have now 50 units of energy. Among them, only one unit is converted to kinetic energy.

(i) Heat fluxes from the ground surface and condensation of water vapor

Figure 5.2 shows the vertical distribution of heat. Six units are emitted as sensible heat to the atmosphere, and 24 units are received from condensation of water vapor and 20 units of energy are added to heat the atmosphere directly in the form of short-wave radiation. All of this energy is eventually emitted back to space by long-wave radiation.

The mechanism of release of latent heat is not simple. Yanai and Esbensen (1973) calculated the vertical distribution of the moisture sink and heat source from observed data. (see figure 5.3) Whenever the condensation heat is released as a result of cumulus convection the vertical transfers of latent and sensible heat are intensified. Q_2 and Q_1 are the moisture sink and the heat source, respectively,

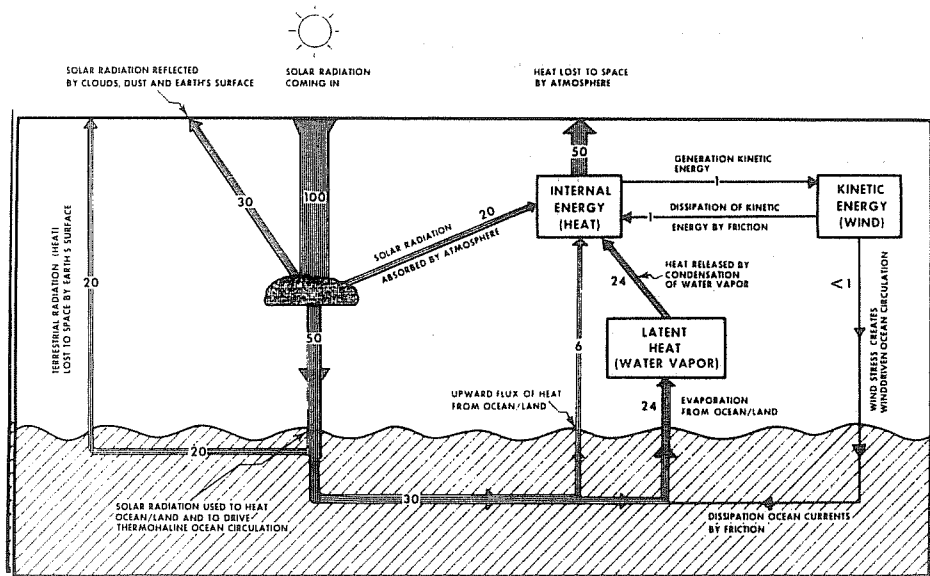


Fig.5.1 The "weather machine" of the earth, a schematic drawing of the flow of energy in the atmosphere-earth system. A value of 100 units is assigned to the incoming flux of solar energy ($0.5 \text{ cal cm}^{-2} \text{ min}^{-1}$). All values represent annual averages for the entire atmosphere. For simplicity, no energy boxes have been drawn for the ocean or land.

(after Oort, 1971)

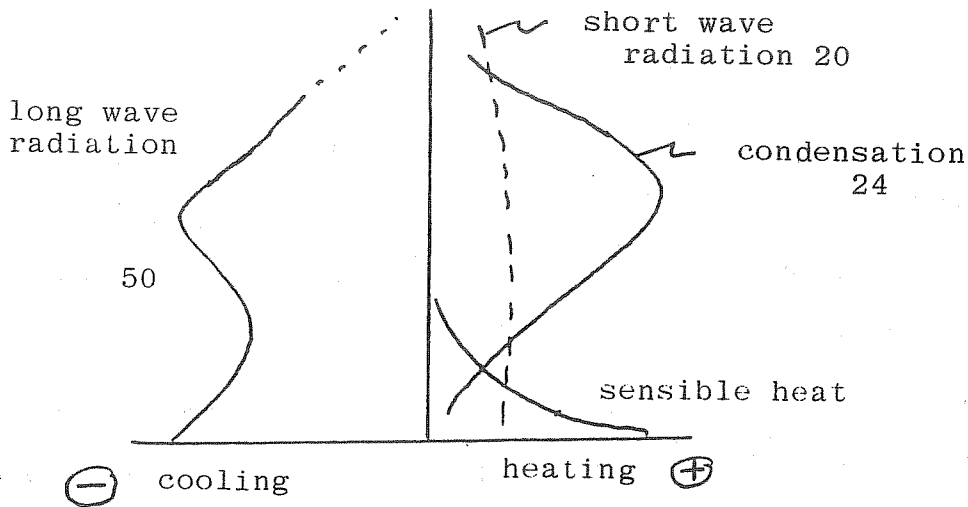


Fig. 5.2

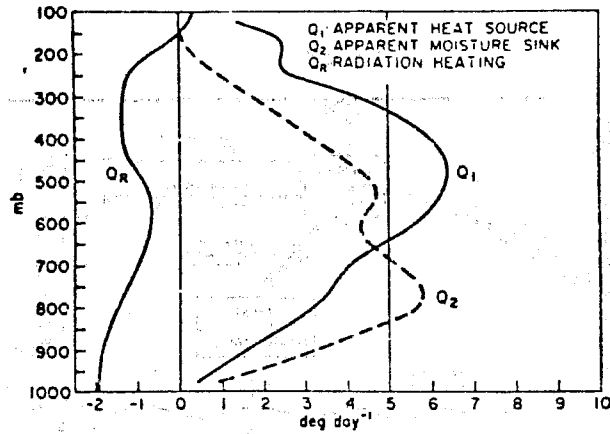


Fig. 5.3 The mean apparent heat source Q_1 (solid) and moisture sink Q_2 (dashed). On the left is the radiational heating rate given by Doplick (1970).

(Yanai, Esbensen and Chu, 1973)

calculated from observations of water vapor and temperature. The effect of eddy transport inside cumulus clouds is partially included in Q_1 and Q_2 .

They are defined by

$$Q_1 = L(c-e) - \frac{\partial}{\partial p} \overline{s'\omega'} + Q_R,$$

$$Q_2 = L(c-e) + L \frac{\partial}{\partial p} \overline{q'\omega'}$$

where c is the rate of condensation, e the rate of evaporation, Q_R the radiative heating/cooling, L the latent heat, q the mixing ratio of water vapor, s the static energy ($=C_p T + gz$). Q_1 corresponds to the curve in figure 5.2 marked 24 units.

How the sensible heat and latent heat are emitted from the earth's surface and how the eddy motions in cumulus clouds transport the moisture and internal energy vertically are the major problems in the model's physics other than the main dynamics.

The vertical distribution of heat as well as the horizontal distribution of heat are the important influences in controlling the large scale dynamics of the atmosphere, though the latter is rather the solution of the model.

Figure 5.5 was constructed by Newell et al. (1970). The top figure is the net radiative heating, the middle is the sensible heat near and inside the boundary layer and the lowest is the latent heat release. As is known, there are three belts in which centers of condensation heat exist. Tropical release is the largest and is mostly due to cumulus convection. The middle latitude condensation is partly due to cumulus convection and partly large scale condensation. If the three sources and sinks are added together, the result is figure 5.6. Similar data was obtained by Somerville et al. (1974) from their model calculation (figure 5.7). The upper figure is the large-scale supersaturation, and the lower is due to cumulus convection in the GISS model. Figure 5.8 is the rate of heating due to moist convection, condensation and vertical mixing calculated by Manabe and Terpstra (1974) from the global climate model with the modified Kurihara grid.

Comparing these figures, the maximum heating at the equator is $2.8^{\circ}\text{C}/\text{day}$ in the result by Newell et al., $1.5^{\circ}\text{C}/\text{day}$ for Somerville et al., and $4.0^{\circ}\text{C}/\text{day}$ for Manabe et al.

(ii) Conversion between potential and kinetic energy, and the kinetic dissipation.

Although the amount of energy that is converted from internal (or potential) energy to kinetic energy is small, the process is extremely important in the energetics of the atmospheric circulation. This energy is the manifestation of jet streams or the winds associated with

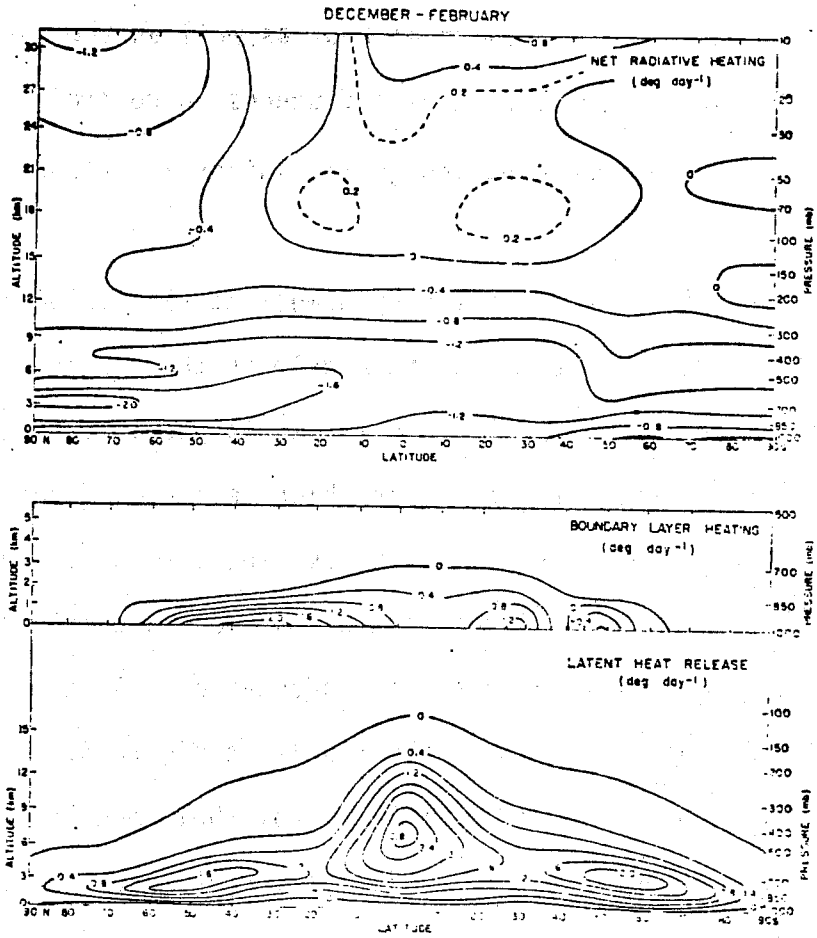


Fig. 5.5 Components of diabatic heating for the atmosphere for December-February. Units : deg day⁻¹.

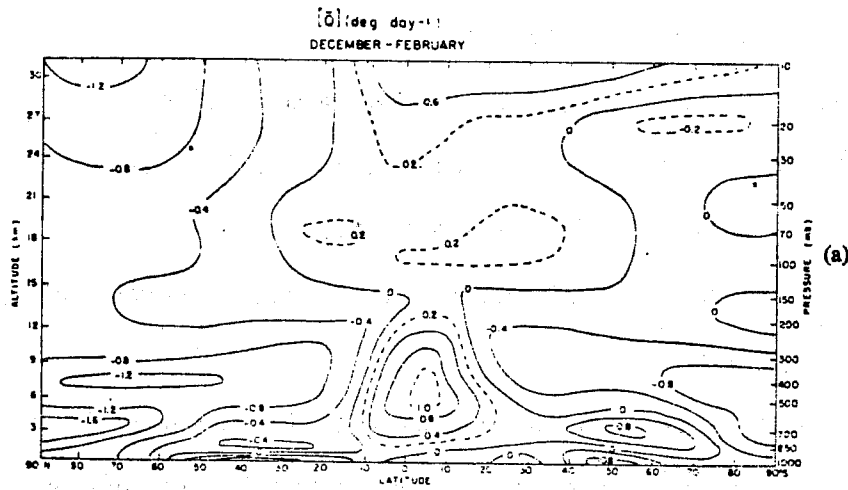
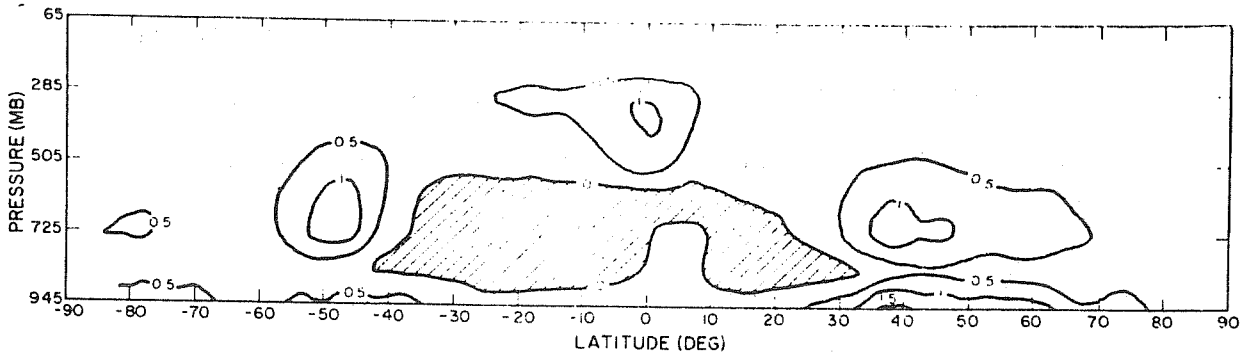


Fig. 5.6



Computed January zonal mean field of heating rates ($^{\circ}\text{C day}^{-1}$) due to large-scale supersaturation. Negative regions are shaded.

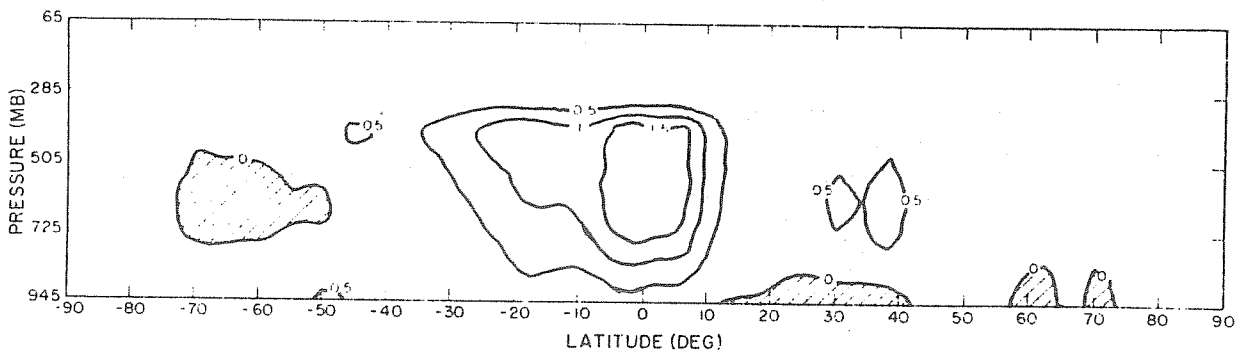


Fig. 5.7 Computed January zonal mean field of heating rates ($^{\circ}\text{C day}^{-1}$) due to parameterized sub grid-scale moist convection. Negative regions are shaded.

(after Somerville et al, 1974)

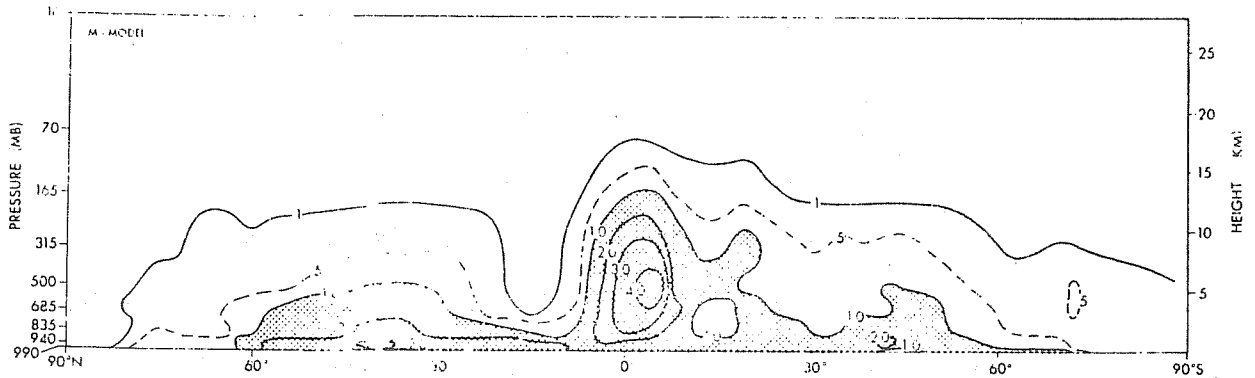


Fig. 5.8 Latitude height distribution of the zonal mean rate of net heating ($^{\circ}\text{K day}^{-1}$) due to moist convection, condensation and vertical mixing in the M model atmosphere

(after Manabe and Terpstra, 1974)

troughs, etc., and they are indeed the targets of our weather forecasts. The smallness of the amount of converted energy is indicative of the delicate imbalance from which the kinetic energy is generated.

The kinetic energy equation averaged over a horizontal domain is written as

$$\frac{\overline{-H}}{\partial t} = - \frac{\overline{-H}}{\partial \omega K} + \frac{\overline{-H}}{[-V \cdot \nabla \phi]} - \epsilon(k) + b(K), \quad (5.1)$$

where $K = \frac{1}{2} (u^2 + v^2)$, the kinetic energy, $(\overline{\quad})^H$ is the horizontal average, $\epsilon(k)$ is the dissipation of kinetic energy, and $b(k)$ is the effect of lateral boundary on K . The second term on the right hand side is the work done by the gradient force of geopotential height, and it is rewritten as

$$\frac{\overline{-H}}{[-V \cdot \nabla \phi]} = - \frac{\overline{-H}}{\frac{\partial \phi \omega}{\partial p}} + \frac{\overline{-H}}{[-\omega \alpha]}, \quad (5.2)$$

where $\alpha = RT/p$, $(-\overline{\omega \alpha})^H$ indicates the conversion of the potential energy to kinetic energy, and $-\frac{\overline{\partial \phi \omega}}{\partial p}^H$ is the divergence of vertical flux of height.

Figure 5.9 shows these terms obtained in the numerical general circulation studies (Smagorinsky, Manabe, and Holloway, 1965). As seen the generation of kinetic energy, $-\overline{\omega \alpha}^H$, appears maximum at the 500 mb level. The vertical flux of geopotential height is directed upward above 700 mb level, whereas it is downward below that level. This implies that the kinetic energy is produced in the middle of the troposphere (probably due to the baroclinic instability), and it is then transferred upward in the upper portion of the atmosphere and downward in the lower part. As a result, the eventual distribution of produced kinetic energy

expressed by the term, $-\overline{\mathbf{V} \cdot \nabla \phi^H}$, shows two maxima, one at 300 mb and one near the ground surface. This kinetic energy is next to be dissipated by viscosity in two principal regions; one is in the planetary boundary layer (PBL) and the other is at the lower portion of jet stream.

Figure 5.10 is the budget study of kinetic energy by Kung (1967), using observed data over North America. The distribution of $-\overline{\mathbf{V} \cdot \nabla \phi}$ is similar to that in figure 5.9, though the dissipation near the surface is much larger than that in the free atmosphere. It is interesting to note that the dissipation (\bar{E} in the figure) in the lower portion of the atmosphere takes place not only the PBL but also in the layer up to 700 mb.

The distribution of $-\overline{\omega \alpha^\lambda}$ is shown schematically in the meridional section (figure 5.11), where $(\overline{\quad})^\lambda$ is the zonal average. There are 4 major sources of kinetic energy or the conversion of available potential energy to kinetic energy. They are two mid-latitude sources at 650 mb level in the northern and southern hemispheres, respectively, one equatorial source at 300 mb level and one polar night region in the stratosphere. The kinetic energy thus produced is then vertically redistributed in terms of $-\overline{\omega \phi^\lambda}$; the direction of the propagation is indicated by arrows.

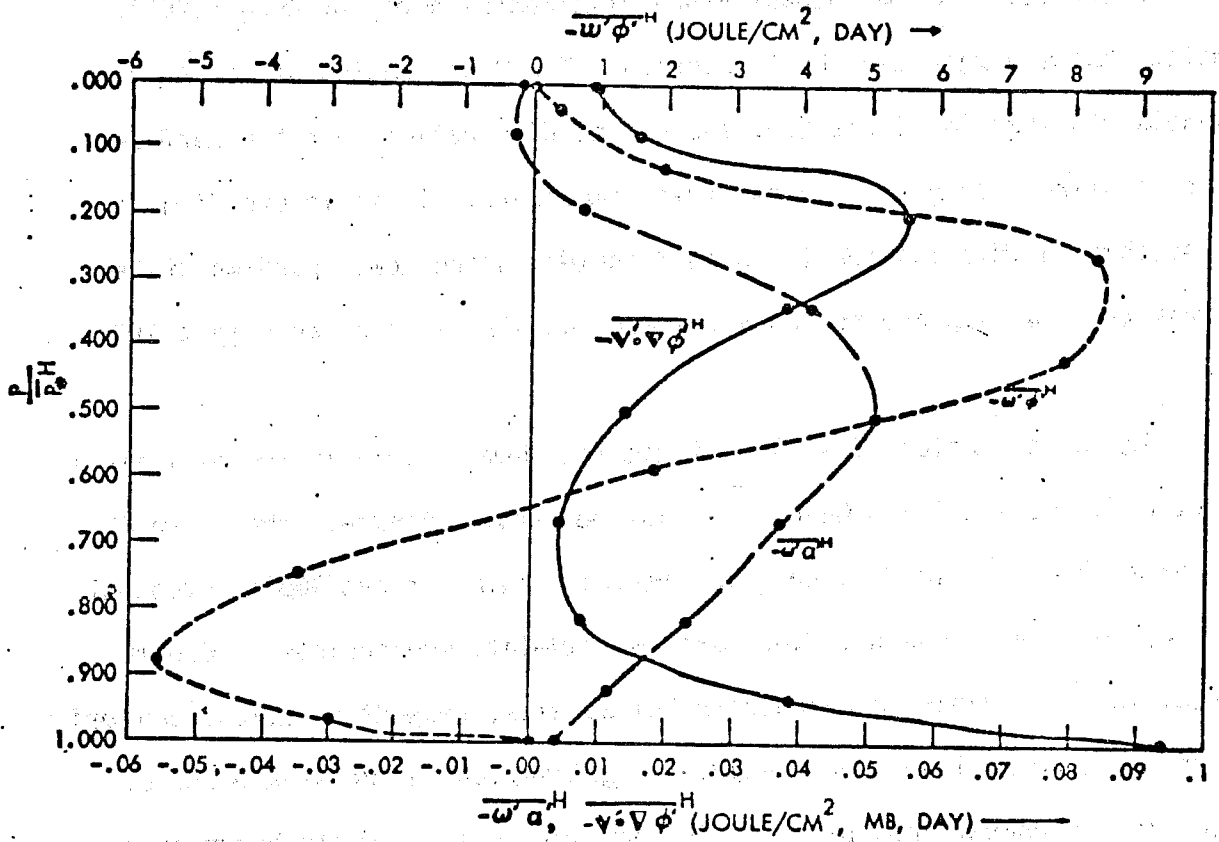


Fig. 5.9 (Smagorinsky, Manabe and Holloway, 1965)

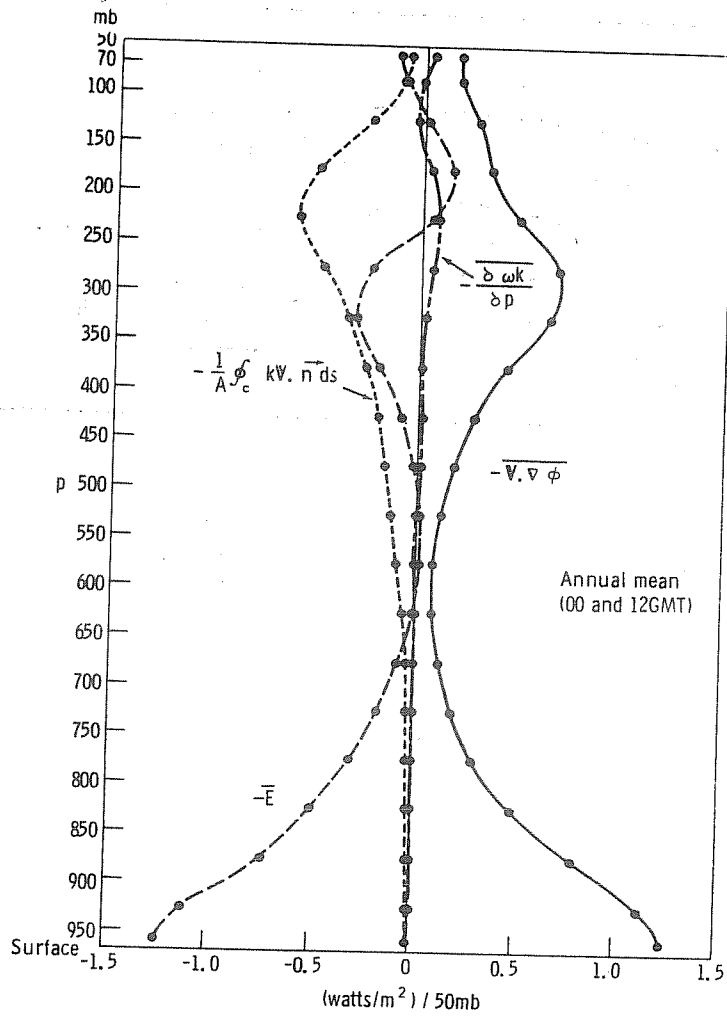


Fig. 5.10 -Multi-annual mean vertical profile of the kinetic energy balance for the 5-yr. period (average of 00 and 12 GMT).

(after Kung, 1967)

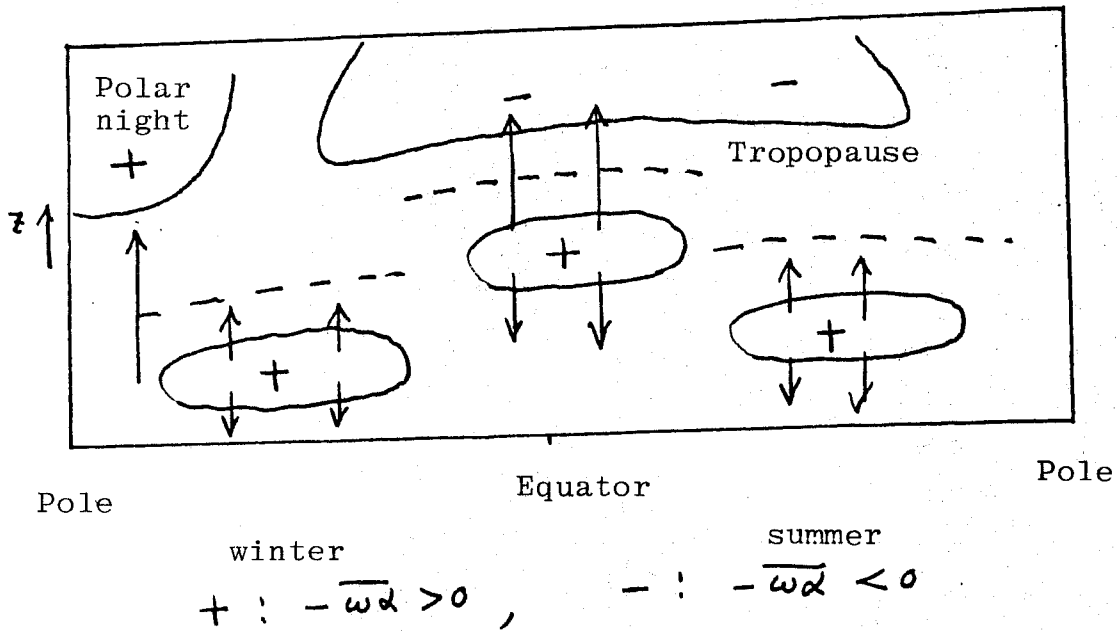


Fig. 5.11

6. The subgrid-scale physics in models

The physics of radiational transfer, condensation of moisture, turbulent transfer, and the kinetic energy dissipation are the important processes associated with the formation of the energy sources and sinks in the atmosphere, and therefore, these effects should be incorporated in numerical prediction models. The mechanisms of these processes are related mostly to the spatially small scale disturbances or even molecular processes.

It is one of the basic characteristics of numerical models, however, that these small scale disturbances can not be included explicitly. This is because (i) the model's atmosphere is discretized by mesh or the distribution of meteorological variables is represented by a truncated series of the expansion of orthogonal functions, and (ii) the mechanisms responsible for these physics are neglected by assumptions (for example, the local buoyancy force is ignored by the hydrostatic assumption).

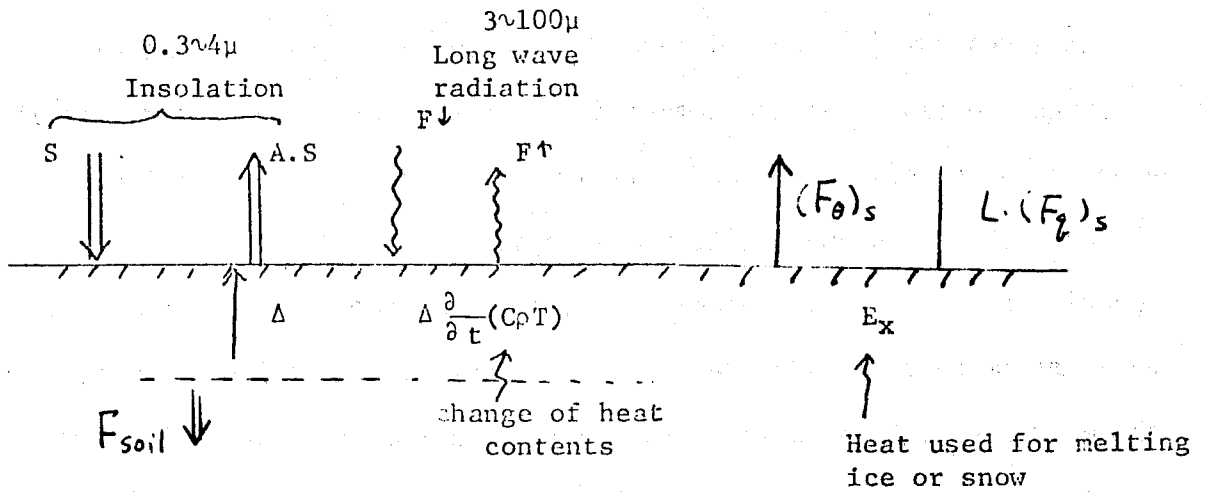
The reasons (i) and (ii) are related to each other in some way. It is often the case that the detailed mechanism can not be properly treated, even if the process is included in a model, because the spatial resolution is too coarse. In any event, these transfer or conversion physics in subgrid-scale are indispensable for simulating the general circulation. One compromise is to include the bulk effect or the ensemble effect of these processes by by-passing the real, detailed processes. The formulation of the ensemble effect in terms of grid-scale variables is called the "parameterization." If the parameterized process of the ensemble effect is adopted, one should, of course, abandon the deterministic

prediction of the sub-grid scale physics.

Thus the parameterized processes that are considered necessary for the medium-range forecasts are: (a) radiation, (b) surface heat balance, (c) drag and heat transfer in the surface layer, (d) PBL transfers, (e) convection due to gravitational instability, (f) vertical mixing, (g) large scale condensation of water vapor, (h) cumulus convection, and (i) lateral mixing.

We will outline some of these subgrid-scale processes below; though radiation is omitted. In this section, however, we will not touch on the sophisticated parameterizations but will come back to them in the later sections.

Process (b): Surface heat balance



$$\Delta \frac{\partial}{\partial t} (c \cdot \rho \cdot T_g) = (1 - A) \cdot S + F_{\downarrow} - F_{\uparrow} - (F_{\theta})_s + F_{soil} - L (F_q)_s - E_x \quad (6.1)$$

where

S: solar radiation arriving at the surface

A: albedo of ground surface

(1-A)S: absorbed solar radiation

F_{\downarrow} : Net downward long wave radiation

F_{\uparrow} : Net upward long wave radiation = σT_g^4

$(F_{\theta})_s$: Sensible heat flux to atmosphere

F_{soil} : Heat conduction from sub-surface (soil, for example)

$L(F_q)_s$: Latent heat flux to atmosphere

E_x : Heat used for melting ice or snow

L: Latent heat of condensation

Process (c) The drag and heat transfer in the surface layer

The drag, heat and moisture transfers in the layer near the surface (the surface and constant-flux layers) are written in the simplest way by the aerodynamical method, i.e.

$$(\tau)_s = \rho \cdot C_D |V(z_k)| \cdot V(z_k), \quad (6.2)$$

$$(F_{\theta})_s = \rho \cdot C_p \cdot C_D |V(z_k)| \{ \theta_s - \theta(z_k) \} \quad (6.3)$$

$$(F_q)_{pot} = \rho \cdot C_D \cdot |V(z_k)| \{ q_{sat}(T_s) - q(z_k) \} \quad (6.4)$$

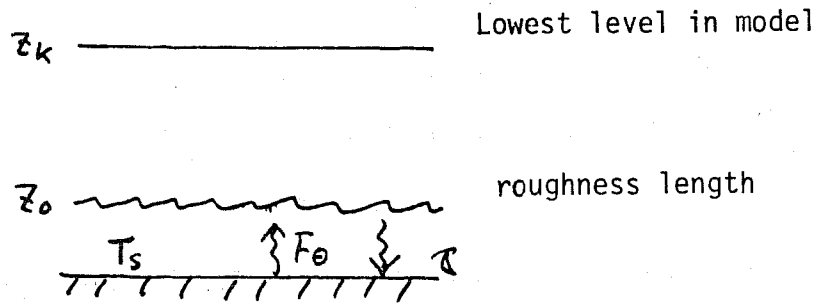


and

$$(F_q)_s = D_w \times (F_q)_{pot}, \quad (6.5)$$

where C_D is the drag coefficient and z_0 is the roughness length, z_k is a level inside the constant-flux layer

$$C_D = \{k_0 / \log (z_k / z_0)\}^2 \quad (6.6)$$



τ , F_0 , F_q are the stress, heat and moisture transfers, respectively. q_{sat} is the saturation mixing ratio of water vapor, T_s is the surface temperature, the suffix S means the surface, D_w is a "wetness" index for the degree of availability of ground water.

$$D_w = \frac{W}{W_k} \quad (6.7)$$

where W is the soil moisture, and W_k is the maximum capacity of soil moisture. W is determined by an equation, and W_k is specified. The drag coefficient C_D is given by Kung (1966).

over sea	$C_D = 1.17 \times 10^{-3}$	winter
	1.07×10^{-3}	summer
over land	$C_D = 3.30 \times 10^{-3}$	winter
	5.24×10^{-3}	summer

Process (d) and (f): The vertical mixing in the planetary boundary layer and the free atmosphere

Neutral mixing-length method

$$\tau = \rho \cdot K_M \frac{\partial V}{\partial z} \quad (6.8)$$

$$F_\theta / C_p = -\rho K_H \frac{\partial \theta}{\partial z}, \quad (6.9)$$

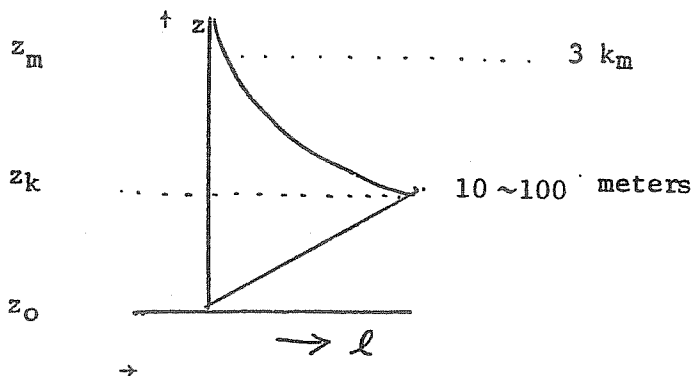
$$F_q = -\rho K_q \frac{\partial q}{\partial z} \quad (6.10)$$

The eddy coefficients are given by

$$K_M = \ell^2 \left| \frac{\partial V}{\partial z} \right|, \quad K_M = K_H = K_q \quad (6.11)$$

where the mixing length ℓ is

$$\ell = \begin{cases} k_0 (z + z_0), & z \leq z_k \\ k_0 (z_k + z_0) \cdot \frac{z_m - z}{z_m - z_k}, & z_k < z \leq z_m \\ 0 & z_m < z \end{cases}$$



Process (e): Dry Convective Adjustment

If the atmosphere is unstably stratified relative to the dry adiabatic lapse rate, the hydrostatic equilibrium breaks down, and consequently the local convection occurs. As a result of the convection, the atmosphere will regain the neutral stratification. The method that is most frequently used for the treatment of this process is the "dry convective adjustment." The scheme operates as follows:

(i) When the lapse rate of a layer exceeds the dry adiabatic lapse rate, the effect of convection is to give rise to a neutral lapse rate throughout the unstable layer.

(ii) The static energy $S=(C_p T + gz)$ (or enthalpy), remains unchanged under the adjustment. These processes are expressed as

$$\frac{\partial}{\partial p} \theta(T + \delta T, p) = 0, \quad (6.12)$$

$$\frac{C_p}{g} \int_{P_B}^{P_T} \delta T dp = 0, \quad (6.13)$$

where δT is the change of temperature due to the convective adjustment. and P_T and P_B are the top and bottom of the layer.

The temperature change at the central level may or may not cause more unstable lapse rate in the neighboring layers. If the former is the case, this process is iterated until the unstable lapse rate is removed.

Process (h): Moist convective adjustment

The conditional unstable stratification is directly modified and adjusted so that the instability is removed. This concept stemmed originally from the theory of radiative-convection, but more recently, from the studies of atmospheric general circulation, i.e., Manabe,

Smagorinsky, and Strickler (1965). By this method, the conditional instability is continuously removed from the solutions of the general circulation model. Otherwise, there is a possibility that the computational breakdown may occur.

The principle is the following:

The moist convective adjustment takes place, if the atmosphere is saturated in any layer where conditional instability prevails.

- (i) The equivalent potential temperature is adjusted to be equal in the vertical throughout the unstable layer.
- (ii) The moist static energy ($C_p T + gz + Lq$) remains unchanged under the adjustment.
- (iii) The relative humidity is bounded by the saturation value.
- (iv) All the moisture condensed precipitates instantaneously.

The mathematical processes are written, by denoting the changes in temperature and mixing ratio of water vapor due to the convective adjustment by δT and δq , as

$$\frac{\partial}{\partial p} \theta_e(T + \delta T, q + \delta q, p) = 0 \quad , \quad (6.14)$$

$$q + \delta q = \gamma_c \cdot q_s(T + \delta T, p) \quad , \quad (6.15)$$

$$\frac{1}{g} \int_{p_B}^{p_T} (C_p \cdot \delta T + L \cdot \delta q) dp = 0 \quad , \quad (6.16)$$

where θ_e is the equivalent potential temperature, i.e.,

$$\theta_e = \theta \cdot \exp(L \cdot q / C_p T) \quad . \quad (6.17)$$

q_s is the saturation mixing ratio. It is also noted that there is a relation between θ_e and the moist static energy ($C_p T + gz + Lq$) as follows

$$-C_p \frac{T}{\theta_e} \frac{\partial \theta_e}{\partial p} \approx - \frac{\partial}{\partial p} (C_p T + gz + Lq) \quad (6.18)$$

The condition corresponds to the "moist adiabat" where the lapse rate is

$$\Gamma'_m = \frac{RT}{C_p p} \cdot \frac{p + \gamma_c \times \frac{0.622 \cdot L \cdot e_s}{RT}}{p + \gamma_c \times \frac{0.622 \cdot L}{C_p} \frac{de_s}{dt}} \quad (6.19)$$

where $r_c = 1$. In practice, $\gamma_c = 0.8$ is often used.

Criticism:

- (1) In reality the cumulus convection can occur even in the case of low relative humidity, say 60%, whereas the convective adjustment requires the relative humidity to be the saturation value.
- (2) The instantaneous adjustment produces a considerable amount of "shock" to the model's computation.
- (3) In reality the lapse rate of temperature often exceeds that of the moist adiabat in the low atmosphere of the tropics, whereas the adjustment forces the equivalent potential temperature to be equal in the vertical.

Attempts to alleviate the difficulties:

- (1) 80% is used for the saturation value of relative humidity.
- (2) In order to reduce the "shock," Gadd and Keers (1970) used the following adjustment.

$$\Gamma_c = \begin{cases} \Gamma_d & \text{for } 0 \leq r \leq r_c \\ \Gamma_d \left(\frac{1-\gamma}{1-\gamma_c} \right) + \Gamma_m \left(\frac{r-r_c}{1-r_c} \right) & \text{for } r_c \leq r \leq 1, \end{cases} \quad (6.20)$$

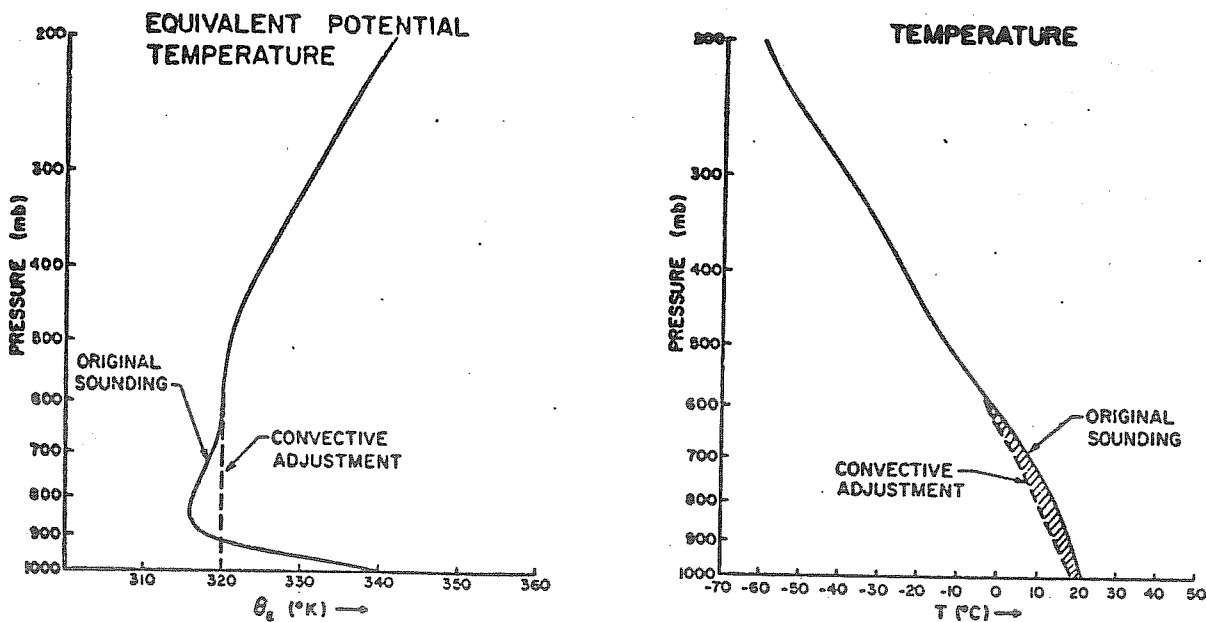


Fig. 6.1 after Krishnamurti and Moxim (1971)

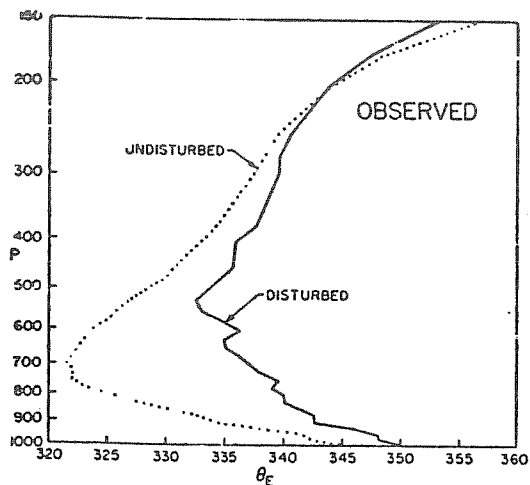


Fig. 6.2: A comparison of the vertical distribution of equivalent potential temperature, θ_e , during disturbed and undisturbed conditions. from Warsh et al. (1970).

T.N. Krishnamurti and Masao Kanamitsu.

where Γ_c is the adjusted lapse rate, Γ_d and Γ_m are the dry and moist adiabatic lapse rate, respectively, r is the relative humidity in tenths and r_c is an empirical criterion which was 0.5 in practice.

(3) Kurihara (1972) tried to include the effect of the entrainment using the lapse rate

$$\Gamma_c = \Gamma_m + E \frac{L}{C_p + 0.622 \cdot L} \frac{dq_s - q}{dT} \quad (6.21)$$

where E is the entrainment factor which is inversely proportional to \sqrt{q} .

The merit of the scheme of moist convective adjustment is simplicity, and therefore, it is easily incorporated in a general circulation model which has been applied in other parts of the world.

In the real atmosphere, the equivalent potential temperature distribution vertically as in figure 6.2. In the undisturbed case, the lapse rate below 700 mb level is conditionally unstable, whereas the lapse rate in the disturbed case comes close to the neutral.

"CISK method (The conditional instability of second kind)

The cumulus heating is assumed to be proportional to the vertical motion at the top of the Ekman boundary layer. In the early attempt at hurricane simulation, the "conditional instability" alone in the conventional sense was considered. It was demonstrated that the instability did not produce hurricanes, but only a single cumulus convection. In order to remove this difficulty, Ooyama (1964) and Charney and Eliassen (1964) proposed new hypothesis on the heating. Based upon the assumption that, cumulus clouds develop in the areas of boundary layer convergence and are permitted to penetrate into the upper unsaturated atmosphere, they hypothesized

that the heating is expressed by a formula as

$$\frac{\alpha}{C_p T} Q = \begin{cases} -\eta \cdot S \cdot \omega^* , & \omega^* < 0 \\ 0 , & \omega^* > 0 \end{cases} \quad \left. \begin{array}{c} \text{↑ ↑} \\ \text{↑ ↑} \\ \omega^* \end{array} \right\} \text{Ekman layer} \quad (6.22)$$

where S is the index of static stability ($= -\alpha \partial \ln \theta / \partial p$), $\alpha = \frac{RT}{p}$, ω^* is the vertical motion at the top of the boundary layer, which is given by

$$\omega^* = \frac{1}{2} D_E \cdot \zeta_g \cdot \sin 2 \varphi . \quad (6.22)$$

$D_E = \sqrt{2K/f}$ the Ekman depth, K is the kinematic eddy viscosity, φ is the angle between the surface geostrophic wind and the surface isobars, ζ_g is the vorticity of the surface geostrophic wind (exactly speaking, ζ_g should be the curl of stress in the boundary layer), η is a non-dimensional parameter which is related to the rate of entrainment and accordingly determines the vertical distribution of heating. Using this formulation, it was possible to demonstrate by the linear analysis the maximum growth rate for scales of a few hundred kilometers instead of the scale of cumulus. Further, it was shown that if $\eta > 1$ the hurricane develops and otherwise there is no destabilizing effect. Thus it is clear that the conditional instability which leads to the development of tropical cyclone is different from the conventional one. In this sense, Charney called new instability the Conditional Instability of Second Kind - CISK.

Criticism: New problems were, however, noticed; the hurricane developed unlimitedly (Ooyama, 1964 and Ogura, 1964), and the vertical distribution of n is not properly specified, though Yamasaki (1968) gave an arbitrary functional form of n . This scheme, CISK, is convenient for theoretical studies and has been used extensively and successfully for the studies of tropical waves. However, the scheme has not been constructed to be usable for the general circulation modelling.

Kuo's type method

Different from the "CISK" method, Kuo's method specifies the vertical distribution of heating. The heating in the free atmosphere is assumed to be dependent on the temperature difference of the model cloud and the cloud environment. It is then postulated that the heat and moisture exchange between clouds and the environmental atmosphere takes place instantaneously by lateral mixing. The procedure is described later.

Process (i) Lateral Mixing

The grid-volume averaged Navier-Stokes equations are written as

$$\left\{ \begin{aligned} \frac{\partial u_i}{\partial t} + u_k \frac{\partial u_i}{\partial x_k} + \frac{\partial}{\partial x_i} \left(\frac{p}{\rho} \right) - \nu \frac{\partial^2 u_i}{\partial x_k^2} &= \overline{\frac{\partial u_i u_k}{\partial x_k}} \\ & \quad k \text{ and } j = 1, 2, 3 \end{aligned} \right. \quad (6.23)$$

$$\frac{\partial u_i}{\partial x_i} = 0 \quad (6.24)$$

2-dimensional case

$$\frac{\partial u_i}{\partial t} = \frac{\partial}{\partial x_1} \left(\frac{p}{\rho} \right) - \left(\frac{\partial \tau_{11}}{\partial x_1} + \frac{\partial \tau_{12}}{\partial x_2} \right), \quad (6.25)$$

$$\frac{\partial u_2}{\partial t} = \frac{\partial}{\partial x_2} \left(\frac{p}{\rho} \right) - \left(\frac{\partial \tau_{21}}{\partial x_1} + \frac{\partial \tau_{22}}{\partial x_2} \right), \quad (6.26)$$

where τ_{ij} is Reynolds stress, i.e.,

$$\tau_{ij} = \overline{u_i u_j} \quad (6.27)$$

Smagorinsky (1963) derived the formulation of the eddy viscosity term based on an assumption on the rate of strain of fluid analogous to

that of an elastic media. The assumption is that "the shear stress is linearly proportional to the rate of deformation," i.e.,

$$\tau_{ij} = K D_{ij} \quad (6.28)$$

where D_{ij} is the deformation of the averaged flow defined by

$$D_{ij} = \frac{\partial u_i}{\partial x_j} + \frac{\partial u_j}{\partial x_i} - \delta_{ij} \frac{\partial u_k}{\partial x_k} \quad (6.29)$$

δ_{ij} being the Kronecker's delta. Using the assumption of energy spectrum, $k^{-5/3}$, one obtains

$$\left\{ \begin{aligned} \frac{du}{dt} &= - \frac{\partial}{\partial x} \frac{p}{\rho} + \frac{\partial}{\partial x} (K D_T) + \frac{\partial}{\partial y} (K D_S), \end{aligned} \right. \quad (6.30)$$

$$\left\{ \begin{aligned} \frac{dv}{dt} &= - \frac{\partial}{\partial y} \frac{p}{\rho} + \frac{\partial}{\partial x} (K D_S) - \frac{\partial}{\partial y} (K D_T), \end{aligned} \right. \quad (6.31)$$

$$\left. \begin{aligned} D_T &= D_{11} = - D_{22} = \frac{\partial u}{\partial x} - \frac{\partial v}{\partial y}, \\ D_S &= D_{12} = D_{21} = \frac{\partial u}{\partial y} + \frac{\partial v}{\partial x}. \end{aligned} \right\} \quad (6.32)$$

$$K = \left(\frac{k_0}{\sqrt{2}} \Delta S \right)^2 |D|. \quad (6.33)$$

$$|D| = \sqrt{D_T^2 + D_S^2} \quad (6.34)$$

If it is assumed that $|D|$ is constant everywhere, K is constant and the parameterized Reynolds stress is written as

$$\frac{du}{dt} = - \frac{\partial}{\partial x} \frac{p}{\rho} + K \nabla^2 u,$$

$$\frac{dv}{dt} = - \frac{\partial}{\partial y} \frac{p}{\rho} + K \nabla^2 v,$$

On the other hand, if K is a function of $|D|$ that is variable in space, this parameterization is called the "non-linear viscosity" formulation; the concept is similar to that in the planetary boundary layer i.e., the vertical eddy viscosity coefficient is proportional to $|\frac{\partial V}{\partial z}|$. According to the experience of practical application, it seems desirable that the eddy coefficient is variable. As the value of k_0 , Smagorinsky used $k_0 = 0.4$, which corresponds to Karman constant, whereas Deardorff considered that $k^0 = 0.14$ is appropriate based on the result of laboratory experiments.

L. F. Richardson derived empirically that the effective diffusion coefficient is proportional to 4/3-th power of the characteristic scale. This is interpreted as

$$K \sim \Delta S^{4/3}$$

In (6.33), one can show that $|D| \sim \Delta S^{-2/3}$, and accordingly, $K \sim \Delta S^{4/3}$.

It is worthy to mention that the equations (6.30), (6.31), and (6.33) can be approximately derived the "closure model" Lilly, 1967, (Deardorff, 1973)

$$\tau_{ij} = \left(\frac{k_0}{\sqrt{2}} \Delta S \right)^2 |D| D_{ij} \quad (6.35)$$

$$\overline{u, \theta} = \frac{5}{2} \left(\frac{k_0}{\sqrt{2}} \Delta S \right)^2 |D| \frac{\partial \theta}{\partial x_i}, \quad (6.36)$$

where 5/2 was derived by Schemm (1974). One criticism of lateral eddy viscosity parameterization is that, (a) K_0 should be small, but often large K_0 is used to aid computational stability, (b) the optimum K_0 could depend upon the mean flow, (c) a counter-gradient $\overline{u, \theta}$ and τ_{ij} is precluded, (d) Leith (1968) pointed out that the grid-cut is normally in the range of k^{-3} instead of $k^{-5/3}$. In that case, the eddy coefficient

is

$$K \sim (\Delta S)^3 |\nabla \zeta|, \quad (6.37)$$

$$\zeta = \frac{\partial v}{\partial x} - \frac{\partial u}{\partial y}. \quad (6.38)$$

The eddy coefficient K is proportional to $(\Delta S)^2$.

REFERENCES

- Arakawa, A., Katayama, A. and Mintz, Y. 1969: Numerical simulation of the general circulation of the atmosphere. Proc. WMO/IUGG Symp. Numer. Wea. Pred. Tokyo, 8-12.
- Charney, J. G., and A. Eliassen, 1964: On the growth of the hurricane depression. J. Atmos. Sci. 21, 68-75.
- Deardorff, J. W. 1971: On the magnitude of the subgrid scale eddy coefficient. J. Comput. Phys. 2, 120-133.
- Deardorff, J. W. 1973: Three-dimensional modelling of the planetary boundary layer. AMS Workshop on Micrometeorology, edited by D. A. Haugen. 271-311.
- Döös, B. R. 1970: Numerical experimentation related to GARP. GARP Publication series. No. 6, GARP WMO-ICSU Joint Organizing Committee, WMO, Geneva, 68 pp.
- Druyan, L. M., R. C. J. Somerville, and W. J. Quirk, 1975: Extended-range forecasts with the GISS model of the global atmosphere. Tech. note. Institute for Space Studies Goddard Space Flight Center, NASA, New York.
- Gadd, A. J. and J. F. Keers, 1970: The representation in a 10-level model atmosphere of sensible and latent heat transfers from the earth's surface to the atmospheric boundary layer. Quart. J. Roy. Met. Soc. 96, 297-308.
- Krishnamurti, T. N. and W. J. Moxim, 1971: On parameterization of convective and non-convective latent heat release. J. Appl. Meteor. 10, No. 1, 3-13.
- Krishnamurti, T. N. and M. Kanamitsu, 1973: A study of a coasting easterly wave. Tellus, 25, No. 6, 568-585.
- Kung, E. C. 1966: Large-scale balance of kinetic energy in the atmosphere. Mon. Wea. Rev. 94, 624-640.
- Kung, E. C. 1967: Diurnal and long-term variations of the kinetic energy generation and dissipation for a five-year period. Mon. Wea. Rev. 95, 593-606.
- Kuo, H. L. 1965: On the formation and intensification of tropical cyclones through latent heat released by cumulus convection. J. Atmos. Sci. 22, 40-63.

- Kurihara, A. 1973: A scheme of moist convective adjustment. Mon. Wea. Rev. 101, No. 7, 547-553.
- Leith, C. E. 1968: Two-dimensional eddy viscosity coefficients, Proceedings Symp. Num. Wea. Pred. Tokyo, 41-44.
- Lilly, D. K. 1967: The representation of small-scale turbulence in numerical simulation experiments. Proceedings of the IBM Scientific Computing Symposium on Environmental Sciences, held on Nov. 14-16 at the Thomas J. Watson Research Center, Yorktown, New York.
- Lilly, D. K. 1972: Wave momentum flux-a GARP problem. Bull. Amer. Met. Soc. 53, No. 1. 17-23.
- Manabe, S., J. Smagorinsky, and R. F. Strickler, 1965: Simulated climatology of a general circulation model with a hydrologic cycle. Mon. Wea. Rev. 93, 769-798.
- Manabe, S., and T. B. Terpstra, 1974: The effects of mountains on the general circulation of the atmosphere as identified by numerical experiments. J Atmos. Sci. 31, No. 1, 3-42.
- Miyakoda, K., J. Smagorinsky, R. F. Strickler, and G. D. Hembree, 1969: Experimental extended predictions with a nine-level hemispheric model. Mon. Wea. Rev. 97, No. 1, 1-76.
- Miyakoda, K., R. F. Strickler, C. J. Nappo, P. O. Baker and G. D. Hembree, 1971: The effect of horizontal grid resolution in an atmospheric circulation model. J. Atmos. Sci. 28, 481-499.
- Miyakoda, K., G. D. Hembree, R. F. Strickler and I. Shulman, 1972: Cumulative results of extended forecast experiments, I. Model performance for winter cases. Mon. Wea. Rev. 100, 836-855.
- Newell, R. E., D. G. Vincent, T. G. Dopplick, D. Ferruzza, and J. W. Kidson, 1970: The energy balance of the global atmosphere. The Global Circulation of the Atmosphere. edited by G. A. Corby, Royal Meteor. Soc. Lond. 42-90.
- Ogura, Y. 1964: Frictionally controlled, thermally driven circulations in a circular vortex with application to tropical cyclones. J. Atmos. Sci. 21, 610-621.
- Oort, A. H. 1971: The atmospheric circulation. The weather machine of the Earth. The Science Teacher. 38, No. 9.
- Ooyama, K. 1964: A dynamical model for the study of tropical cyclone development. Geophysica Intern. 4, 187-198.
- Ooyama, K. 1969: Numerical simulation of the life cycle of tropical cyclones. J. Atmos. Sci. 26, 3-40.
- Palmen, E. H. and C. W. Newton, 1969: Atmospheric circulation systems: Their structure and physical interpretation. Academic Press, Inc. New York, 603 pp.

- Schemm, C. E. 1974: A three-dimensional numerical study of turbulence in homogeneous and convectively unstable fluids. Ph.D. dissertation, Program in Geophysical Fluid Dynamics, Princeton University.
- Smagorinsky, J. 1963: General circulation experiments with the primitive equations: I. The basic experiment. Mon. Wea. Rev. 91, 99-164.
- Smagorinsky, J., S. Manabe, and J. L. Holloway, 1965: Numerical results from a nine-level general circulation model of the atmosphere. Mon. Wea. Rev. 93, 727-768.
- Smagorinsky, J. 1969: Problems and promises of deterministic extended range forecasting. Bull. Amer. Meteor. Soc. 50, No. 5, 286-311.
- Somerville, R. C. J., P. H. Stone, M. Halem, J. E. Hansen, J. S. Hogan, L. M. Duan, G. Russell, A. A. Lacis, W. J. Quirk and J. Tenenbaum, 1974: The GISS model of the global atmosphere. J. Atmos. Sci. 31, 84-117.
- Thompson, P. D. 1961: Numerical weather analysis and prediction. Macmillan Co., New York, 170 pp.
- Yamasaki, M. 1969: Large-scale disturbances in the conditionally unstable atmosphere in low latitudes. Papers Meteor. Geophys. 20, 289-336.
- Yanai, M., S. Esbensen and J. H. Chu, 1973: Determination of bulk properties of tropical cloud clusters from large scale heat and moisture budgets. J. Atmos. Sci. 30, 611-627.

7. Effects of the subgrid-scale processes on the general circulation

In order to investigate the impact of the subgrid-scale physics on the general circulation, a comparison test was made by including or excluding some processes in or from a prediction model (Miyakoda and Strickler, 1975). First the simplest 3-dimensional model without any subgrid-scale process (the mountain is included) was run with a real data initial condition for a winter case. This run blew up at 2-1/4 days. It was found that a gravitational instability occurred over the Himalayas. For the second trial, therefore, the simplest model with the "dry convective adjustment" was used. It ran for 10 days without any trouble. However, the predicted flow fields contain considerable wiggling indicating the production of computational gravity waves. Thus the simplest model is the model in which the basic three-dimensional dynamics with a dry convective adjustment and the lateral eddy viscosity terms included. Let us call it "Model 1."

In this way, 4 models with different degrees of parameterization of subgrid-scale processes were prepared for sensitivity testing.

Model 1: Dry convective adjustment, Lateral mixing.

Model 2: Physics in Model 1, plus Surface drag (C_D is constant everywhere), and Vertical momentum diffusion up to 3 km.

Model 3: Physics in Model 2, plus Insolation and long-wave radiation, and Sensible heat flux at the surface.

Model 4: Physics in Model 3, plus Water vapor cycle, Heat release from condensation, and Moist convective adjustment.

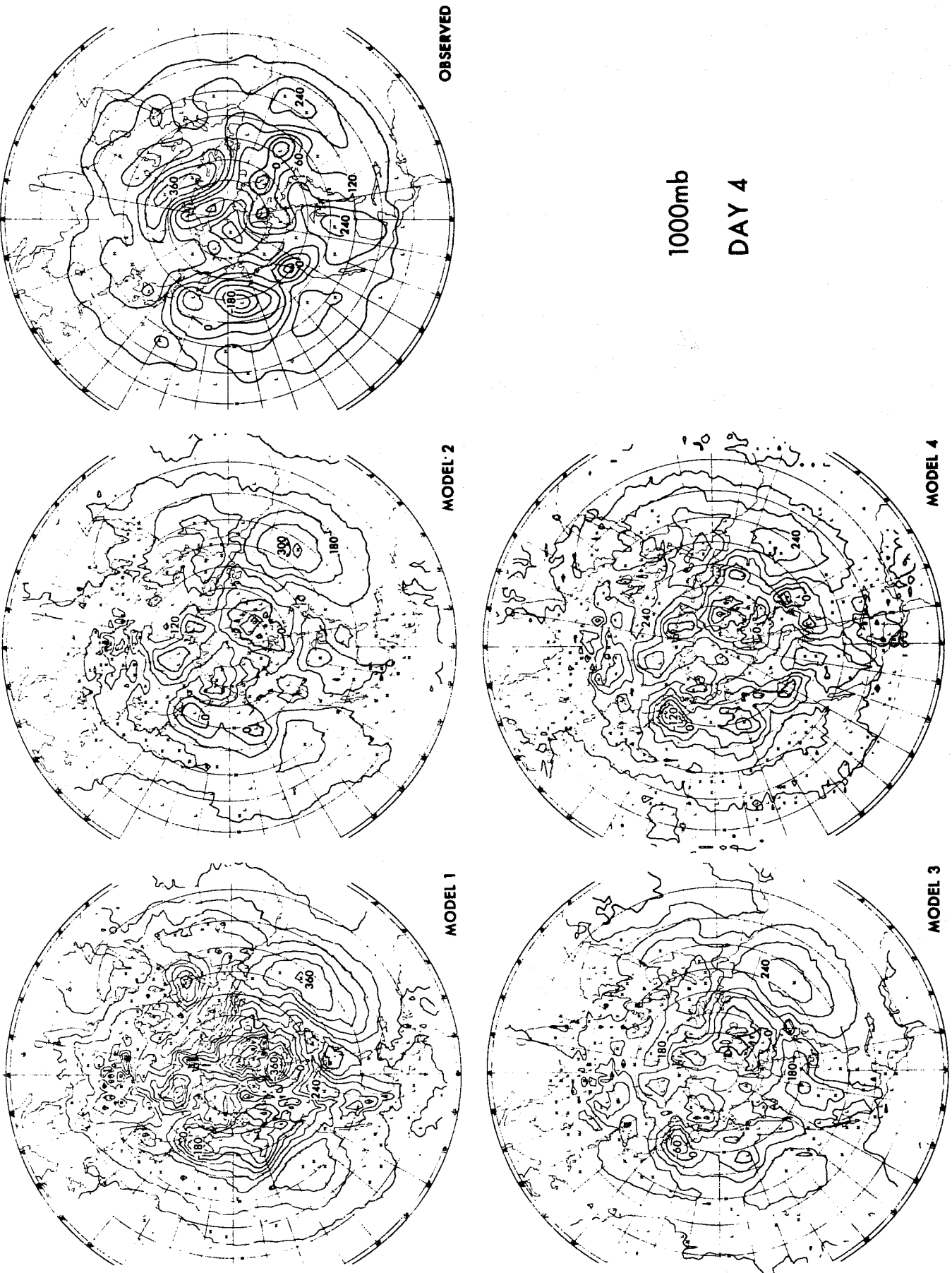


As seen, Model 4 is a full general circulation model, though the prediction of soil moisture, and the feed-back effect on the earth's albedo, etc., of snow accumulation are not incorporated. The difference between Model 4 and Model 3 is exclusively the processes related to water vapor. Applying these models to a January case, 10 day forecasts were carried out with each model. The results are shown by the forecast maps as well as the prediction scores of the rms errors and the correlation coefficients verified against the observation.

The 4th day forecasted maps of geopotential height contours at 1000 mb level are displayed in figure 7.1, where the NMC analysis is used as the observation map. It is pronounced that Model 1 map has an extremely large amplitude due to the omission of the surface friction.

In Model 2, the surface drag and the vertical diffusion of momentum was included. Accordingly, the amplitudes of the predicted 1000 mb height patterns were appreciably reduced. Comparing to the observation it appears that the reduction is excessive. Furthermore, cyclones over the ocean were totally suppressed probably due to the omission of land-sea contrast. Model 3 improved this point. Particularly the positions of anticyclones and cyclones were well adjusted to the ocean and continent distribution. We experienced in other experiments that the presence of ocean-continent contrast is crucial for a 4 day forecast of a rapid development of a cyclone over the ocean.

In Model 4, the amplitudes of the waves were considerably increased, particularly over the ocean. Cyclones and anticyclones are now located at the right positions; for example, see the Atlantic anticyclone. Note that the wiggling is increased in the 1000 mb map of Model 4, probably due to the "moist convective adjustment."



1000mb
DAY 4

Fig. 7.1

These features can be seen in the verification scores. Figures 7.2 and 7.3 are the rms error of 1000 mb height, and the correlation coefficient between the observed and forecast anomalies of 1000 mb height as a function of time. The rms error shows that Model 4 gave the best result for 7 days, then Model 3, Model 2, and Model 1. The error of Model 1 is very large. These points agree well with what we saw in the maps. On the other hand, the correlation curves indicate that the skill is in the order of Model 4, Model 1, Model 3, and Model 2. The correlation coefficients tend to indicate the degree of phase coincidence between two maps, whereas the rms error reflects more the amplitude coincidence. It is interesting to note that Model 1 is the 2nd best. This may imply that the surface drag might tend to destroy the useful information in Model 2, where the value of the surface drag coefficient is equally $C_D = 2 \times 10^{-3}$ over land and sea. In Delsole et al. (1971)'s study, it was pointed out that the impact of the land-sea difference in the surface drag coefficient is very large.

Let us next proceed to the 500 mb maps (figure 7.4). The difference of forecast maps is delicate, and yet one may see that Model 1 is the best; Model 4 is also good; but Model 2 and Model 3 are poor. It is surprising that in Model 2 the surface drag and the vertical mixing modified the flow patterns in the upper level appreciably. The trough over the U.S. and the cut-off cyclone over the Caspian Sea were considerably damaged. In Model 3 the flow pattern became further deteriorated; the contours are very smooth.

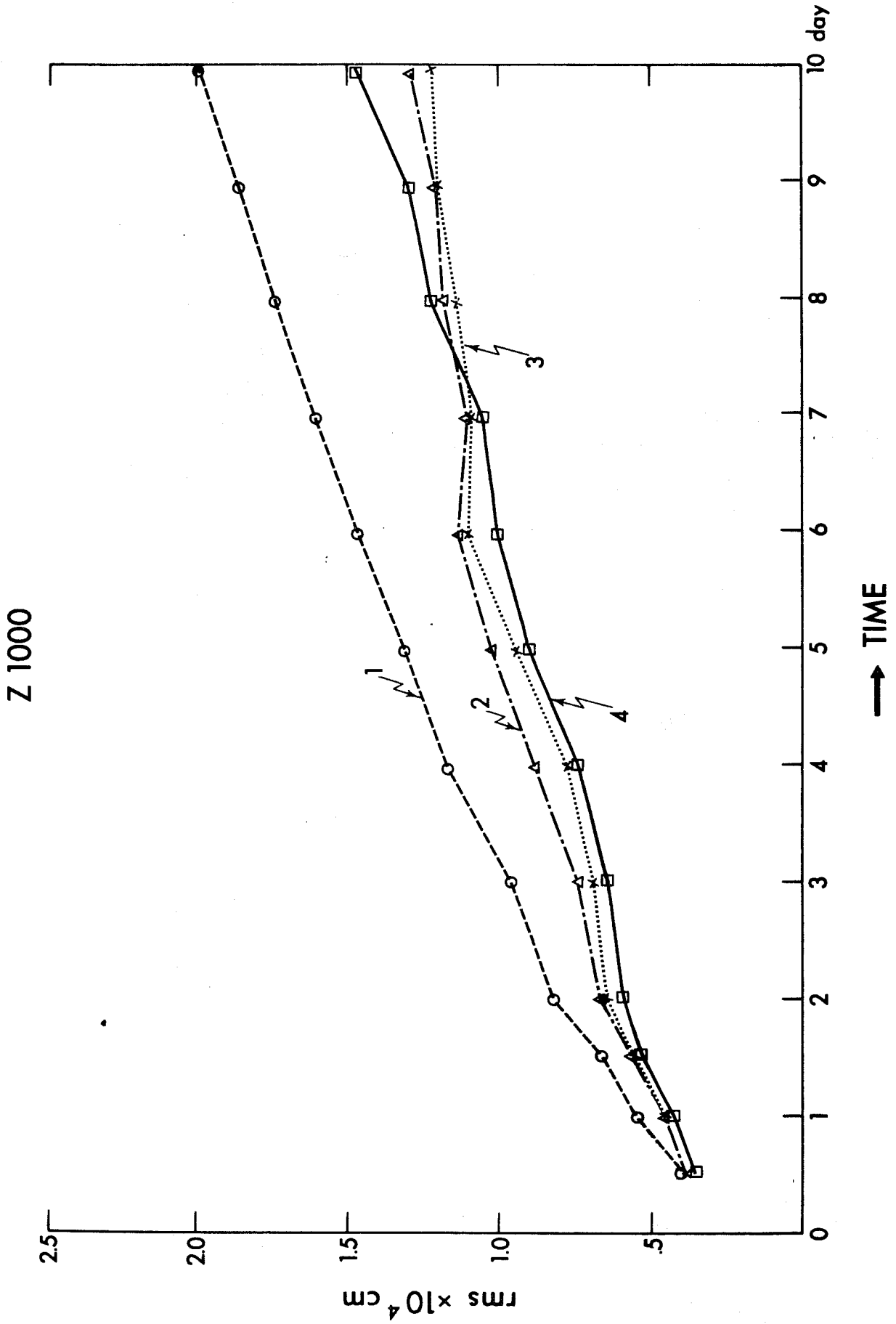


Fig. 7.2

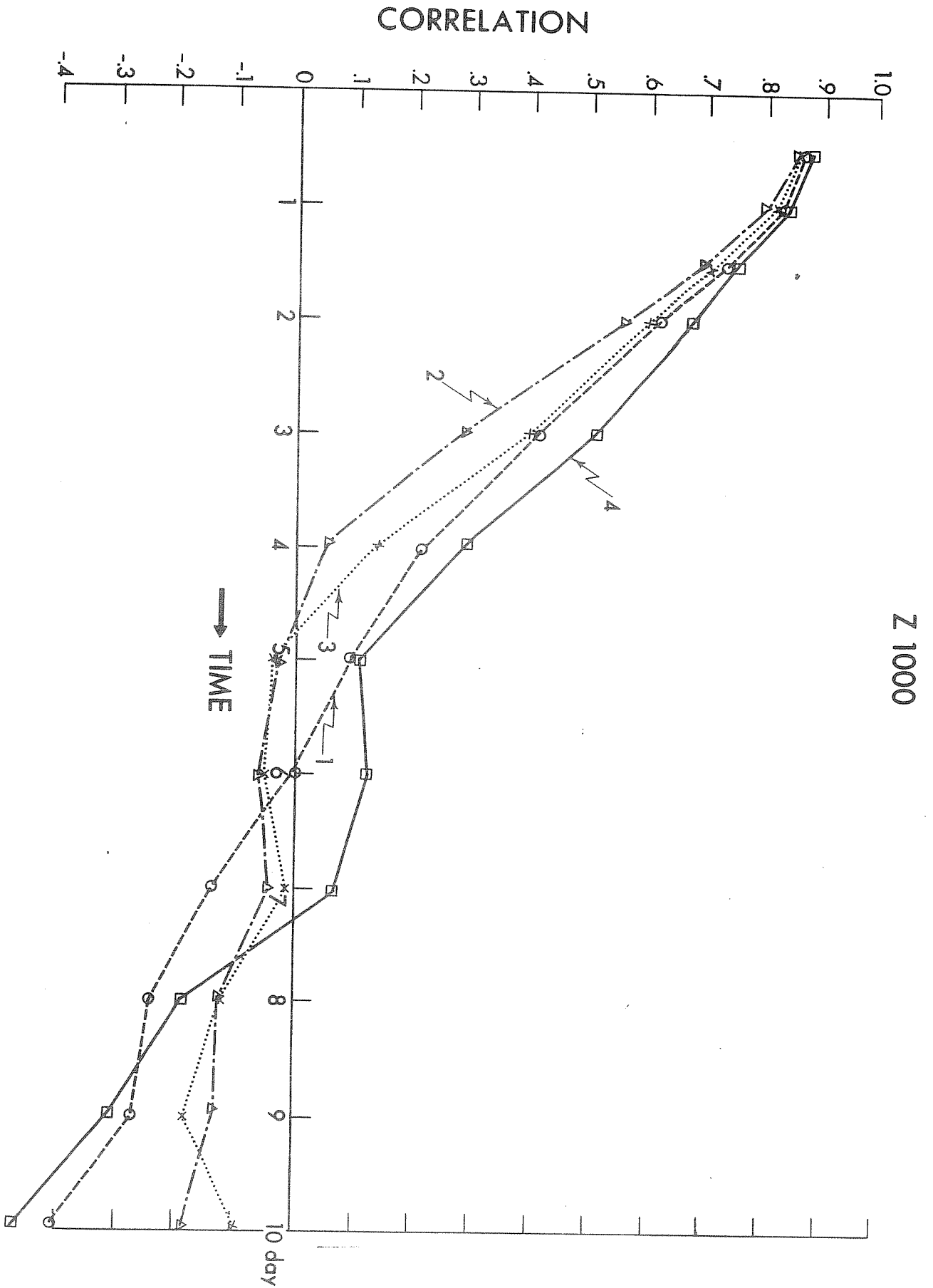
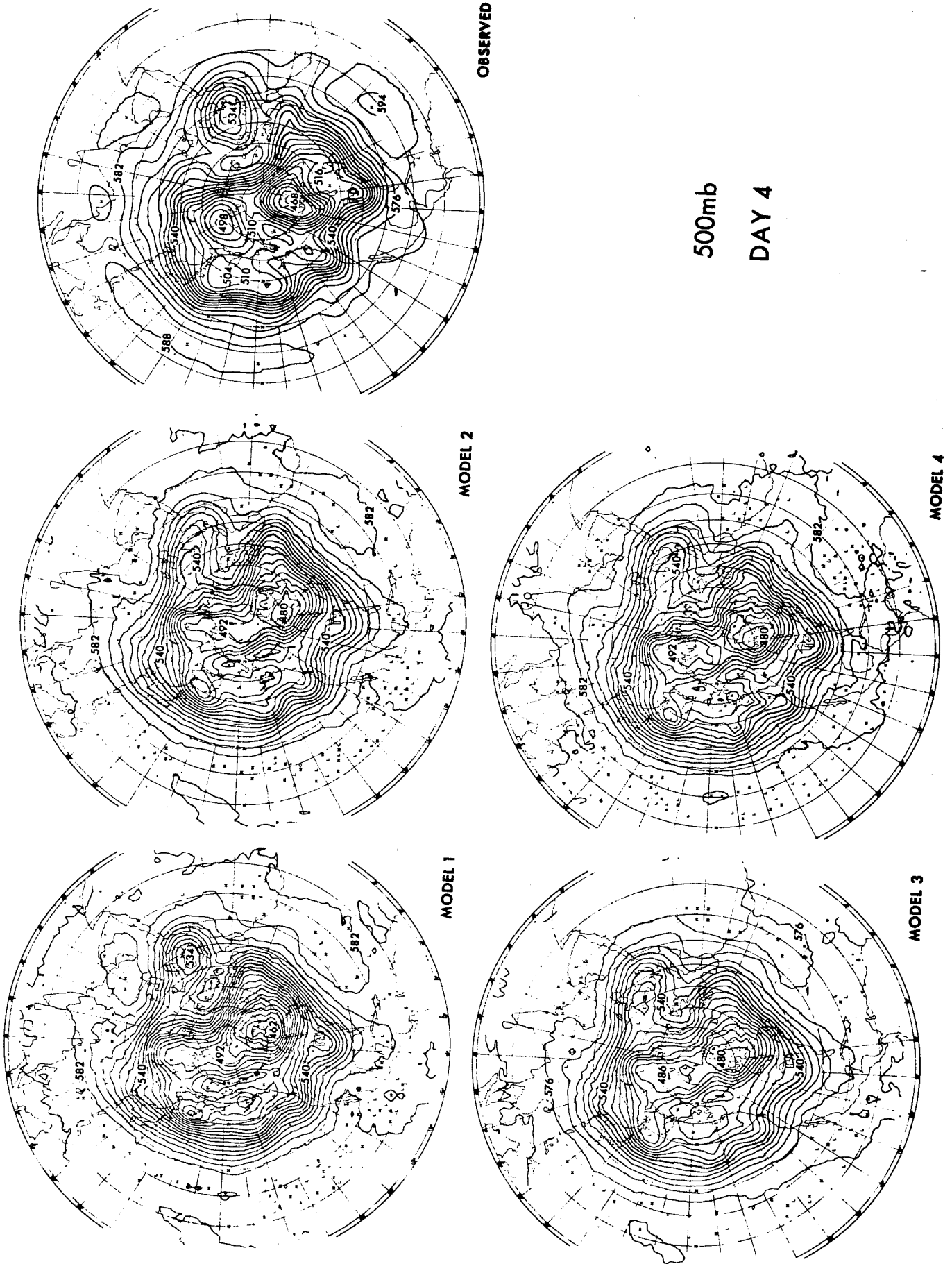


Fig. 7.3



500mb
DAY 4

Fig. 7.4

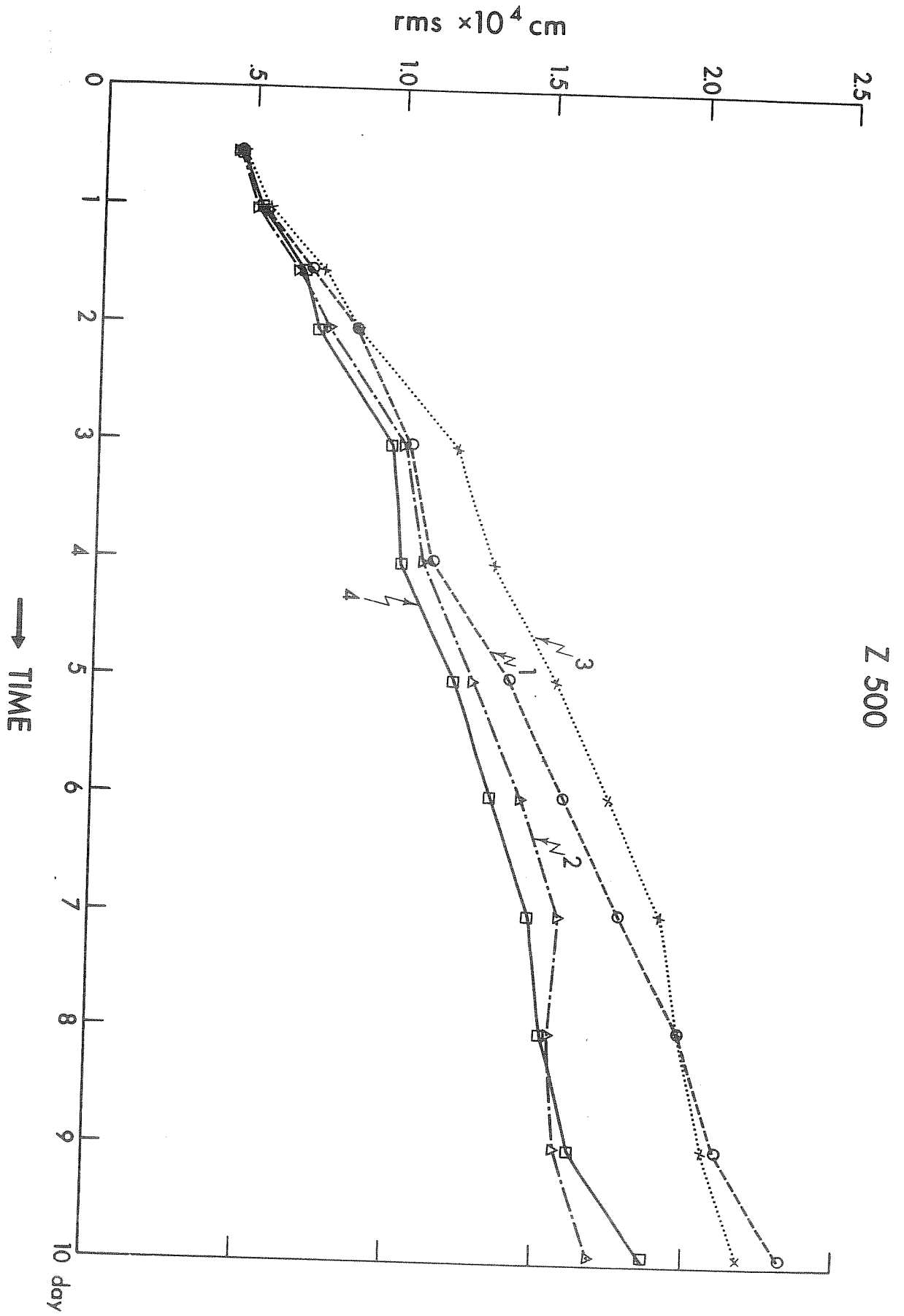


Fig. 7.5

CORRELATION

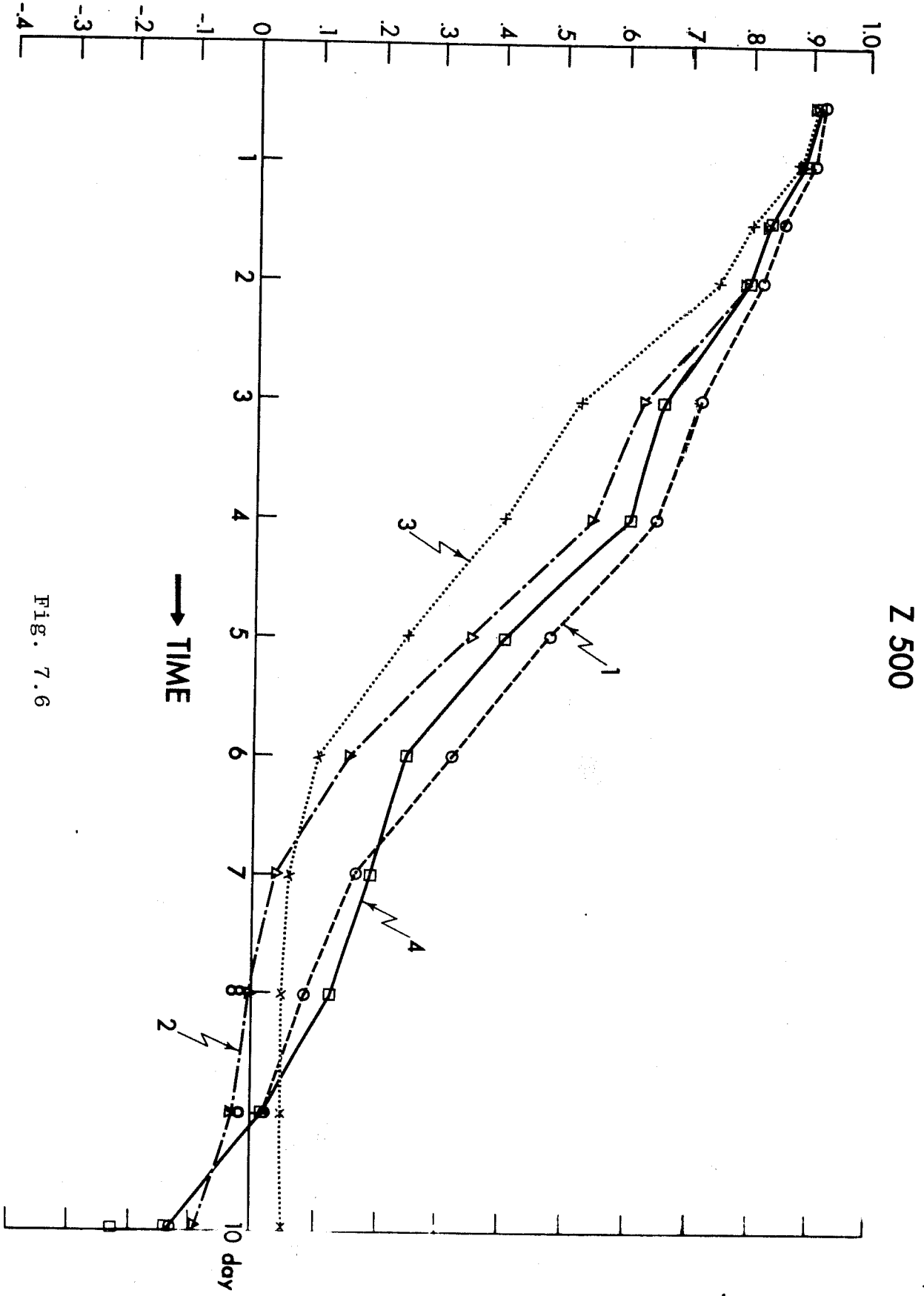


FIG. 7.6

Furthermore, the value of geopotential height in the tropics is noticeably decreased compared with the observation and other forecasts. It appears that the dry convective adjustment was much too active due to the increase of vertical instability which resulted both from insolation and from the specification of sea surface temperature. On the other hand, Model 4 recovers and makes a good forecast. The flow pattern was sharply activated by the presence of water vapor and released heat.

The rms error of the 500 mb maps (figure 7.5) indicated this feature exactly. Model 4 is a drastic improvement over Model 3. The correlation coefficients also shows that Model 4 is far better than Model 3, though Model 1 turned out the best in this score. Remember, however, that the rms error for Model 1 is not the best.

The sensitivity test seems to indicate that the subgrid scale physics affect appreciably the flow field at the surface. However, the influence of these physics on the upper level flow is delicate. If one takes an individual physics, it certainly affected the flow at the upper level but the collective effect of all the physics was small, indicating that many effects tend to counter each other. The net effect, therefore, may show up later; probably the effect ascends gradually from the surface.

This experiment seems to imply that the water vapor effect is very important in improving the medium-range forecast. It also indicates that the surface drag and vertical diffusion should be formulated better than was done on Models 2, 3, and 4.

The importance of moisture for the general circulation has been recognized in numerical experiments of long-time integration by Manabe

et al. (1967, 1970). They compared the runs of the "dry" model with the "moist" model, where "dry" model means that the "swamp" is assumed everywhere at the ground surface and the humidity is assumed to be always at saturation, and the "moist" model is the full physics model as we mentioned earlier but the land-sea contrast was not included in either models. In figure 7.7 the conversion of eddy potential energy to kinetic energy is compared for the dry and moist model cases. In the case of the dry model, conversion of energy is larger than in the case of moist model, because latent heat diminishes the role of sensible heat transfer. (see figure 7.8). This indicates that the generation of eddy kinetic energy is decreased in the moist model compared with that in the dry model. (see figure 7.9 and 7.10).

Figures 7.9 and 7.10 are the spectral analyses of the conversion term $\overline{-w'\alpha'}$ in terms of the zonal wave number at different levels for the dry and moist models, respectively. The moist model has a peak at level of 0.5 which is about one-fourth of that in the dry model. Interesting aspect in the spectral analysis is that the dry model indicates that the most unstable region is at wave numbers 4-10, which agrees with the conventional theory of baroclinic instability. On the other hand, the moist model shows the instability exists in the lower wavenumber, i.e., planetary scale waves.

In this way, the role played by water vapor in the general circulation seems to be substantial not only quantitatively but also qualitatively. This feature is amplified even more in the tropics.

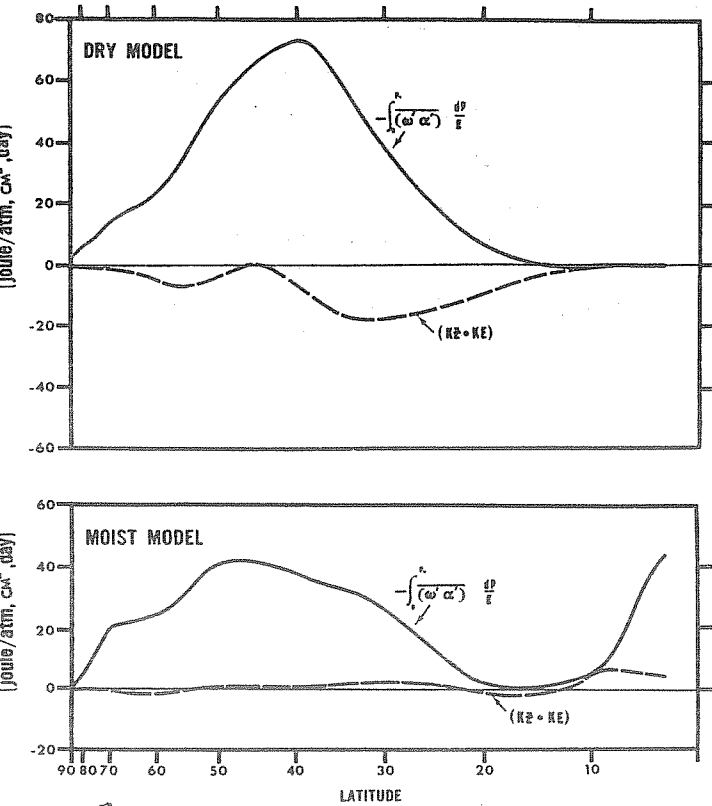


Fig. 7.7 - Latitudinal distribution of the conversion of potential energy $(-\frac{1}{g} \int_0^{\lambda} \overline{\omega' \alpha'} \lambda \alpha P)$ and the energy transfer from zonal to eddy kinetic energy for both dry and moist models, averaged over 264th day to 283d day (dry model), 158th day to 177th day (moist model).

(Manabe et al, 1967)

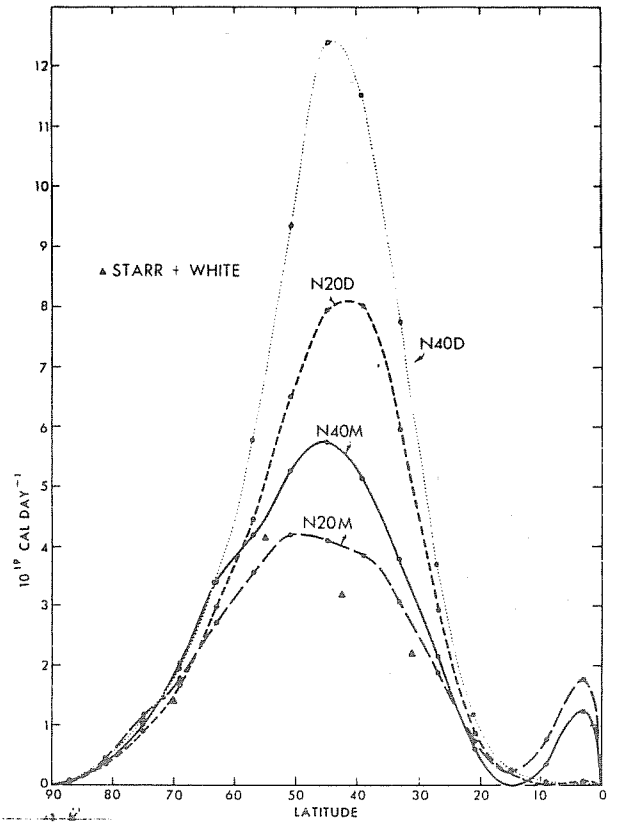


Fig. 7.8 - Latitudinal distributions of poleward transport of sensible heat by the large-scale eddies in various models. The rates of transport in the actual atmosphere, which were obtained by Starr and White (1954), are also plotted as solid triangles.

(Manabe et al, 1970)

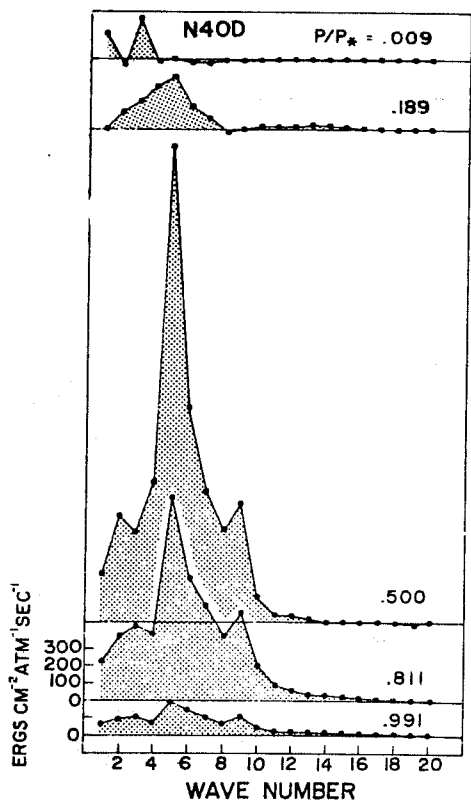


Fig. 7.9: Spectral distribution of the conversion term

_____A at various levels
 $(-\omega)_n(\alpha)_n$ in the N40D
 atmosphere. Here,

_____A
 (\quad) indicates the

average for the area between
 15° and 81° latitude.

(Manabe et al, 1970)

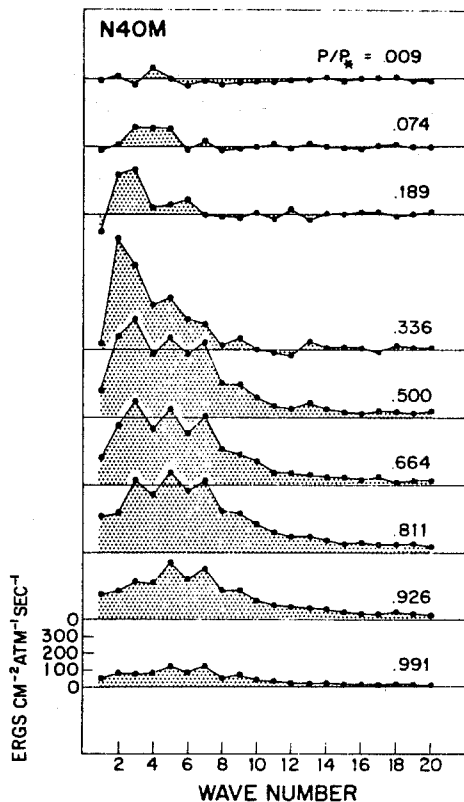


Fig. 7.10: Spectral distribution of the conversion term

_____A
 $(-\omega)_n(\alpha)_n$ at various levels in the N40M atmosphere.

Here, _____A indicates the average for the area between
 (\quad) 15° to 81° latitude.

8. Simulation of rain- and snow-fall distributions

In the previous section, we concluded that the process of water vapor is very important in simulating the earth's general circulation. The question may be asked: how good have the numerical models simulated the rain distribution. Two types of studies will be shown here. One is the global rain distribution in the general circulation studies, and the other is the results of the 2 week prediction experiments.

First, the latitudinal distribution of rainfall and evaporation simulated by the old and recent general circulation models are shown in figures 8.1, 8.2, and 8.3. The models are: 9-level GFDL model (Holloway and Manabe, 1971), 2-level RAND model (Gates et al. 1971), 11-level GFDL model (Manabe and Holloway, 1975) and 9-level GISS model (Somerville et al., 1974). The GFDL models are all based on the moist convective adjustment for the cumulus convection. RAND model used Arakawa's 1969 version but the scheme was modified. The rain distributions in the early models (figure 8.1) were poorly simulated. On the other hand, GISS and GFDL 1975 models produced the reasonable distributions (figure 8.2 and 8.3). Although the moist convective adjustment was equally used, the early GFDL model's result (figure 8.1) is quite different from the recent GFDL model (figure 8.3a), where the differences are the model's grid distribution, the sea surface temperature particularly over the equatorial ocean, and the seasonal variation. The large amount of precipitation at the equator in the 11-level GFDL model was due to the intense rainfall over land (figure 8.3c).

Gates (1975) has recently compared the zonally averaged January precipitation rates as simulated by 7 general circulation models, i.e.,

RAND (1975), UCLA (1973), British Meteorological Office (1975), NCAR (1971), GISS (1974), GFDL(1971) and GFDL (1974). Perhaps it can be safely said that recent models bear better resemblance to the so-called observation, and that the specification of accurate sea surface temperature is very important for the simulation of the tropical rain.

The horizontal distribution of simulated rainfall for winter and summer cases are shown in figures 8.4 and 8.5. The tropical belt rains, particularly the ITCZ rains, are well simulated. The seasonal change of the ITCZ was also well reproduced by the model, where the sea surface temperature is the dominant factor in controlling the shift of location.

Summarizing above, it can be said that the climatological distribution of tropical rain is fairly well simulated with the moist convective adjustment.

The simulated distribution of evaporation is shown in figures 8.3 and 8.6 (Manabe and Holloway, 1975). The intense evaporation regions over the ocean are well simulated except near the west coasts of all continents.

Let us next look at the rain- and snow-falls simulated by the GFDL prediction model. This result is the accumulation of 12 winter cases for 10 days each (Miyakoda and Hembree, 1975). As seen in figure 8.7, the detailed distribution of rainfall is not well simulated. The intense precipitation area over the Mississippi Valley was entirely misplaced, though the intensity of 6 cm/day in observed climatology agrees well with 5 cm/day in the forecasts. In the general circulation studies (see figure 8.4), the result is very similar, indicating that the intense precipitation over the Gulf Stream in the model result may be responsible for this error. Returning to the forecast result (figure 8.7) we also see that the rain

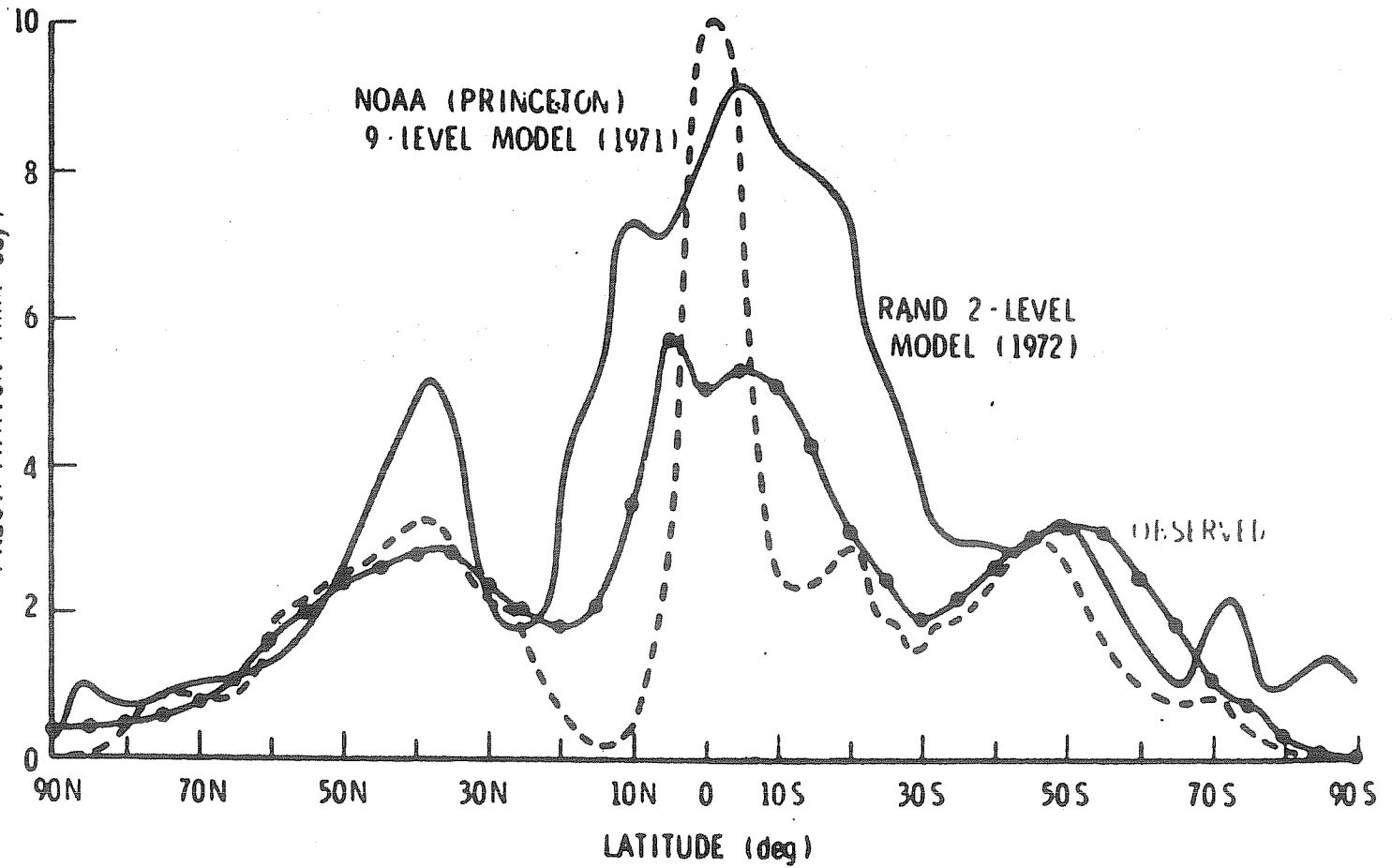


Fig. 8.1: The zonal averages of January precipitation rate as simulated by the original 2-level model (Gates et al (1971)) and by the 9-level GFDL model (Holloway and Manabe (1971)). The observed data are from Schutz and Gates (1971).

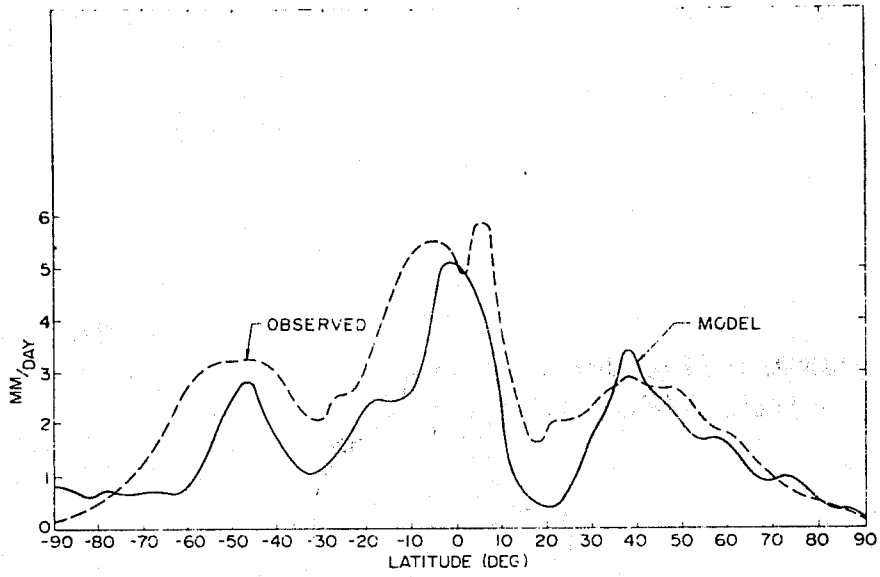


Fig. 8.2a Latitudinal variation of computed January zonal mean precipitation and observed December-February zonal mean precipitation from Lvovitch and Ovtchinnikov (1964), as analyzed by Schutz and Gates (1971).

(Somerville et al, 1974)

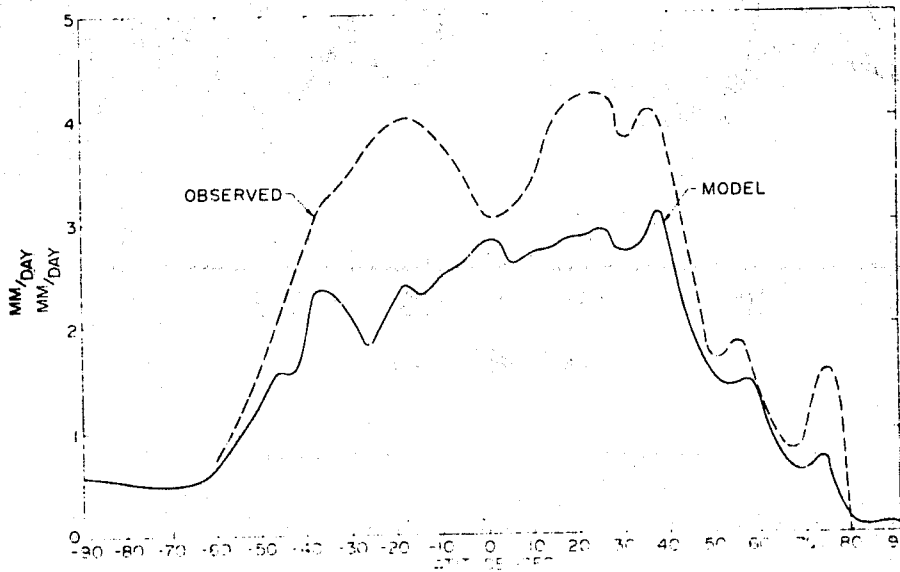


Fig. 8.2b Latitudinal variation of computed January zonal mean surface evaporation and observed January zonal mean surface evaporation from Budyko (1963), as analyzed by Schutz and Gates (1971).

(Somerville et al, 1974)

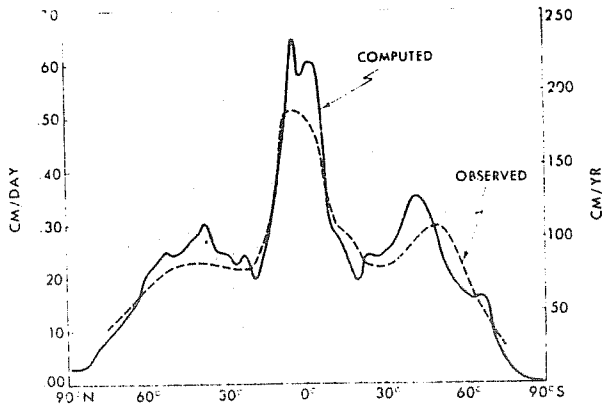


Fig. 8.3a: Latitudinal distribution of the annual mean rate of precipitation computed by model (solid line) and observed (Budyko, 1956) (dashed line).

(Manabe and Holloway, 1974)

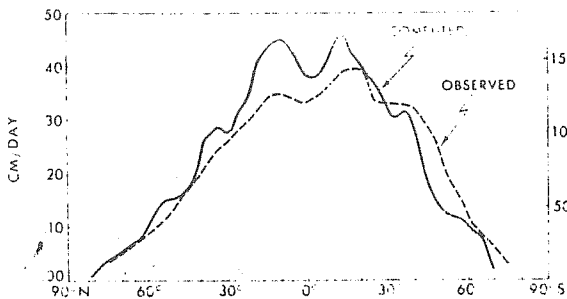


Fig. 8.3b: Latitudinal distribution of annual mean rate of evaporation computed by model (solid line) and derived from observed data (Budyko, 1963) (dashed line).

(Manabe and Holloway, 1974)

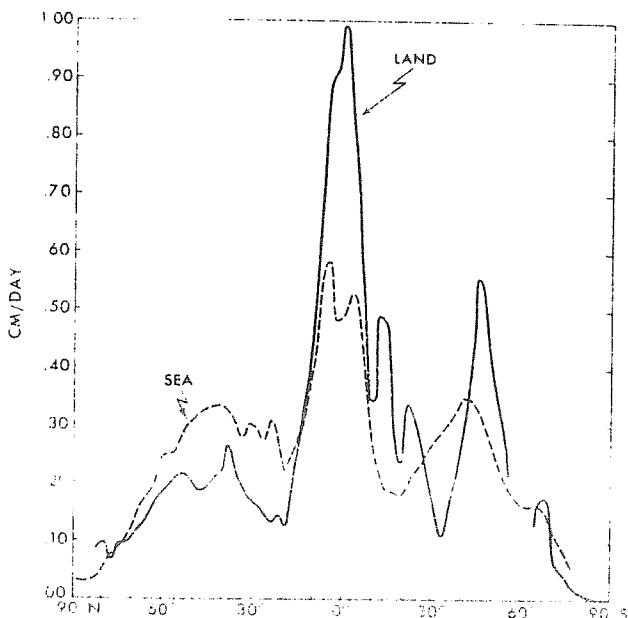
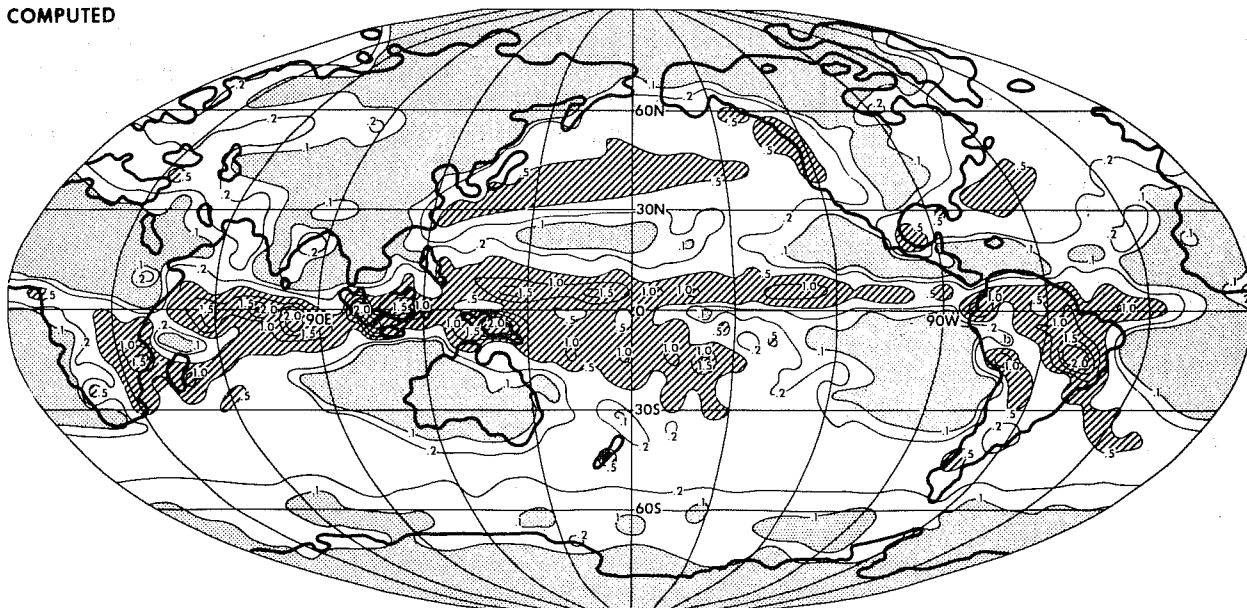


Fig. 8.3c: Latitudinal distribution of the annual mean simulated precipitation rate broken down into zonal means over land (solid line) and over sea (dashed line).

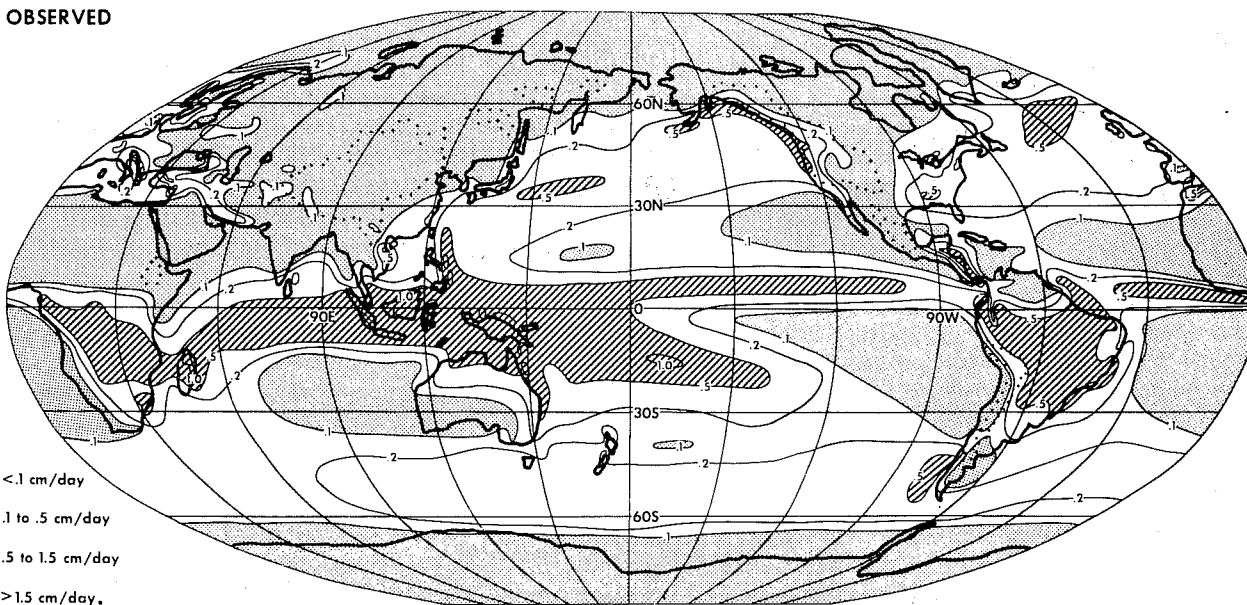
(Manabe and Holloway, 1974).



COMPUTED



OBSERVED







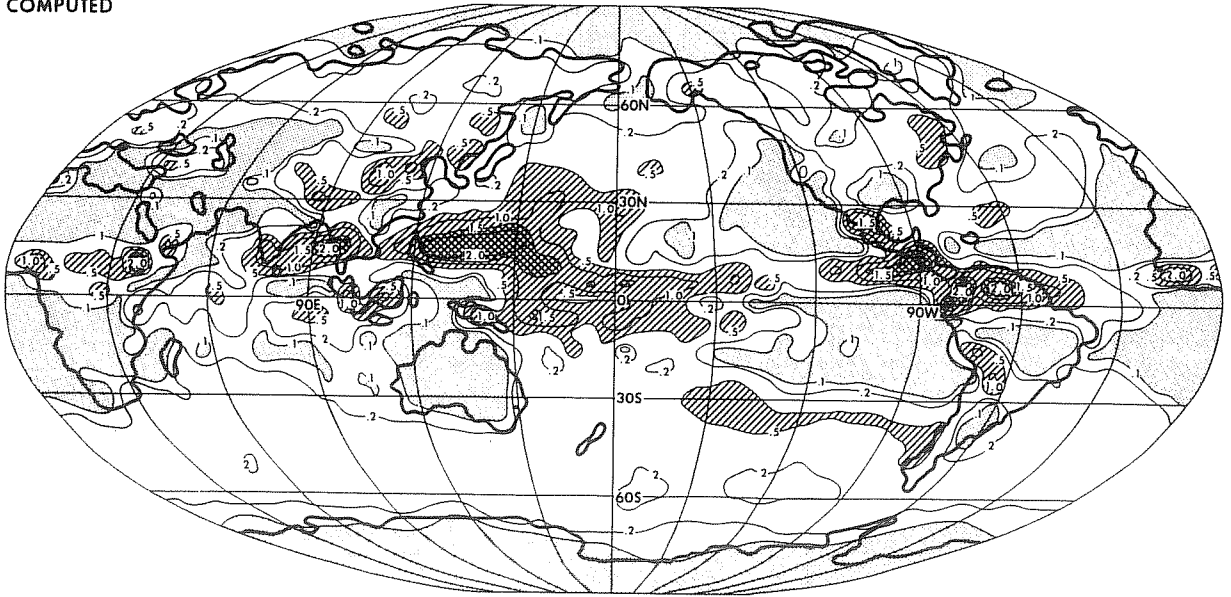
-  < 0.1 cm/day
-  0.1 to 0.5 cm/day
-  0.5 to 1.5 cm/day
-  > 1.5 cm/day.

Fig. 8.4 Global distribution of the mean rate of precipitation computed by the model simulation (top) compared with that estimated by Möller [1951] from observed data (bottom) for December, January, and February.

(Manabe and Holloway, 1974)

COMPUTED



OBSERVED

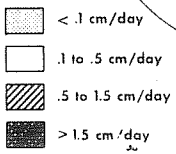
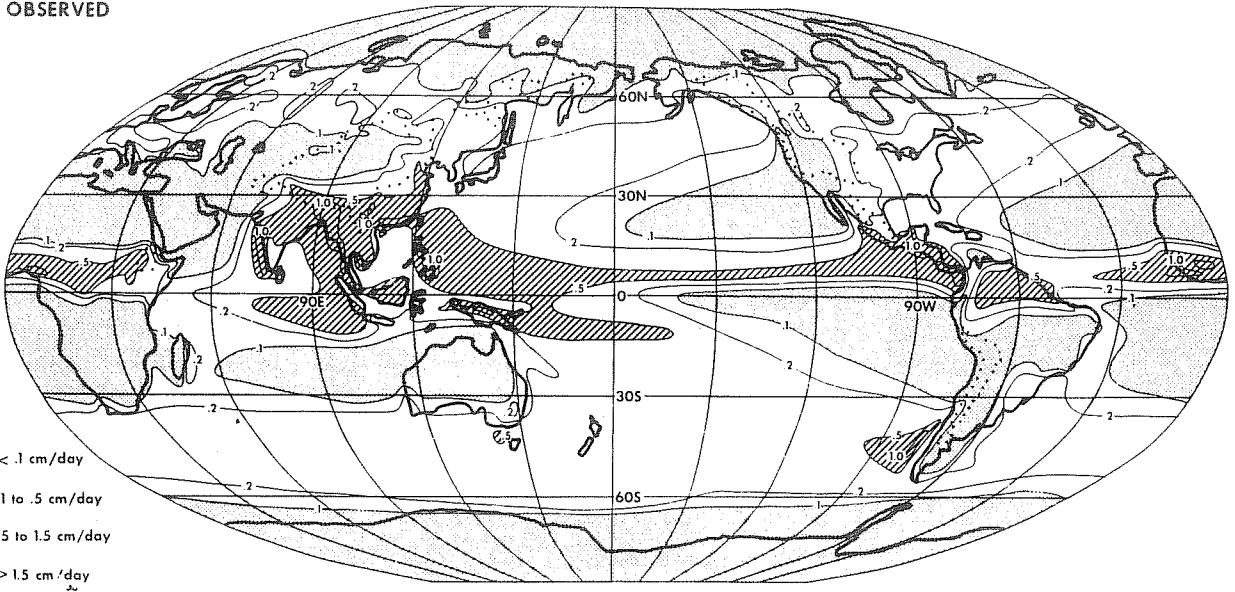
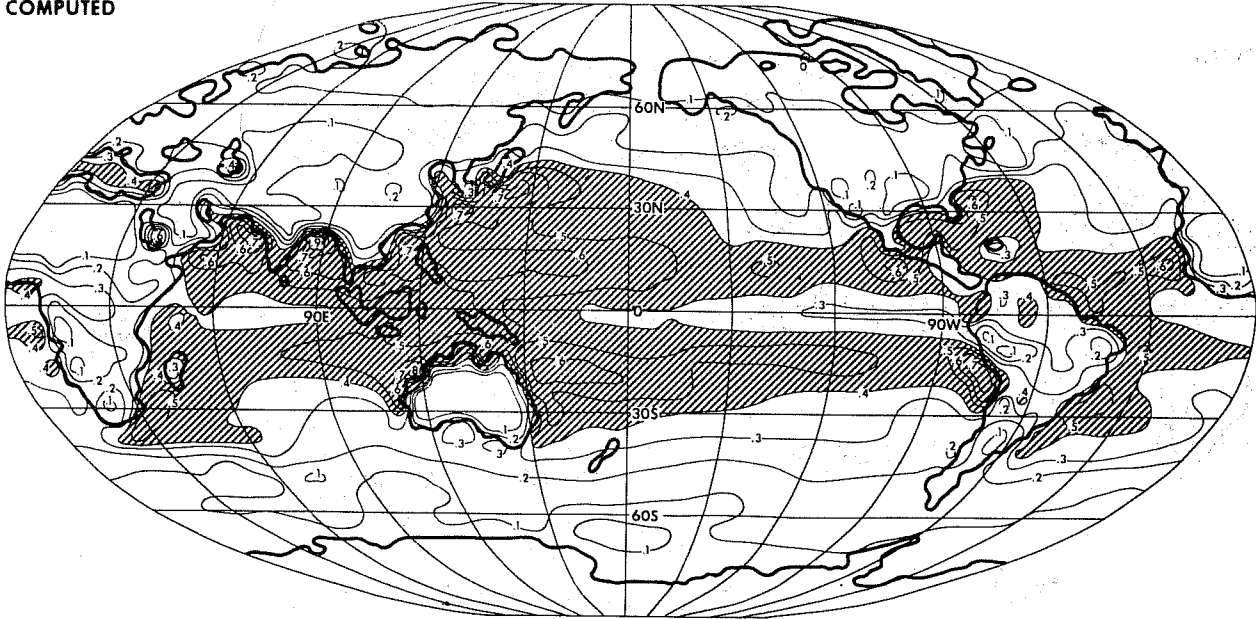


Fig.8.5 same as Fig.8.4 but for June, July, and August.

COMPUTED



OBSERVED

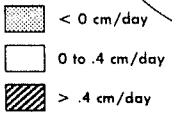
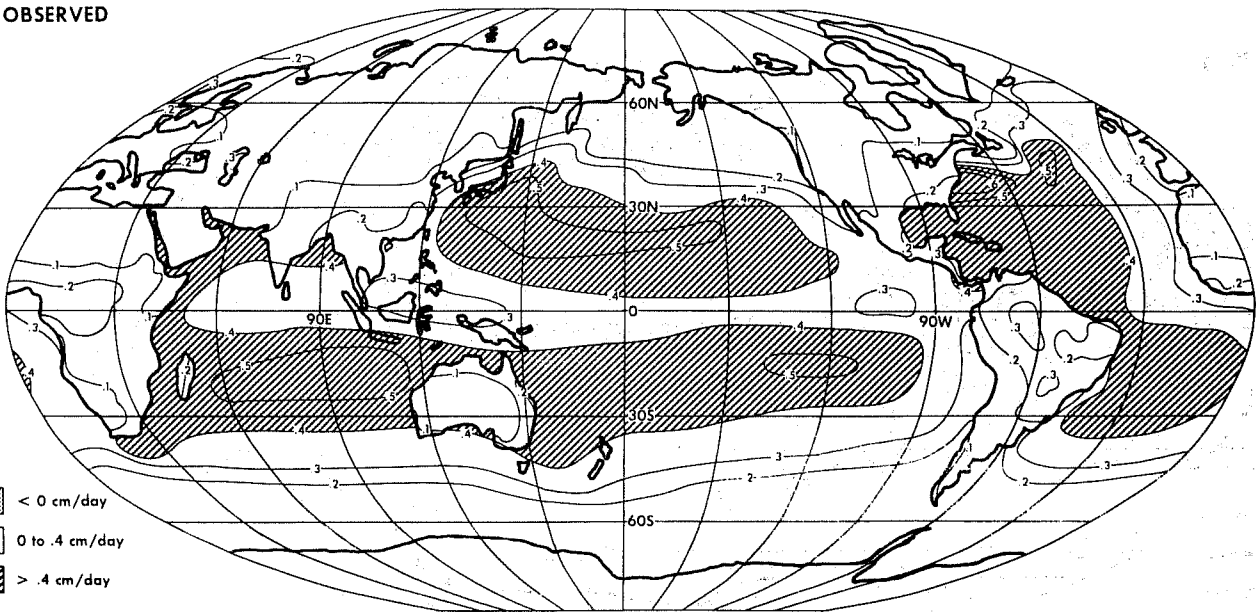


Fig. 8.6 : Global distribution of annual mean rate of evaporation simulated by the model (top) compared with that derived by Budyko (1963) from observed data (bottom).

(After Manabe and Holloway, 1974)

forecast in the western part of the U.S. does not agree well with the observation. The main reason is clearly the smoothness of the mountains in the model.

In figure 8.8, the snow-fall forecasts for 12 winter cases is compared to the observed climatology. The agreement is not excellent, but the amount of snow fall and the overall distribution are surprisingly well simulated. The major differences are: the real mountains induced spotty patterns in the observed distribution and the regions in the lee of the Great Lakes show large local effects.

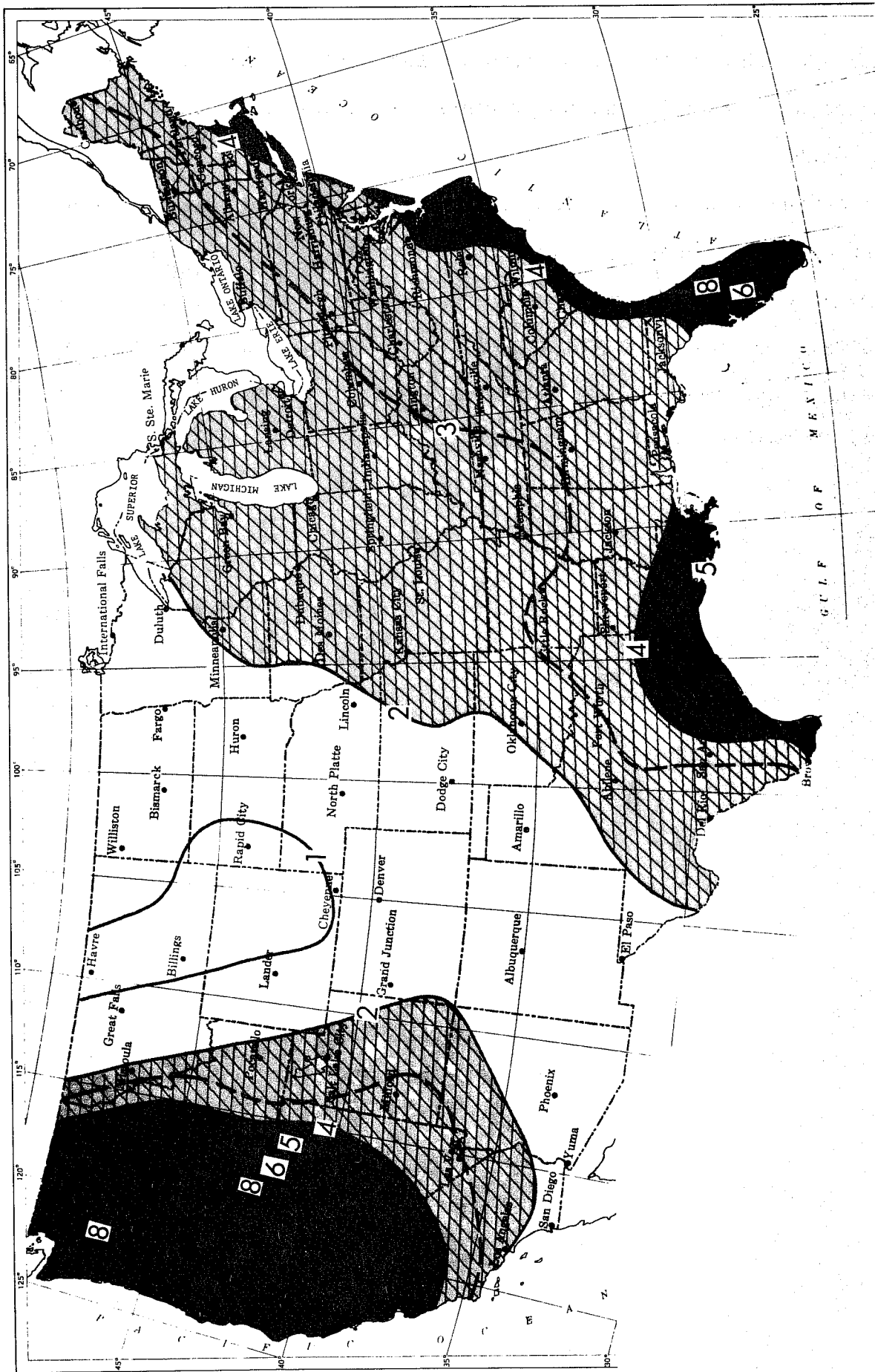


Fig. 8.7a. Predicted rain (Mikayoda, Hembree et al, 1975).

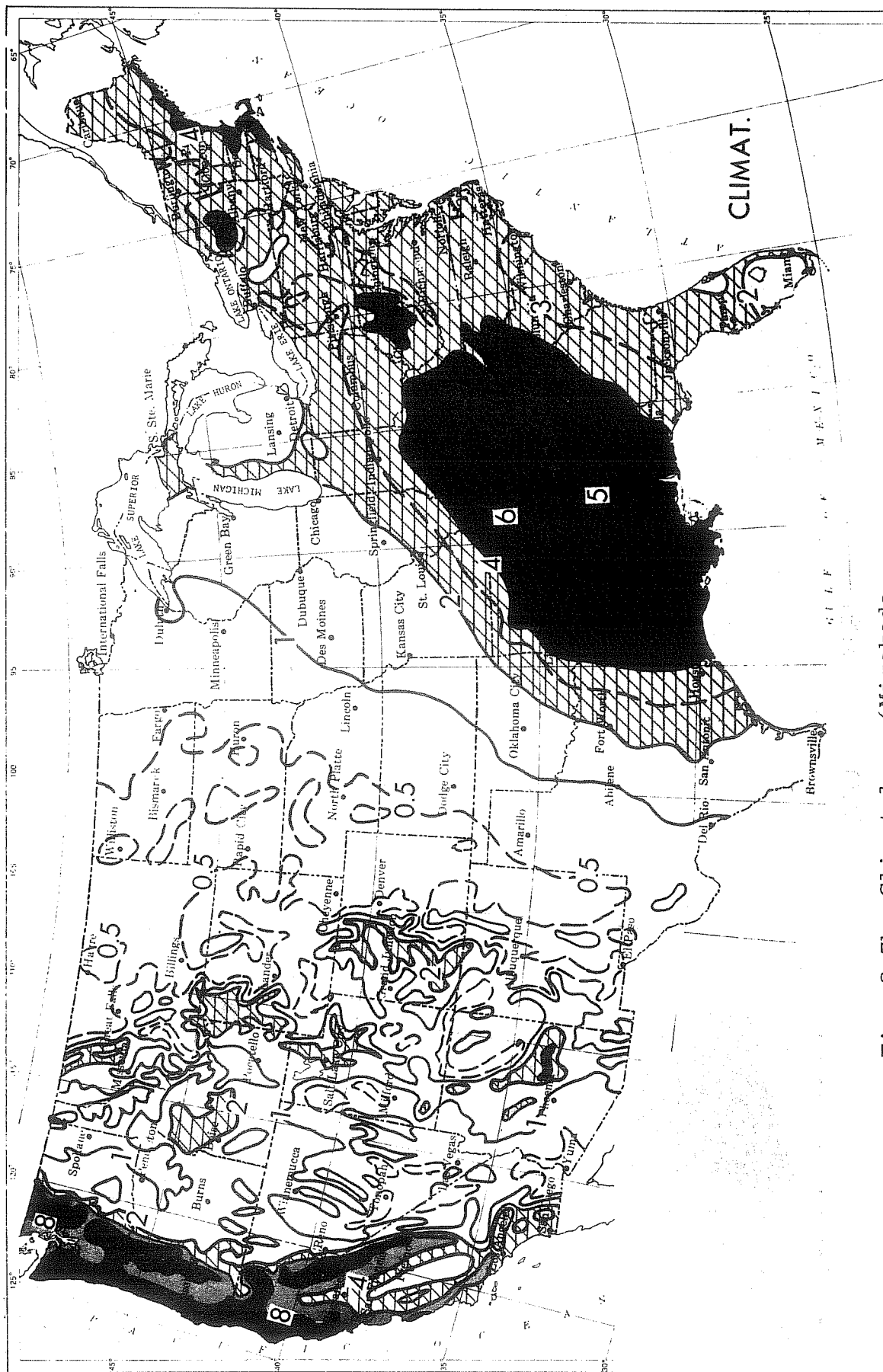


Fig. 8.7b Climatology (Miyakoda, Hembree et al, 1975)

SNOW INCH/MONTH

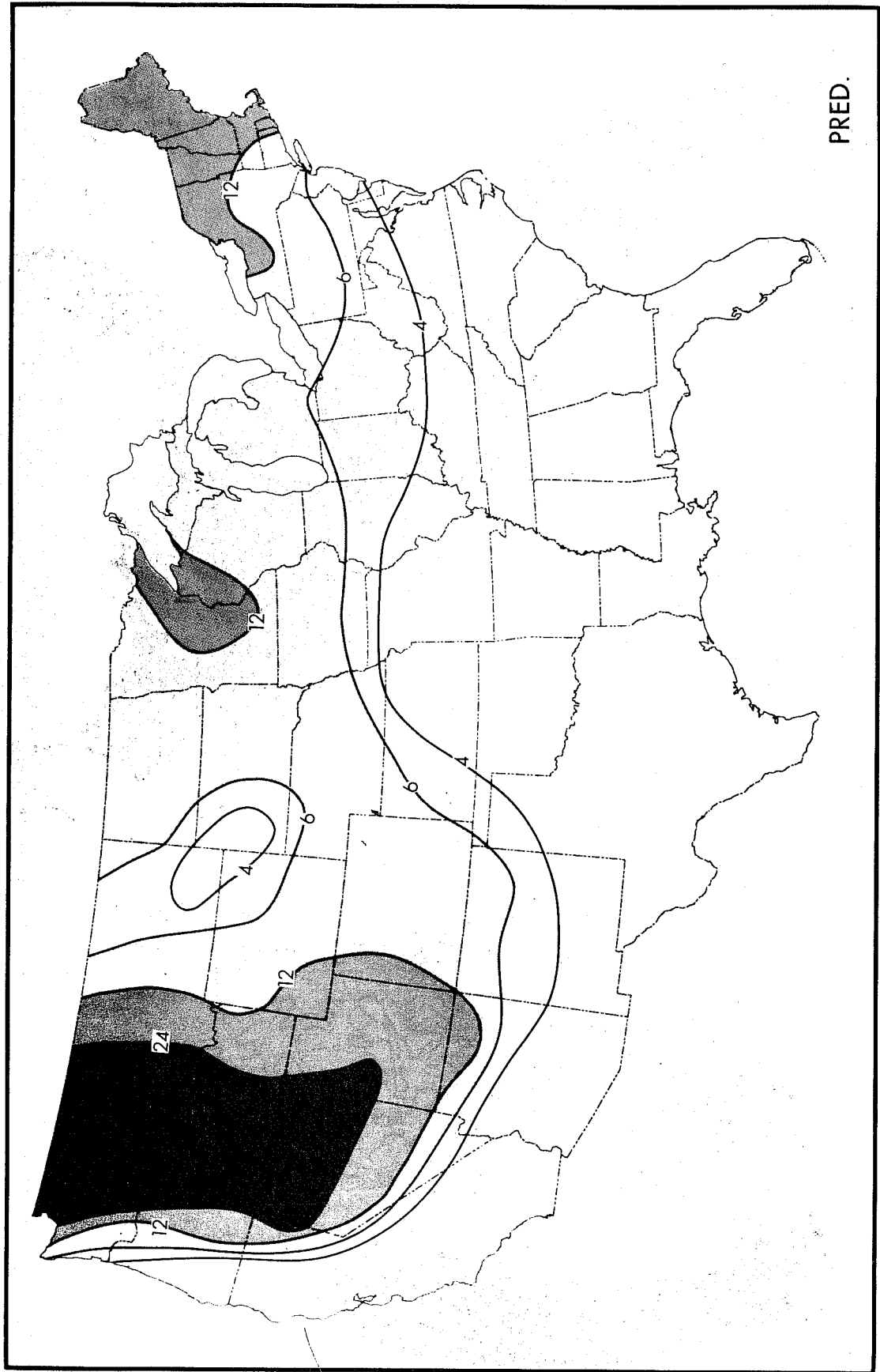


Fig. 8.8a (Miyakoda, Hembree et al. 1975)

SNOW INCH/MONTH

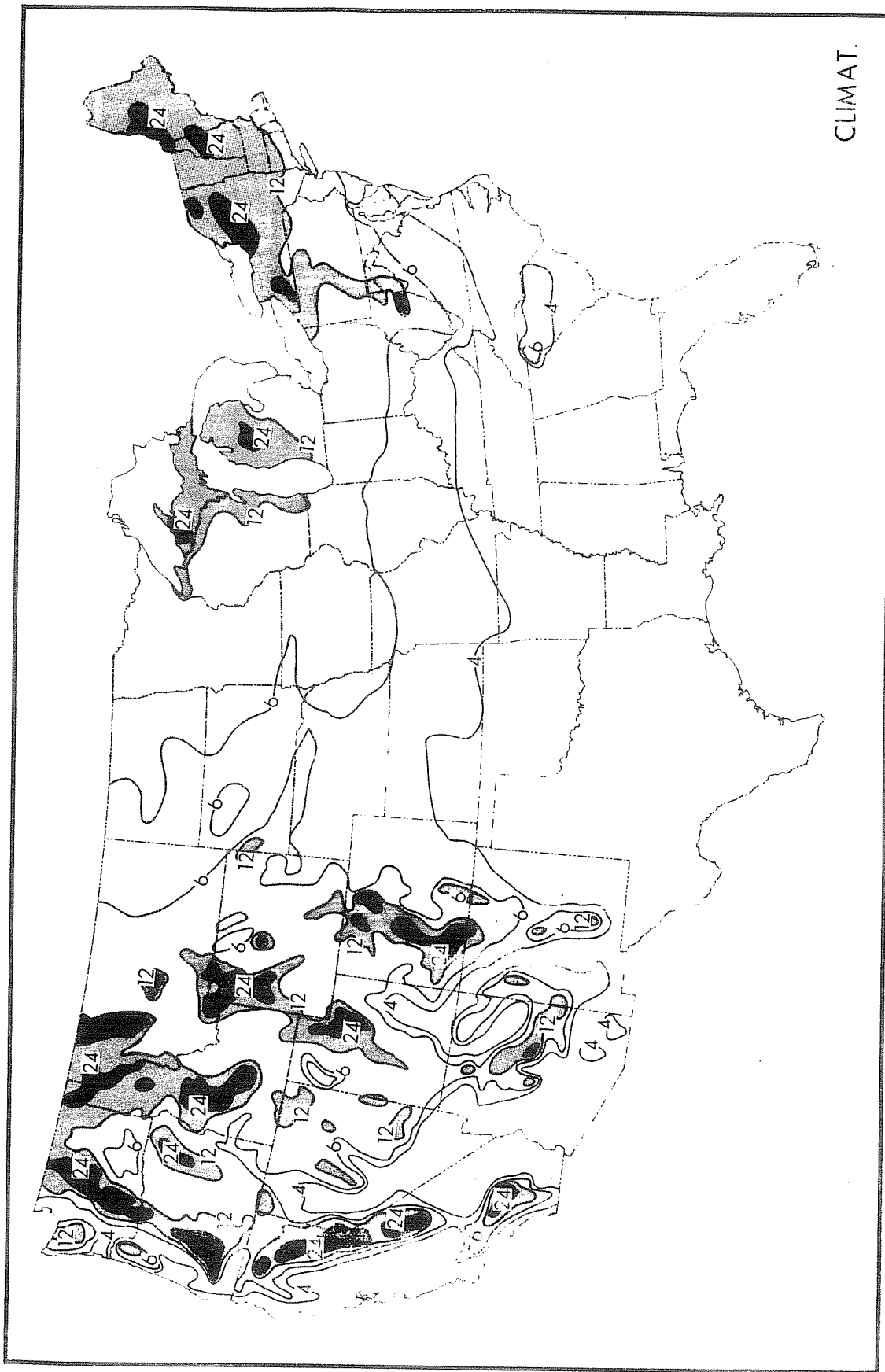


Fig. 8.8b (Miyakoda, Hembree et al, 1975)

9. Possible factors to improve the medium-range forecasts

In order to discuss the possible factors to improve the medium-range forecasts, it is necessary to specify our "present reference level" of forecasts. Let us assume in this lecture that our prediction model is the one which we mentioned in section 4, i.e., the GFDL "1967 version model," and the initial data are given by NMC, Washington, D. C.

The predictive performance of the model described in section 4 may be summarized as follows. The skill of the forecasts measured in terms of the correlation coefficients is such that the 1000 mb score becomes zero at the 8th day, the 500 mb score at the 10th day, and the 50mb score at the 12th day. Some pronounced defectiveness in the forecasts are the following. The temperature errors start at the surface; this feature is quite normal. But in our forecasts, the errors are particularly large after several days, exceeding the persistence error. The error developed over the oceans, i.e., the Aleutian area and the Icelandic and North Siberian areas. The amplitude of the planetary scale wave components is substantially underestimated, and the baroclinic waves are also weak. The forecasted jet streams appear weak and overly smoothed. The meandering in the computed westerlies is appreciably weaker than in the observed. As for the features of the general circulation, shortcomings are found in the weak eddy kinetic energy (25% lower than the observation), the overcooled atmosphere (about 2°C in the troposphere), and the overly intense zonal wind.

In view of these defects, I feel that the possible factors to improved these forecasts are, in the order of importance: the accuracy

of the initial data, the horizontal resolution of the model, the parameterization of cumulus convection, the planetary boundary layer process, the vertical resolution of the model, the initialization of the initial condition, the accurate sea surface temperature, the vertical diffusion, the diurnal variation, the cloud cover and the hydrology. Of course, this order is not based on a quantitative assessment, but is determined rather speculatively. We will discuss some of the items above in further detail. In this section, the problems of the spatial resolution of the model and also of the initial data will be discussed, and the problems of the refinement of the subgrid-scale processes will be treated in separate sections.

(a) The spatial resolution

The effect of the model's resolution on the short-range forecasts was discussed earlier. It might be somewhat surprising that the space resolution is important even for the medium range forecasts, because normally people think that only the spatially large scale features are important in a longer time integration. It turns out, however, that even the large scale components of flow are affected by the space resolution for a long time. The reason is simple that the dynamics of the atmosphere in our problem is non-linear. The problem was discussed by Manabe and Hunt (1968), Manabe et al. (1970), Wellck, Kasahara et al. (1971) Miyakoda, Strickler et al. (1971) Baer and Alyea (1971), Rasmussen (1973), and Puri and Bourke (1974).

Manabe et al. (1970) demonstrated (figure 9.1) how different the rainfall patterns are depending upon the lateral grid resolution, $N=20$

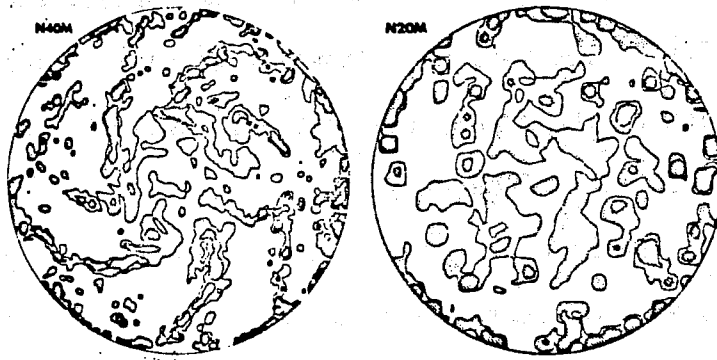


Fig. 9.1 - Stereographic map of daily precipitation (cm day^{-1}) on model day 173. Shading indicates areas of precipitation; slashed-line shading, area of daily precipitation in excess of 1.0 cm day^{-1} ; dotted shading, area of daily precipitation in excess of 0.1 cm day^{-1} ; circular boundary, Equator.

(Manabe et al, 1970)

or $N=40$ ($\Delta S = 540$ and 270 km , respectively at the middle latitude). The figure is a comparative display of two precipitation patterns at a particular day. In the high resolution model, the rain patterns are well concentrated along frontal zones stretching from the high-latitude to the lower latitudes, thus the features look more realistic than in the other case.

Miyakoda, Strickler et al. (1971) also tested predictions with three different resolution models, i.e., $N=20$, $N=40$, and $N=80$ ($\Delta S = 135 \text{ km}$). Figures 9.2 and 9.3 are the 500 mb and 1000 mb geopotential height maps at the 8th day by the different models. The effect of the resolution is striking. In the $N=20$ maps, the height pattern has no resemblance to either the $N=80$ maps or the observation. In the 1000 mb map, the distribution of cyclones and anticyclones in the $N=20$ map appears totally dispersed and accordingly obscure, whereas in the $N=80$ map the major

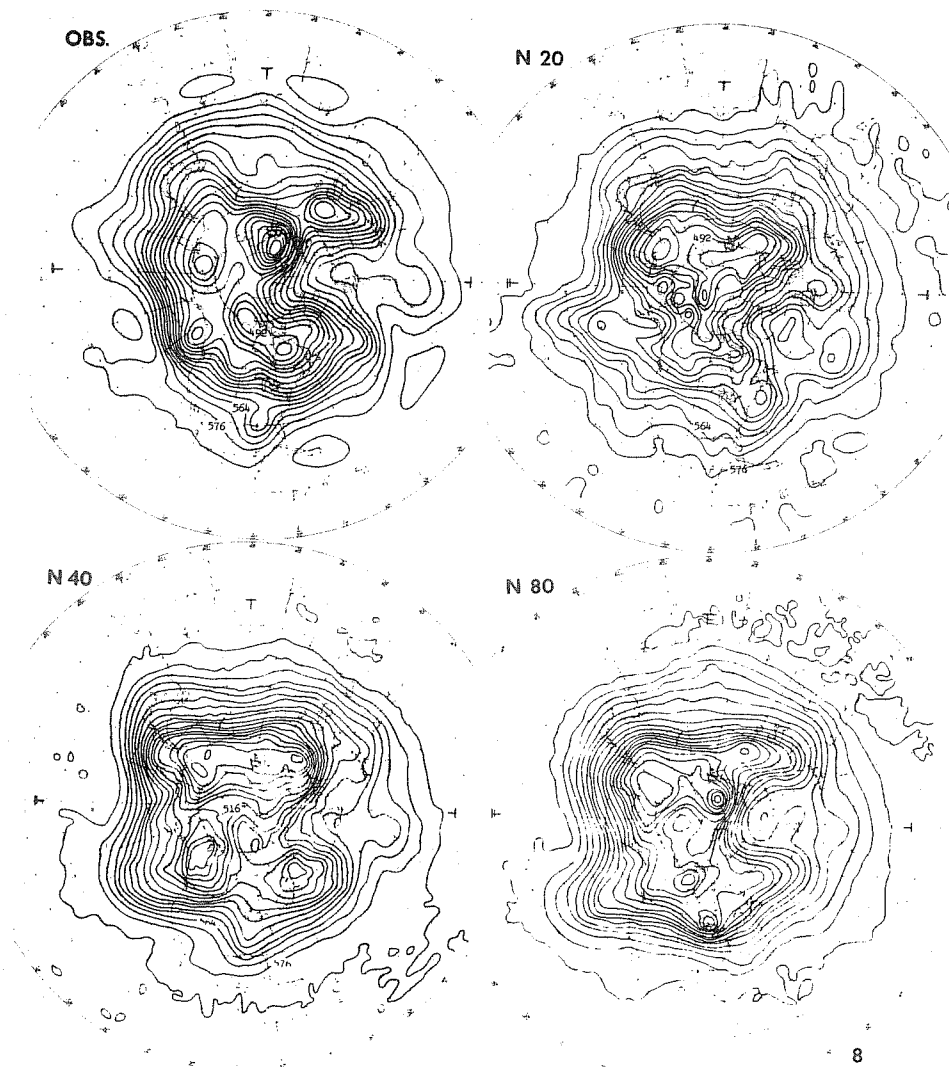


Fig. 9.2: The 500mb geopotential heights on the 8th day. The interval and units are the same as in Fig.2. (Miyakoda, Strickler et al, 1971).

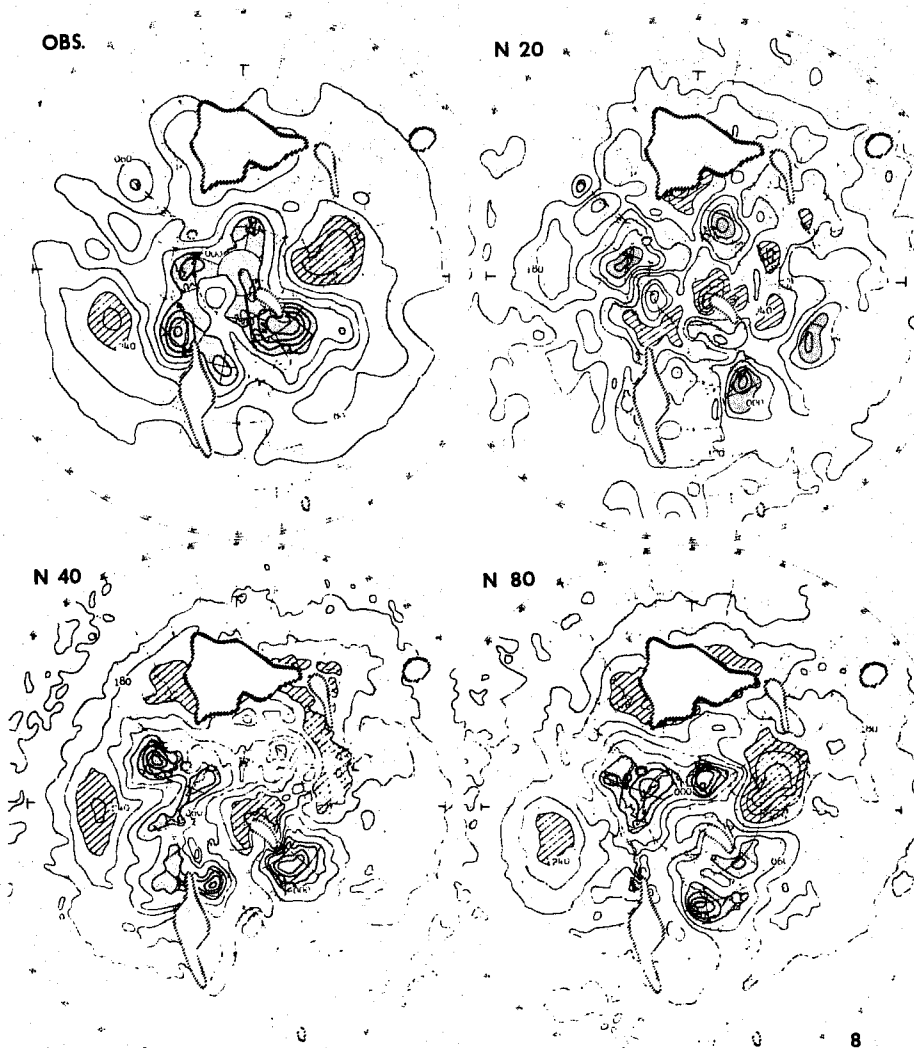


Fig. 9.3: The 100 mb geopotential heights on the 8th day. The anticyclone areas with height values $>240\text{m}$ are batched, and the cyclone areas with values <0 are stippled. The loci of small segmented lines mark the mountain areas. (Miyakoda, Strickler, et al, 1971).

anticyclones are well organized and well predicted. The N=40 maps seem much better than the N=20 maps.

The verification scores were calculated for two cases, i.e., January, 1964 and 1966. Figures 9.4 and 9.5 are the rms errors and the correlation coefficients as a function of forecast time. Overall the superiority of N=80 and N=40 forecasts over N=20 forecasts is clear. The fact that the

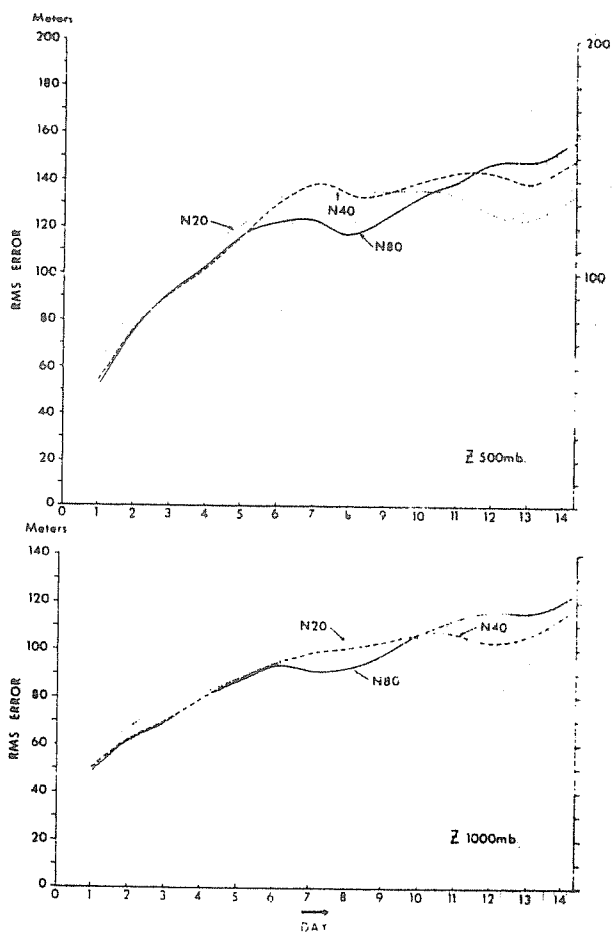


Fig. 9.4 The standard deviations of error of the predicted potential height at 500 and 1000 mb.

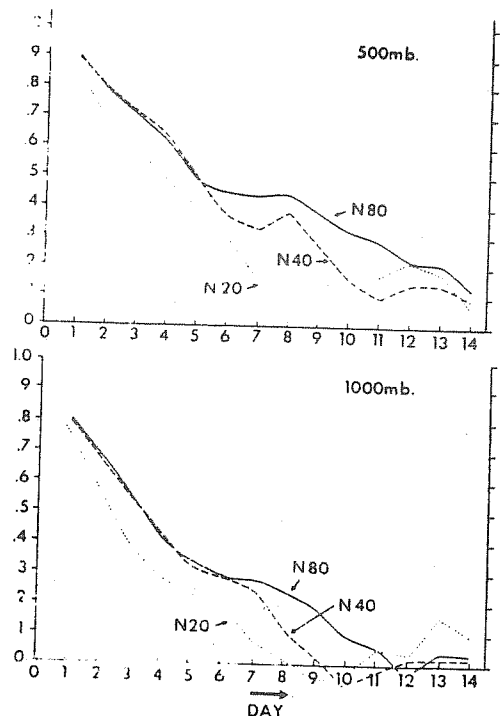


Fig. 9.5 The correlation coefficients between the observed and the predicted anomalies of geopotential heights for 500 and 1000 mb.

Miyakoda, Strickler et al, 1971)

rms error did not show the superiority of the N=80 over N=20 in a pronounced way is due to the wiggles in the contours of the 1000 mb maps.

The effect of the resolution on the eddy kinetic energy, K_E , is shown in the meridional plane in figure 9.6, where K_E is averaged over 10 days from the beginning of the forecast for each resolution case and also averaged zonally. It is natural that the intensity of eddy kinetic energy is increased with an increase in space resolution. The maximum observed value of K_E is 13.7×10^2 ergs. cm^{-2} , and the area of large values extends

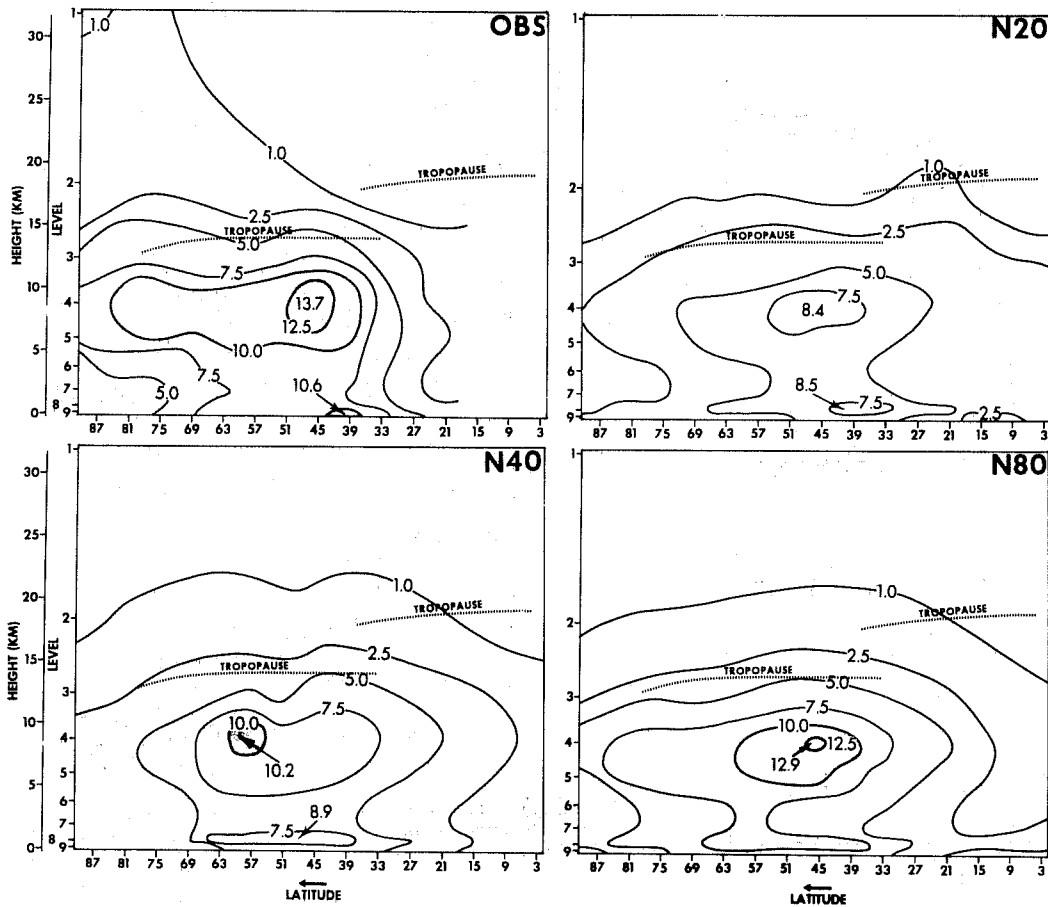


Fig. 9.6 Meridional sections of eddy kinetic energy, $\frac{1}{2}(\overline{u'^2} + \overline{v'^2})$, in units of 10^2 ergs cm^{-2} . The regions where the intensity $> 10^2$ ergs cm^{-2} are stippled. The maxima are plotted.

(after Miyakoda et al, 1971)

to the polar frontal region. The maximum values in the predictions are 8.4×10^2 , 10.2×10^2 and 12.9×10^2 ergs. cm^{-2} for $N=20$, $N=40$, and $N=80$, respectively. In this experiment, k_0 in the non-linear viscosity term was 0.25, and K_E in the figure are not only the results of space resolution but also are greatly influenced by the viscosity effect, since the term is a function of $(\Delta S)^2$. It is noted that, so far as K_E is concerned, $N=80$ model is close to the satisfactory level.

The intensity of K_E also benefits from the condensation heat. Figure 9.7 shows the latitudinal distribution of rain. The high resolution model gives more rain.

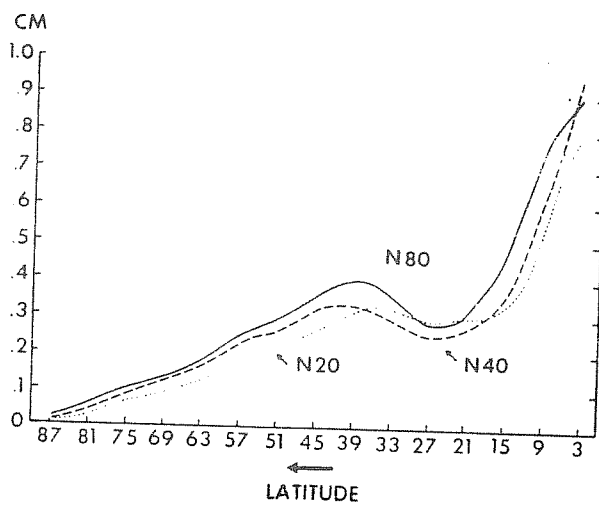


Fig.9.7 Latitudinal distribution of precipitation.

The effect of the space resolution on the wave behavior was studied. Figures 9.8-9.11 are the results of the trough-ridge diagram at the 500 mb level for the middle latitude. Figure 9.8 is the original data; figure 9.9, 9.10 and 9.11 are for the wavenumbers 1-2, 3-5, and 6-10. It is understandable that the propagation speed is considerably distorted by the

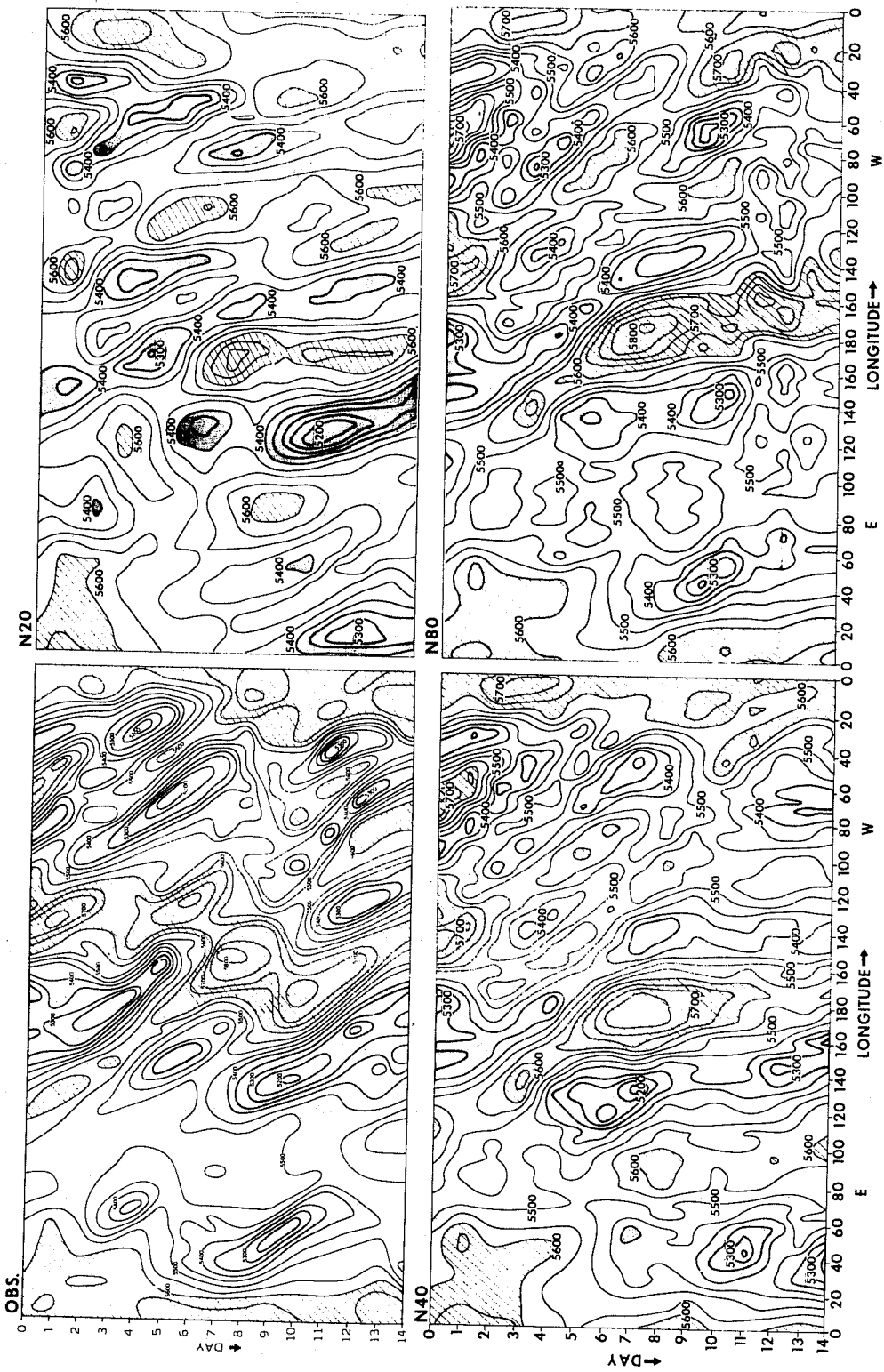


Fig. 9.8: The 500mb trough-ridge diagrams, in metres, for the latitude zone between 35 and 45N. The ordinate indicates the time from 0 through 14 days. The ridge areas with geopotential height values >5600m are hatched, and the trough areas with values <5400m are stippled.



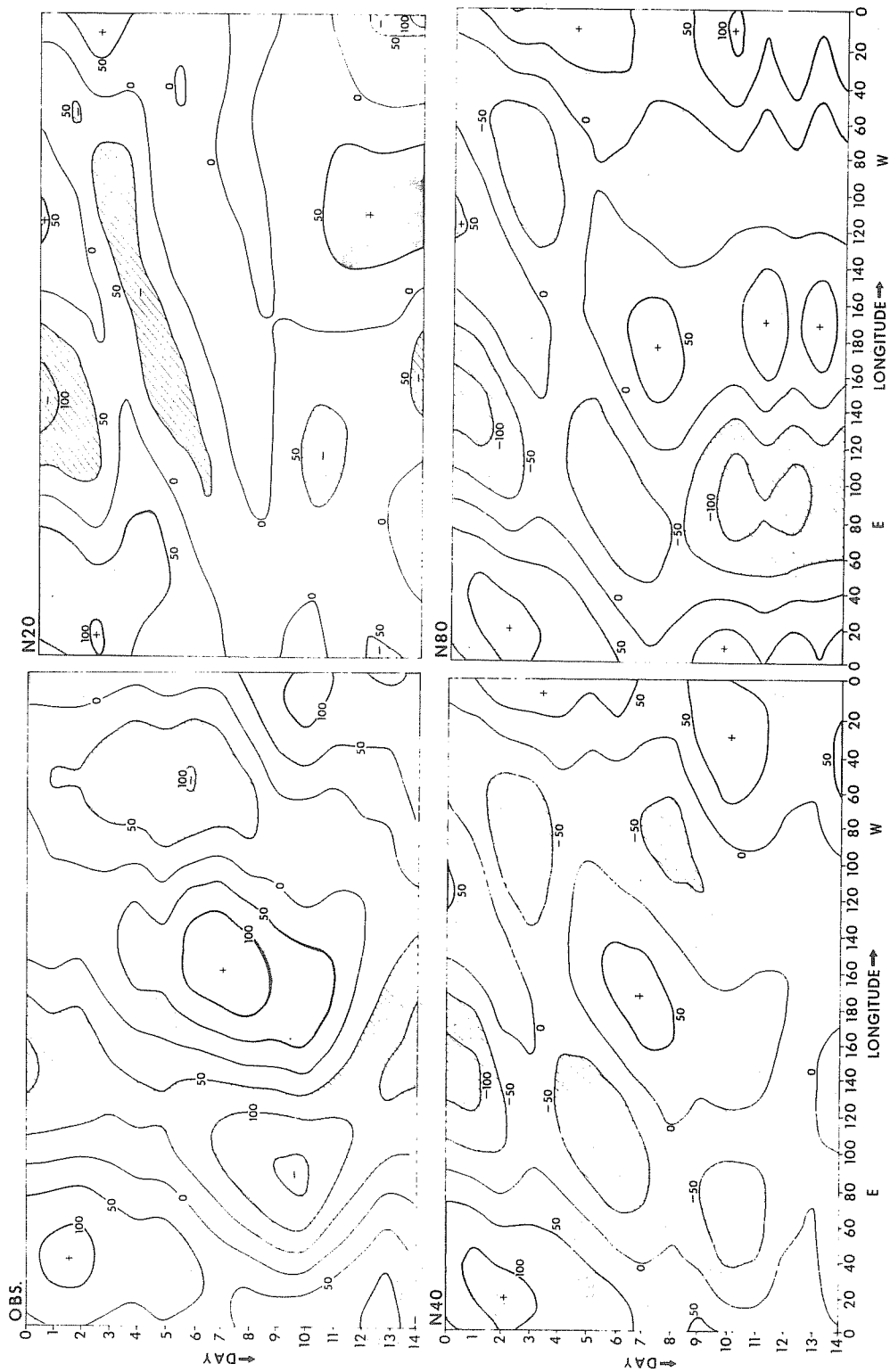


Fig. 9.9: The synthesized trough-ridge diagrams, with contours in metres, for wavenumbers 1 and 2.

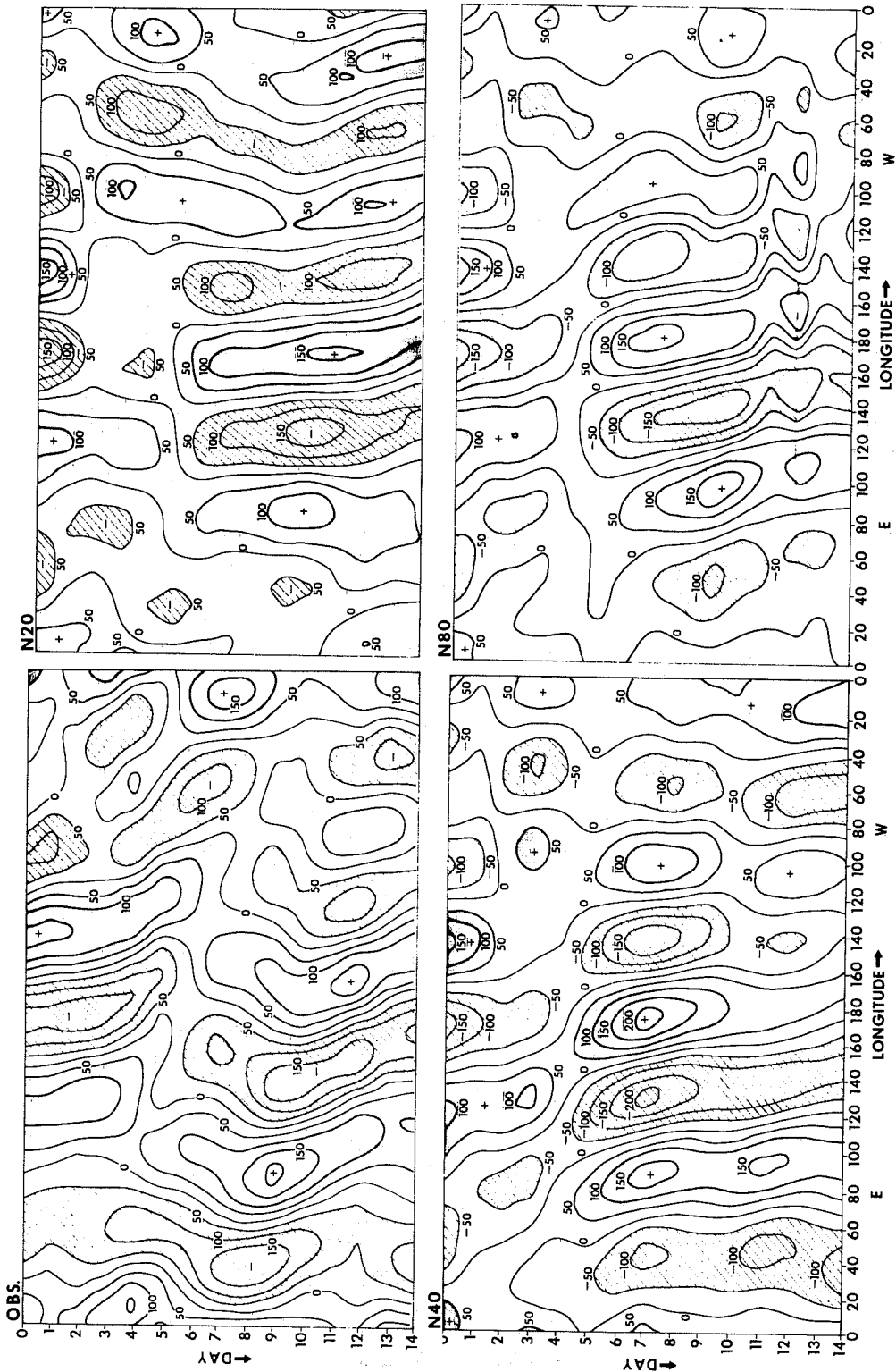


Fig. 9.10: Same as Fig. 9.9 except for wavenumbers 3-5.

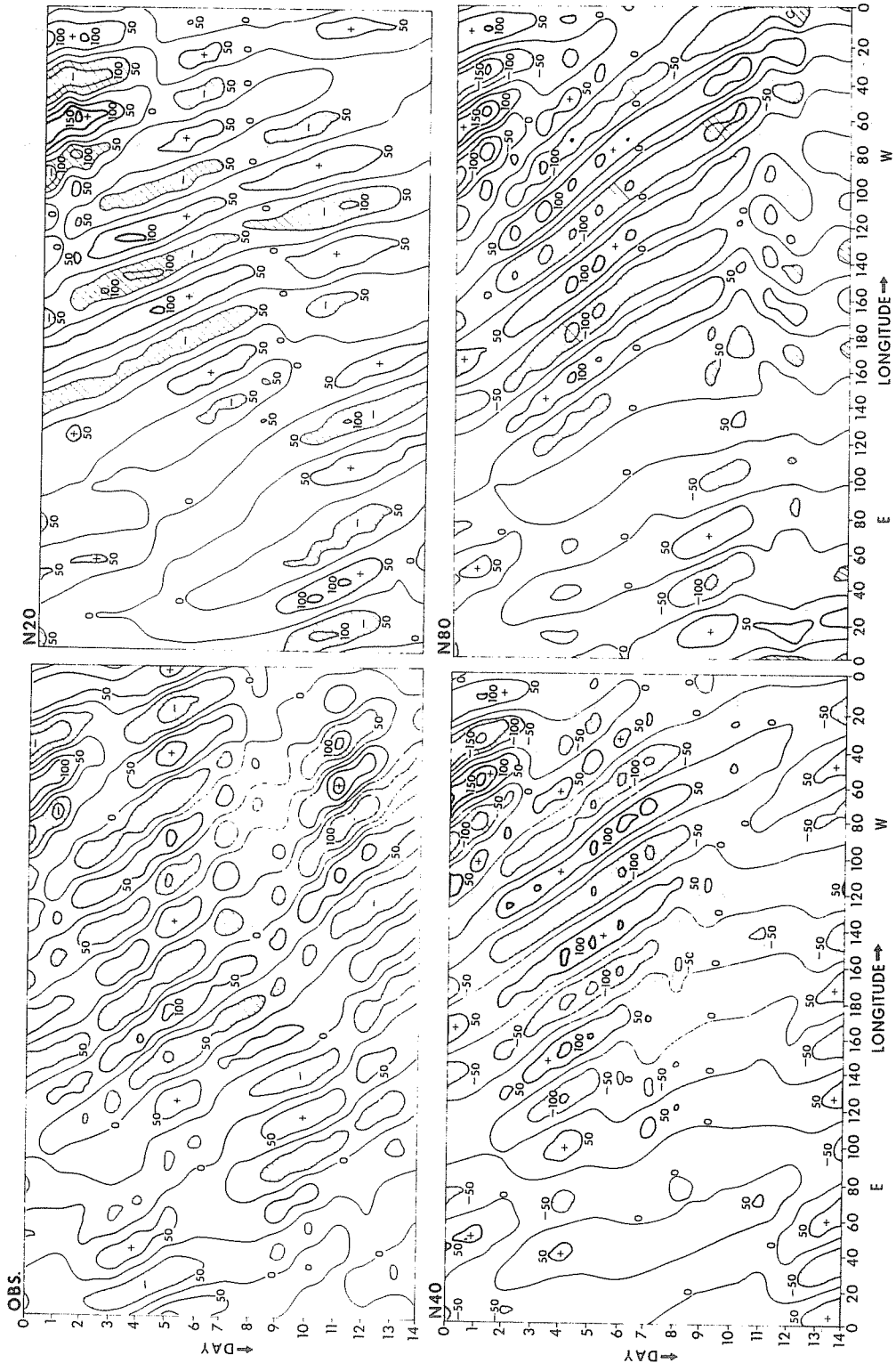


Fig. 9.11: The synthesized trough-ridge diagrams for wavenumbers 6-10.

truncation error in the wavenumber 6-10. The N=40 gives a satisfactory result in this respect. It is intriguing that for the planetary waves (wavenumber 1-2), space resolution is dominant. Figure 9.9 indicates that the resolution affects not only the phase of the waves but also wave amplitude. The higher the model resolution, the larger is the amplitude of the planetary waves. This fact has been recognized by a number of groups; Fawcett in NMC, Manabe and Smagorinsky (1967), (see figure 9.12), and Welck, Kasahara et al. (1971). The reason has not been

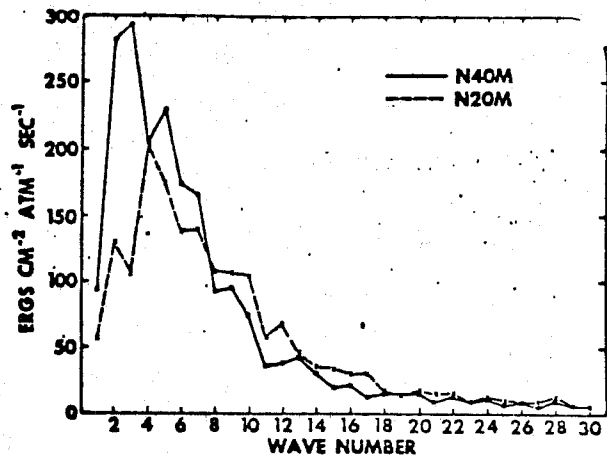


Fig. 9.12: Spectral distribution (hemispheric average) of the rate of change of eddy kinetic energy by the production term P(n). (Manabe et al, 1967).

investigated thoroughly, but one speculation is that the high resolution model produces more condensation heat and that the rain bands formed are of wavenumber 1-3, particularly the planetary scale waves.

In connection with the wave spectrum, the NCAR group obtained the kinetic energy spectra for different resolution models (Wellck, Kasahara et al, 1971). Figure 9.13 is the result of spectral distribution of eddy kinetic energy per unit mass as a function of the zonal wavenumber k at 40°N at the 4.5 km and 7.5 km levels. The upper left and right pictures are for the 10° and 5° meshes (approximately $\Delta S = 1,100$ km and 550 km), and the lower left picture is for the 2.5° mesh. The lower right is the observed distribution from Julian et al. (1970), Saltzman and Fleischer (1962), and Kao (1966). The slanting line in each figure shows a k^{-3} distribution as reference.

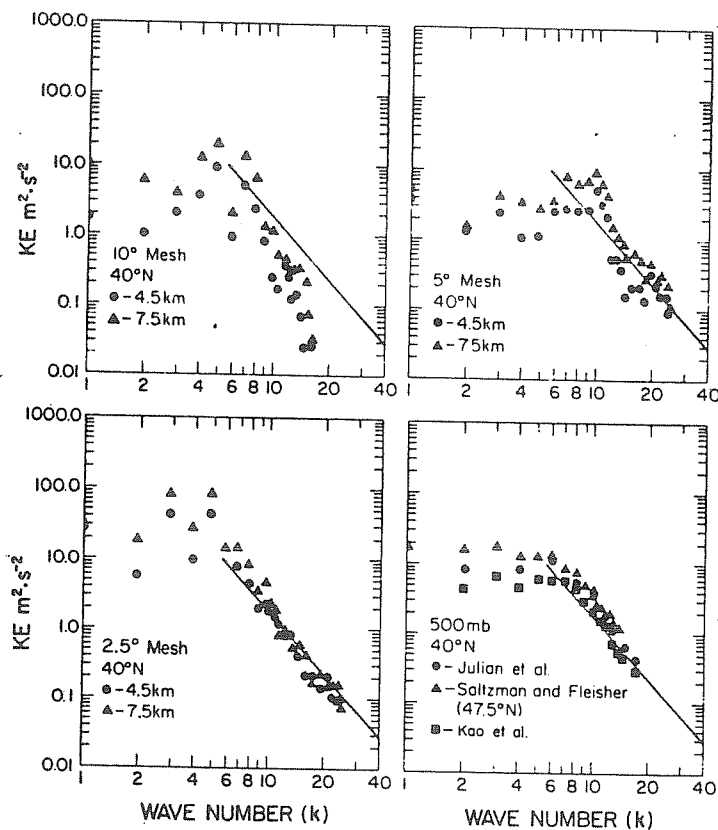


Fig.9.13 —Same as figure 19, except computed at different altitudes as indicated.

(after Wellck, Kasahara et al, 1971)

The vertical resolution of the model has considerable effect on the features of the general circulation. Figure 9.14 is the zonal mean winds in the meridional section for two different resolutions, i.e., the 9-level and the 18-level models, where both have $N=20$ horizontal resolution. (Manabe and Hunt, 1968). In the 9-level model, the middle latitude jet is connected with the stratospheric jet, whereas in the 18-level model, the two jets are clearly separated as they should be.

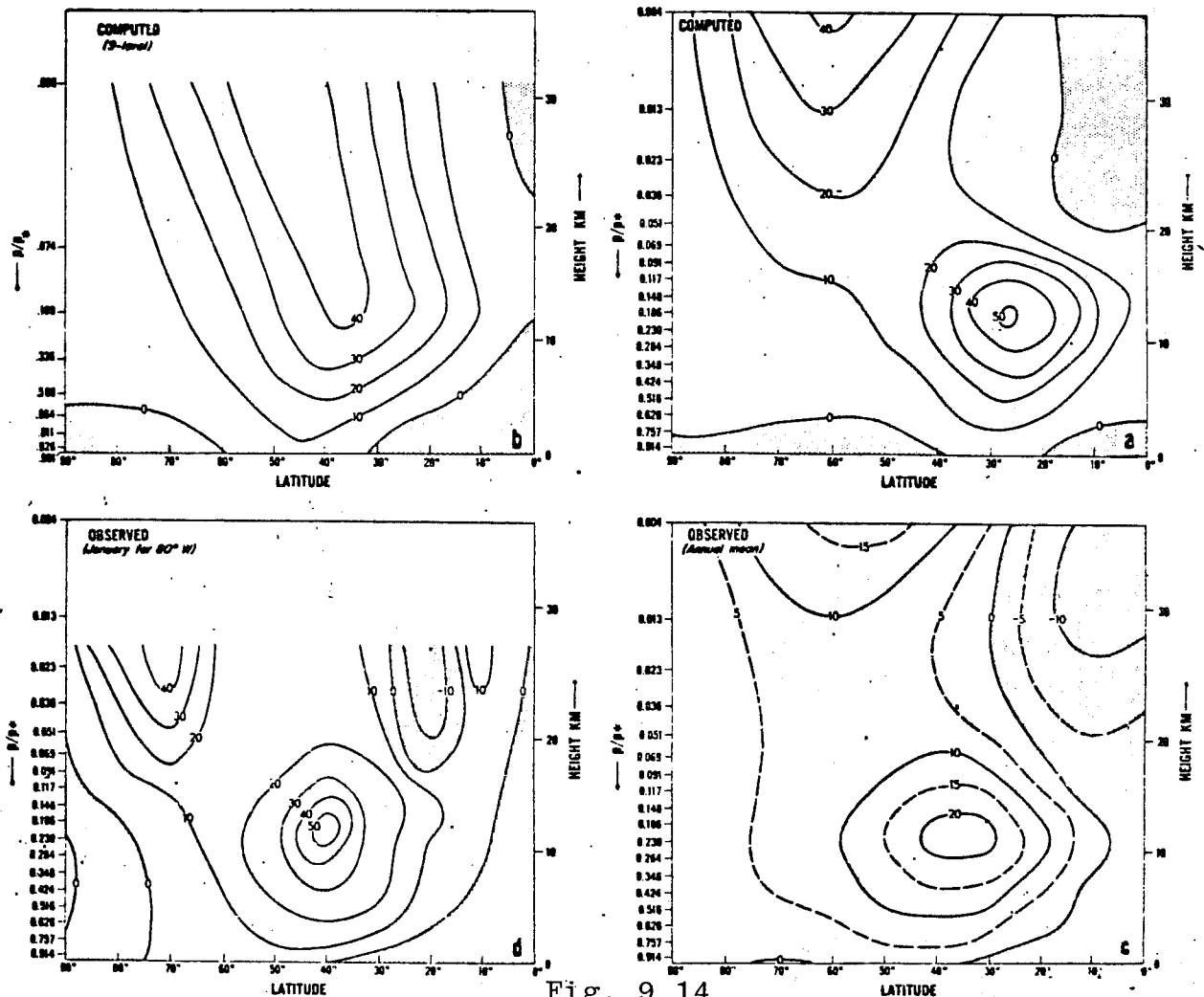


Fig. 9.14

The latitude-height distribution of the zonal mean zonal wind. In the upper half of the figure winds computed by the 18- and 9-level models are shown on the right and left respectively. In the lower half observed annual mean winds (principally Starr and collaborators) and also winds at 80°W for January (Kochanski [11]) are given for comparison. Shaded areas are regions of easterly winds. (Units: m./sec.) (After Manabe and Hunt, 1968).

Let us next look at a recent result obtained at GFDL (Miyakoda, Strickler et al. 1975). The resolution experiments were made for $N=20$, $N=40$, and $N=80$, also for the vertical resolution of $L=9$ at $L=18$. The results are shown with various maps in the manner as in figure 9.15. Figure 9.16 is the temperature forecast at 30 mb for the 4th day. As seen the 9-level models are all far from the observation, whereas, the 18-level models gave better results. The geopotential height maps at 10 mb for the 4th day are shown in figure 9.17. One may see clearly the superiority of the 18-level over the 9-level model in these forecasts. But the horizontal resolution seems to be not very influential, so far as these patterns are concerned except in the phase speed. On the other hand, the forecasts of the 500 mb height are affected by the horizontal resolution (figures 9.18 and 9.19 for the 4th day and 8th day, respectively). The patterns of the $N=20$ model are quite different from those of the $N=80$ model even at the 4th day and more so at the 8th day. Looking at the 8th day maps, one may see that the cyclones of the 500 mb maps are excessively deeper in the 18-level models of $N=20$ and $N=40$ resolution but not for $N=80$. The statistics revealed that the conversion of eddy kinetic energy from potential energy, $-\overline{\omega' \alpha'}$ is greater in the $L=18$ models than in $L=9$ models, supporting the statement above.

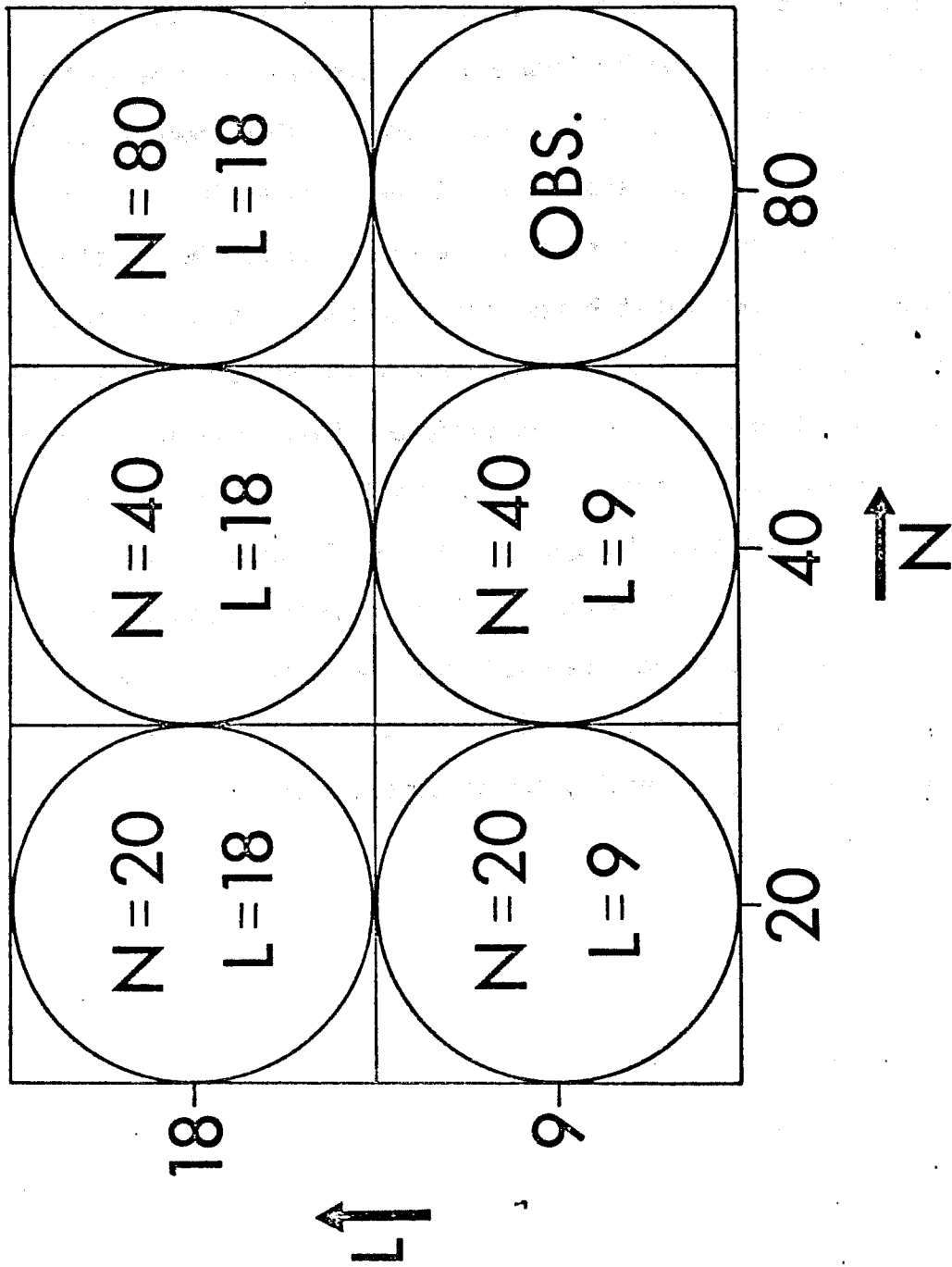
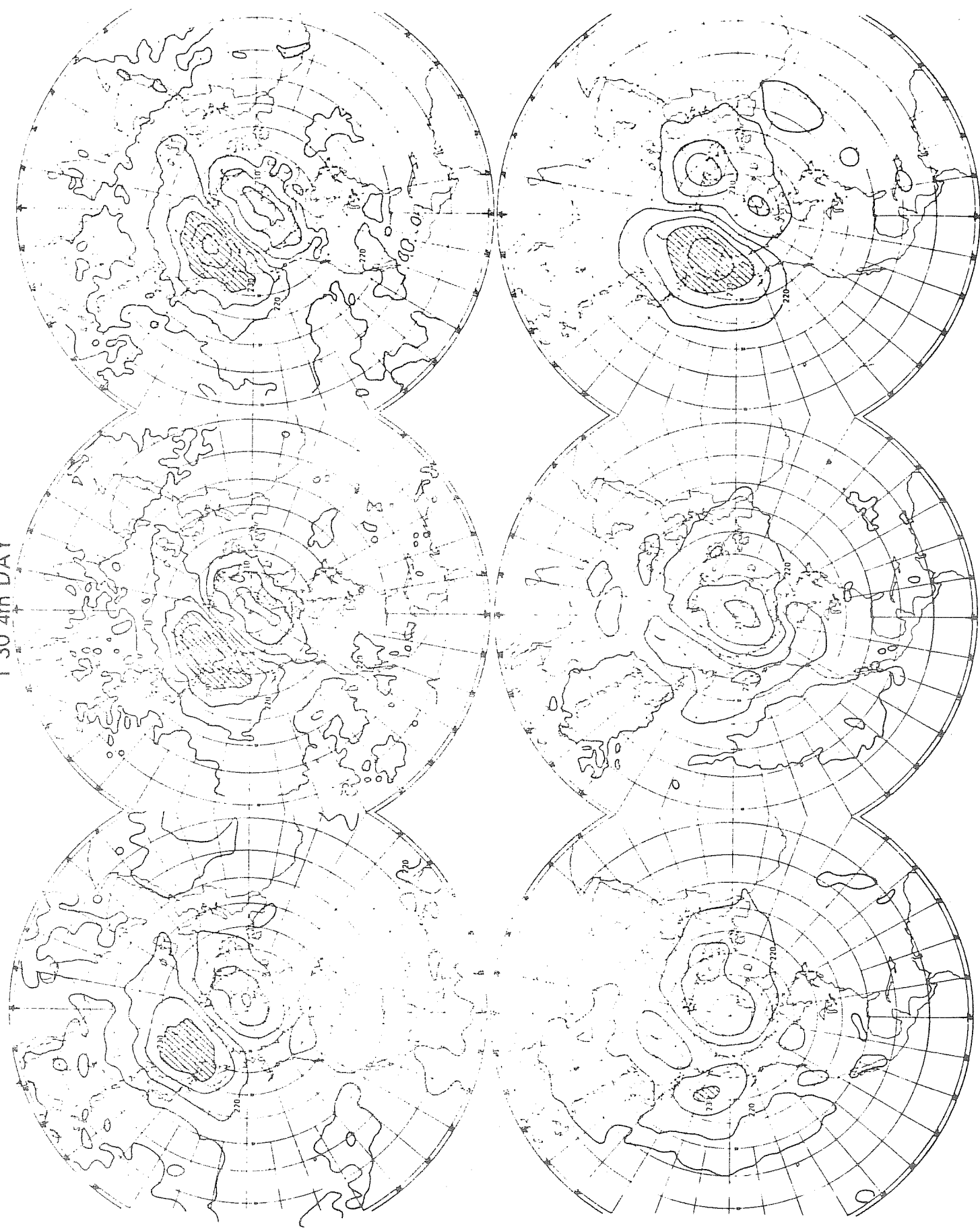


Fig. 9.15



130 4m DAT

(Miyakoda, Strickler et al, 1975)

Fig. 9.16

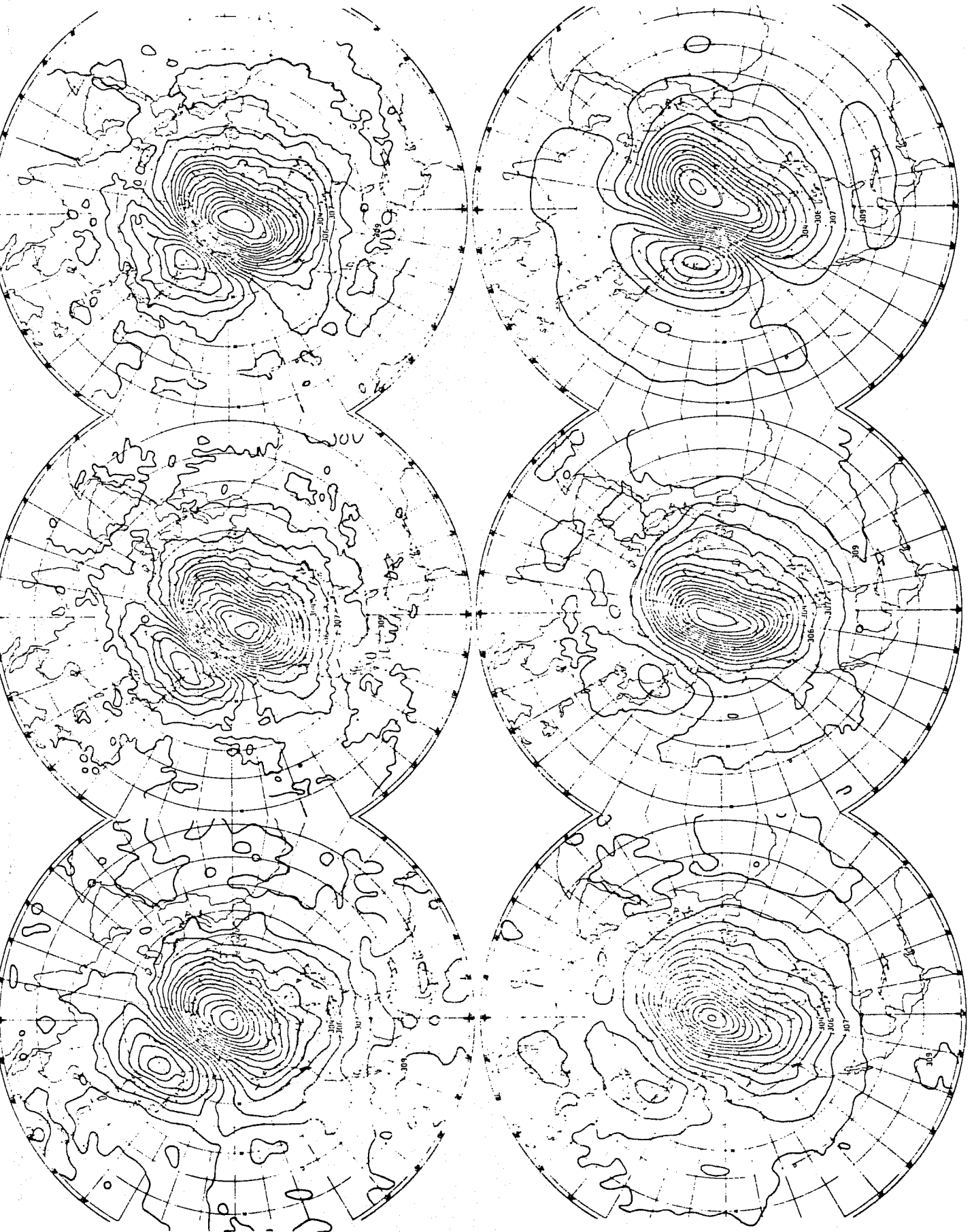
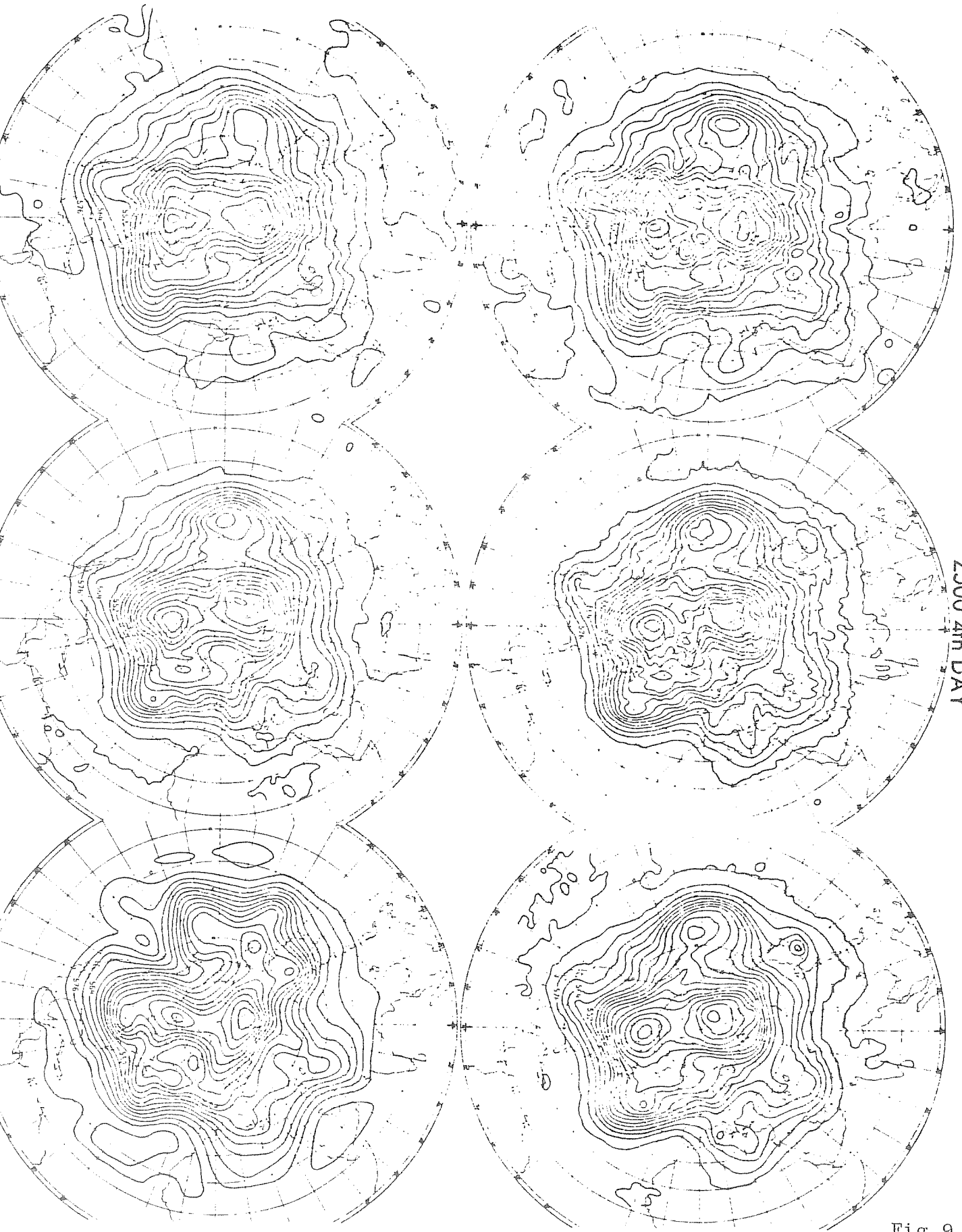


Fig. 9.17 (Miyakoda, Stricklor et al. 1975)



Z500 4th DAY

Fig.9.18

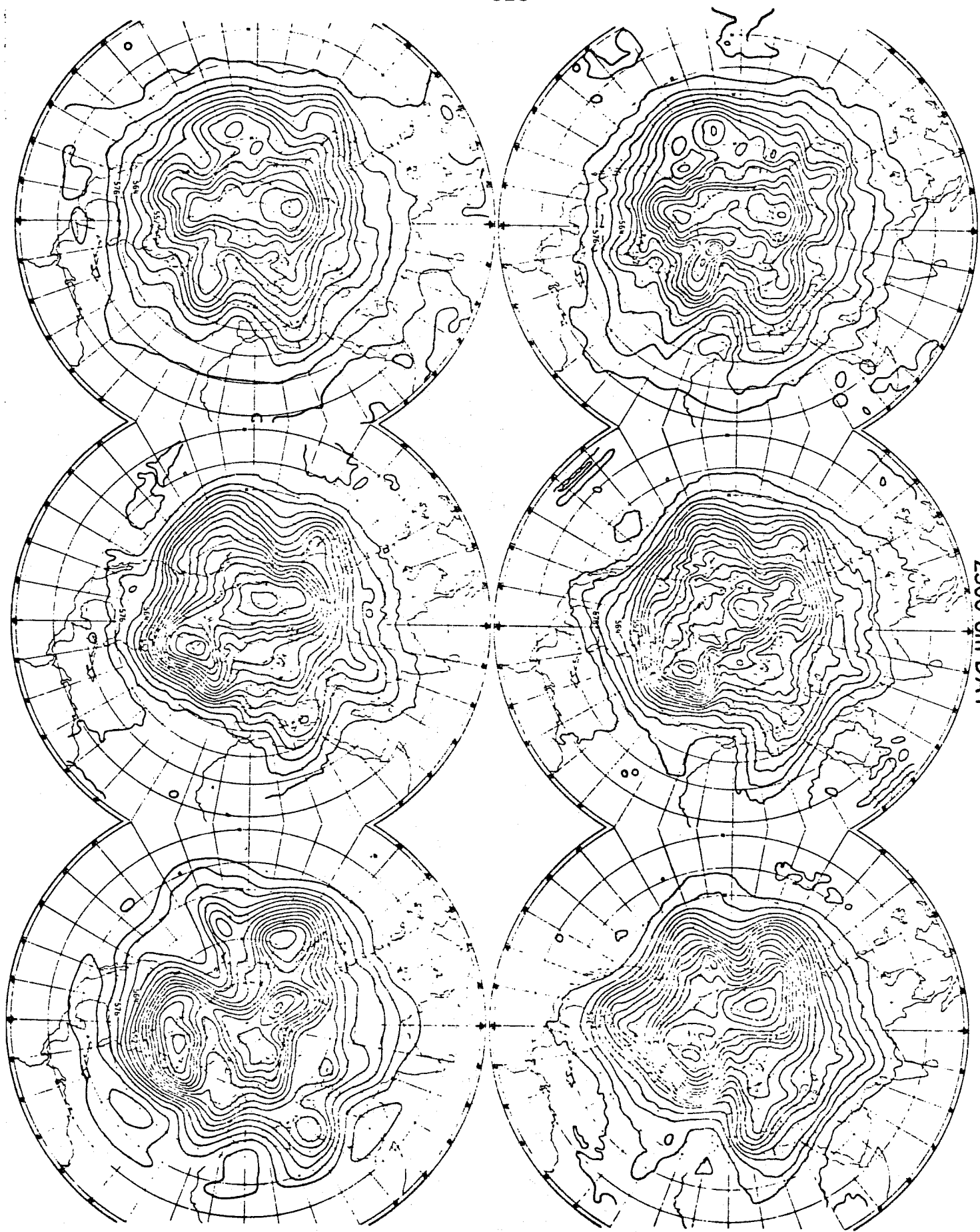


Fig.: 9.19:

(b) Initial data

For the medium-range forecasts, the initial data is the important factor in determining the quality of the forecasts. Even for the one-month forecast, the initial condition is still dominant. Figure 9.20 shows the development of the rms temperature error at 500 mb in the experiment of 12 winter cases which was described earlier.

The chart is the longitude-time diagram, from which one may see how the temperature error propagated and grew. It is clearly shown that the large error that started at longitude 140°E - 160°W which is over the Pacific Ocean and also at 60°W - 20°W which is over the Atlantic Ocean, was propagated eastward at a speed of about 10° per day. It is surmised that the accuracy of the analysis over the ocean is not good.

The way to reduce this type of initial error is to utilize the satellite data. A great deal of effort has been expended along this line. It is well known that satellite cloud pictures are very extensively used for nowcast, but not very much for map analyses except Hall, Nagle and Kelly's attempts. Concerning the usefulness of vertical temperature soundings, several studies have been reported, but the conclusions have been mostly pessimistic.

Recently Halem, GISS, has reported that the 4 day forecasts were substantially improved by using the VTPR data. According to his study, what is important is the frequency as well as the distribution of data rather than the accuracy of the temperature sounding. Figure 9.21 is the latitudinal distribution of yield per grid point per day, for the DST (Data System Testing) period, May 1 through 26, 1974. Compared with the amount of data operationally available (marked NESS), GISS

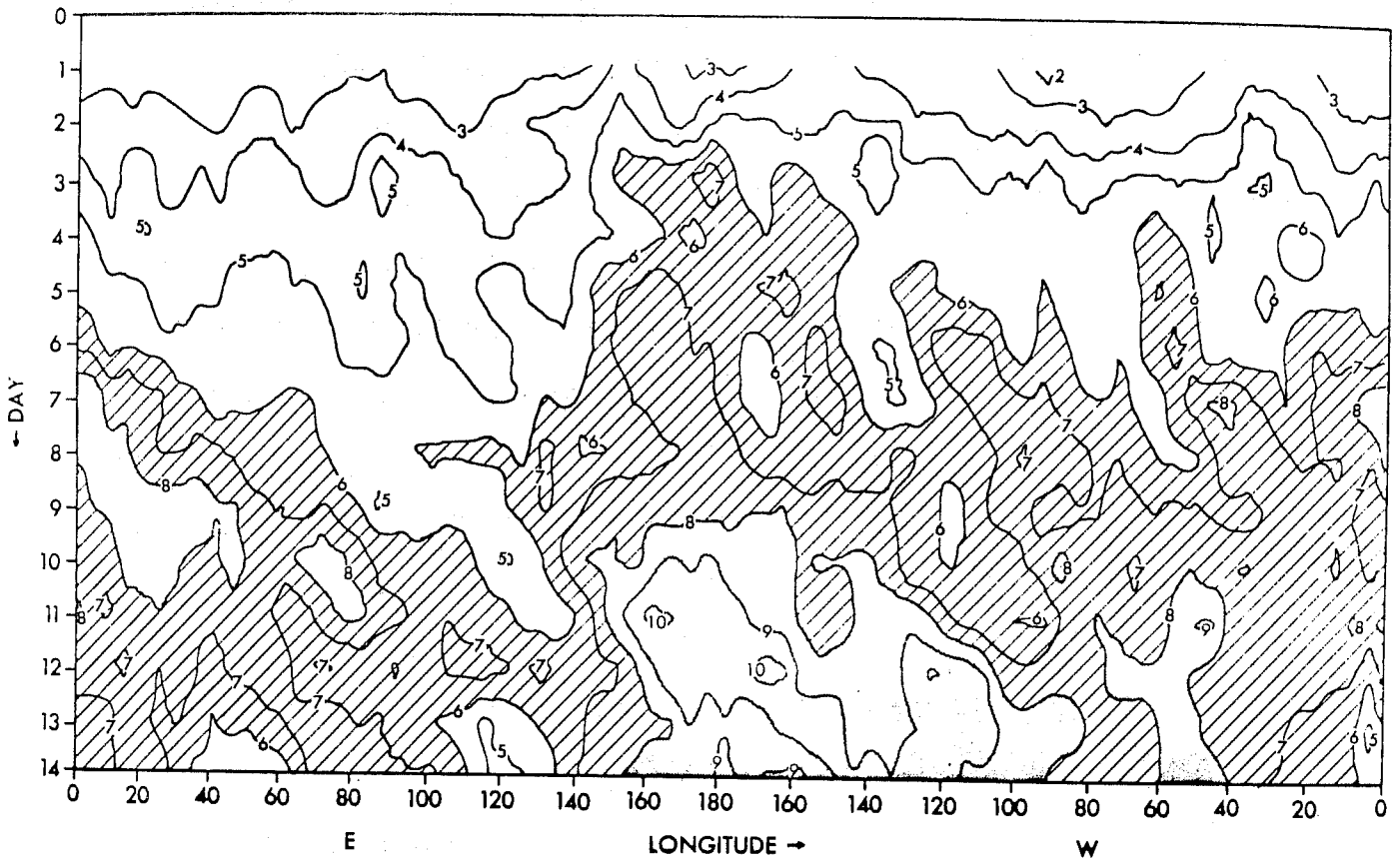


Fig. 9.20: The time-longitude chart of the root-mean-square temperature error $\sqrt{E(\delta T)}$ for the zonal belt between 35° and 45° latitude in units of $^{\circ}\text{K}$.

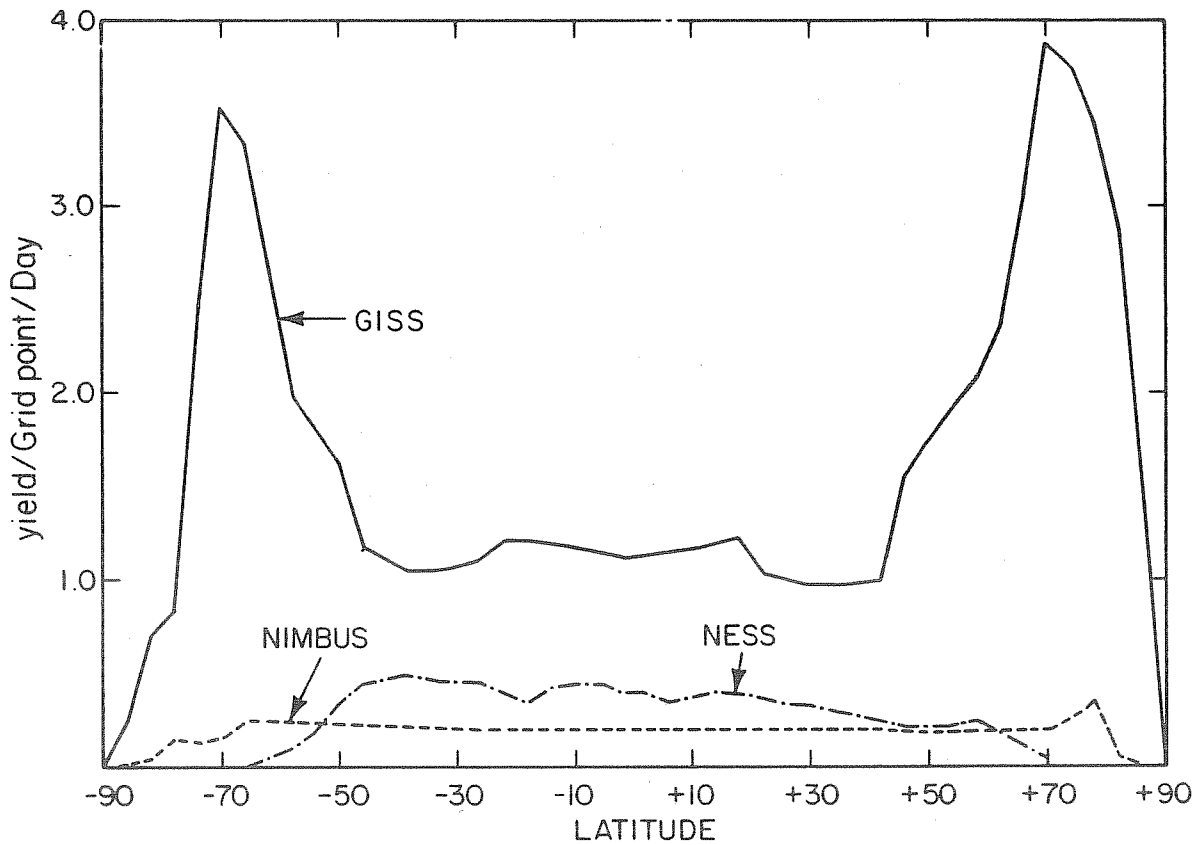


Fig. 9.21: The Average Yields of the derived sounder temperature (After Halem, 1975).

yielded a large number of data. The two maxima at 70°N and S are due to the overlapping of the satellite scanning patterns.

Halen (1974) used 4 different initial data sets from which forecasts are generated. The initial data is the following. Temperatures, winds and pressures over land are borrowed from the NMC operational upper air analysis north of 18°. Over the oceans, radiosonde reports are inserted directly. Aircraft reports and cloud winds are not used, but the 300 mb wind analysis of NMC is used instead. At the surface, pressure and temperatures are borrowed from the NMC analysis.

Experiment A contained no additional input. On the other hand, the initial data for experiment D is obtained in a similar manner except that the full yeild of the GISS-derived VTPR soundings are inserted into the model. Experiment B includes only one-third of the GISS-derived VTPR soundings, which is the same amount as that used in the NMC operational analysis. Experiment C uses the NMC operational analysis everywhere.

Figure 9.22 is the rms error of the surface pressure over North America. The difference between Experiment / and Experiment D is 15%

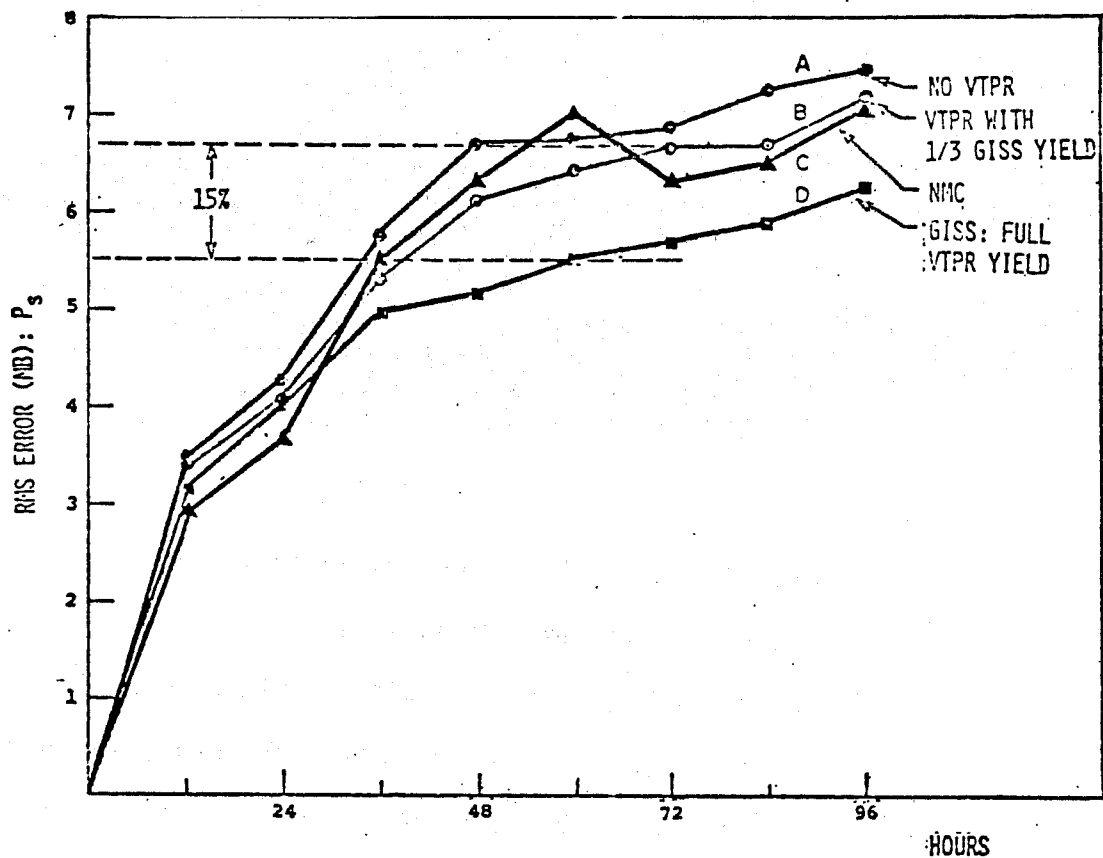


Fig. 9.22: Average forecast surface pressure errors as compared with NMC surface analysis over the U.S. (Halem, 1974).

of the total error at the 3rd or 4th day. This is the first example in which a sizeable improvement was achieved by the use of satellite vertical soundings.

We believe that the 4-dimensional analysis has been steadily advanced. (Bengtsson, 1975). Figure 9.23 is an example of the full 4-dimensional analysis at the 200 mb level during the GATE (GARP Atlantic Tropical Experiment) period, processed by Miyakoda, Umscheid et al. (1975); the result is compared with the NMC Flattery objective analysis. The two maps are very similar, but the 4-dimensional analysis turned out to be excessively smooth. The benefit from the 4-dimensional approach is realized over the tropics and the Southern Hemisphere more than anywhere else.



VERSION 3

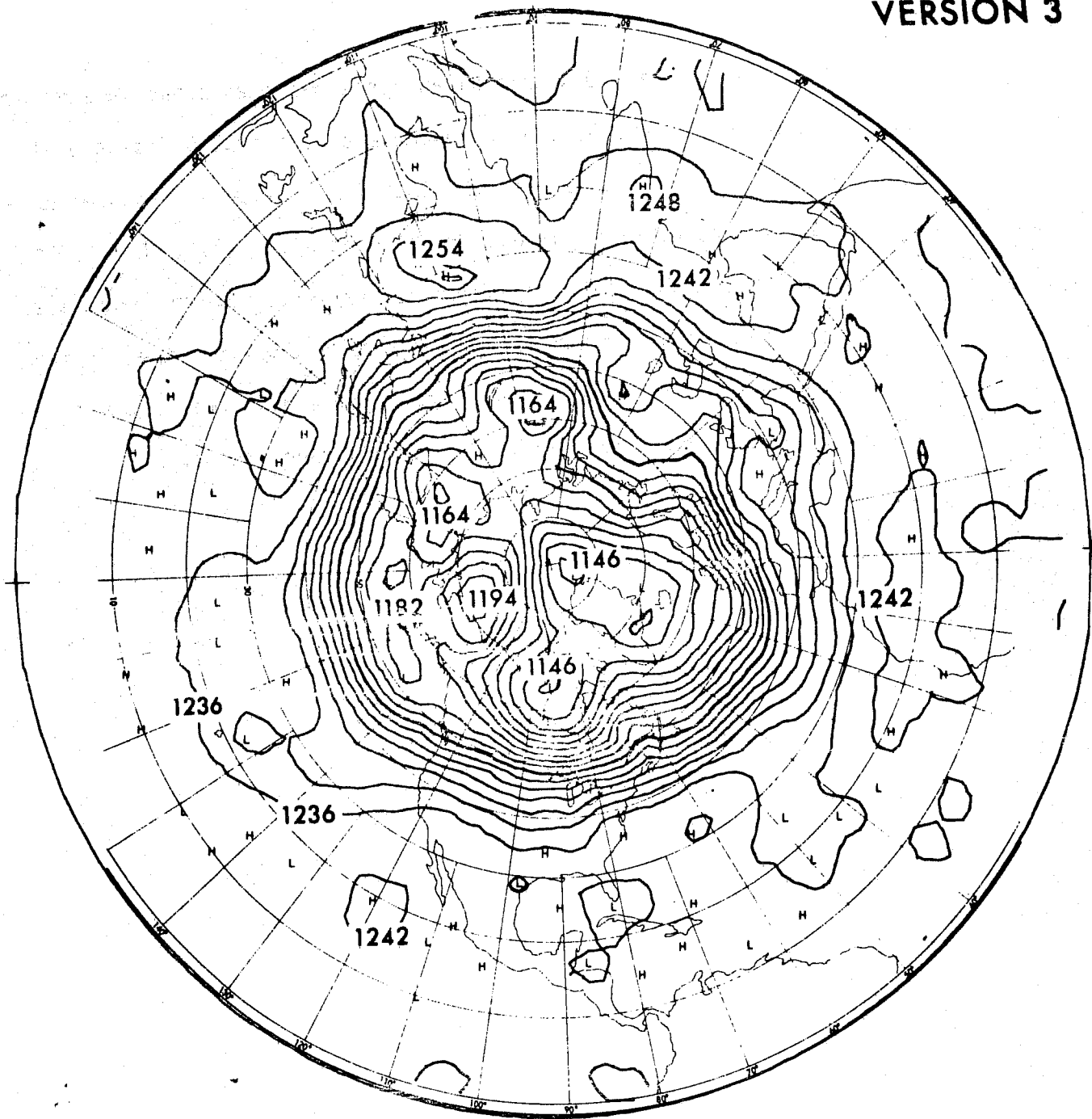


Fig. 9.23a

200 mb map 4-dimensional
(Miyakoda, Umscheid et al, 1975)

NMC

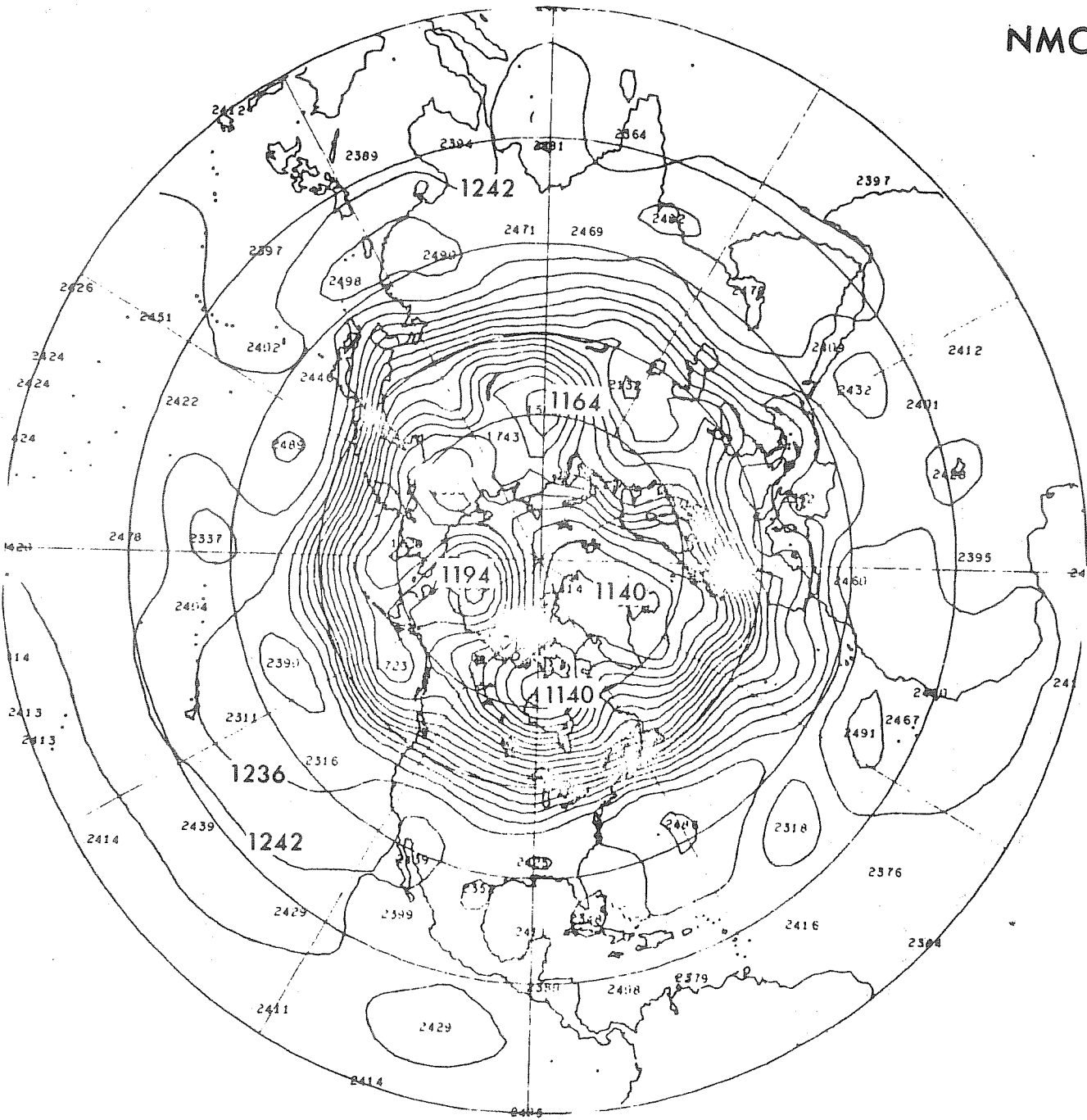


Fig. 9.23b 200 mb NMC

VERSION 3

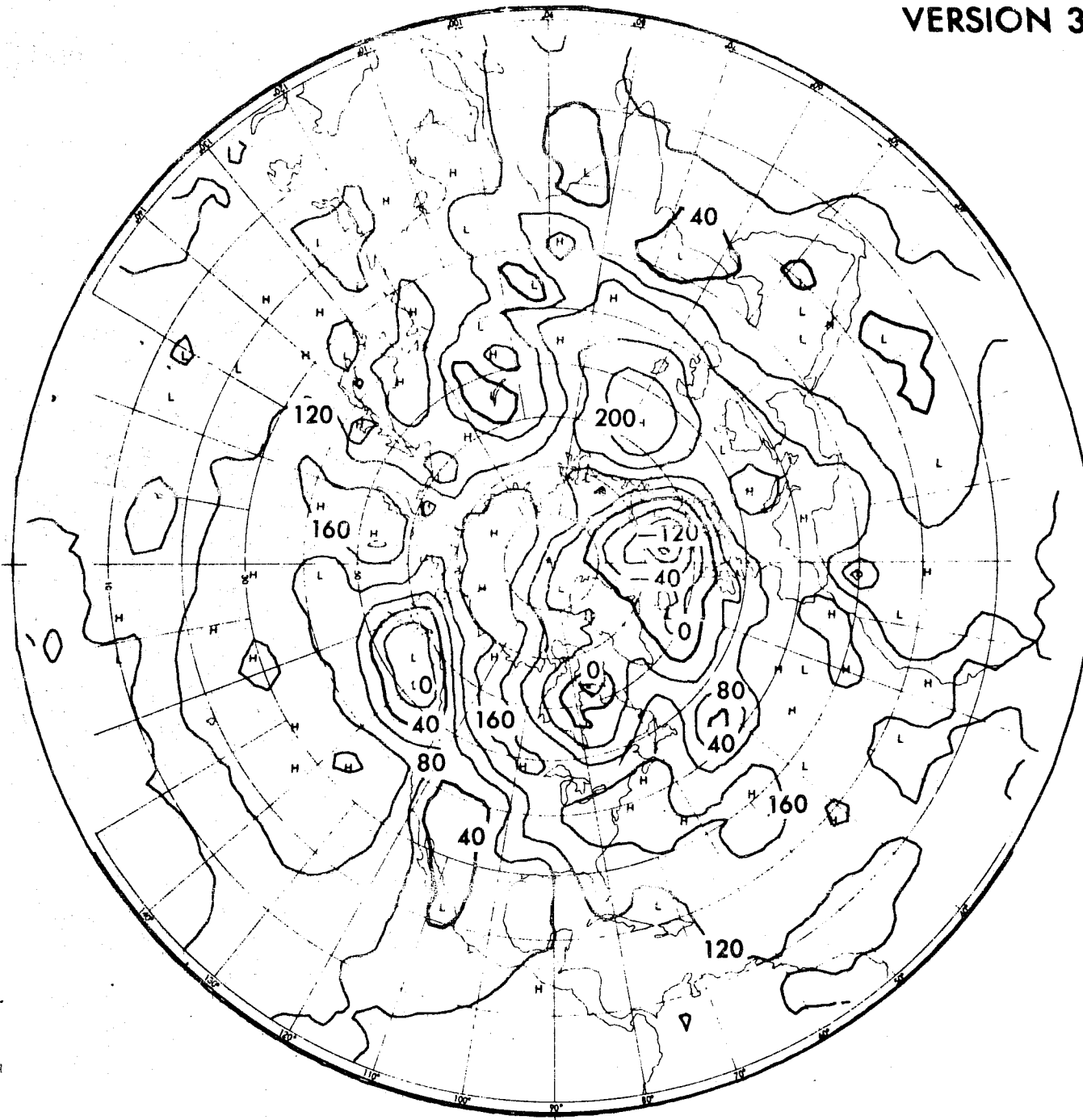


Fig. 9.23c 1000 mb 4-dimensional

NMC

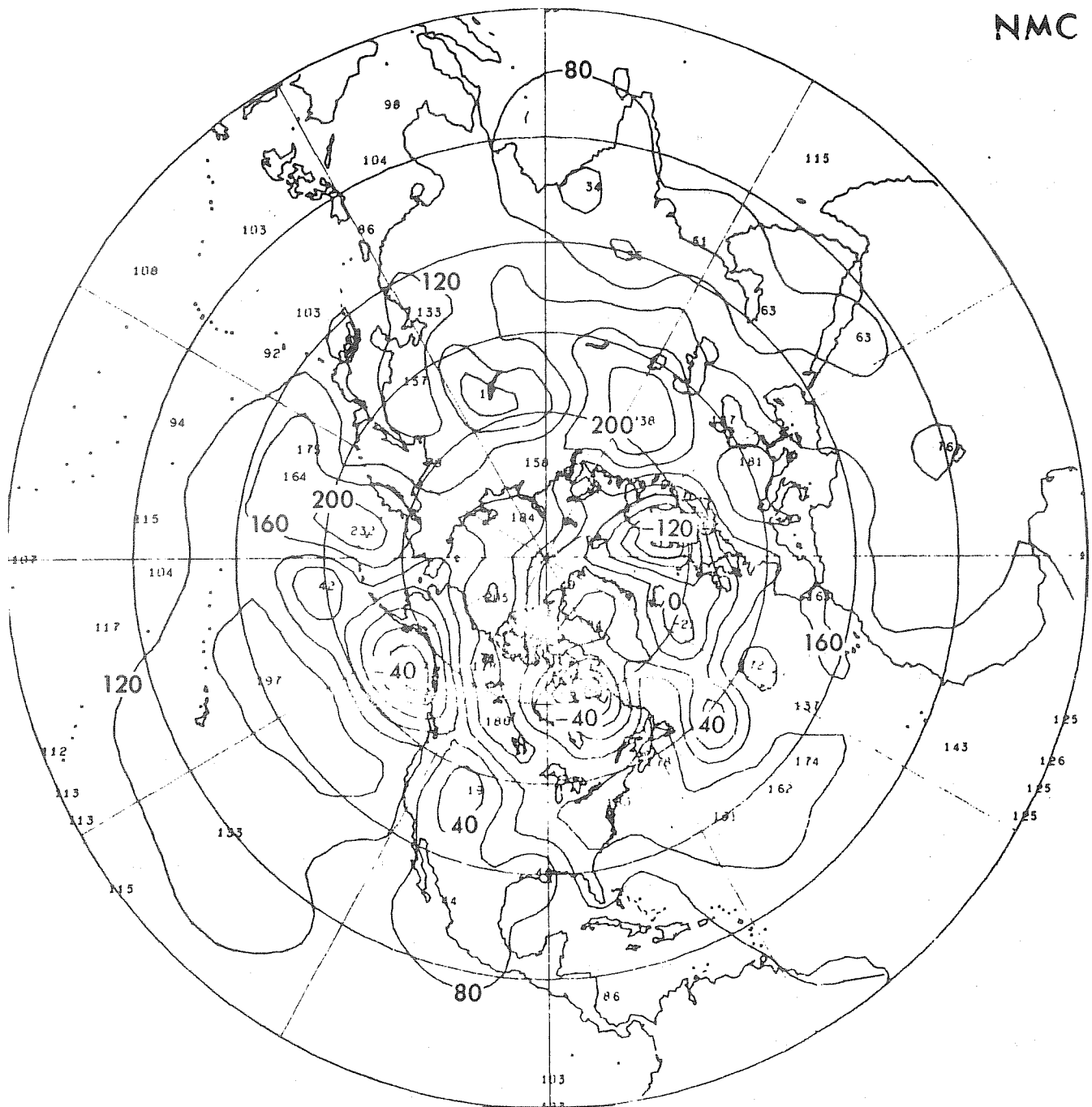


Fig. 23d 1000 mb NMC

References for the sections 7, 8, and 9

- Baer, F. and F. N. Alyea, 1971: Effect of spectral truncation on general circulation and long-range prediction. J. Atmos. Sci. 28, No. 4, 457-480.
- Bengtsson, L. 1975: Four-dimensional data assimilation of meteorological data. GARP Publication WMO-ICSU, JOC Series No. 15, 76 p.
- Budyko, M. I. 1963: Atlas of the heat balance of the earth. Moscow, Gidrometeorizdat, 69 pp.
- Delsol, F., K. Miyakoda, and R. H. Clarke, 1971: Parameterized processes in the surface boundary layer of an atmospheric circulation model. Quart. J. Roy. Meteor. Soc. 97, No. 412, 181-208.
- Fawcett, E. B. 1969: Systematic errors in operational baroclinic prognoses at the National Meteorological Center. Mon. Wea. Rev. 97, No. 9, 670-682.
- Gates, W. L., E. S. Batten, A. B. Kahle, and A. B. Nelson, 1971: A documentation of the Mintz-Arakawa two-level atmospheric general circulation model. RAND, Santa Monica, Calif. ARPA Order No. 189-1.
- Gates, W. L. 1975: Numerical modeling of climatic change: a review of problems and prospects. RAND Corporation.
- Halem, M. 1974: Results of forecasting impact of VTPR data. GISS Review 4-7.
- Halem, M. 1975: GARP PProject report on May 1974 data system test. GODDARD Space Flight Center, Greenbelt, Maryland
- Holloway, J. L. and S. Manabe, 1971: Simulation of climate by a global general circulation model. I. Hydrologic cycle and heat balance. Mon. Wea Rev. 99, No. 5, 335-370.
- Julian, P. R., W. M. Washington, L. Hembree, and C. Ridley, 1970: On the spectral distribution of large scale atmospheric kinetic energy. J. Atmos. Sci. 27, NO. 3, 376-387.
- Kao, S. K. and L. L. Wendell, 1970: The kinetic energy of the large-scale atmospheric motion in wavenumber frequency space. J. Atmos. Sci. 27, 359-375.
- Manabe, S, and J. Smagorinsky, 1967: Simulated climatology of a general circulation model with a hydrologic cycle: II. Analysis of the tropical atmosphere. Mon. Wea. Rev. 95, No. 4, 155-169.
- Manabe, S. and B. G. Hunt, 1968: Experiments with a stratospheric general circulation model: I. RAdiative and dynamic aspects. Mon. Wea Rev. 96, No. 8, 477-502.

- Manabe, S., J. Smagorinsky, J. L. Holloway, and H. M. Stone, 1970: Simulated climatology of a general circulation model with a hydrologic cycle: III. Effects of increased horizontal computational resolution. Mon. Wea. Rev. 98, No. 3, 175-212.
- Manabe, S. and J. L. Holloway, 1975: The seasonal variation of the hydrologic cycle as simulated by a global model of the atmosphere. J. Geophys. Res. 80, No. 12, 1617-1649.
- Miyakoda, K., R. F. Strickler, C. J. Nappo, P. O. Baker, and G. D. Hembree, 1971: The effect of horizontal grid resolution in an atmospheric circulation model. J. Atmos. Sci. 28, 481-499.
- Miyakoda, K. and Staff members, 1973: ANother attempt at simulating the stratospheric sudden warming with increased vertical and horizontal grid resolution models. PResented to Symposium on Difference and Spectral Methods for Atmosphere and Ocean Dynamics Problems, Novosibirsk, USSR, 17-23 September, 1973.
- Miyakoda, K. and R. F. Strickler, 1975: The effects of the subgrid-scale processes on the general circulation. (to be published)
- Miyakoda, K. and G. D. Hembree, 1975: Cumulative results of extended forecast experiments. III. Precipitation. (to be published)
- Miyakoda, K., L. Umscheid, D. H. Lee, J. Sirutis, R. Lusen, and F. Pratte, 1975: The near-real time global four-dimensional analysis experiment during the GATE period, Part I. (submitted to J. Atmos. Sci.)
- Puri, K. and W. Bourke, 1974: Implications of horizontal resolution in spectral model integrations. Mon. Wea. Rev. 102, No. 5, 333-347.
- Rasmussen, E. 1973: An investigation of truncation errors in a barotropic primitive equations model on spectral form. GARP Program on Numerical Experimentation - April Progress Report. 114-115.
- Saltzman, B. and A. Fleischer, 1960: The exchange of kinetic energy between larger scales of atmospheric motion. Tellus, 12, 374-377.
- Saltzman, B. and S. Teweles, 1964: Further statistics on the exchange of kinetic energy between harmonic components of the atmospheric flow. Tellus, 16, No. 4, 432-435.
- Saltzman, B. and A. Fleischer, 1962: Spectral statistics of the wind at 500 mb. J. Atmos. Sci. 19, No. 3, 195-206.
- Schultz, C. and W. L. Gates, 1971: Global climatic data for surface, 800 mb, 400 mb: January, Rept. R-915-ARPA, Rand Corporation
- Somerville, R. C. J. P. H. Stone, M. Halem, J. E. Hansen, J. S. Hogan, L. M. Druyan, G. Russell, A. A. Lacis, W. J. Quirk, and J. Tenenbaum, 1974: The GISS model of the global atmosphere. J. Atmos. Sci. 31, 84-117.

Wellck, R. E., A. Kasahara, W. M. Washington, and G. DeSanto, 1971: Effects of horizontal resolution in a finite-difference model of the general circulation. Mon. Wea. Rev. 99, 673-683.

Wiin-Nielsen, A. 1967: On the annual variation and spectral distribution of atmospheric energy. Tellus, 19, No. 4, 540-559.

10. Refined parameterization of the PBL processes

The planetary boundary layer (PBL) is defined as the layer which the surface effect influences directly and sizably, and in which turbulent motion is intense. The PBL is divided into the interfacial layer and the turbulent PBL (see figure 10.1). The former layer extends from the surface to the roughness height, Z_0 , in which the molecular viscosity plays a substantial role. In the latter the eddy motion is dominant in transferring the atmospheric element such as momentum, heat and moisture. This layer can technically be divided into the "constant-flux layer" and the rest of the PBL. In the constant-flux layer, the wind stress, heat and moisture fluxes are approximately ($\pm 20\%$) constant with height. This assumption enables one to set up some simple relationships for the eddy transfer. This layer normally extends from the level of Z_0 to 20-100 meters. The entire turbulent PBL is characterized by a vertically well mixed layer, in which the virtual potential temperature is constant with height, and the mixing ratio of water vapor is also almost constant (figure 10.2) (Malkus, 1958). The depth of the PBL varies diurnally over land from 0 to 2 km, and the depth over sea is about 200-500 meters.

There seem to be three approaches for the treatment of the PBL, i.e., the multi-layer model, the mixed layer model and the method of the drag and heat transfer laws (Rossby number similarity theory). The multi-layer model includes the K-theory approach, the eddy viscosity method, and the closure model, though the first two approaches can be derived from the closure model as limiting cases. (Monin, 1965, Donaldson, 1973, Deardorff, 1973, Mellor and Yamada, 1974.)

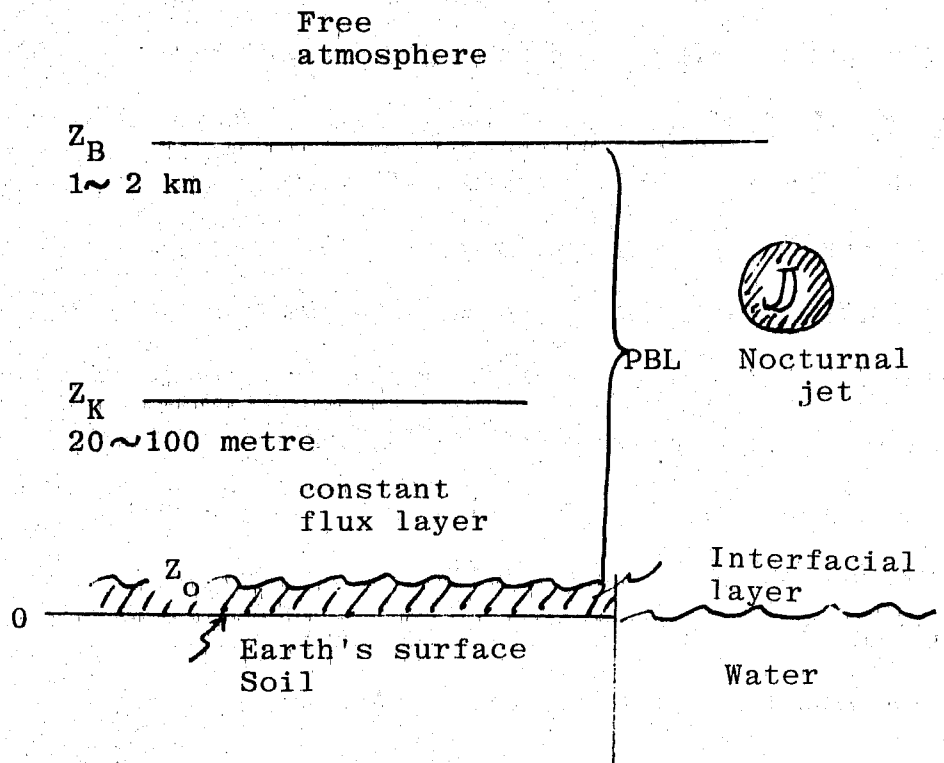


Fig. 10.1

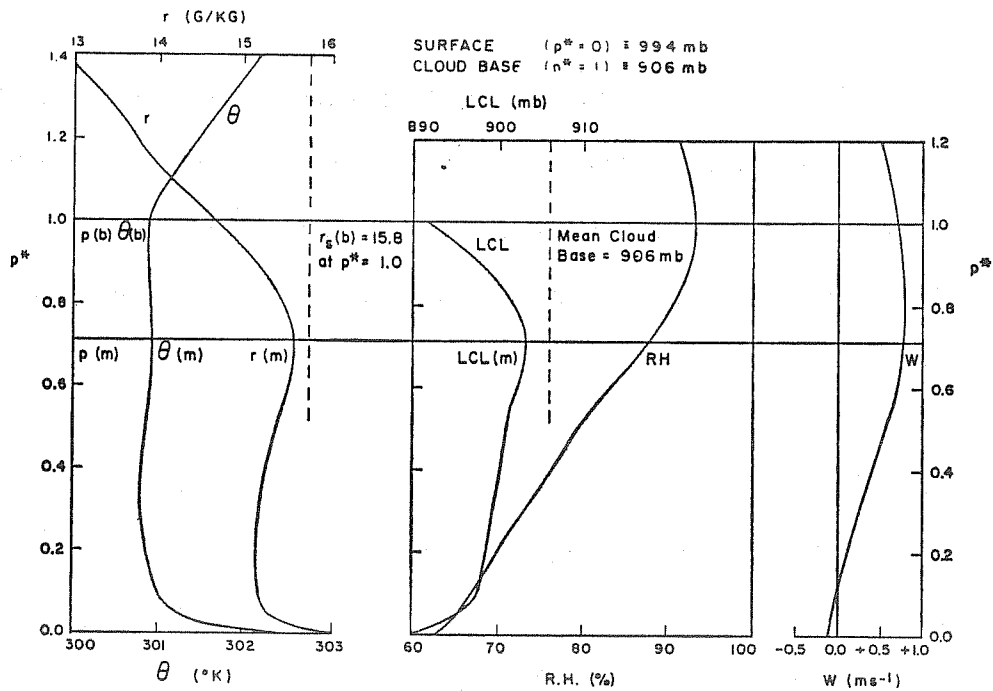


Fig. 1 Mean profile for 14 radiosonde ascents through cloud-base of potential temperature (θ), mixing ratio (r), lifting condensation level (LCL), relative humidity (RH), perturbation vertical velocity (w). (After Betts et al, 1974).

For numerical prediction models, the closure model is quite appropriate. With this approach, it is possible to resolve some special features of the PBL. For example, the nocturnal jet can be reproduced. The horizontal advectations of elements and baroclinicity can be incorporated. No special consideration is required for the equatorial boundary layer. In addition, even in the case that the top of PBL is obscure, no difficulty is presented.

Recently, mixed layer models (Ball, 1960, Lilly 1968) have received considerable attention in conjunction with cumulus parameterization.

In the UCLA version of cumulus parameterization (Arakawa and Schubert, 1974), the depth of the PBL is a fundamental parameter for cloud specification, because the top of the PBL corresponds to the cloud base.

In the following, we will select three problems for discussion from the standpoint of the modelling of general circulation, i.e., closure models, the depth of the PBL, and the constant-flux layer. The detailed survey of the PBL parameterization in General Circulation Models was made by Bhumralkar (1975).

(i) Turbulent closure models

The development of the mean Reynolds stress closure model has a long history, but the application to the atmospheric boundary layer is recent, i.e., Monin (1965), Donaldson and Rosenbaum (1968), Donaldson (1973), Deardorff (1973), Mellor (1973), and Lumley and Khajeh-Nouri (1974).

All variables are divided into ensemble mean variables and eddies, and turbulent transport equations are set up. The equations of the first order (mean) variables and eddies are written as

The eqs. of mean motion

$$\frac{\partial \bar{u}_j}{\partial t} + \frac{\partial}{\partial x_k} (\bar{u}_k \bar{u}_j + \overline{u_k' u_j'}) = - \frac{\partial \bar{p}}{\partial x_j} - \delta_{j3} \frac{g}{\theta_0} \bar{\theta} + \nu \nabla^2 \bar{u}_j \quad (10.1)$$

The thermodynamic equation

$$\frac{\partial \bar{\theta}}{\partial t} + \frac{\partial}{\partial x_k} (\bar{u}_k \bar{\theta} + \overline{u_k' \theta'}) = K \nabla^2 \bar{\theta} \quad (10.2)$$

where \bar{p} is the mean kinematic pressure, θ_0 is the constant potential temperature, ν the kinematic viscosity and K the kinematic heat conductivity. (or thermal diffusivity).

$$\begin{aligned} \frac{\partial u_i'}{\partial t} + \frac{\partial}{\partial x_k} (\bar{u}_i u_k' + \bar{u}_k u_i' + u_i' u_k' - \overline{u_i' u_k'}) \\ = - \frac{\partial p'}{\partial x_i} - \delta_{i3} \frac{g}{\theta_0} \theta' + \nu \nabla^2 u_i' \end{aligned} \quad (10.3)$$

$$\frac{\partial \theta'}{\partial t} + \frac{\partial}{\partial x_k} (\bar{\theta} u_k' + \bar{u}_k \theta' + u_k' \theta' - \overline{u_k' \theta'}) = K \nabla^2 \theta' \quad (10.4)$$

The equations of the 2nd order correlations are written as

$$\begin{aligned}
 & \frac{\partial \overline{u_i' u_j'}}{\partial t} + \frac{\partial}{\partial x_k} [\overline{\bar{u}_k u_i' u_j'} + \overline{u_k' u_i' u_j'}] \\
 & + \frac{\partial}{\partial x_j} \overline{p' u_i'} + \frac{\partial}{\partial x_i} \overline{p' u_j'} \\
 & = - \overline{u_i' u_k'} \frac{\partial \bar{u}_j}{\partial x_k} - \overline{u_j' u_k'} \frac{\partial \bar{u}_i}{\partial x_k} \\
 & - \frac{g}{\theta_0} (\delta_{i3} \overline{u_j' \theta'} + \delta_{j3} \overline{u_i' \theta'}) \\
 & + \nu \frac{\partial^2}{\partial x_k \partial x_k} \overline{u_i' u_j'} - 2\nu \frac{\partial u_i'}{\partial x_k} \frac{\partial u_j'}{\partial x_k} + \overline{p' \left(\frac{\partial u_i}{\partial x_j} + \frac{\partial u_j}{\partial x_i} \right)}, \quad (10.5)
 \end{aligned}$$

$$\begin{aligned}
 & \frac{\partial}{\partial t} \overline{u_i' \theta'} + \frac{\partial}{\partial x_k} [\overline{\bar{u}_k u_i' \theta'} + \overline{u_k' u_i' \theta'}] + \frac{\partial}{\partial x_i} \overline{p' \theta'} \\
 & = - \overline{u_i' u_k'} \frac{\partial \bar{\theta}}{\partial x_k} - \overline{\theta' u_k'} \frac{\partial \bar{u}_j}{\partial x_k} - \delta_{i3} \frac{g}{\theta_0} \overline{\theta'^2} + \overline{p' \frac{\partial \theta'}{\partial x_i}} \\
 & + (\nu + K) \frac{\partial^2}{\partial x_k \partial x_k} \overline{u_i' \theta'} - \frac{\partial}{\partial x_k} (\nu u_i' \frac{\partial \theta'}{\partial x_k} + K \theta' \frac{\partial u_i'}{\partial x_k}) \\
 & - (\nu + K) \frac{\partial u_i'}{\partial x_k} \frac{\partial \theta'}{\partial x_k}, \quad (10.6)
 \end{aligned}$$

$$\begin{aligned}
 & \frac{\partial \overline{\theta'^2}}{\partial t} + \frac{\partial}{\partial x_k} [\overline{u_k \theta'^2} + \overline{u_k' \theta'^2}] = - 2 \overline{u_k' \theta'} \frac{\partial \bar{\theta}}{\partial x_k} + K \frac{\partial^2}{\partial x_k \partial x_k} \overline{\theta'^2} \\
 & - 2 K \frac{\partial \theta'}{\partial x_k} \frac{\partial \theta'}{\partial x_k}. \quad (10.7)
 \end{aligned}$$

Thus we have equations for all the correlations as follows

$$\begin{pmatrix} \overline{u_1'^2} & \overline{u_1'u_2'} & \overline{u_1'u_3'} & \overline{u_1'\theta'} \\ \overline{u_2'u_1'} & \overline{u_2'^2} & \overline{u_2'u_3'} & \overline{u_2'\theta'} \\ \overline{u_3'u_1'} & \overline{u_3'u_2'} & \overline{u_3'^2} & \overline{u_3'\theta'} \\ \overline{\theta'u_1'} & \overline{\theta'u_2'} & \overline{\theta'u_3'} & \overline{\theta'^2} \end{pmatrix} \quad (10.8)$$

Before proceeding further it may be helpful to examine physical meanings of the terms appearing in the equation of the eddy kinetic energy. If these equations for u_1' , $u_2'^2$ and $u_3'^2$ are added, the equation of eddy kinetic energy is obtained. From here on, dropping the dash notation, we have

$$b^2 = \overline{u_k u_k}, \quad (10.9)$$

$$\begin{aligned} \frac{\partial b^2}{\partial t} + \underbrace{\frac{\partial}{\partial x_k} u_k b^2}_{\text{advection}} + \underbrace{\frac{\partial}{\partial x_k} (\overline{u_k u_\ell u_\ell})}_{\text{diffusion by eddies}} + \underbrace{2 \overline{u_k p}}_{\text{redistribution by pressure velocity interaction}} \\ = - 2 \underbrace{\overline{u_k u_\ell} \frac{\partial u_\ell}{\partial x_k}}_{\text{Interaction of the Reynolds stresses and the mean flows}} - 2 \underbrace{\frac{g}{\theta_0} \overline{w\theta}}_{\text{generation by buoyancy}} \\ + \underbrace{\nu \frac{\partial^2 b^2}{\partial x_k \partial x_k}}_{\text{diffusion by molecular viscosity}} - 2\nu \underbrace{\overline{\frac{\partial u_\ell}{\partial x_k} \frac{\partial u_\ell}{\partial x_k}}}_{\text{viscous dissipation}} \end{aligned} \quad (10.10)$$

Introducing the closure assumptions, the triple correlations appearing in the equations of the 2nd order correlations are written as follows

$$\overline{u_i u_j u_k} = - b \cdot \lambda_1 \left(\frac{\partial \overline{u_j u_j}}{\partial x_k} + \frac{\partial \overline{u_i u_k}}{\partial x_j} + \frac{\partial \overline{u_j u_k}}{\partial x_i} \right), \quad (10.11)$$

$$\overline{u_k u_j \theta} = - b \cdot \lambda_2 \left(\frac{\partial \overline{u_k \theta}}{\partial x_j} + \frac{\partial \overline{u_j \theta}}{\partial x_k} \right), \quad (10.12)$$

$$\overline{u_i \theta^2} = - b \lambda_3 \left(\frac{\partial \overline{\theta^2}}{\partial x_i} \right) \quad (10.13)$$

The terms of the pressure-velocity correlations which are called "energy redistribution terms," are substituted by Rotta's (1951) assumption, i.e.,

$$\begin{aligned} p \left(\frac{\partial u_i}{\partial x_j} + \frac{\partial u_j}{\partial x_i} \right) = & - \frac{b}{3\ell_1} \left(\overline{u_i u_j} - \frac{1}{3} \delta_{ij} b^2 \right) \\ & + c \cdot b^2 \left(\frac{\partial \overline{u_i}}{\partial x_j} + \frac{\partial \overline{u_j}}{\partial x_i} \right). \end{aligned} \quad (10.14)$$

$$p \frac{\partial \theta}{\partial x_i} = - \frac{b}{3\ell_2} \overline{u_i \theta} - \frac{1}{3} \delta_{i3} \frac{g}{\theta_0} \overline{\theta^2}. \quad (10.15)$$

The viscous dissipation is expressed, based upon Kolmogoroff's (1941) hypothesis, i.e.,

$$\nu \frac{\partial u_i}{\partial x_k} \frac{\partial u_j}{\partial x_k} = \frac{2}{3} \frac{b^3}{\Lambda_1} \delta_{ij} \quad (10.16)$$

$$2K \frac{\partial \theta}{\partial x_k} \frac{\partial \theta}{\partial x_k} = + 2 \frac{b}{\Lambda_2} \overline{\theta^2} \quad (10.17)$$

In this way, the equations in the closure model are written as

$$\begin{aligned} \frac{D\overline{u^2}}{Dt} &= \frac{\partial}{\partial z} \left(b\lambda_1 \frac{\partial \overline{u^2}}{\partial z} + v \frac{\partial \overline{u^2}}{\partial z} \right) \\ &- 2 \overline{wu} \frac{\partial \overline{u}}{\partial z} - \frac{b}{3\lambda_1} \left(\overline{u^2} - \frac{b^2}{3} \right) - \frac{2}{3} \frac{b^3}{\lambda_1}, \end{aligned} \quad (10.18)$$

where

$$\frac{D}{Dt} = \frac{\partial}{\partial t} + \overline{u}_k \frac{\partial}{\partial x_k} \quad (10.19)$$

$$\frac{D\overline{v^2}}{Dt} = \text{-----} \quad (10.20)$$

$$\frac{D\overline{w^2}}{Dt} = \text{-----} \quad (10.21)$$

$$\begin{aligned} \frac{D\overline{uv}}{Dt} &= \frac{\partial}{\partial z} \left(b\lambda_1 \frac{\partial \overline{uv}}{\partial z} + v \frac{\partial \overline{uv}}{\partial z} \right) \\ &- \overline{wu} \frac{\partial \overline{v}}{\partial z} - \overline{wv} \frac{\partial \overline{u}}{\partial z} - \frac{b}{3\lambda_1} \overline{uv}, \end{aligned} \quad (10.22)$$

$$\frac{D\overline{uw}}{Dt} = \text{-----} \quad (10.23)$$

$$\frac{D\overline{vw}}{Dt} = \text{-----} \quad (10.24)$$

$$\begin{aligned} \frac{D\overline{u\theta}}{Dt} &= \frac{\partial}{\partial z} \left(b\lambda_2 \frac{\partial \overline{u\theta}}{\partial z} + K \overline{u} \frac{\partial \overline{\theta}}{\partial z} + v\theta \frac{\partial \overline{u}}{\partial z} \right) \\ &- \overline{uw} \frac{\partial \overline{\theta}}{\partial z} - \overline{\theta w} \frac{\partial \overline{u}}{\partial z} - \frac{b}{3\lambda_2} \overline{u\theta}, \end{aligned} \quad (10.25)$$

$$\frac{D\overline{v\theta}}{Dt} = \text{-----} \quad (10.26)$$

$$\frac{D\overline{w\theta}}{Dt} = \text{-----} \quad (10.27)$$

$$\frac{D\overline{\theta^2}}{Dt} = \frac{\partial}{\partial z} (b\lambda_2 \frac{\partial \overline{\theta^2}}{\partial z} + K \frac{\partial \overline{\theta^2}}{\partial z}) - 2 \overline{w\theta} \frac{\partial \overline{\theta}}{\partial z} - 2 \frac{b}{\Lambda_2} \overline{\theta^2}. \quad (10.28)$$

Mellor and Yamada (1974) proposed a hierarchy of systems, using an anisotropy parameter. The anisotropy factors, a_{ij} and c_i are defined by

$$\left\{ \begin{array}{l} \overline{u_i u_j} = \left(\frac{\delta_{ij}}{3} + a_{ij} \right) b^2, \\ a_{ij} = 0 \\ \overline{u_i \theta} = c_i b \overline{\theta^2}, \end{array} \right. \quad (10.29)$$

$$\quad (10.30)$$

where for the isotropic turbulence, $a_{ij} = c_i = 0$. Let us also consider the characteristic flow speed U and Length L . In the expression

$$\frac{Db^2}{Dt} = \frac{\partial b^2}{\partial t} + u_k \frac{\partial b^2}{\partial x_k},$$

we assume that the second term has an order of magnitude $\frac{Ub^2}{L}$. The Level 4 model is a system in which most of the terms in the equations of (10-18)-(10-28) are retained, and therefore, most complicated. The Level 3 model is derived by neglecting the terms of $\mathcal{O}(a^2)$ and $\mathcal{O}(c^2)$, where it is assumed that $a_{ij} = \frac{U}{L} \frac{b^2}{\epsilon}$ and the advection and diffusion terms become $\mathcal{O}(a)$, ϵ being the dissipation. In this model, therefore,

$$\frac{D\overline{uv}}{Dt} = \frac{D\overline{uw}}{Dt} = \frac{D\overline{u\theta}}{Dt} = \dots = 0,$$

and equations (10.22), (10.23), (10.24), (10.25), (10.26), (10.27) become the algebraic equations. However, two equations remain the differential equations with time, i.e.,

$$\frac{Db^2}{Dt} = \text{-----} ,$$

$$\frac{D\overline{\theta^2}}{Dt} = \text{-----} .$$

The Level 2 model is derived by neglecting the terms of $\mathcal{O}(a^2)$ and $\mathcal{O}(c^2)$, where it is assumed that $a^2\xi = \frac{U}{L} \frac{b^2}{s}$ and the advection and diffusion terms become $\mathcal{O}(a^2)$. In this model,

$$\frac{Db^2}{Dt} = \frac{D\overline{\theta^2}}{Dt} = 0 ,$$

and all equations are algebraic. The Level 1 model is derived by neglecting the terms of $\mathcal{O}(a)$, under the same assumption as for the Level 2 model.

Level 1 model is a simplest system which may correspond to the KEYPS approach.*

Here we summarize their Level 1, 2, 2.5 and 3 models. In practice, we found that Level 2 or 2.5 models are simple, stable computationally and useful.

Let us start with the first order equation, omitting the bar notation for the first order variables i.e.,

$$\frac{du}{dt} = \text{-----} + \frac{\partial}{\partial z} (-\overline{uw} + v \frac{\partial u}{\partial z}) , \tag{10.31}$$

$$\frac{dv}{dt} = \text{-----} + \frac{\partial}{\partial z} (-\overline{vw} + v \frac{\partial v}{\partial z}) , \tag{10.32}$$

$$\frac{d\theta}{dt} = \text{-----} + \frac{\partial}{\partial z} (-\overline{w\theta} + K \frac{\partial \theta}{\partial z}) . \tag{10.33}$$

$$b^2 = \overline{u^2} + \overline{v^2} + \overline{w^2} \tag{10.34}$$

\overline{uw} , \overline{vw} , and $\overline{w\theta}$ are obtained in the following way.

* H. Panofsky commented that some people prefer to call the scheme "PSYKO."



((Level 1 model))

$$\begin{pmatrix} -\overline{uw} \\ -\overline{vw} \end{pmatrix} = \ell^2 \left| \frac{\partial V}{\partial z} \right| \cdot S_M \cdot \begin{pmatrix} \frac{\partial u}{\partial z} \\ \frac{\partial v}{\partial z} \end{pmatrix}, \tag{10.35}$$

$$-\overline{w\theta} = \ell^2 \left| \frac{\partial V}{\partial z} \right| \cdot S_H \cdot \frac{\partial \theta}{\partial z}, \tag{10.36}$$

where

$$S_M = \begin{cases} G_1 \cdot (1-R_f)^{1/2} & \text{if } R_f \leq 1.0 \\ 0 & \text{if } R_f > 1.0 \end{cases} \quad (10.37)$$

$$S_H = \begin{cases} H_i \cdot (1-R_f)^{1/2} \\ [1 - 3 \times 0.53 \frac{R_f}{1-R_f}] & \text{if } R_f \leq 0.38 \\ 0 & \text{if } R_f > 0.38, \end{cases} \quad (10.38)$$

flux Richardson number,

$$R_f = \frac{\beta g \overline{w\theta}}{\overline{uw} \frac{\partial u}{\partial z} + \overline{vw} \frac{\partial v}{\partial z}} \quad (10.39)$$

((Level 2 Model))

(10.35) and (10.36) are the same, but

$$S_M = \begin{cases} G_2 \cdot (1-R_f)^{1/2} \cdot S_M^{3/2} & \text{if } R_f \leq 0.21 \\ 0 & \text{if } R_f > 0.21 \end{cases} \quad (10.40)$$

$$S_H = \begin{cases} H_2 \cdot (1-R_f)^{1/2} \cdot S_M^{1/2} \cdot \tilde{S}_H & \text{if } R_f \leq 0.21 \\ 0 & \text{if } R_f > 0.21 \end{cases} \quad (10.41)$$

where \tilde{S}_M and \tilde{S}_H are functions of R_f .

R_f is obtained explicitly as a solution of a quadratic equation of R_i (see Yamada, 1975). It is found, however, that the following approximations are quite accurate.

$$\begin{cases} R_f = R_i (1.485 - 2.35 R_i) & \text{for } R_i \geq 0 \\ R_f = 1.44 R_i & \text{for } R_i < 0 \end{cases} \quad (10.42)$$

((Level 2.5 model))

This portion is based on Yamada (1975).

$$\begin{pmatrix} -\overline{uW} \\ -\overline{vW} \end{pmatrix} = K_M \cdot \begin{pmatrix} \frac{\partial u}{\partial z} \\ \frac{\partial v}{\partial z} \end{pmatrix}, \quad (10.43)$$

$$-\overline{w\theta} = K_H \frac{\partial \theta}{\partial z}, \quad (10.44)$$

where

$$\begin{aligned} K_M &= A_1 \ell [(1-3c)b^5 + 3b^2 \mathcal{G}_f + 3A_2 \ell^2 x \\ &\times [(B_2 \ell - 3A_2)(b^3 + 3\mathcal{G}_f) - 3(4A_1 + B_2) \cdot c \cdot b^3] \beta g \frac{\partial \theta}{\partial z}] \\ &\div (b^4 + 6A_1^2 \ell^2 b^2 \left| \frac{\partial W}{\partial z} \right|^2 + 3\ell^2 A_1 A_2 \beta g \frac{\partial \theta}{\partial z} x \\ &\times \left\{ 6A_1 \ell^2 (B_1 - 3A_2) \left| \frac{\partial W}{\partial z} \right|^2 + \left(7 + \frac{B_2}{A_1} \right) b^2 \right. \\ &\left. + 9A_2 \ell^2 (4A_1 + B_2) \beta g \frac{\partial \theta}{\partial z} \right\}], \end{aligned} \quad (10.45)$$

$$\begin{aligned} K_H &= A_2 \cdot \ell [(b^3 + 3\mathcal{G}_f) - 6A_1 \cdot \ell \cdot K_H \left| \frac{\partial W}{\partial z} \right|^2] \\ &\div [b^2 + 3A_2 \ell^2 (4A_1 + B_2) \beta g \frac{\partial \theta}{\partial z}] \end{aligned} \quad (10.46)$$

$$\mathcal{G}_f = \frac{4}{3} A_1 \cdot \ell \frac{\partial}{\partial z} \left[\lambda_1 b \frac{\partial b^2}{\partial z} \right], \quad (10.47)$$

$$\lambda_1 = 0.27 \cdot \ell, \quad (10.48)$$

$$(A_1, A_2, B_1, B_2) = (0.78, 0.79, 15.0, 8.0) \quad (10.49)$$

β is the thermal expansion coefficient.

The turbulence intensity, b^2 , is obtained from the prognostic equation, i.e.,

$$\frac{d}{dt} \left(\frac{b^2}{2} \right) = \frac{\partial}{\partial z} \left[\frac{5}{3} \lambda_1 b \frac{\partial}{\partial z} \left(\frac{b^2}{2} \right) \right] - \overline{uw} \frac{\partial u}{\partial z} - \overline{vw} \frac{\partial v}{\partial z} + \beta g \overline{w\theta} - \frac{b^3}{\mathcal{L}_1} \quad (10.50)$$

This is solved under the boundary condition that $b^2 = B_1^{2/3} u_*^2$ at $z=0$.

((Level 3 model))

$$\begin{pmatrix} -\overline{uw} \\ -\overline{vw} \end{pmatrix} = K_M \begin{pmatrix} \frac{\partial u}{\partial z} \\ \frac{\partial v}{\partial z} \end{pmatrix}, \quad (10.51)$$

$$-\overline{w\theta} = K_H \frac{\partial \theta}{\partial z} - M_H \cdot b \cdot \overline{\theta^2}, \quad (10.52)$$

where K_M , K_H , and M_H are functions of $\left| \frac{\partial W}{\partial z} \right|$, $\frac{\partial \theta}{\partial z}$, b , $\overline{\theta^2}$ and ℓ .

Equation for b^2 is the same as (10.50). In addition, we have

$$\frac{d}{dt} \left(\frac{\overline{\theta^2}}{2} \right) = \frac{\partial}{\partial z} \left[b \lambda_3 \frac{\partial}{\partial z} \left(\frac{\overline{\theta^2}}{2} \right) \right] - \overline{w\theta} \frac{\partial \theta}{\partial z} - b \frac{\overline{\theta^2}}{\mathcal{L}_2} \quad (10.53)$$

((Level 4 model))

Omitted.

In all models, the length scale ℓ is given tentatively by an empirical formula similar to the one by Blackadar, (1962),

$$\ell = \frac{kz}{1 + \frac{kz}{\ell_0}}, \quad \ell_0 = \frac{\int_0^\infty bz \rho dz}{\int_0^\infty b \rho dz} \quad (10.54)$$

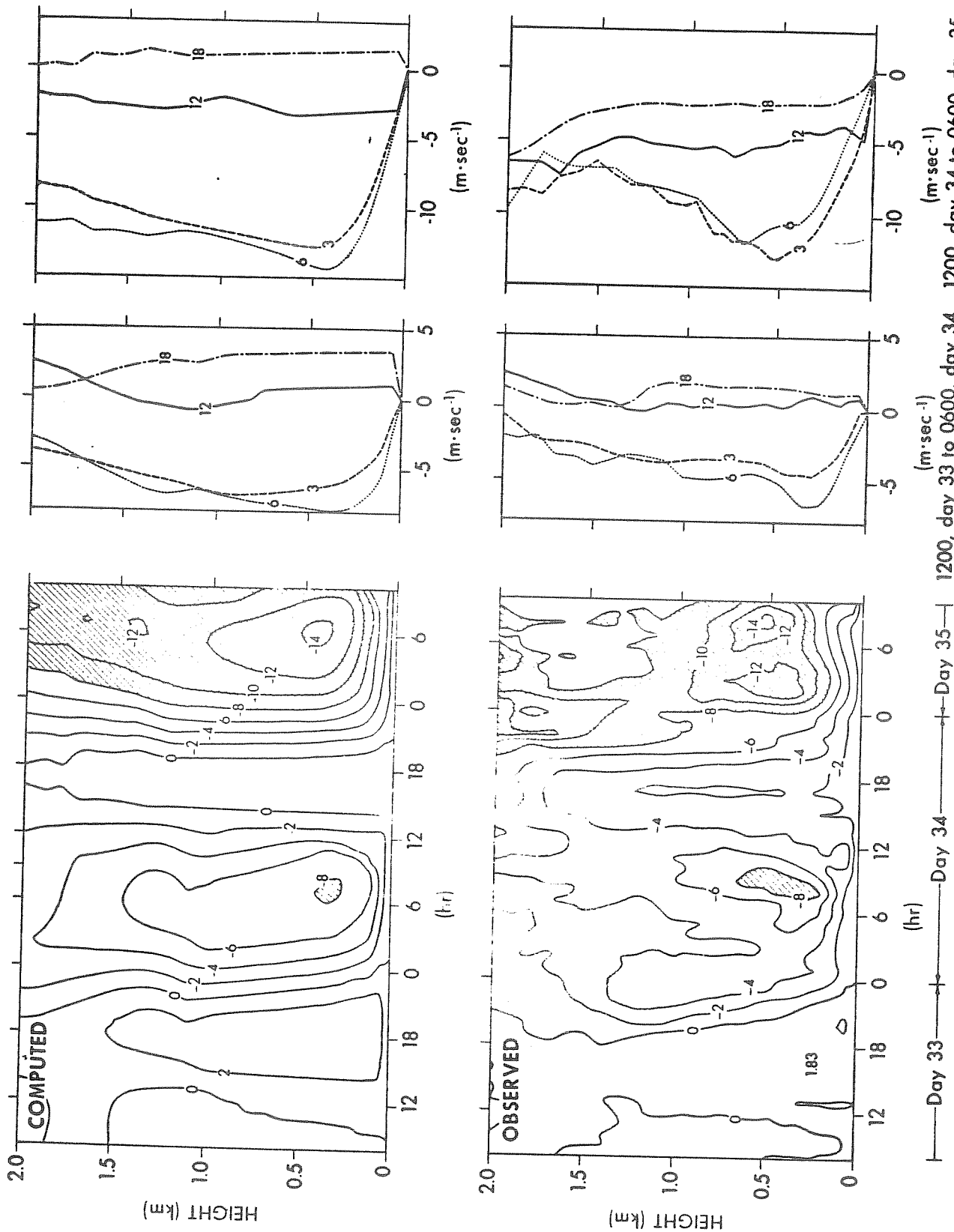


Fig. 10.3: (After Yamada and Mellor, 1975)

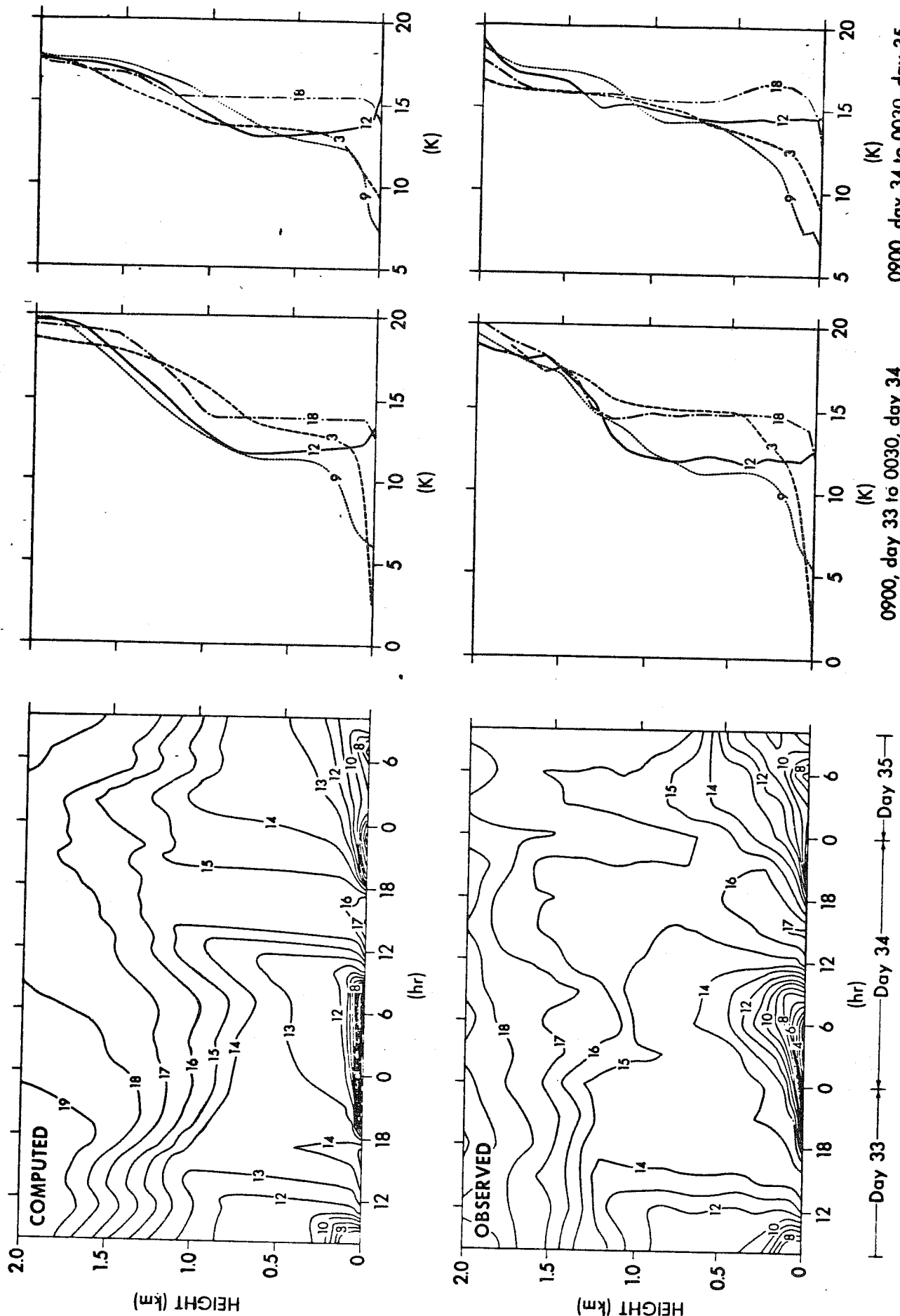


Fig. 10.4: (After Yamada and Mellor, 1975)

It was shown that the calculated mean winds and temperature fields are less dependent on the choice of λ .

Level 3 model has been used by Mellor and Yamada (1974) and Yamada and Mellor (1975). The hierarchy of the model used by the well-known numerical study of Deardorff (1973) corresponds to the level 4 model. Wyngaard et al. (1974) used a model equivalent to level 4 model. This model can approximate the counter-gradient transport, and give a sharp top of the PBL. On the other hand, further simplified Level 2 and 2.5 models do not allow the counter-gradient heat flux. It was shown that in Level 2 model, the PBL depth is shallower by about 100 meters than in the Level 3 or 4 models. However, the Level 2.5 model gives much closer solutions. Lewellen and Teske (1973) used a model similar to the level 2.5. The "eddy coefficient method based on subgrid turbulence kinetic energy equation" advocated by Deardorff is Level 2.5 model. In other words, Level 1, 2, 2.5, and 3 models are the so-called eddy viscosity scheme for momentum and Level 4 model is not in this category, while Level 1, 2, and 2.5 models are the eddy viscosity scheme for heat, and Level 3 and 4 models are not. The downward heat flux is a manifestation of strong "entrainment" at the top of PBL which leads to the deepening of the PBL depth with a sharp interface between the PBL and the free atmosphere. However, the down-gradient heat flux schemes can also have the deepening of the PBL, though the sharpness of the interface is reduced to the extent of the model's hierarchy. The process is called the "encroachment" (Carson and Smith, 1974).

Figure 10.3 and 10.4 are the results of the simulation of the Wangara data with the Level 3 model (Yamada and Mellor, 1975). Figure 10.3 is

the diurnal variation of the v-component, (see the nocturnal jet at 300 meters) and figure 10.4 is that of the virtual potential temperature.

(ii) The depth of the mixed layer

The theory of the mixed layer was developed for the atmosphere, ocean and the water in laboratory experiments. For the atmosphere, the concept and techniques were advanced by Ball (1960), Lilly (1968), Lavoie (1968), Deardorff et al. (1969), Betts (1972, 1973), Deardorff (1972, 1973, 1974), Zilitinkevitch (1972, 1975), Tennekes (1973), Carson (1973), Stull (1973), Smith and Carson (1974), Randall and Arakawa (1975). For the ocean and the water in tanks, the problem was pursued by Kraus and Turner (1967), Kato and Phillips (1969), Denman and Miyake (1974), Pollard et al. (1973), Gill and Turner (1975). It is interesting to note that for the atmospheric mixed layer, the "Jump Model" is treated in which the virtual potential temperature $\Delta\theta_v$ has a sharp increase at the top of the layer, whereas for the ocean model this jump is not emphasized.

In the observations, $\Delta\theta_v$ is sometimes clearly noticeable, particularly when the boundary layer is expanding and entrainment at the top of the layer is active. Figure 10.5 is the diurnal variation of the boundary layer height ($h(t)$ in this figure) over land. Between 6 and 14 hours the entrainment is strong. After 18 hours, a new boundary layer is formed, but the cause is the cooling at the ground surface.

We will discuss the derivation of the boundary layer height, Z_B . The first relation is the definition of the time change of Z_B , i.e.,

$$\frac{dz_B}{dt} = w + w_E, \quad (10.55)$$

where w is the prevailing large scale vertical velocity at the top of the

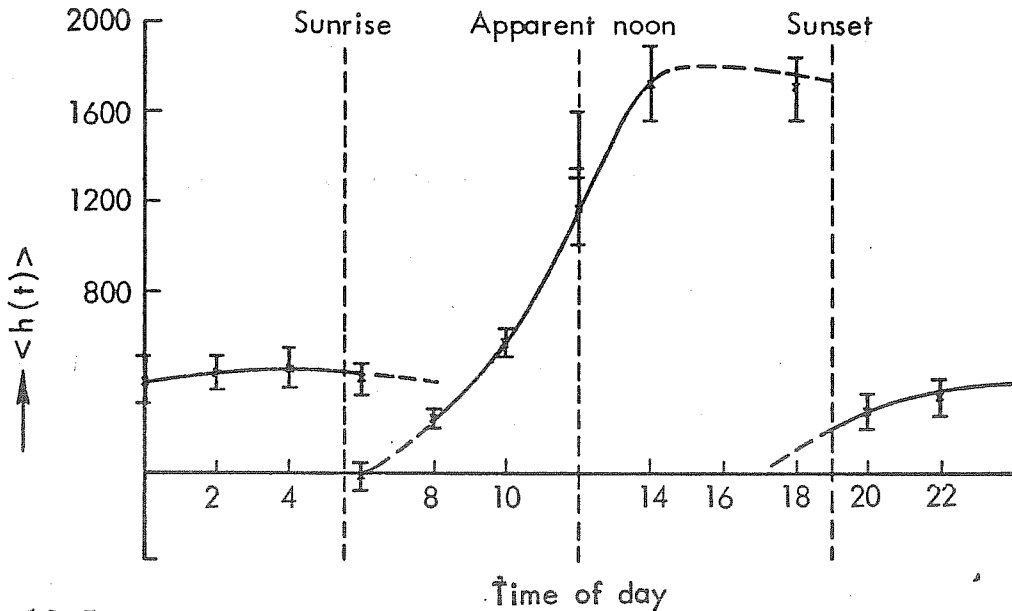


Fig. 10.5: The mean boundary-layer thickness, $\langle h(t) \rangle$, deduced for the O'Neill data and plotted with standard errors as functions of time of day, t , in Mean Solar Time. (Carson, 1973).

PBL, and W_E is the entrainment (including "encroachment"). The second equation is for W_E . From the continuity relation at the jump of potential temperature, it follows that

$$\begin{aligned}
 W_E &= - \frac{(\overline{w\theta})_B}{\Delta\theta} \\
 &= - \frac{(F_\theta)_B}{\Delta\theta}, \tag{10.56}
 \end{aligned}$$

if $\Delta\theta \neq 0$. $(\quad)_B$ is the value at $Z=Z_B$. When $\Delta\theta \rightarrow 0$, W_E is given by

$$W_E = \frac{(F_\theta)_s - (F_\theta)_B}{Z_B \left(\frac{\partial\theta}{\partial Z} \right)_{B+}} \tag{10.57}$$

where $\left(\frac{\partial\theta}{\partial Z} \right)_{B+} \neq 0$ and $Z_B \neq 0$, $(\quad)_{B+}$ is the value just above $Z=Z_B$.

After sunset, the entrainment is not governed by the thermal turbulence transfer; in this case (Deardorff, 1971),

$$W_E = 0.025 \rho u_* \left(1 - \frac{Z_B f}{0.35 u_*} \right) \quad (10.58)$$

As a formula which is applicable for a wide range of conditions, Deardorff (1975) suggested

$$W_E = \frac{1.8 (\overline{w\theta})_S \left[1 - 1.1 \frac{u_*^3}{w_*^3} \left(1 - 3 \frac{Z_B f}{u_*} \right) \right]}{\left[Z_B \left(\frac{\partial \theta}{\partial z} \right)_{B+} + \frac{g \cdot w_*^2}{\theta_0 Z_B} \left(1 + 0.8 \frac{u_*^2}{w_*^2} \right) \right]} \quad (10.59)$$

where

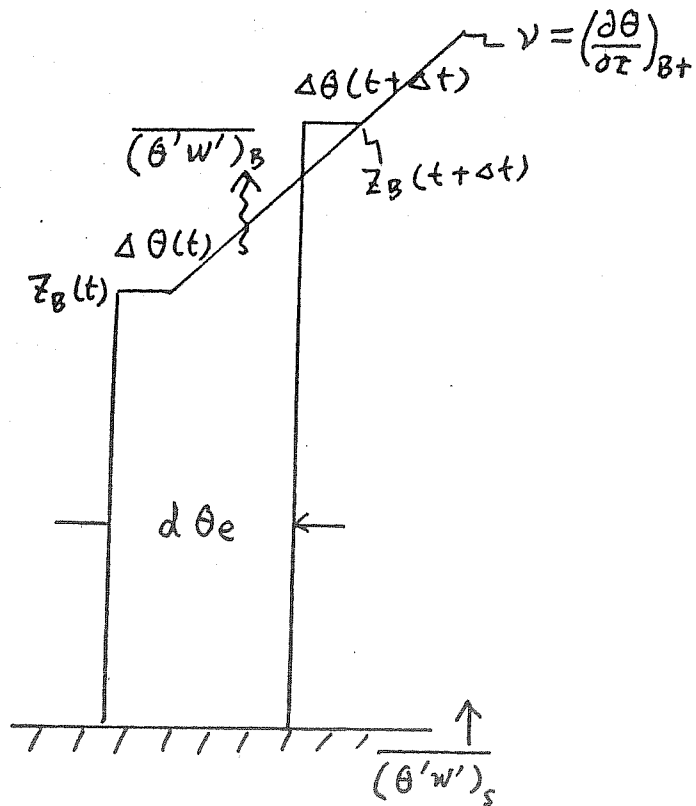
$$w_* = \left[\frac{g}{\theta_0} (\overline{w\theta})_S Z_B \right]^{1/3} \quad (10.60)$$

In order to close this system, another equation is needed; that is, the energy conservation equation. In figure 10.6, one may derive the equation as

$$\begin{aligned} & (\overline{\theta w})_S - (\overline{\theta w})_B \\ &= \frac{d}{dt} \left[\frac{1}{2} v Z_B^2 - Z_B \Delta \theta \right], \end{aligned} \quad (10.61)$$

where $v = \left(\frac{\partial \theta}{\partial z} \right)_{B+}$. Combining (10.55), (10.56), and (10.60), the equation for $\Delta \theta$ is obtained as

$$\begin{aligned} \frac{d\Delta \theta}{dt} &= -v \frac{(\overline{\theta w})_B}{\Delta \theta} + \frac{(\overline{\theta w})_B - (\overline{\theta w})_S}{Z_B} \\ &+ \left(v - \frac{\Delta \theta}{Z_B} \right) w. \end{aligned} \quad (10.62)$$



$$\begin{cases} d\theta_e + d(\Delta\theta) = \gamma \cdot dz_B \\ \overline{(\theta w)}_s - \overline{(\theta w)}_B = \frac{d}{dt} \int z_B d\theta_e \end{cases}$$

Fig. 10.6

For the case that $\Delta\theta = 0$ or $Z_B = 0$, another consideration is needed. Thus the equations (10.55), (10.56), (10.62) make a complete set of equations, including the condition that Z_B changes discontinuously, for example, after sunset.

For the atmosphere in which water vapor is included, the situation is very complicated and some modifications are needed.

First of all, the moist static energy or the potential energy, is used. $\Delta\theta$ is positive in the tropical region, whereas Δh is negative due to the effect of water vapor. Water vapor transfer is the dominant process rather than sensible heat transfer in the tropics. Secondly, stratus clouds could be formed inside the boundary layer. In this case, it is necessary requirement to consider differential radiational cooling for the entrainment (Randall and Arakawa, 1974). In addition, subsidence as a compensation for the cloud mass flux has to be taken into account.

Randall and Arakawa proposed the equations for the PBL depth,

$$\delta p = p_s - p_B \text{ as,}$$

$$\frac{\partial \delta p}{\partial t} + \nabla(\delta p V) = \cancel{g \rho w_E} + g(\rho w_E - M_B), \quad (10.63)$$

where M_B is the cloud mass flux, p_s and p_B are the pressures at the surface and the top of PBL. The entrainment is given by

$$\rho g w_E = \frac{-(\rho \overline{wh})_B + (Q_R)_{B+} - (Q_R)_B}{\Delta h} \quad (10.64)$$

where Δh is the jump of moist static energy ($h = C_p T + gz + Lg$) and Q_R is the radiational effect in the case of a cloud-topped boundary layer.

For the case that $\Delta h = 0$, a different formula is used. The equation of Δh is given by

$$\begin{aligned} \frac{\partial \Delta h}{\partial t} = & - \Delta(\mathbf{W} \cdot \nabla h_{B+}) - \mathbf{W} \cdot \nabla(\Delta h) \\ & + g \rho w_E \left[\left(\frac{\partial h}{\partial p} \right)_B - \left(\frac{\partial h}{\partial p} \right)_{B+} \right] \\ & + g \left[- \left(\frac{\partial \rho \overline{wh}}{\partial p} \right)_B + (Q_R)_{B+} - (Q_R)_B \right] \end{aligned} \quad (10.65)$$

Carson and Smith (1974) treated the jumps for momenta as well, i.e.,

Δu and Δv

Carson and Smith (1974) treated the jumps for momenta as well, i.e., Δh and Δv .

(iii) Constant-flux layer

In principle, the multi-layer models can be applied in the entire turbulent PBL if a considerably higher grid resolution is provided in the surface layer. In the prediction model of the general circulation, however, it seems uneconomical to use such finite resolution. For this reason, a further parameterization is used for the constant flux layer. The scheme is known as the "Monin-Obukhov" version (Lumley and Panofsky, 1964, and Monin and Yaglom, 1966)

$$\tau = \rho |W_*| W_* \quad , \quad (10.66)$$

$$(F_\theta)_s = -\rho \cdot C_p |W_*| \theta_* \quad , \quad (10.67)$$

$$(F_q)_{\text{pot}} = -\rho |W_*| q_* \quad , \quad (10.68)$$

$$(F_q)_o = D_w (F_q)_{\text{pot}} \quad (10.69)$$

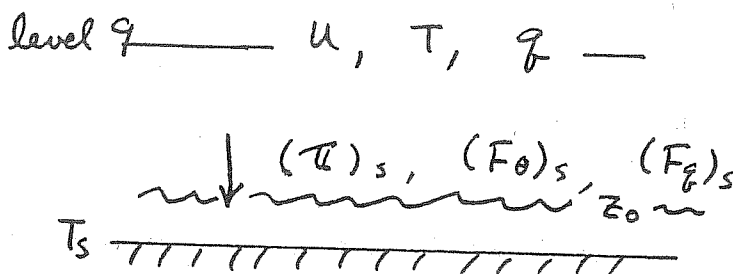


Fig. 10.7

where τ is the wind stress, $(F_\theta)_s$ and $(F_q)_s$ are the sensible and latent heat fluxes at the surface or level z_0 , $(F_q)_{pot}$ is the potential evaporation, W_* is the friction velocity, D_w is the availability of moisture. Then we have

$$\frac{k_0 z}{W_*} \frac{\partial W}{\partial z} = \varphi_m, \quad (10.70)$$

$$\frac{k_0 z}{\theta_*} \frac{\partial \theta}{\partial z} = \varphi_h, \quad (10.71)$$

$$\frac{k_0 z}{q_*} \frac{\partial q}{\partial z} = \varphi_q. \quad (10.72)$$

Therefore

$$W(h) - W(z_0) = W_* [f_m(h/L) - f_m(z_0/L)] \quad (10.73)$$

$$\theta(h) - \theta(z_0) = \theta_* [f_h(h/L) - f_h(z_0/L)], \quad (10.74)$$

$$q(h) - q_{sat}(T_s) = q_* [f_q(h/L) - f_q(z_0/L)]. \quad (10.75)$$

The functional forms of f_m and f_h are given by Businger et al. (1971)

$$f_m(\zeta) = \frac{1}{k_0} \int \frac{\varphi_m(\zeta)}{\zeta} d\zeta \quad (10.76)$$

$$f_m(\zeta) = \begin{cases} \frac{1}{k_0} \int \frac{1 + 4.7\zeta}{\zeta} d\zeta & \text{for stable strat } (\zeta \geq 0) \end{cases} \quad (10.77)$$

$$\begin{cases} \frac{1}{k_0} \int \frac{d\zeta}{\zeta (1 + 9(-\zeta))^{1/3}} & \text{for unstable strat. } (\zeta < 0) \end{cases} \quad (10.78)$$

$$f_h(\zeta) = \frac{1}{k_0} \int \frac{\varphi_h(\zeta)}{\zeta} d\zeta \quad (10.79)$$

$$f_h(z) = f_q(z)$$

$$= \begin{cases} \frac{1}{k_0} \int \frac{0.74 + 4.7 \zeta}{\zeta} d\zeta & \text{for stable strat. } (\zeta \geq 0) \\ \frac{1}{k_0} \int \frac{0.74}{\zeta(1 + 51(-\zeta))^{1/3}} d\zeta & \text{for unstabl strat. } (\zeta < 0) \end{cases}$$

(10.80)

(10.81)

(10.77) and (10.80) are integrated and written as

$$f_m(\zeta) - f_m(\zeta_0)$$

$$= \frac{1}{k_0} [\ln \frac{\zeta}{\zeta_0} + 4.7 (\zeta - \zeta_0)], \text{ for } \zeta \geq 0$$

(10.82)

$$f_h(\zeta) - f_h(\zeta_0)$$

$$= \frac{1}{k_0} [0.74 \ln \frac{\zeta}{\zeta_0} + 4.7 (\zeta - \zeta_0)], \text{ for } \zeta \geq 0$$

(10.83)

These formula are valid for the entire region of stable stratification (not only for the near neutral case).

Monin's length L is defined by

$$L = \frac{- \frac{\rho}{k_0 g} |W_*|^3}{\frac{g}{C_p \theta_0} [(F_\theta)_s + 0.61 C_p \theta_0 (F_q)_s]}$$

(10.84)

The roughness height z_0 is given by

$$z_0 = \begin{cases} 16.82 \text{ cm over land for the annual mean} \\ 0.032 \frac{W_*^2}{g} \text{ over sea} \end{cases}$$

(10.85)

This type of model was tested previously by Delsol et al. (1971).

One is the conventional neutral aerodynamic method described in section 8 (it is called Experiment A), in which the

drag coefficient C_D is 2×10^{-3} everywhere. The second is the same model as the first, but $C_D = 4.3 \times 10^{-3}$ over land and $C_D = 1.1 \times 10^{-3}$ over sea (Experiment B). The third is the model in which the Monin Obukhov process is included (Experiment C). The result of effective C_D in Experiment C is shown in figure 10.8. The sensible heat flux $H_0 = -(F_\theta)_s$ and the wind stress $\tau_0 (=|\tau|_s)$ are shown as a function of forecast time in figure 10.9. The heat flux averaged over the Northern Hemisphere is increased in Experiment C compared with the other experiments. On the other hand, the wind stress is less in Experiment C over the ocean than in Experiment A. This may suggest that this type of drag is better for forecasting in view of the sensitivity study described earlier.

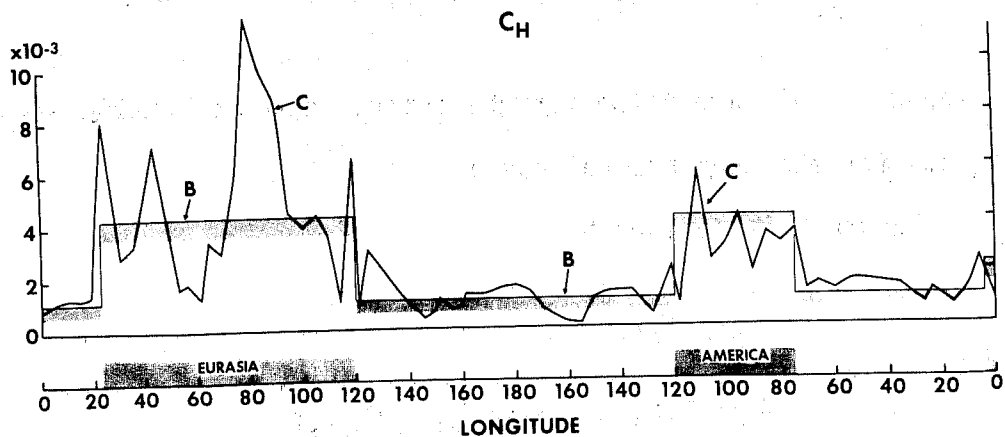


Fig. 10.8: The zonal profiles of the 1,000 mb height (upper), the 24-hourly rate of precipitation (middle) in Experiments A, B and C. The lower figure is the effective drag coefficient C_D for heat flux in Experiment C and the usual drag coefficient C_D in Experiment B. All profiles are for the 6th day. (Delsol, Miyakoda and Clarke, 1971).

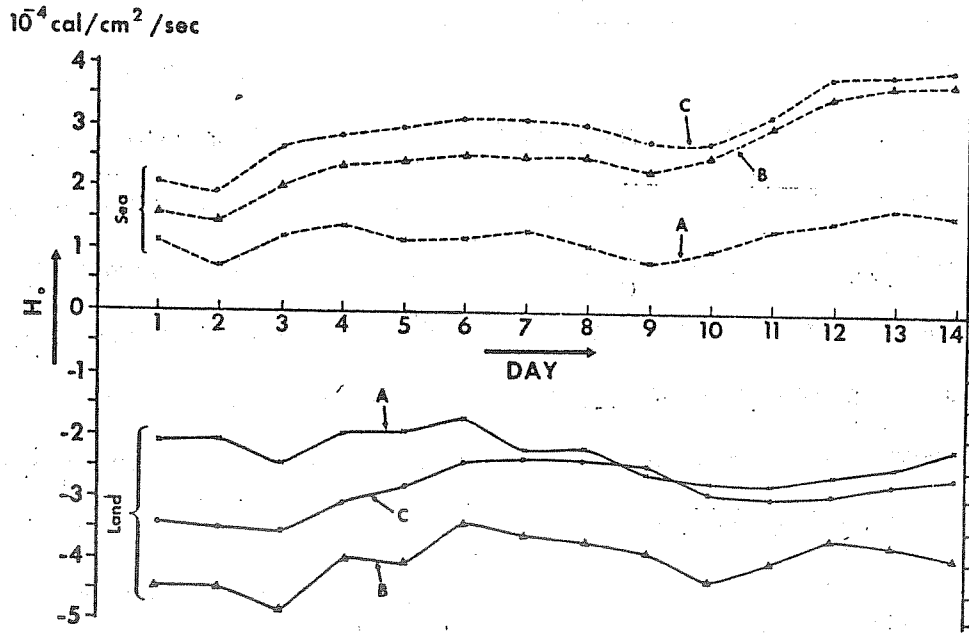


Figure 6. Time variation of the hemispheric average of the heat flux H_o over land and sea in Experiments A, B and C.

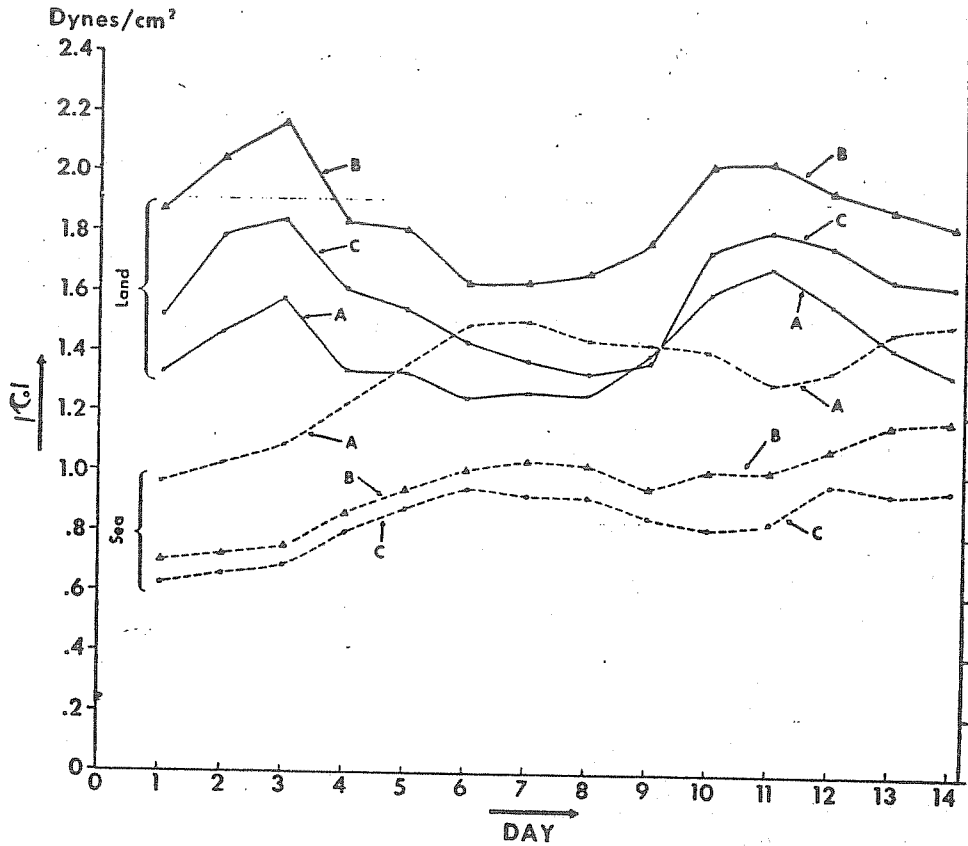


Fig. 10.9: Time variation of the hemispheric average of the stress $|\tau_o|$ over land and sea in Experiment A, B and C. (Delsol, Miyakoda and Clarke, 1971).



11. Refined parameterization of cumulus convection

The essential difference between the transfer by cumulus convection and the PBL turbulence transfer is that condensation heat is involved in the former. The released heat creates the local buoyancy which accelerates the vertical velocity inside cumulus clouds. This intensified current transports the sensible heat, water vapor and momentum upwards through the clouds. The clouds are so-to-speak chimneys, though they have porous side-walls, and moisture and heat are collected from the environment through the side-walls. The heat lifted to the top of the chimneys is emitted there. Thus the enthalpy is increase in the upper levels, and decreased in the lower levels.

These cumulus cloud processes prevail particularly in the tropics, though the activity is also important even in the extratropics. Cumulus convection is expected to occur when the conditional gravitational instability exists. Figure 11.1 shows a typical vertical distribution in the tropics of the static energy ($gz + C_p T$), the latent heat (Lq), and the moist static energy ($gz + C_p T + Lq$). The "hot towers" penetrate deep into the stable layer in

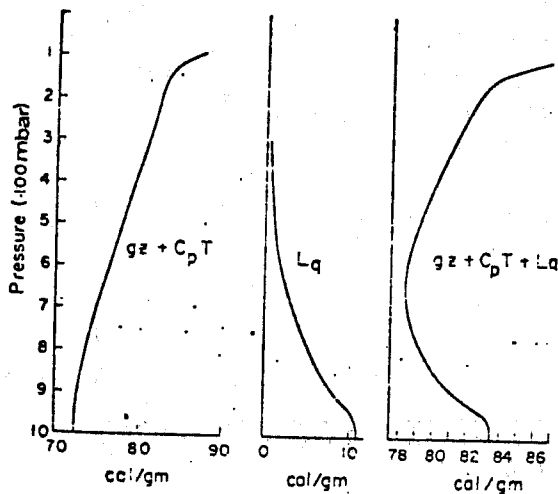


Fig. 11.1a Vertical profiles of $gz + c_p T$, of Lq , and of $gz + c_p T + Lq$ for the mean tropical atmosphere over the western parts of the tropical oceans in summer.

$S = C_p T + gz$: static energy (or enthalpy)

$h = S + L q$: moist static energy

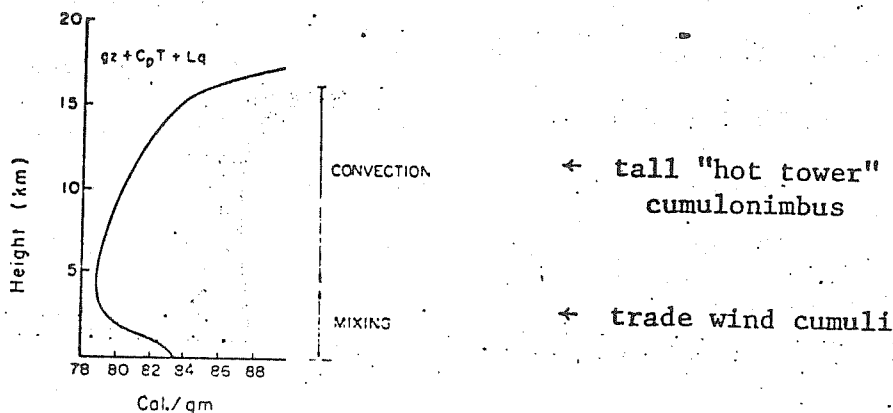


Fig. 11.1b: Vertical distribution of total energy in the mean tropical atmosphere and model illustrating mechanisms of vertical energy transport: trade wind cumulus clouds up to the level where the total energy reaches its minimum, and "hot tower" cumulonimbus convection to the high troposphere (Riehl and Malkus, 1958).

forms of cumulonimbus (Riehl and Malkus, 1958).

How the internal energy is distributed in the vertical is one of the major problems in the cumulus convection. It is certain that the water vapor supply from the bottom of the chimneys is crucial. The low-level convergence is controlled not only by the convergence in the PBL flow but also by the sucking from the processes inside the cloud.

The vertical distribution of the dumped heat and the horizontal position of the heating relative to the tropical wave phase are the important factors to determine the dynamic characteristics of tropical waves. The instability study along this line was made theoretically by Yamasaki (1968, 1969), Lindzen (1970, 1971, 1972), Ooyama (1969), Hayashi (1970, 1971, 1974), Holton (1971, 1972), Murakami (1972), and Chang and Piwowar (1974). The consensus appears to be that the condensation heat is important for the intensification of tropical waves, but controversy still exists, for example, as to whether or not the wavelength of the mixed Rossby-gravity wave (Yanai-Maruyama wave) is primarily determined by the mid-latitude forcing (Mak, 1969, Lamb, 1975).

In this respect, the numerical general circulation model provided the seemingly reasonable solutions for tropical waves with the moist convective adjustment (Hayashi, 1974, and Tsay, 1974), though a theoretical explanation is still needed. In section 8, the results of rain simulation mainly with the moist convective adjustment were described. The agreement of the calculated rainfall with the observation is surprisingly good, so far as the time averaged tropical rain is concerned. The merit of the method is its simplicity.

The shortcomings of the method are: that a high content of moisture results in the model atmosphere and the "shock" associated with the process is rather strong. We showed the NMC rain forecasts in section 2, which is based on the large-scale condensation and the moist convective adjustment. In summer, the forecasts become very poor, particularly in the mountainous regions. It is not clear what causes this difficulty in the forecasts. Perhaps the predictability of summer rainfall is intrinsically limited. Or perhaps the parameterization scheme is inadequate for this type of rain.

Concerning cumulus convection parameterization, a number of ideas have been proposed. At least, two methods are noted, i.e., Kuo's method and Arakawa's method. Compared with the moist convective adjustment, they are relatively complicated and sophisticated.

(i) Kuo's method

This method was first proposed by Kuo (1965), and then modified by Rosenthal (1969, 1970), Sundquist (1970), Krishnamurti and Moxim (1971) and Krishnamurti and Kanamitsu (1973). Kuo has recently modified his own scheme (Kuo, 1974), though the part for deep cumulus convection is not very different from the original.

For the deep convection, the amounts and the vertical distribution of the latent heat and sensible heat are determined by the temperature difference between the cloud and the environment, where latent heat is supplied by the low-level convergence of moisture.

The rate of heating Q_c is given by

$$Q_c = a \frac{(\theta_c - \theta)}{\tau}, \quad (11.1)$$

where θ_c is the potential temperature in clouds, $\theta_c - \theta$ is, therefore, the buoyancy, a is the fraction of cloud, and τ is average life of deep cumulus convection. The fraction of cloud is determined by the formula as

$$a = \frac{\tau M_t (1 - b)}{M_c} \quad (11.2)$$

where M_t is the horizontal convergence of moisture ($1 - b$) is the fraction of moisture convergence that is condensed, and M_c is the amount of moisture required for saturation.

First take the net convergence of moisture into the vertical column of the air by the large-scale flow plus the evaporation from the ground

$$M_t = -\frac{1}{g} \int_0^{p_s} \nabla \cdot (W q) dp + \text{Evaporation} \quad (11.3)$$

This amount is then assumed to go into the making of convective clouds, increasing the temperature and moisture content of the cloud region. The rates of heating and moistening are assumed to be proportional to the difference of temperature and water vapor content between the cloud and the environmental atmosphere; they are,

$$M_{C1} = - \frac{1}{g} \int_{P_B}^{P_T} [q_s(T_c) - q] dp, \quad (11.4)$$

$$M_{C2} = - \frac{1}{g} \int_{P_B}^{P_T} \frac{C_p}{L} (T_c - T) dp. \quad (11.5)$$

M_{C1} and M_{C2} are, therefore, the amounts of moisture required to bring the environmental mixing ratio of water vapor q and temperature T to the moist adiabatic values q_c and T_c , respectively. $M_c = M_{C1} + M_{C2}$ is the amount of moisture required to form a cloud over the entire area.

$$\langle \quad \rangle = \frac{-1/g}{(P_B - P_T)} \int_{P_B}^{P_T} (\quad) dp.$$

Therefore

$$Q_c = \frac{g(1-b) \cdot L \cdot M_t \cdot (T_c - T) \left(\frac{p_0}{p} \right)^{R/C_p}}{C_p (P_B - P_T) \langle T_e - T + \frac{L}{C_p} q_s (T_s) - q \rangle}. \quad (11.6)$$

The formula of T_c is not shown here; the effect of entrainment on T_c can be included.

Merit: This scheme gives a clearer physical picture of the warming than the moist convective adjustment and CISK method. In particular, compared with CISK method, the vertical distributions of heating and moisture are specified. Compared with the convective adjustment, the "shocking" would be reduced.

In the 1974 version, the application condition of the parameterization is specified as

$$\left\{ \begin{array}{l} D_1 D_2 \cdot \Delta \theta_e > \text{constant} \end{array} \right. \quad (11.7)$$

$$\left\{ \begin{array}{l} -\tau_0 \cdot \omega_b > 3(p_s - p_c) \end{array} \right. \quad (11.8)$$

where D_1 , D_2 , and $\Delta\theta_e$ are shown in figure 11.3, w_b is the maximum low level p-velocity, $p_s - p_c$ is the lift needed for the surface air at level p_s to become saturated, and τ_0 is the duration period of the large-scale flow.

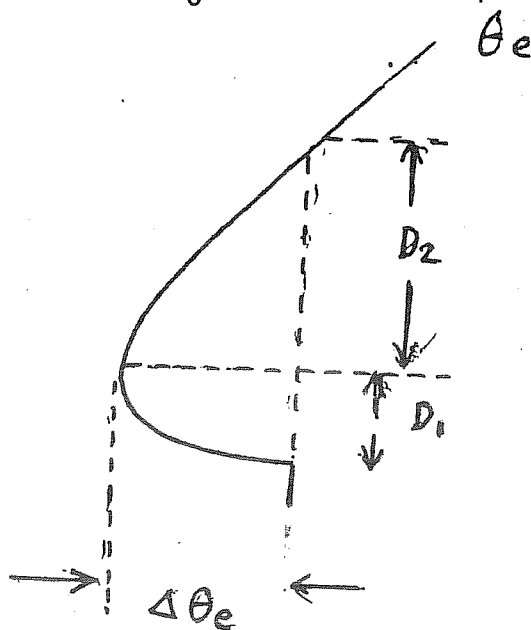


Fig. 11.3

(ii) The Arakawa's method

Perhaps this is the most sophisticated and elaborate scheme which has ever existed. The approach is considered to be the upper limit as a parameterization in many respects, i.e., the attempt in approaching realism, the elegance of the theory and the numerical complexity.

The basic kinematics in the cloud scale including entrainment and detrainment are straightforward and precise, and the general concept on the mutual action of the PBL and cumulus convection is included. This line of thought has a long tradition since Ooyama (1964, 1969), who applied these concepts to the numerical study of hurricane development. The kinematics was also developed by Ooyama (1971), Arakawa (1969, 1971), and Yanai (1971).

First version of the Arakawa method was proposed in 1969. (Arakawa, 1969). This method was used numerical general circulation models successfully by Gates et al. (1971), Somerville et al (1974), and Caselski (1974). In this version, however, the cloud mass flux was given rather heuristically. The theory was not quite sophisticated, and lacked generality, and was not complete.

In the 1974 version, this aspect has been totally improved. The theory has been closed by the concept of the cloud work function, A , (Arakawa function). The cloud mass flux can be derived from this assumption. The theory was presented by Arakawa and Schubert (1974), and the practical procedure was described by Chao, Lord and Arakawa (1975).

(a) The basic equations of s and q

We will outline the 1974 version model, omitting the detail. Let us start with the equations as

$$\frac{\partial \overline{ps}}{\partial t} + \text{-----} = \rho L(c - e) - \frac{\partial (\overline{\rho w})'s'}{\partial z}, \quad (11.9)$$

$$\frac{\partial \overline{pq}}{\partial t} + \text{-----} = -\rho(c - e) - \frac{\partial (\overline{\rho w})'q'}{\partial z}, \quad (11.10)$$

where c is the condensation, e is the evaporation, and s is the static energy. The correlation terms are expressed by

$$\begin{aligned} \overline{(\rho w)'s'} & \equiv M_c (S_c - \tilde{S}), \\ \overline{(\rho w)'q'} & \equiv M_c (q_c - \tilde{q}), \end{aligned} \quad (11.11)$$

where M_c is the cloud mass flux defined by

$$\begin{aligned} M_c &= \sum_i \rho w_i \sigma_i \\ &= \rho w_c \sigma \quad , \end{aligned} \tag{11.12}$$

w_i is the vertical flux inside the i^{th} cloud, σ_i is the fraction area of the i^{th} cloud w_e , s_c , and q_c are the vertical velocity, static energy and mixing ratio of water vapor for clouds, \tilde{s} and \tilde{q} are those for environment. Inserting (11.11) into (11.9) and (11.10) the basic equations are rewritten as

$$\frac{\partial \overline{p s}}{\partial t} + \text{-----} = \rho L(c - e) - \frac{\partial}{\partial z} [M_c (s_c - \tilde{s})], \tag{11.13}$$

$$\frac{\partial \overline{p q}}{\partial t} + \text{-----} = - \rho(c - e) - \frac{\partial}{\partial z} [M_c (q_c - \tilde{q})]. \tag{11.14}$$

The continuity equations for the cloud mass flux including the effects of entrainment and detrainment are written under the assumption of the steadiness,

$$E - D - \frac{\partial M_c}{\partial z} = 0 \quad , \tag{11.14}$$

$$E \tilde{s} - D s_c - \frac{\partial M_c s_c}{\partial z} + \rho L c = 0, \tag{11.15}$$

$$E \tilde{q} - D q_c - \frac{\partial M_c q_c}{\partial z} - \rho c = 0, \tag{11.16}$$

where E and D are the entrainment and detrainment.

Using (11.15) and (11.16) and eliminating the term including c, the basic equations (11.9) and (11.10) are transformed to

$$\frac{\partial \overline{p s}}{\partial t} + \text{-----} = - E s + D s_c - L e + \frac{\partial M_c \tilde{s}}{\partial z} \tag{11.17}$$

$$\frac{\partial \overline{pq}}{\partial t} + \text{-----} = - E \tilde{q} + D q_c + e + \frac{\partial M_c \tilde{q}}{\partial z} \quad (11.18)$$

Similarly, the equations of motion are written as

$$\frac{\partial \overline{pu}}{\partial t} + \text{-----} = - E \tilde{u} + D u_c + \frac{\partial M_c \tilde{u}}{\partial z} \quad (11.19)$$

$$\frac{\partial \overline{pv}}{\partial t} + \text{-----} = - E \tilde{v} + D v_c + \frac{\partial M_c \tilde{v}}{\partial z} \quad (11.20)$$

These four equations are the basic equations. However, using (11.14), we eliminate E, and

$$\frac{\partial \overline{ps}}{\partial t} + \text{-----} = D (S_c - \tilde{S}) - \rho L e + M_c \frac{\partial \tilde{S}}{\partial z} \quad (11.21)$$

$$\frac{\partial \overline{pg}}{\partial t} + \text{-----} = D (q_c - \tilde{q}) + \rho e + M_c \frac{\partial \tilde{q}}{\partial z} \quad (11.21)$$

The term of condensation, c, and the terms of eddy transfer are modified and the term c is not included any more. These equations were derived by Ooyama (1971) and Arakawa (1971). The next question is how M_c is derived, and what are s_c and q_c and e.

(b) The relations inside the clouds and the buoyancy for clouds

Assuming that the temperature at the cloud base is equal to that of the environment, we have, for the i-th cloud,

$$s_i - \bar{s} \approx \frac{1}{1+\gamma} (h_i - \bar{h}^*), \quad (11.22)$$

$$q_i - \bar{q}^* \approx \frac{\gamma}{1+\gamma} \frac{1}{L} (h_i - \bar{h}^*), \quad (11.23)$$

where

$$\gamma = \frac{L}{C_p} \left(\frac{\partial \bar{q}^*}{\partial T} \right)_p, \quad (11.24)$$

$$\bar{h}^* = \bar{s} + L \bar{q}^*,$$

q^* is the saturation moisture.

It is also assumed that the maximum height of cloud top is equal to the vanishing buoyancy level. This level is determined by using the virtual static energy S_v as

$$S_{vi} - \bar{S}_v = 0, \tag{11.25}$$

where S_{vi} is the value of the i^{th} cloud, and \bar{S}_v is approximately the value of environment and

$$S_v \equiv S + C_p T (0.608 q - \ell), \tag{11.26}$$

ℓ is the liquid water. Using (11.22), (11.23), (11.25), and (11.26), we have at the vanishing buoyancy level,

$$h_i - \hat{h}^* = 0, \tag{11.27}$$

where

$$\hat{h}^* = \bar{h}^* - \frac{(1+\gamma) \cdot L \cdot \epsilon}{1+\gamma \cdot \epsilon \cdot 0.608} [0.608 (\bar{q}^* - q) - \hat{\ell}], \tag{11.28}$$

$\hat{\ell} = \ell_i$ at this level

$$\epsilon = C_p T/L$$

(c) The criterion for the occurrence of cumulus convection

Figure 11.4 shows the general relation among various moist static energies. \bar{h}^* is the saturation value, \bar{h}_B is the value in the mixed layer,

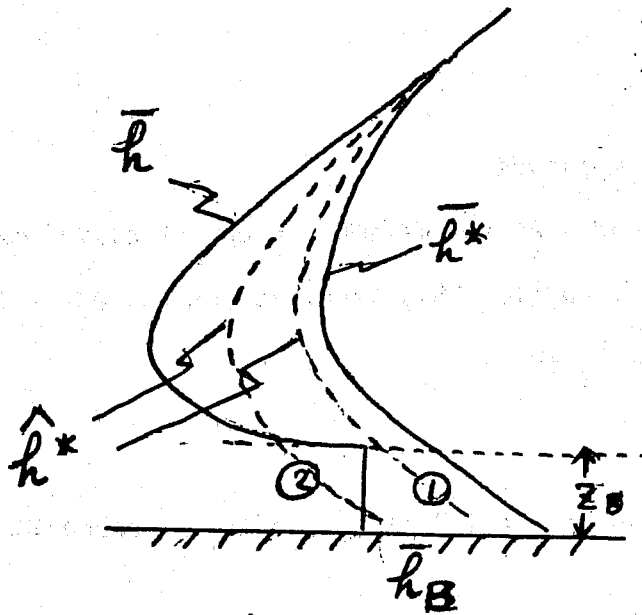


Fig.11.4

\hat{h}^* is the virtual moist static energy defined above, and z_B is the depth of PBL. The occurrence criterion for cumulus convection is given by

$$\bar{h}_B > \hat{h}^* \quad \text{at } z = z_B, \quad (11.29)$$

since the excess of \bar{h}_B over \hat{h}^* is the buoyancy force.

Note that the lifted condensation level was not used in this approach.

(d) Cloud spectrum

Arakawa and Schubert (1974) introduced the concept of the cloud spectrum, since there are varieties of clouds whose heights are different. In the theory, they used instead of the cloud heights, the rate of entrainment λ as the independent variable for the spectrum. Thus the total cloud mass flux is expressed by

$$\begin{aligned}
 M_c(z) &= \int m(z, \lambda) d\lambda \\
 &= \int m_B(\lambda) \cdot \eta(z, \lambda) d\lambda,
 \end{aligned}
 \tag{11.30}$$

where η is the factor indicating the cumulative effect of entrainment, and $m_B(\lambda)$ is the cloud mass flux at the cloud base for the spectrum λ , η is assumed to obey a simple entrainment relation such as

$$\frac{\partial \eta}{\partial z} = \lambda \eta.
 \tag{11.31}$$

As shown in figure 11.5, if there is no entrainment, i.e., $\lambda=0$, η has the perpendicular line reaching the maximum. On the other hand, if λ becomes large, i.e., the entrainment increased, η becomes large rapidly but it does not reach high level.

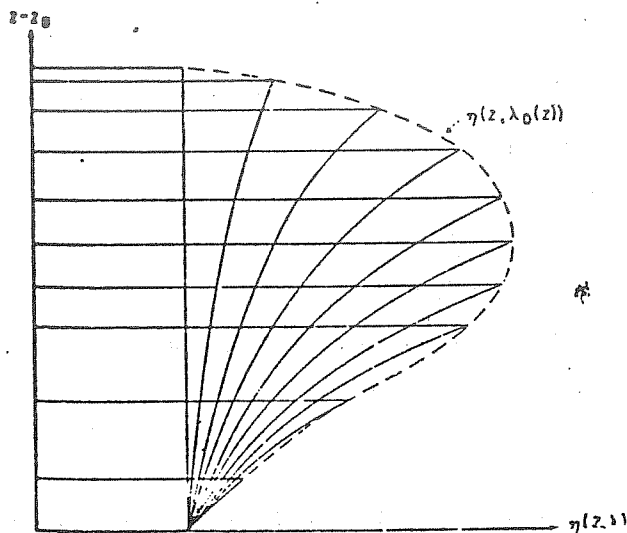


Fig. 11.5: Schematic profiles of the normalized mass flux $n(z, \lambda)$ for various λ . the envelope of the curves is $n[z, \lambda_D(z)]$. (Arakawa and Schubert, 1974).

In Arakawa's method, therefore, λ and the cloud top, i.e., the vanishing buoyancy level, $Z_D(\lambda)$, are calculated. From eq. (11.14), (11.15), and (11.16), we have

$$E - D - \frac{\partial M_C}{\partial z} = 0 \quad (11.32)$$

$$E \tilde{h} - D h_C - \frac{\partial M_C \cdot h_C}{\partial z} = 0. \quad (11.33)$$

For the individual cloud sub-ensemble, we have

$$E(z) = \int e(z, \lambda) \cdot m_B(\lambda) d\lambda, \quad (11.34)$$

$$D(z) = \int d(z, \lambda) \cdot m_B(\lambda) d\lambda. \quad (11.35)$$

Therefore, inserting these formulas in (11.32), (11.33), we have

$$e \tilde{h} - \frac{\partial \eta \cdot h_C}{\partial z} = 0 \quad (11.36)$$

$$e - \frac{\partial \eta}{\partial z} = 0, \quad (11.37)$$

where we are concerned about the layers below the detrainment level, so that $d=0$. From the two equations, one can derive

$$\frac{\partial}{\partial z} (\eta \cdot h_C) = \frac{\partial \eta}{\partial z} \tilde{h}, \quad (11.38)$$

where $\hat{h} \doteq \tilde{h}$. Integrating this equation under the boundary condition that $h_C = \bar{h}_B$ at $Z=Z_B$, we have

$$h_C(z, \lambda) = \frac{1}{\eta} \left[\bar{h}_B + \lambda \int_{Z_B}^z \eta(z', \lambda) \tilde{h}(z') dz' \right]. \quad (11.39)$$

The vanishing buoyancy level, Z_D , is obtained such that

$$h_C(z, \lambda) = \hat{h}^*(z). \quad (11.40)$$

In other words, λ and $Z_D(\lambda)$ are found by solving the equation (11.40) with the auxiliary equation (11.31) and (11.39).

An example of $h_c(z, \lambda)$ is shown in figure 11.6 The spectrum $m_B(\lambda)$ was obtained from observation by Ogura and Cho (1973), and Yanai et al. (1974), Cho and Ogura (1974) in figures 11.8, 11.7, and 11.9

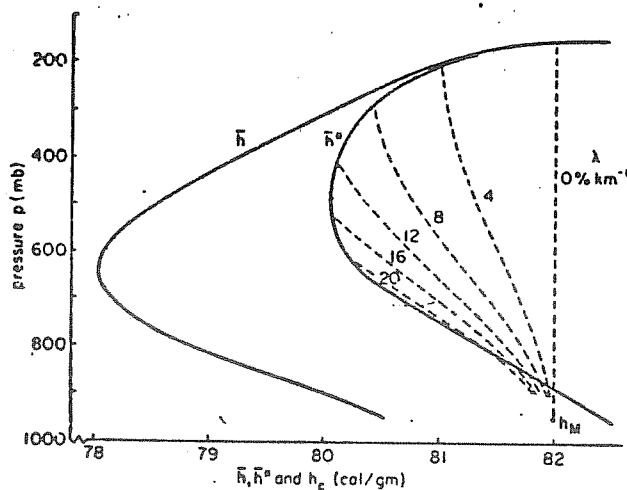


Fig. 11. Vertical profiles of $\bar{h}(p)$, $\bar{h}^*(p)$ and $h_c(p, \lambda)$; $h_c(p, \lambda)$ lines are dashed and labeled with the value of λ in percent per kilometer. Profiles of \bar{h} and \bar{h}^* were obtained from Jordan's (1958) "mean hurricane season" sounding. The top p_B of the mixed layer is assumed to be 950 mb; h_M is assumed to be 82 cal gm^{-1} .

Observations

Ogura and Cho (1973), Yanai et al. (1974)

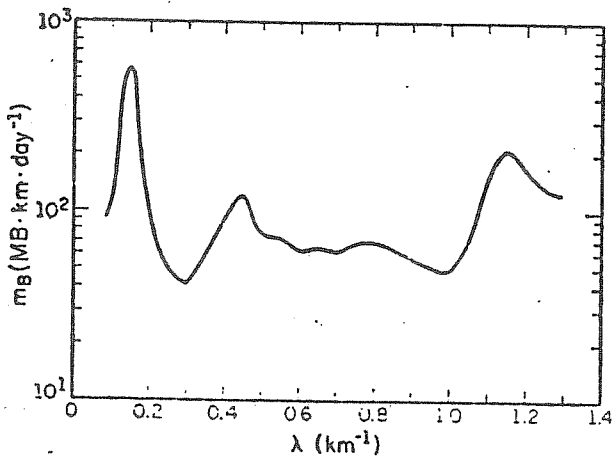


Fig.11.7: Spectral distribution of the vertical mass flux as a function of the entrainment rate λ , computed from Eq.(40). (Yanai et al).

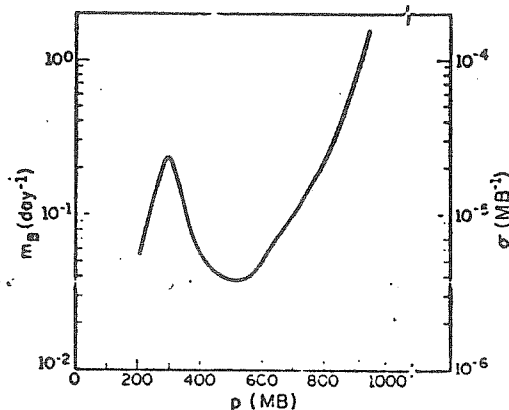


Fig.11.8: Spectral distribution of the vertical mass flux as a function of the cloud top height, computed from Eq.(40). (after Ogura and Cho, 1973).

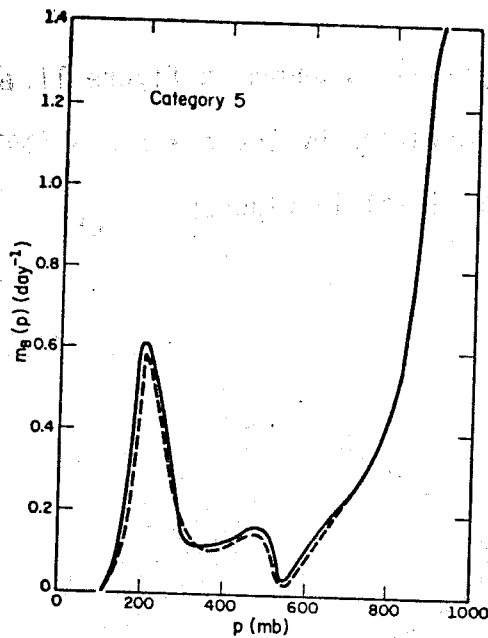


Fig. 11.9 (Cho and Ogura, 1974)

(e) Determination of M_B

In order to determine the cloud mass flux, another condition is required. Arakawa and Schubert (1974) hypothesized that cumulus convection occurs such that the work done by the large scale environmental circulation is balanced with the work done by cumulus convection. In practice, they introduced a "cloud work function," A , which is the work done by buoyancy force due to the heating of convection inside clouds as well as the large scale environmental flow. The functional form is given by

$$A(\lambda) = \int_{Z_B}^{Z_D} \frac{g}{c_p \bar{T}} \eta(z, \lambda) [S_c(z, \lambda) - \bar{S}(z)] dz, \quad (11.41)$$

where η is the normalized cloud mass flux and $\frac{g}{c_p \bar{T}} (S_e - \bar{S})$ is the buoyancy force exerted on the clouds. Then they assumed that

$$\frac{dA}{Dt} = 0 \quad (11.42)$$

This is the most important and crucial assumption in UCLA's parameterization.

As stated above dA/dt is divided into two parts, i.e.,

$$\frac{dA}{dt} = \left(\frac{dA}{dt} \right)_c + \left(\frac{dA}{dt} \right)_{Ls}, \quad (11.43)$$

where c and Ls denote the cumulus convection term and the large-scale environmental circulation term. It can be shown that the first term is written in terms of m_B as

$$\left(\frac{dA}{dt} \right)_c = \int_0^{\lambda_{max}} K(\lambda, \lambda') m_B(\lambda') d\lambda', \quad (11.44)$$

where $K(\lambda, \lambda')$ is the kernel which represents the contribution of other clouds λ' to the cloud λ in question. The term $\left(\frac{dA}{dt} \right)_{Ls}$ does not include m_B at all, i.e.,

$$\left(\frac{dA}{dt} \right)_{Ls} = F(\lambda) \quad (11.45)$$

Thus we have

$$\int_0^{\lambda} K(\lambda, \lambda') m_B(\lambda') d\lambda' + F(\lambda) = 0 \quad (11.46)$$

m_B is solved for the given $F(\lambda)$ and $K(\lambda, \lambda')$. $m_B(\lambda)$ must satisfy either

$$m_B > 0 \quad \text{and} \quad \int K \cdot m_B d\lambda' + F = 0 \quad (11.47)$$

or

$$m_B = 0 \quad \text{and} \quad \int K m_B d\lambda' + F < 0. \quad (11.48)$$

The numerical algorithm to obtain $F(\lambda)$ and $k(\lambda, \lambda')$ is described by Chao, Lord, and Arakawa (1974). First $F(\lambda)$ is calculated in the following way. Using the provisional temperature and moisture fields that are predicted



by the large-scale processes alone over the time interval Δt , the temporary change of $A(\lambda)$ is calculated, and it corresponds to $F(\lambda)$;

$$F(\lambda) = \left(\frac{dA}{dt} \right)_{Ls} \cdot \Delta t.$$

$K(\lambda, \lambda')$ is the rate of increase of $A(\lambda)$ for type λ clouds through the modification of the environment by type λ' clouds per unit m_B . Thus $K(\lambda, \lambda')$ is calculated in the following way. First predict temperature and moisture field over Δt with unit mass flux $m_B(\lambda')$ and zero $m_B(\lambda'')$ for all λ'' such that $\lambda'' \neq \lambda'$. Then the resulting change of $A(\lambda)$ due to the predicted variables, divided by Δt , gives $K(\lambda, \lambda')$.

12. Comparison tests with the refined parameterizations.

Despite the importance of the problem, the papers on comparative studies of the subgrid-scale processes are few in number, (Delsole et al, 1971; Elsberry and Harrison, 1972; Ceselski, 1973; and Washington and Baumhefner, 1974). The first paper (Delsole et al, 1971) investigated the effect of the boundary layer parameterization, and concluded that the effect of land-sea contrast of surface drag is the most substantial of the boundary layer processes, and secondly, that the PBL processes could be important. Nevertheless, the predicted flow field in the extra-tropics reflects little influence by the different parameterization schemes after ten days. The second paper (Elsberry and Harrison, 1972) reported the test of 24 hour forecasts for the Caribbean area with 3 different schemes of latent heat parameterization. The schemes selected were those of Kuo (1965), Pearce-Riehl (1968), and Rosenthal (1968), though the first and the third methods are similar to each other. The conclusion by Elsberry and Harrison was that the three schemes behaved quite similarly in the prediction of the low center, although the regions of precipitation maxima were quite different. So far as the case of non-developing tropical disturbances is concerned, the Pearce-Riehl method most closely predicted the region of actual precipitation maximum. The third paper (Ceselski, 1973) studied the effect of various schemes of cumulus convection, i.e., the CISK method based on Yamasaki, Kuo's method, the moist convective adjustment, and the Arakawa 1969 version. The conclusion from 48 hour forecasts was that all parameterizations produced forecasts of a similar nature; however, the convective adjustment

and the Arakawa 1969 version appears to be less desirable for real data forecasting because they showed excessive heating and produced disorganized weather systems.

Washington and Baumhefner (1974) applied two schemes of cumulus convection parameterization to the NCAR general circulation model, i.e., the moist convective adjustment and the method of Krishnamurti and Moxim (1971). However, the moist convective adjustment they used is slightly different from what was described earlier; the adjustment follows the moist adiabat for upward motion and the dry adiabat for downward motion. The experiments indicated that "the two methods lead to moderate differences in statistics, but it is difficult to conclude which is better overall." They also mentioned that "the Krishnamurti-Moxim scheme leads to tropical lapse rates closer to observed than the convective adjustment, but the rainfall rates are smaller than observed, and the overall temperatures in the tropics are colder than normal."

Summarizing the above three papers, it may be said that the subgrid-scale processes of various versions gave the similar flow patterns for one-day or two-day or even ten-day forecasts, though the precipitations appeared quite different. Anyway, the results of these experiments turned out to be inconclusive, and it is felt that further study is definitely required. In GFDL, such comparative study is under way (Miyakoda and Sirutis, 1975). It was intended originally to present here the results of this experiment, but it is clear that it is not possible, since the experiment is not finished.

The only thing that has been achieved so far is the construction of three different models and to make ten-day predictions with two of the

models. The tentative names of the three models are: A-model, E2-model, and F1-model. A and E2 models use the moist-convective adjustment, whereas F1-model uses the recent Arakawa scheme for the parameterization of cumulus convection. For the vertical mixing in the PBL and free atmosphere, A-model uses the mixing-length approach, where the mixing-length is zero above about the 3km level; E2-model uses the Mellor-Yamada's turbulence closure level 2 model, and the F1-model employed the mixed-layer method in the PBL and no mixing in the free atmosphere except inside cumulus convection. For the surface layer processes, A-model uses Prandtl's aerodynamical method for the case of neutral stratification; E2-model uses Monin-Obukhov version, and F1-model employed Deardorff's drag law and heat and moisture transport method. Heat conduction in the soil is included in the E2 and F1 models only.

Figures 11.1 and 11.2 are the latitudinal distribution of the ten-day averaged rainfall and evaporation for the A and E2 models. It is interesting to note that the difference is extremely large, indicating that the boundary layer processes are very influential on the condensation and evaporation in the tropics (in addition to the sea surface temperature). Figure 11.3 and 11.4 are the zonally averaged zonal component of wind at the tenth day in the meridional section for A-model and E2-model, respectively. In A-model, the easterlies in the equatorial region are weak, whereas in E2-model they are strong, which favorably corresponds to reality. It appears that the vertical mixing in Mellor-Yamada's closure model is operating at that level; the importance has already been mentioned by Stone et al. (1975), though in our case the equivalent eddy viscosity coefficient is much smaller than theirs. A



Fig.11.1: Rainfall

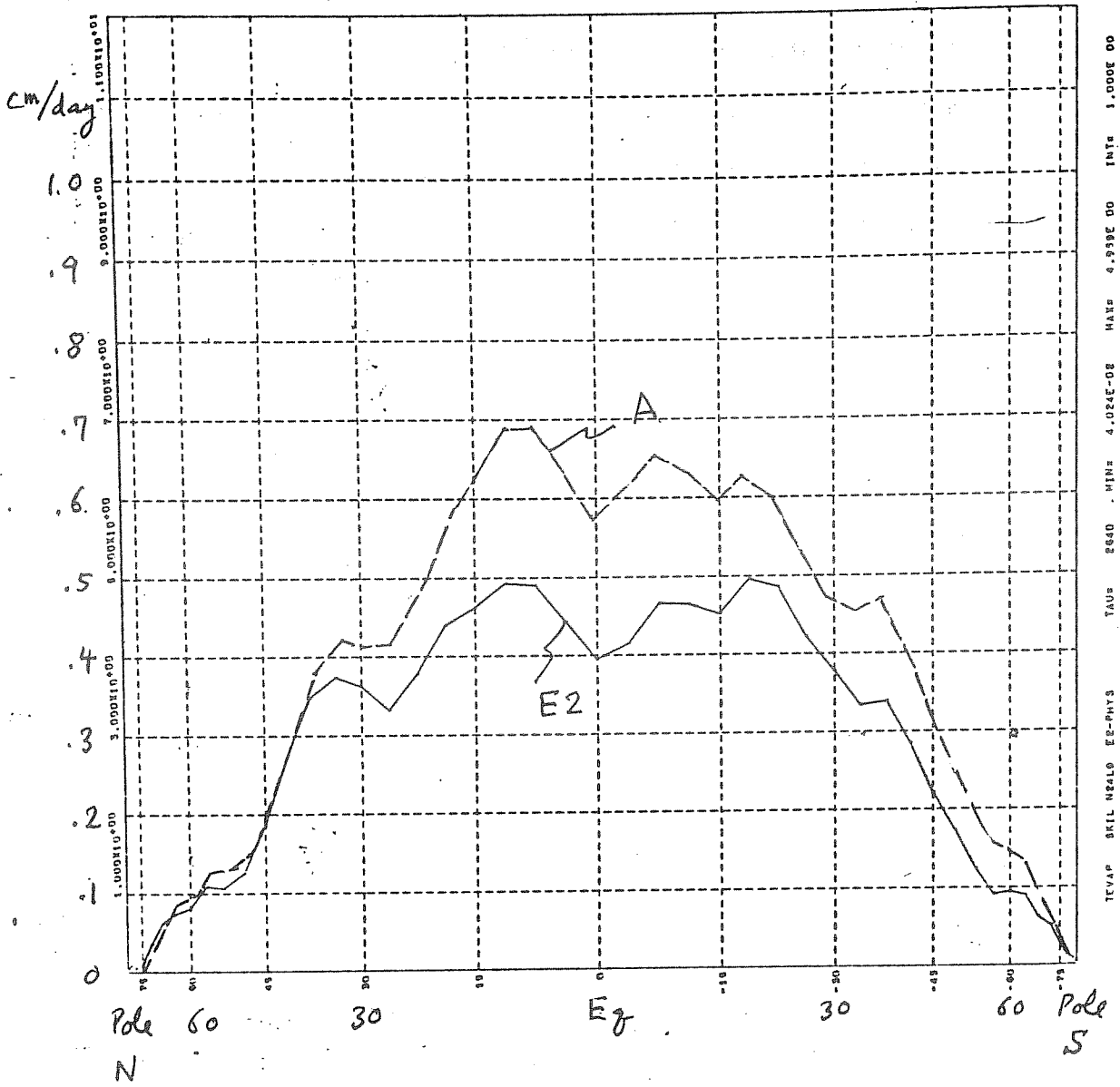


Fig.11.2: Evaporation

similar effect can be seen in the mid-latitudes; the intensity of the westerlies is weaker in E2-model than in A-model. The weaker westerlies correspond more closely to observation. The importance of vertical mixing was also pointed out by Lilly (1972).

F1-model ran for about two days, but it was noticed that the rate of condensation is too large over land, indicating that some trouble exists in the processes of the surface layer as well as in the treatment of soil moisture.

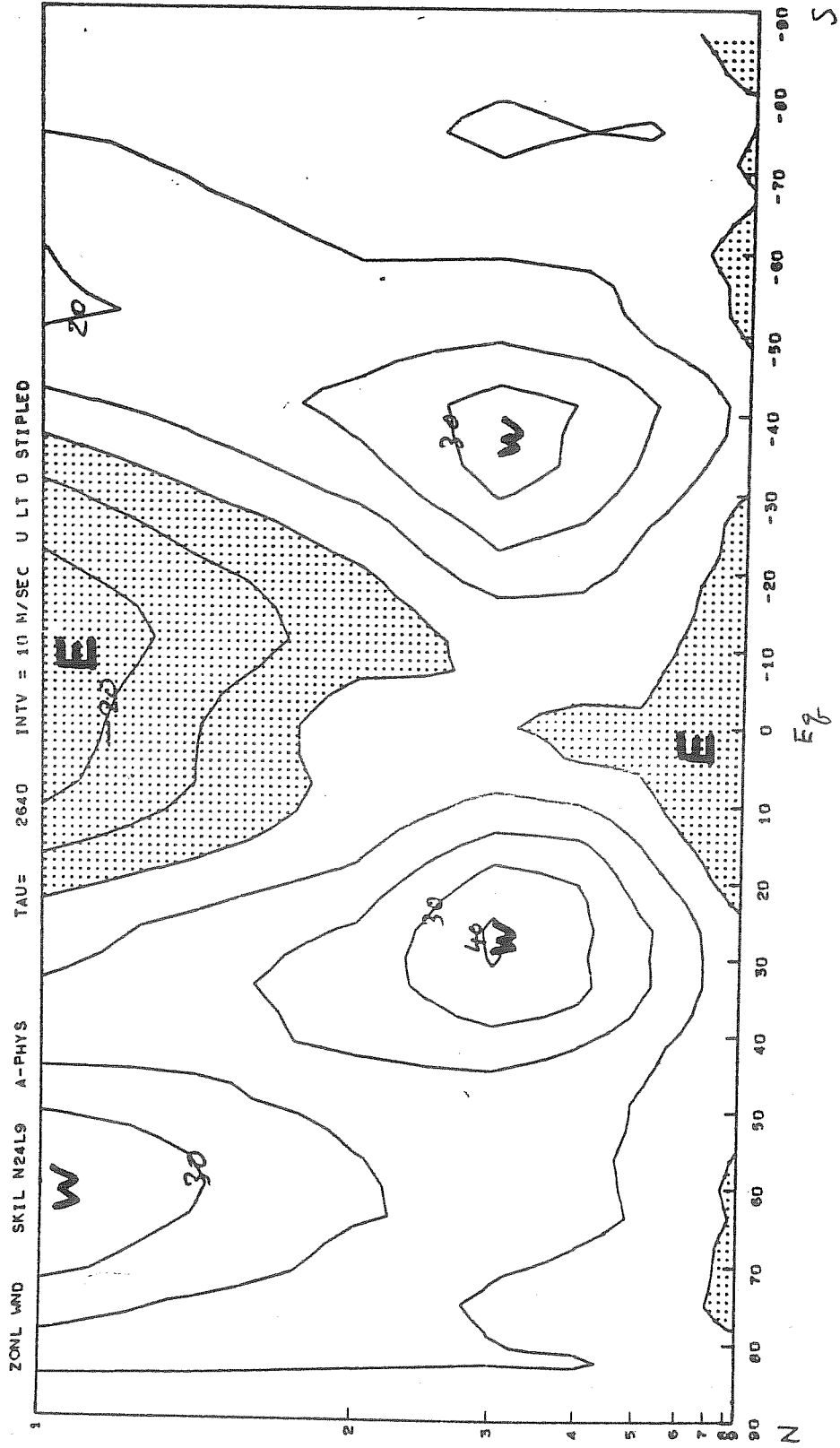


Fig.11.3: A-model

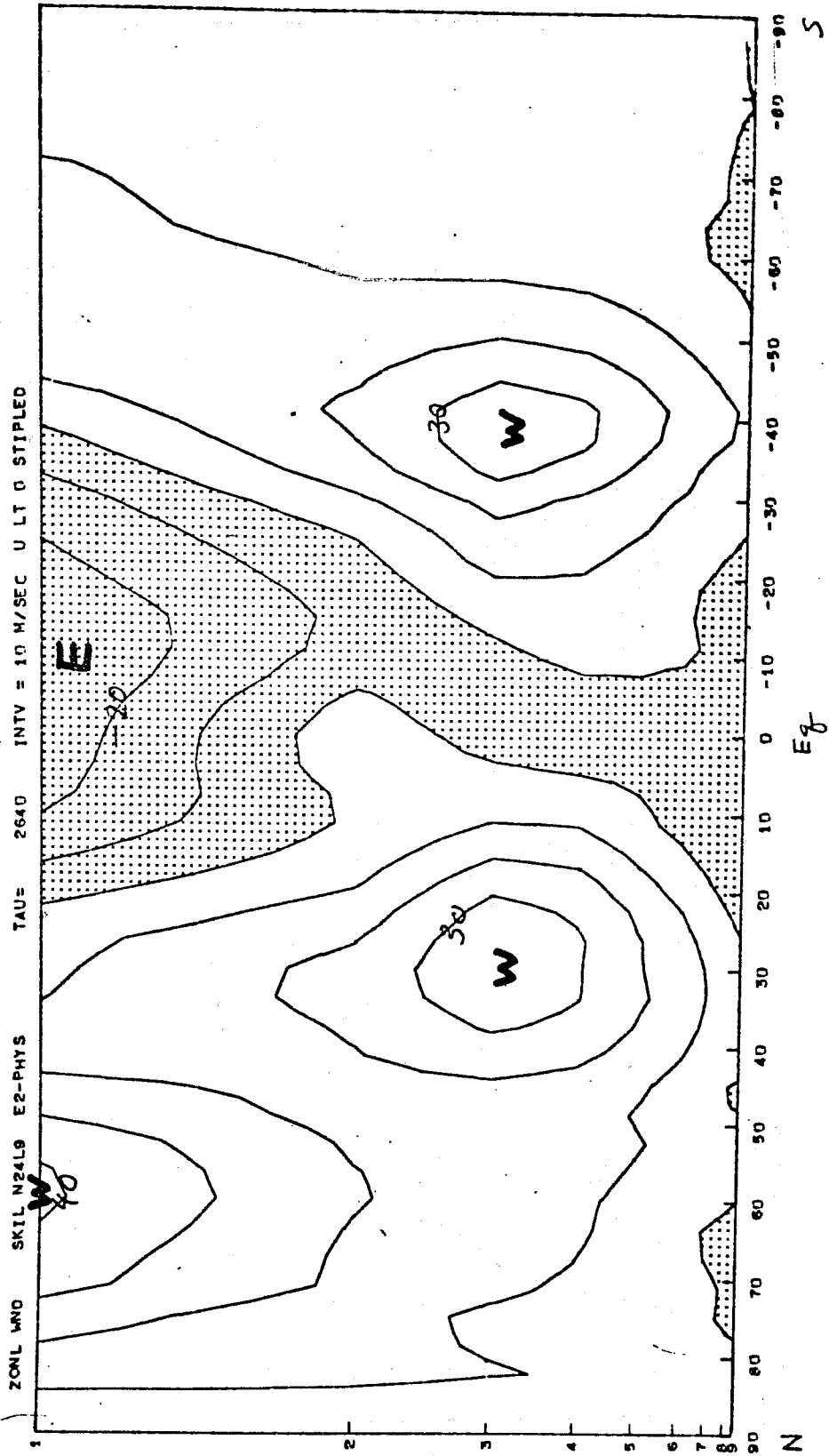


Fig.11.4: E2-model

REFERENCES FOR SECTIONS 10, 11, AND 12

- Arakawa, A. 1969: Parameterization of cumulus convection, Proc. WMO/ICSU Sym. Num. Wea. Pred., Tokyo, 26 Nov - 4 Dec. 1968, Japan Meteor. Agency IV. 8, 1-6.
- Arakawa, A. and W. H. Schubert, 1974: Interaction of cumulus cloud ensemble with the large-scale environment, Part I, J. Atmos. Sci. 31, 674-701.
- Ball, B. K. 1960: Control of inversion height by surface heating. Quart. J. Roy. Met. Soc., 86, 483-494.
- Betts, A. K. 1973: Non-precipitating cumulus convection and its parameterization. Quart. J. Roy. Met. Soc., 99, 178-196.
- Betts, A. K., F. J. Dugan, and R. W. Grover, 1974: Residual errors of the VIZ radiosonde hygrometer as deduced from observations of sub-cloud layer structure. Bull. Amer. Meteor. Soc., 55, No. 9, 1123-1125.
- Blackadar, A. K. 1962: The vertical distribution of wind and turbulent exchange in a neutral atmosphere. J. Geophys. Res. 67, 3095-3102.
- Bhumralkar, C. M. 1975: Parameterization of the planetary boundary layer in atmospheric general circulation models - a review. RAND. ARPA Order No. 189-1.
- Bhumralkar, C. M. 1975: A survey of parameterization techniques for the planetary boundary layer in atmospheric circulation models. RAND. ARPA Order No. 189-1.
- Bretherton, F. P. 1971: GARP and clear air turbulence. Bull. Amer. Met. Soc. 52, No. 1, 17-21.
- Businger, J. A., J. C. Wyngard, Y. Izumi, and E. F. Bradley, 1971: Flux profile relationships in the atmospheric surface layer. J. Atmos. Sci. 28, 181-189.
- Carson, D. J. 1973: The development of a dry inversion-capped convectively unstable boundary layer. Quart. J. Roy. Met. Soc., 99, 450-467.
- Carson, D. J. and F. B. Smith, 1974: Thermodynamic model for the development of a convectively unstable boundary layer. Advances in Geophys., 18A, Academic Press, Inc., New York, San Francisco, London., 111-124.
- Ceselski, B. F. 1973: A comparison of cumulus parameterization techniques. Tellus, 25, No. 5, 459-478.
- Ceselski, B. F. 1974: Cumulus convection in weak and strong tropical disturbances. J. Atmos. Sci. 31, No. 5, 1241-1255.

- Chang, C. P. and T. M. Piowar, 1974: Effect of a CISK parameterization on tropical wave growth. J. Atmos. Sci., 31, 1256-1261.
- Chao, W., S. Lord, and A. Arakawa, 1974: A parameterization of cumulus convection for numerical models of the atmosphere. Notes at Workshop. 25 March - 4 April, 1974, UCLA.
- Chen, W. Y. 1974: Energy dissipation rates of free atmospheric turbulence. J. Atmos. Sci., 31, 2222-2225.
- Clarke, R. H. 1970: Recommended methods for the treatment of the boundary layer in numerical models of the atmosphere. Australian Met. Mag., 18, 51-73.
- Corby, G. A., A. Gilchrist, and R. L. Newson, 1972: A general circulation model of the atmosphere suitable for long period integrations. Quart. J. Roy. Met. Soc., 98, 809-833.
- Deardorff, J. W. 1972: Parameterization of the planetary boundary layer for use in general circulation models. Mon. Wea Rev. 100, 93-106.
- Deardorff, J. W. 1973: The use of subgrid transport equations in a three-dimensional model of atmospheric turbulence. ASME Publication, 1-10.
- Deardorff, J. W. 1975: Three-dimensional numerical study of the height and mean structure of a heated planetary boundary layer. NCAR.
- Delsole, F., K. Miyakoda, and R. H. Clarke, 1971: Parameterized processes in the surface boundary layer of an atmospheric circulation model. Quart. J. Roy. Met. Soc., 97, No. 412, 181-208.
- Denman, K. L. and M. Miyake, 1973: Upper layer modification at ocean station PAPA: observations and simulation. J. Phys. Oceanog., 3, 185-196.
- Donaldson, C. duP and H. Rosenbaum, 1968: Calculation of the turbulent shear flows through closure of the Reynolds equations by invariant modeling. ARAP Rept. 127, Aeronaut. Res. Associates of Princeton, Princeton, N. J.
- Donaldson, C. duP. 1973: Construction of a dynamic model of the production of atmospheric turbulence and the dispersal of atmospheric pollutants. Workshop on Micrometeorology, Boston. Amer. Meteor. Soc., 313-390.
- Elsberry, R. L. and E. L. Harrison, 1972: Effects of parameterization of latent heating in a tropical prediction model. J. Appl. Meteor. 11, No. 2, 255-267.
- Gill, A. E. and J. S. Turner, 1975: A comparison of seasonal thermocline models with observation. (to be published).
- Hayashi, Y. 1970: A theory of large-scale equatorial waves generated by condensation heat and accelerating the zonal wind. J. Meteor. Soc Japan, 48, 140-160.

- Hayashi, Y. 1971: Large-scale equatorial waves destabilized by convective heating in the presence of surface friction. J. Meteor. Soc., Japan, 49, 458-466.
- Hayashi, Y. 1974: Spectral analysis of tropical disturbances appearing in a GFDL general circulation model. J. Atmos. Sci., 31, 180-218.
- Holton, J. M. 1971: A diagnostic model for equatorial wave disturbances; the role of vertical shear of the mean zonal wind. J. Atmos. Sci., 29, 55-64.
- Holton, J. M. 1972: Waves in the equatorial stratosphere by tropospheric heat sources. J. Atmos. Sci., 29, 368-375.
- Kato, H. and O. M. Phillips, 1969: On the penetration of a turbulent layer into stratified fluid. J. Fluid. Mech., 37, 643-655.
- Kuo, H. L. 1965: On formation and intensification of tropical cyclones through latent heat release by cumulus convection. J. Atmos. Sci. 22, 40-63.
- Kuo, H. L. 1974: Further studies of the parameterization of the influence of cumulus convection on large-scale flow. J. Atmos. Sci., 31, No. 5, 1232-1240.
- Kraus, E. B. and J. S. Turner, 1967: A one-dimensional model of the seasonal thermocline: II. The general theory and its consequences. Tellus, 19, 1, 98-106.
- Lamb, V. R. 1973: The response of a tropical atmosphere to middle latitude forcing. Ph.D. thesis, Dept. Meteor., UCLA.
- Lavoie, R. 1972: A mesoscale numerical model of lake-effect storms. J Atmos. Sci., 29, 1025-1040.
- Lewellen, W. S. and M. Teske, 1973: Prediction of the Monin-Obukhov similarity functions from an invariant model of turbulence. J. Atmos. Sci., 30, 1340-1345.
- Lilly, D. K. 1967: The representation of small-scale turbulence in numerical simulation experiments. Proc. IBM Sci., Computing Symp. Environmental Sci., IBM Form No. 320-1951, 195-210.
- Lilly, D. K. 1968: Models of cloud-topped mixed layers under a strong inversion. Quart. J. Roy. Meteor. Soc., 94, 292-309.
- Lilly, D. K. 1972: Wave momentum flux - a GARP problem. Bull. Amer Meteor. Soc., 53, No. 1, 17-23.
- Lindzen, R. S. 1970: Internal equatorial planetary scale waves in shear flow. J. Atmos. Sci., 27, 394-407.
- Lindzen, R. S. 1971: Equatorial planetary waves in shear. Part I., J Atmos. Sci., 28, 609-622.

- Lindzen, R. S. 1974: Wave-CISK in the tropics. J. Atmos. Sci. 31, 156-179.
- Lumley, J. L. and H. A. Panofsky, 1964: The structure of atmospheric turbulence. Interscience Monographs and Text in Physics and Astronomy 12. Interscience Publishers, New York, 239 pp.
- Lumley, J. L. and B. Khajeh-NOURI, 1974: Computational modeling of turbulent transport. Turbulent Diffusion in Environmental Pollution, Edited by F. N. Frenkile, and R. E. Munn., Acad. Press Inc., New York.
- Mak, M. K. 1969: Laterally driven stochastic motions in the tropics. J Atmos. Sci., 21, 41-64.
- Malkus, J. S. 1958: On the structure of the trade wind moist layer. Papers Phys. Oceanogr. Meteor., 13, No. 2, 47 pp.
- Mellor, G. L. 1973: Analytic prediction of the properties of stratified planetary surface layers. J. Atmos. Sci. 30, 1061-1069.
- Mellor, G. L. and T. Yamada, 1974: A hierarchy of turbulence closure models for planetary boundary layers. J. Atmos. Sci. 31, No. 7, 1791-1806.
- Miyakoda, K. and J. Sirutis, 1975: Comparative global predictions experiments on parameterized subgrid-scale vertical eddy transports. (to be published).
- Monin, A. S. 1965: On the symmetry properties of turbulence in the surface layer of air. Izvestia. Atmos. and Oceanic Physics. 1, No. 1, 45-54.
- Monin, A. S. and A. M. Yaglom, 1966: Statistical hydromechanics, Part I: The mechanics of turbulence. Translation U.S. Dept. of Commerce, Joint Publications Research Service No. 37, 763. Washington, D. C. 605 pp.
- Murakami, T. 1972: Equatorial tropospheric waves induced by diabatic heat sources. J. Atmos. Sci., 29, 827-836.
- Ooyama, K. 1974: A dynamical model for the study of tropical cyclone development. Geophysics Intern., 4, 187-198.
- Ooyama, K. 1969: Numerical simulation of the life cycle of tropical cyclones. J. Atmos. Sci., 26, 3-40.
- Ooyama, K. 1971: A theory on parameterization of cumulus convection. J. Meteor. Soc., Japan, 49, (special issue), 744-756.
- Ogura, Y. and H. R. Cho, 1973: Diagnostic determination of cumulus cloud populations from observed large-scale variables. J. Atmos. Sci., 30, 1276-1286.
- Paegle, J. and G. E. Rasch, 1973: Three-dimensional characteristics of diurnally varying boundary-layer flows. Mon. Wea. Rev., 101, 746-756.

- Pandolfo, J. P. and C. A. Jacobs, 1972: Numerical simulations of the tropical air-sea planetary boundary layer. Boundary-layer Meteor. 3, 15-46.
- Pearce, R. P. and H. Riehl, 1968: Parameterization of convective heat and momentum transfer suggested by analysis of Caribbean data. Proc. WMO - ICSU Symp. Num. Eea. Pred., Tokyo, 1, 75-84.
- Pollard, R. T., P. B. Rhines, and O.R.Y. Thompson, 1973: The deepening of the wind-mixed layer. Geophys. Fluid Dyn., 3, 381-404.
- Randall, D. A. and A. Arakawa, 1974: A parameterization of the planetary boundary layer for numerical models of the atmosphere. Workshop of UCLA Atmos. General Circulation Model, March 25 - April 4, 1974, Dept. Meteor. UCLA.
- Riehl, H. and J. S. Malkers, 1958: On the heat balance in the equatorial trough zone. Geophysics, 6, 503-538.
- Rosenthal, S. L. 1969: Numerical experiments with a multi-level primitive equation model designed to simulate the development of tropical cyclones, Experiment I. ESSA Technical Memorandum, ERLTM-NHRL No. 82.
- Stone, P. H., W. J. Quirk, and R. C. J. Somerville, 1974: The effect of small-scale vertical mixing of horizontal momentum in a general circulation model. Mon. Wea. Rev. 102, 765-771.
- Stull, R. B. 1973: Inversion rise model based on penetrative convection. J. Atmos. Sci., 30, 1092-1099.
- Sundquist, H. 1970: Numerical simulation of the development of tropical cyclones with a 10-level model. Part I. Tellus, 22, 359-390.
- Tennekes, H. 1973: A model for the dynamics of the inversion above a convective boundary layer. J. Atmos. Sci., 30, 558-567.
- Trout, D. and H. A. Panofsky, 1969: Energy dissipation near the tropopause. Tellus, 21, 355-358.
- Tsay, C. Y. 1974: Analysis of large-scale wave disturbances in the tropics simulated by an NCAR global circulation model. J. Atmos. Sci., 31, 330-339.
- Washington, W. M. and D. P. Baumhefner, 1974: Use of numerical models for tropical climate simulation and forecasting. Reprint No. I, International Tropical Meteor. Mtg., 31, Jan - 7 Feb. 1974, Nairobi, Kenya.
- Wyngaard, J. C. 1973: On surface layer turbulence. Workshop on Micro-meteorology, Edited by D. A. Haugen, 101-149, Boston, Amer. Meteor. Soc.

- Wyngaard, J. C., O. R. Coté, and K. S. Rao, 1974: Modeling the atmospheric boundary layer. Turbulent Diffusion in Environmental Pollution, edited by F. N. Frenkiel and R. E. Munn, Academic Press, N.Y.
- Yamada, T. 1975: The critical Richardson number and the ratio of the eddy transport coefficients obtained from a turbulence closure model. J. Atmos. Sci., 32, No. 5, 926-933.
- Yamada, T. and G. L. Mellor, 1975: A simulation of the WANGARA atmospheric boundary layer data. (to be published).
- Yamasaki, M. 1968: A tropical cyclone model with parameterized vertical partition of released latent heat. J. Met. Soc. Japan, 46, 202-214.
- Yamasaki, M. 1969: Large-scale disturbances in a conditionally unstable atmosphere in low latitudes. Papers Meteor. Geophys. 20, 289-336.
- Yanai, M. 1971: A review of recent studies of tropical meteorology relevant to the planning of GATE. GATE Experiment Design Proposal, WMO-ICSU, Annex I.
- Yanai, M., S. Esbensen, and J. H. Chu, 1973: Determination of bulk properties of tropical cloud clusters from large-scale heat and moisture budgets. J. Atmos. Sci., 30, 611-627.
- Zilitinkevitch, S. S. 1972: On the determination of the height of the Ekman boundary layer. Boundary-layer Meteor., 3, 141-147.